



# Testing scale invariance in a two-dimensional Bose gas : preparation and characterization of solitary waves

Brice Bakkali-Hassani

## ► To cite this version:

Brice Bakkali-Hassani. Testing scale invariance in a two-dimensional Bose gas: preparation and characterization of solitary waves. Quantum Gases [cond-mat.quant-gas]. Sorbonne Université, 2021. English. NNT : 2021SORUS375 . tel-03591031

**HAL Id: tel-03591031**

**<https://theses.hal.science/tel-03591031>**

Submitted on 28 Feb 2022

**HAL** is a multi-disciplinary open access archive for the deposit and dissemination of scientific research documents, whether they are published or not. The documents may come from teaching and research institutions in France or abroad, or from public or private research centers.

L'archive ouverte pluridisciplinaire **HAL**, est destinée au dépôt et à la diffusion de documents scientifiques de niveau recherche, publiés ou non, émanant des établissements d'enseignement et de recherche français ou étrangers, des laboratoires publics ou privés.



**THÈSE DE DOCTORAT DE SORBONNE UNIVERSITÉ**

préparée par

**BRICE BAKKALI-HASSANI**

**TESTING SCALE INVARIANCE IN A TWO-DIMENSIONAL BOSE GAS:  
PREPARATION AND CHARACTERIZATION OF SOLITARY WAVES**



Soutenue le 10 décembre 2021 devant le jury composé de :

M. Gabriele FERRARI .....	Rapporteur
M. David GUÉRY-ODELIN .....	Rapporteur
Mme. Leticia TARRUELL .....	Examinatrice
M. Xavier LEYRONAS .....	Examineur
M. Jérôme BEUGNON .....	Membre invité
M. Jean DALIBARD .....	Directeur de thèse

Travail réalisé au laboratoire Kastler Brossel, au sein du Collège de France.



## Abstract

At a sufficiently large phase-space density, a Bose gas can be described by a macroscopic wave function subject to nonlinear dynamics. Degenerate Bose gases now constitute a major platform in the study of self-trapped nonlinear fields known as solitons or solitary waves. Up to now, most experimental observations of solitons have been restricted to one-dimensional situations, where they are generically stable. On the contrary, multi-dimensional solitary waves are more prone to instabilities and thus more challenging to observe experimentally. In this thesis, we produce solitary waves in a two-dimensional ultracold bosonic system. After presenting our experimental setup, we demonstrate our ability to produce deterministically a Townes soliton, a celebrated solution of the nonlinear Schrödinger equation in two dimensions. Our novel approach is based on a two-component mixture: starting from a uniform bath of atoms in a given internal state, we imprint the soliton wave function using an optical transfer to another state. We show that the soliton can exist with various sizes, a hallmark of the scale invariance present in the underlying model. We then confirm the relation linking the soliton atom number to the interaction strength. Our experimental observations are supported by further numerical and theoretical considerations. These studies also allow us to go beyond the simplest model sustaining a Townes soliton, by considering effects beyond the mean-field description. Finally, we propose a few experiments aimed at characterizing excited, moving, as well as colliding solitons.

## Résumé

Lorsque la densité dans l'espace des phase d'un gaz de bosons identiques devient suffisamment élevée, il peut alors être décrit par une fonction d'onde macroscopique sujette à une dynamique non linéaire. Ces gaz quantiques sont aujourd'hui devenus des plateformes incontournables dans l'étude des solitons, objets fondamentaux de la physique non linéaire, aussi connus sous le nom d'ondes solitaires. Jusqu'à maintenant, l'essentiel des observations expérimentales de solitons a été limité à des situations unidimensionnelles, où les solitons sont stables naturellement. À l'inverse, les ondes solitaires de plus grande dimension sont généralement fragilisées par la présence d'instabilités dynamiques, rendant leur étude expérimentale plus difficile. Dans cette thèse, nous produisons des ondes solitaires à partir d'un système de bosons bidimensionnel. Après avoir présenté notre dispositif expérimental, nous montrons comment préparer de façon déterministe un soliton de Townes – une solution remarquable de l'équation de Schrödinger non linéaire en dimension deux. Notre approche s'appuie sur l'utilisation d'un gaz à deux composantes : à partir d'un échantillon uniforme d'atomes dans un état interne donné, nous imprimons la fonction d'onde du soliton grâce à un transfert optique vers un autre état. Nous vérifions que le soliton peut exister sous diverses tailles, confirmant ainsi l'invariance d'échelle du modèle physique sous-jacent. Nous confirmons également la relation liant le nombre d'atomes contenu dans le soliton et la force des interactions. Nos observations expérimentales sont corroborées par des études numériques et théoriques. Par ailleurs, ces considérations nous permettent d'étudier la physique au-delà du modèle simple comportant un soliton de Townes, en considérant des effets allant au-delà du champ moyen. Finalement, nous proposons quelques expériences vouées à étudier les excitations, le mouvement et les collisions de tels solitons.





# Remerciements

C'est avec un immense plaisir et une émotion particulière que je dédie ces premières lignes à toutes les personnes qui m'ont, de près ou de loin, permis de mener à bien cette longue aventure qu'est une thèse de doctorat.

Ces remerciements vont tout d'abord à mes directeurs de thèse, Jérôme Beugnon et Jean Dalibard. Jérôme, tu m'as transmis l'essentiel de ce que je retire de ce travail de recherche. D'une aide indispensable au quotidien sur l'expérience, tu m'as aussi permis de travailler à ma manière, me laissant explorer des pistes qui ne paraissaient pas toujours évidentes, m'aidant à ajuster la trajectoire lorsque nécessaire. Merci pour tes conseils, ton écoute et tes patientes relectures du manuscrit. Jean, tes enseignements – dont la limpidité fait l'unanimité – ainsi que ta façon de guider les discussions sur la physique ont profondément modifié ma vision des sciences. Merci pour ta disponibilité et pour tes suggestions qui ont fait mûrir de longues heures de réflexion, en particulier au moment où l'écriture de ce manuscrit touche à sa fin. Merci également à Sylvain Nascimbène qui a énormément contribué aux travaux que je rapporte ici, par ses nombreux apports et ses propositions toujours éclairantes, lors de nos réunions et en dehors.

J'ai eu la chance d'intégrer une équipe exceptionnelle dès mon arrivée au laboratoire. Maintenant que ce doctorat touche à son terme, je perçois d'autant mieux ce que ces personnes m'ont apporté. Merci à Jean-Loup qui concluait l'écriture de son manuscrit au moment de mon stage, et avec qui j'ai fait mes premiers pas sur l'expérience. Merci à Raphaël qui, par ses conseils avisés et son sens physique, a grandement contribué aux performances de cette expérience, depuis sa construction jusqu'à nos plus récents projets. Merci à Patricia qui m'a fait bénéficier de sa grande expérience, de sa rigueur et de son enthousiasme pendant mes deux premières années de doctorat. Merci à Édouard pour ses conseils et pour avoir partagé son vaste savoir tout au long de ma thèse, jusqu'à son départ. Enfin, merci à vous d'avoir amorcé une série d'expériences dont ce travail est le prolongement naturel.

Les générations de doctorant se succédant, ce fut bien vite à mon tour d'accueillir les nouveaux-venus. Tout d'abord, un immense merci à Chloé avec qui j'ai eu la chance de travailler durant ces trois dernières années. Et pas des moindres ! Merci pour ton aide, ton soutien, ces discussions et ces réflexions essentielles, tout ce sans quoi ce projet n'aurait pu ressembler à ce qui est retranscrit ci-après. C'était le moins que l'on puisse attendre d'un binôme qui fonctionne si bien. Merci mille fois de m'avoir confié Sohan, un petit chat un tantinet turbulent mais si mignon à la fois. Merci également à Yiquan qui nous a apporté énormément durant les deux années de son contrat post-doctoral. Un grand merci ensuite à Guillaume. Arrivé en pleine crise sanitaire, tu as fait preuve d'une persévérance et d'une rigueur épatantes. Merci à Franco qui, tout juste débarqué, est venu épauler Guillaume dans la construction d'une nouvelle expérience. À terme, celle-ci remplacera le dispositif dont je rapporte ici les aventures. Merci à vous deux de rester sur tous les fronts, vous

montrant chaque fois curieux de comprendre ce que nous mijotons à côté. Il ne fait pas de doutes que l'équipe Rubidium a encore de très beaux jours devant elle.

La vie de laboratoire ne serait pas la même sans compter toutes les personnes qui habitent ou ont habité le deuxième étage du bâtiment E. Merci à celles et ceux qui ont rendu ces années si enrichissantes, aussi bien humainement que scientifiquement, aussi bien autour d'un café, d'un croissant, d'un cake banane-Nutella, que d'une pinte de bière. Merci à Chayma, Raphaël, Thomas, Manel, Nicolas, An, Bertrand, Merlin, Alexis, Alexandre, Sébastien, Tanish, Rémy, Aurélien, Julien, Jean-Baptiste, Quentin, Tristan, Sarah, Virgin. Merci à Raphaël Lopes et Alexei Ourjountsev qui ont toujours été disponibles lorsque je les sollicitais. Merci à Carmen Toderasc et à toute l'équipe administrative du LKB pour leur aide si précieuse. Merci également aux amis du rez-de-chaussée, Paul, Léa, Rémy, Andrea, Brice, Rodrigo, et à toutes celles et ceux que j'ai eu la chance de cotoyer au Collège de France. Merci enfin à Nicolas Treps, mon parain pendant ces trois années, pour son écoute ainsi que ses conseils.

Ce travail n'aurait pas été ce qu'il est sans le soutien inconditionnel de mes proches, de mes amis et de ma famille. Merci à mes parents d'avoir été toujours présents et pleins d'enthousiasme. Un grand merci à mon frère et à ma soeur pour qui l'aventure du doctorat n'est pas si étrangère. Merci à mes comparses sans qui ces années de thèse aurait été nettement moins marrantes, je pense bien évidemment à Bruno et à Tristan. D'où qu'ils lisent ces lignes, je leur dis simplement bonjour. Merci à François qui saura, probablement mieux que moi, expliquer le contenu de cette thèse, le tout en musique. Merci à Elisa qui a rendu cette dernière année de doctorat si merveilleuse, et qui m'a accompagné dans les jours les plus difficiles de la rédaction de ce manuscrit. Merci enfin à toutes celles et ceux qui ont été là durant ces années, Marius, Maxime, Simon, Ayman, Lisa, Lina, Alice, Elise, Serena, Pierre, Gaspard, Damien, Francesca, Artiom, Radu-Alexandru, Perrine, Sarah, tous les voisins du 142 rue d'Avron et toute l'équipe du centre Emmaüs Pyrénées.

# Contents

<b>Introduction</b>	<b>11</b>
<b>1 Production of planar Bose gases</b>	<b>17</b>
1.1 Experimental sequence . . . . .	17
1.1.1 Preliminary steps . . . . .	18
1.1.2 A tunable horizontal confinement . . . . .	22
1.1.3 Some calibrations . . . . .	26
1.2 Preparation of binary mixtures . . . . .	29
1.2.1 Internal degrees of freedom . . . . .	29
1.2.2 Magnetic dipole-dipole interactions . . . . .	33
1.3 Conclusion . . . . .	36
<b>2 Description of a two-dimensional Bose gas</b>	<b>37</b>
2.1 Description at zero temperature . . . . .	37
2.1.1 The nonlinear Schrödinger equation . . . . .	37
2.1.2 Ground state and dynamics . . . . .	40
2.1.3 Symmetries in two dimensions . . . . .	43
2.2 Description at finite temperature . . . . .	46
2.2.1 Classical field formalism . . . . .	47
2.2.2 Description at low temperature . . . . .	48
2.2.3 Berezinskii-Kosterlitz-Thouless transition . . . . .	50
2.3 Conclusion . . . . .	52
<b>3 Physics of Townes soliton</b>	<b>53</b>
3.1 Solitons of the nonlinear Schrödinger equation . . . . .	53
3.1.1 Solitons in one dimension . . . . .	54
3.1.2 Multidimensional solitons . . . . .	58
3.2 Properties of the Townes soliton . . . . .	62
3.2.1 Stationary states of the 2D NLSE . . . . .	62
3.2.2 Stability of the Townes soliton . . . . .	66
3.3 Wave-packet collapse . . . . .	68
3.3.1 Conditions for collapse . . . . .	68
3.3.2 Collapse dynamics . . . . .	70
3.4 A recent experiment . . . . .	71
3.4.1 Quench of a 2D Bose gas . . . . .	71
3.4.2 Modulational instability . . . . .	71
3.5 Conclusion . . . . .	73

<b>4</b>	<b>Realization of a Townes soliton</b>	<b>75</b>
4.1	Effective one-component dynamics . . . . .	75
4.1.1	Weak depletion regime . . . . .	75
4.1.2	Preparation and detection . . . . .	78
4.1.3	An example dynamics . . . . .	81
4.2	Dynamics of a Townes profile . . . . .	82
4.2.1	Various atom numbers . . . . .	83
4.2.2	Check of scale invariance . . . . .	86
4.2.3	Finite-depletion regime . . . . .	88
4.3	Conclusion . . . . .	89
<b>5</b>	<b>Single-component description of a binary mixture</b>	<b>91</b>
5.1	Two-component description . . . . .	91
5.1.1	An immiscible mixture . . . . .	91
5.1.2	Spin bubbles . . . . .	94
5.2	Effective one-component description . . . . .	98
5.2.1	Turning the coupled NLSEs into a single one . . . . .	98
5.2.2	A microscopic point-of-view . . . . .	102
5.3	Beyond the nonlinear Schrödinger equation . . . . .	104
5.3.1	Polaron physics . . . . .	104
5.3.2	The influence of finite temperature . . . . .	104
5.3.3	Beyond mean-field effects . . . . .	105
5.4	Conclusion . . . . .	107
<b>6</b>	<b>Perspectives on spin bubbles dynamics</b>	<b>109</b>
6.1	Stability and elementary excitations . . . . .	109
6.1.1	Methods . . . . .	110
6.1.2	Weak depletion regime . . . . .	111
6.1.3	Surface modes . . . . .	113
6.1.4	The experimental point-of-view . . . . .	115
6.2	Collisions of Townes solitons . . . . .	116
6.2.1	Collisions under the cubic NLSE . . . . .	116
6.2.2	Extension to a binary mixture . . . . .	119
6.3	Conclusion . . . . .	120
	<b>Summary and outlook</b>	<b>121</b>
<b>A</b>	<b>Elementary excitations of the Townes soliton</b>	<b>123</b>
A.1	Continuous symmetries . . . . .	123
A.2	Stability analysis . . . . .	125
A.3	Neutral modes and symmetries . . . . .	126
<b>B</b>	<b>Variational method</b>	<b>129</b>
<b>C</b>	<b>Anisotropic contribution of MDDI</b>	<b>131</b>
<b>D</b>	<b>Perturbative expansions for data analysis</b>	<b>135</b>
D.1	Dynamics of Townes profiles . . . . .	135
D.2	Dynamics of Gaussian profiles . . . . .	136

<b>E Numerical recipes for the 2D NLSE</b>	<b>137</b>
E.1 Resolution in 2D . . . . .	137
E.2 Using radial coordinates . . . . .	140
<b>F Induced interactions</b>	<b>143</b>
F.1 A single impurity . . . . .	143
F.2 The effective potential . . . . .	146
<b>G Elementary excitations of spin bubbles</b>	<b>149</b>
<b>H Publications</b>	<b>153</b>
<b>Bibliography</b>	<b>189</b>



# Introduction

The *wave function* is a fundamental concept in quantum physics. This function associates a complex-valued probability amplitude to each possible configuration of a physical system. In non-relativistic quantum mechanics, the state of any isolated system of particles can be described in this manner. Because its evolution is described by a linear wave equation – the Schrödinger equation – the wave function behaves essentially like other waves do, be it sound or light. In particular, this wave-like description brings the possibility to observe *interference* phenomena, which arise when multiple waves associated to the same field overlap. The duality between a wave-like and a corpuscular behavior is itself at the origin of several difficulties in the interpretation of quantum mechanics. Experimentally, quantum interference can now be observed using mesoscopic systems, such as large molecules for instance [1–3]. Nonetheless, the description of most macroscopic systems in terms of a wave function is out of reach. Indeed, the number of arguments of this function then scales like the number of particles. Moreover, interactions between particles generically lead to complicated correlations that cannot be disentangled. As a corollary, the observation of interference phenomena is usually unrealistic for such systems.

For a many-body system, there are specific situations which allow a description with much less degrees of freedom. For instance, if an assembly of indistinguishable particles occupies the same state, then it is sufficient to use a single-particle wave function – the *macroscopic wave function* – to describe the whole system. When the number of particles is so large that one can neglect its discrete nature, the problem can be reduced to a *classical field theory* for this macroscopic wave function. In such cases, the corresponding state bears a well-defined phase and can lead to interference phenomena. This *coherent* field has thus a lot in common with the electromagnetic field emitted by a laser source. This reasoning can also be extended to a situation where only a few single-particle states are massively populated. In this case, the macroscopic state will be described by a field involving the same number of components as there are relevant states.

Which conditions can lead to such a behavior? First of all, the particles should be *bosons* since they can occupy the same quantum state. Remarkably, the above situation appears as a direct consequence of the phenomenon of *Bose-Einstein condensation*, initially predicted for an ideal system of massive bosons [4]. Below a certain critical temperature, a macroscopic fraction of the particles is expected to accumulate in the state of lowest energy. This transition is thus a manifestation of the gregarious nature of bosons. A description in terms of a classical field has been fruitful in the case of superfluid Helium 4, which was realized to exhibit quantum mechanical properties on a large scale soon after its discovery [5]. This also applies to the Ginzburg-Landau theory of superconductivity [6] for which the notion of a common state is meaningful only for pairs of electrons, the latter being fermions. In both situations, this classical field description is supported by the observation of coherent phenomena, such as Josephson oscillations or quantized vortices.



Moreover, there is a deep connection between these two behaviors and the phenomenon of Bose-Einstein condensation. However, interactions are never rigorously absent for massive particles and, in these situations, the use of a macroscopic wave function is mostly phenomenological. Indeed, a rigorous derivation of a classical field theory from microscopic principles is hindered by the presence of strong interactions and the induced correlations.

Experimentally, ultracold quantum gases provide an important realization of a *weakly-interacting system*. Since the first demonstration of Bose-Einstein condensation in 1995 [7, 8], these dilute, defect-free, isolated and fully tunable systems have become a major tool in the study of many-body quantum phenomena. In an early and spectacular experiment, two separated condensates were made overlapping and displayed an interference pattern [9]. This – and many other experiments – confirmed the wave-like properties of ultracold bosonic systems, often referred to as *coherent matter-waves*. On the theoretical point-of-view, the macroscopic state of the system can be understood using a single-particle nonlinear wave equation for the macroscopic wave function, the so-called nonlinear Schrödinger equation (NLSE). In the context of superfluid systems, this equation is also known as the Gross-Pitaevskii equation. Most developments presented in this thesis will rely on this model. In the weakly-interacting regime, the nonlinear term can be obtained directly by treating all interactions in a mean-field picture. Although the full quantum problem is itself linear with respect to the many-body wave function, the appearance of an effective nonlinearity is the price to pay for this considerable simplification.

Since they can be described using a nonlinear wave equation, quantum gases soon became a novel platform for the study of *nonlinear phenomena*. While the importance of linear physics does not need to be debated, nonlinear physical phenomena have become a central and transverse research field over the second half of the twentieth century. In particular, physicists have realized that nonlinear wave equations, although more difficult to grasp and to analyze mathematically, could lead in general to much richer behaviors. Historically, nonlinear physics have first become a prominent research axis in the context of hydrodynamics. Indeed, the Navier-Stokes equations on its own can yield a multitude of nonlinear behaviors such as various types of instabilities [10].

*Solitons* are probably some of the most important and fascinating objects in nonlinear physics. In mathematical terms, solitons can be defined as stationary solutions of nonlinear wave equations. They typically arise from the compensation of a linear dispersion effect by a nonlinear contraction mechanism. Solitons were first discovered in the context of hydrodynamics, for one-dimensional (1D) problems. In 1845, J. S. Russell [11] described a solitary elevation of water propagating in a narrow channel. Importantly, his observations could not be interpreted using a linear wave equation. At that time, the impact of this discovery was already undeniable at the theoretical level. Yet, the generality and the scope of the concept of solitons could not be properly appreciated, both on the theoretical and the experimental side. Following the work of Zabusky & Kruskal [12] in 1965, solitons were shown to be extremely general and stable solutions for some 1D problems. More generally, solitons are encountered in a broad range of physical settings, including nonlinear photonics, hydrodynamics, superconductors, polymers, plasmas, and even high-energy physics [13].

In dimension larger than one, the creation, the manipulation and the observation of self-bound fields is a central challenge [14]. Indeed, there exists a great variety of such states, in particular because these can feature a nontrivial topology. Moreover, the dynamics and the interactions between such objects bring an even richer phenomenology [15]. In parallel,

the introduction of multiple components in the field degrees of freedom can also lead to new behaviors and can yield composite solitons. Unfortunately, the solitons present in the most simple NLSE models are generically unstable with respect to small perturbations, a property less present in 1D systems. To circumvent this issue, numerous strategies have been proposed theoretically to protect these states against instabilities, and few of these experiments have been implemented.

Let us discuss specifically the case of nonlinear optics. Soon after the invention of lasers in 1960, it was realized that the propagation of coherent and intense light beams through matter was significantly affected by nonlinear (Kerr) effects. Moreover, in a stationary situation well captured by the paraxial approximation, this behavior can be described using the NLSE by replacing the time variable by the distance on the propagation axis. This culminated with the first observations of nonlinear self-trapping of light [16–19], and soliton propagation in optical settings [20, 21]. Intriguingly, it turns out that light and matter – which are fundamentally of very different nature – can be described in a unified framework under specific conditions.

In this thesis, we will be interested in the celebrated *Townes soliton*. This soliton is a localized solution of the 2D NLSE with a cubic nonlinearity. More precisely, it is the unique real, nodeless, and axially symmetric solution of the 2D NLSE. The Townes soliton was first predicted by Chiao et al. [17] and Talanov [18] in the context of self-trapping of intense laser beams in nonlinear media. This soliton bears some peculiar properties inherited from the 2D NLSE. For instance, its  $L^2$ -norm is fixed by the strength of the nonlinearity. Furthermore, it can be formed with any size, a hallmark of the *scale invariance* of the 2D NLSE. However, the Townes soliton is unstable as small deviations away from equilibrium can lead to the collapse of the field. For all these reasons, the quest for this soliton has triggered a myriad of experimental works in nonlinear optical settings.

The toolbox of the cold-atom physicist is particularly well adapted to the preparation and the study of multidimensional fields, especially when complex state engineering is required. On the one hand, the availability of high-resolution optical systems allows the *in-situ* observation of quantum gases with unprecedented accuracy. On the other hand, a great variety of initial states and Hamiltonians can now be tailored. For instance, the geometry of these systems can be controlled using a great variety of optical potentials. This has allowed the observation of dark and bright solitons in quasi-1D geometry in pioneering experiments [22–24]. Furthermore, spatial light modulators now allow the production of ever-more complex light-field configurations. Such techniques can be used to design optical box potentials [25] or to imprint specific phase profiles on the atomic wave function. In addition, atomic species naturally come with an internal structure which allows the exploration of multi-component or spinor physics [26]. This was recently illustrated by the realization of magnetic solitons in two-component [27] or spin-1 Bose-Einstein condensates [28].

Interestingly, quantum gases also offer the possibility to go beyond a description in terms of a classical field. In particular, the use of Feshbach resonances [29] has allowed to explore strongly correlated phases of matter, while staying in the dilute regime where a theoretical treatment is still conceivable. Is it possible to observe effects beyond the mean-field description, without leaving the regime of weak interactions? In 2015, Petrov [30] positively answered this question by introducing the concept of *quantum droplets*. Experimentally, such droplets have now been realized using either binary mixtures of quantum gases described by short-range interactions [31, 32] and single-component systems

of highly-magnetic atoms where dipole-dipole interactions play a significant role [33, 34]. In both cases, the interactions – treated at the mean-field level – are set to be weakly attractive, yielding an unstable situation *a priori*. The inclusion of quantum fluctuations – going beyond the mean-field description – then provides a repulsive effect with a different scaling in density which can stabilize the system. Eventually, the balance between these two mechanisms defines an equilibrium density. A large system would feature a flat-top density profile over a large region, similarly to an incompressible fluid. These constitute an important realization of stabilized multidimensional fields.

Quantum droplets bear strong analogies with other systems encountered in condensed matter physics, such as Helium droplets [35–37]. In this last case, however, the densities and the effect of interactions make the system not amenable to a rigorous theoretical treatment. The discovery of dilute quantum droplets has thus opened new directions to gain insight on quantum liquids. Furthermore, these systems also allow to study exotic phases of matter such as *supersolids*, which were predicted in 1970 by Leggett in the context of solid Helium [38]. According to the current definition, a supersolid should present both superfluid properties and an interaction-induced periodic density modulation. Interestingly, the NLSE with a well-chosen nonlocal nonlinearity can support a ground state with supersolid properties [39]. Emergent platforms having demonstrated signatures of supersolidity include dipolar quantum gases [40–42], systems interacting strongly with optical cavities [43], spin-orbit-coupled BECs [44].

In this manuscript, I present our recent realization of a Townes soliton using a two-component planar Bose gas [45]. Our experimental apparatus allows us to prepare cold bosonic samples confined in two dimensions (2D), with a versatile potential in the horizontal plane. At zero temperature, one can faithfully use a description in terms of a classical field satisfying the 2D NLSE. Since interactions in the system are all repulsive, our situation seems *a priori* incompatible with the attractive interactions required to observe a Townes soliton. We developed a novel approach using a two-component system. In the case where one component is in a strong minority, one obtains effectively attractive interactions between the atoms in this component. In contrast with other recent studies of 2D solitary waves emerging from a dynamical instability [46, 47], we *deterministically* prepared a Townes soliton using an optical transfer. Finally, we also draw fruitful analogies between our system and the behavior of quantum droplets.

I will now detail the content of this thesis.

- In **Chapter 1**, I describe the experimental platform which allows us to prepare planar samples of Rubidium 87. In particular, I discuss the techniques used for tailoring controllable optical fields, as reported in [48]. This is crucial to prepare binary systems with arbitrary spin distributions.
- In **Chapter 2**, I provide some theoretical tools to describe the weakly-interacting 2D Bose gas. I also justify the use of the NLSE for studying this system even at low (but finite) temperature.
- In **Chapter 3**, I discuss the existence and the properties of solitons, focusing on the single-component NLSE with attractive interactions. In particular, I introduce the celebrated Townes soliton and discuss its main features.
- In **Chapter 4**, I present our main experimental results concerning the deterministic preparation and the characterization of Townes solitons using a two-component

planar Bose gas. Starting from a uniform bath of atoms in a given state, our protocol consists in imprinting the wave function of the Townes soliton using an optical transfer to another state. Throughout this manuscript, this novel composite system will be called a *spin bubble*.

- In **Chapter 5**, I justify the use of a single-component attractive NLSE for interpreting the results of Chapter 4, even though the system is made of two components with only-repulsive interactions. This mapping is rooted in the immiscible character of the binary mixture.
- In **Chapter 6**, I propose a few directions for future characterizations of spin bubbles. More precisely, I determine the excitation spectrum of spin bubbles in various regimes. I also investigate the outcome of binary collisions of Townes solitons.
- In the various appendices gathered at the end of the manuscript, I complement some of our results and derive some others step-by-step.

During my thesis, I had the opportunity to work on several other projects using this experimental setup. Most of these results not being detailed in the manuscript, I now dedicate a few lines to mention them. A list of the four corresponding publications can be found in Appendix H. The weakly-interacting 2D Bose gas has specific properties, both at equilibrium and from a dynamical point-of-view. In [49], we related far-from-equilibrium dynamics of distinct initial systems linked by scaling transformations. We also reported the discovery of breathing solutions of the nonlinear dynamics. The emergence of a superfluid phase in 2D at low temperature is described by a peculiar phase transition, the so-called Berezinskii-Kosterlitz-Thouless phase transition. A noteworthy signature of this transition shows up in the first-order correlation function of the system, which quantifies the spatial coherence of the atomic field. This function decays exponentially fast in the normal phase, whereas it is expected to show a power-law behavior in the superfluid phase. A determination of this correlation function using matter-wave experiments has been reported in the thesis of Raphaël Saint-Jalm [50]. During this last year, we developed a spectroscopic method analogous to Ramsey interferometry for our many-body system. Using this method, we could measure the so-called Tan’s contact accross the BKT transition [51]. We could also reveal the subtle effect of magnetic dipole-dipole interactions in a 2D geometry [52]. Finally, our exploration of immiscible binary mixtures started with the study of the demixion instability [53].



# Chapter 1

## Production of planar Bose gases

This thesis explores some aspects specific to quantum planar systems. For a two-dimensional (2D) system of atoms with mass  $m$ , density  $n$  and temperature  $T$ , the importance of quantum statistics on collective properties is quantified by the so-called *phase-space density*

$$\mathcal{D} = n\lambda_{\text{th}}^2, \quad (1.1)$$

which compares the inter-particle distance  $\sim n^{-1/2}$  to the thermal wavelength  $\lambda_{\text{th}} = \sqrt{2\pi\hbar^2/mk_B T}$ . At standard temperatures,  $\lambda_{\text{th}}$  gives the typical extension of individual wave packets. A large system reaches the regime of *quantum degeneracy* when this wavelength gets of the order of the inter-particle distance, or equivalently when  $\mathcal{D}$  becomes of order unity. As a celebrated example, preparing an assembly of bosons at a large phase-space density in 3D may allow one to observe Bose-Einstein condensation [4], i.e. the macroscopic accumulation of particles in the state of lowest energy. *Quantum gases* thus offer a unique access to exotic states of matter [54]. However, the preparation of such systems requires the control of both the internal and the external degrees of freedom of individual atoms.

In this chapter, we present the setup used throughout this thesis to produce 2D degenerate samples of gaseous Rubidium 87 ( $^{87}\text{Rb}$ ), a bosonic isotope with one valence electron and a nuclear spin  $I = 3/2$  [55]. While many species can now be brought to quantum degeneracy, atomic vapors of  $^{87}\text{Rb}$  keep the advantage of being easily cooled and manipulated. Since most of the current setup was built before my arrival in the group, we refer the reader to the previous Master and PhD theses [50, 53, 56–58] for detailed characterizations. As we show in Sec 1.1, we are able to create a single slab of atoms in the quasi-2D regime, with a fully programmable in-plane geometry. The central topic of this thesis is the study of solitons using binary mixtures. In Sec 1.2, we show how to manipulate the internal degree of freedom of the atoms for the preparation of two-component planar Bose gases.

### 1.1 Experimental sequence

We first summarize the ingredients for the preparation of 2D systems with an arbitrary geometry in the horizontal plane. The preliminary steps for all our experiments are presented in Subsec 1.1.1, while Subsec 1.1.2 is devoted to the description of our horizontal confinement. Finally, some calibrations needed to characterize the system are detailed in Subsec 1.1.3.

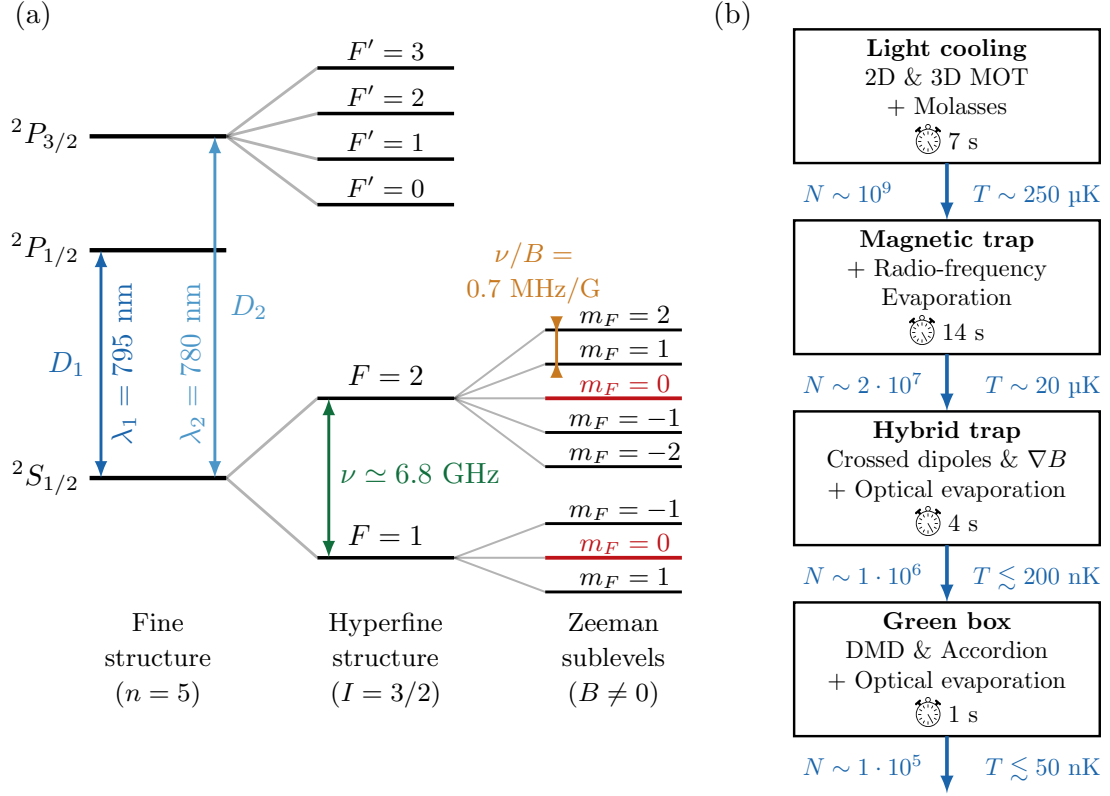


Figure 1.1: (a) Internal structure of  $^{87}\text{Rb}$ . We depicted only levels relevant for the experiments. All states have a principal quantum number  $n = 5$  for the valence electron. Light on the  $D_2$  line is slightly red-detuned with respect to the  $(F = 2 \rightarrow F' = 3)$  cycling transition, used for laser-cooling. The hyperfine splitting in the electronic ground state manifold lies in the micro-wave domain, and the degeneracy between the various Zeeman sublevels is lifted in the presence of a magnetic field  $B$ . The two states figured in red,  $|F = 1, m_F = 0\rangle \equiv |1\rangle$  and  $|F = 2, m_F = 0\rangle \equiv |2\rangle$ , are the protagonists of our experimental findings. (b) Time-line of the experimental sequence showing the duration of the main time-steps. The resulting atom number  $N$  and the temperature  $T$  are represented after each box.

### 1.1.1 Preliminary steps

In the following, we consider only the low-lying states of  $^{87}\text{Rb}$ . The relevant part of its energy structure is thus shown in Fig 1.1(a). At low magnetic field, internal levels are characterized by their total (integer) angular momentum  $F$  and its projection along a quantization axis, indexed by  $m_F$ . Our setup exploits the usual techniques for preparing a degenerate alkali Bose gas, as summarized in Fig 1.1(b). Each experimental sequence lasts approximately 30 s and is computer-controlled with the software Cicero-Word generator. In the next paragraphs, we detail the various preliminary steps.

#### Laser cooling

In a vacuum system with pressure  $\sim 10^{-7}$  mbar, a piece of solid Rb is heated up to  $65^\circ$ . A 2D magneto-optical trap (MOT) captures a tiny part of the vapor which rises from it. An adjacent glass-cell of dimension  $105 \times 25 \times 25 \text{ mm}$  under higher vacuum

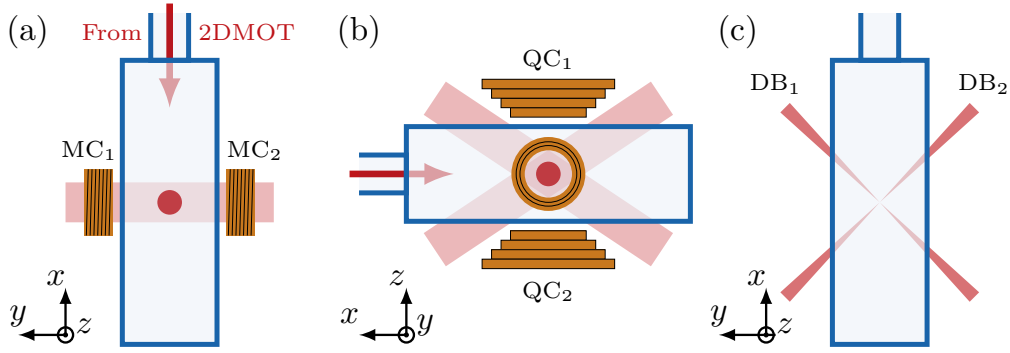


Figure 1.2: Preliminary steps. A 3D magneto-optical trap is loaded from an adjacent 2D MOT via a pushing laser beam (red arrow). The 3D MOT is made of six laser beams and a quadrupolar magnetic field produced by the coils  $MC_x$  ( $x = 1, 2$ ). (a) Top view of the glass cell. The cloud is depicted as a red dot (not at scale). (b) Side view. Are also shown the conical coils  $QC_x$  for the magnetic trap. (c) Top view, with the two crossed dipole beams  $DB_x$  loaded from the magnetic trap.

(pressure  $< 10^{-10}$  mbar) is loaded using a laser pushing beam, as shown in Fig 1.2(a-b). Simultaneously, a 3D MOT is switched on at the center of the cell. All laser beams are produced from a laser with wavelength 780 nm, and cooling is performed on the  $D_2$ -line using the ( $F = 2 \rightarrow F' = 3$ )-cycling transition. A quadrupolar magnetic field is generated by two coils in anti-Helmoltz configuration along the  $x$ -axis.

After loading the 3D MOT for 7 s, approximately  $10^9$  atoms end up trapped in the region where the six MOT beams overlap, at a temperature of 250  $\mu$ K and isolated from any material support. The MOT is then compressed by ramping the laser-light detuning. A molasses time-step follows for further cooling. Eventually, atoms undergo an optical pumping stage and are transferred into the hyperfine ground state  $F = 1$ .

### Magnetic and optical traps, evaporative cooling

The cloud is subsequently transferred to a magnetic trap. This trap is made of a pair of conical coils mounted along the vertical  $z$ -axis in anti-Helmoltz configuration, see Fig 1.2(b). Since only low-field seekers are trapped, we retain only atoms in state  $|F = 1, m_F = -1\rangle$ , which represent  $\simeq 1/3$  of the total atom number. After compressing the trap for increasing the collision rate, radio-frequency evaporation is performed during 12 s. Atoms with a large energy are forced to leave the trap and the remaining ones re-thermalize with a lower mean energy. At this stage, one is left with a cloud of  $\sim 2 \times 10^7$  atoms at a temperature of 20  $\mu$ K.

Afterwards, the trap is decompressed and the cloud is transferred into a hybrid trap, formed by a crossed optical dipole trap – produced from two infrared lasers operating at 1064 nm – and a magnetic-field gradient for gravity compensation, see Fig 1.2(c). Optical evaporation is performed during 3 s after which one obtains a degenerate cloud containing  $\simeq 5 \cdot 10^5$  atoms, leading to a Thomas-Fermi radius of approximately 6  $\mu$ m along the vertical direction and 15  $\mu$ m in the horizontal plane.



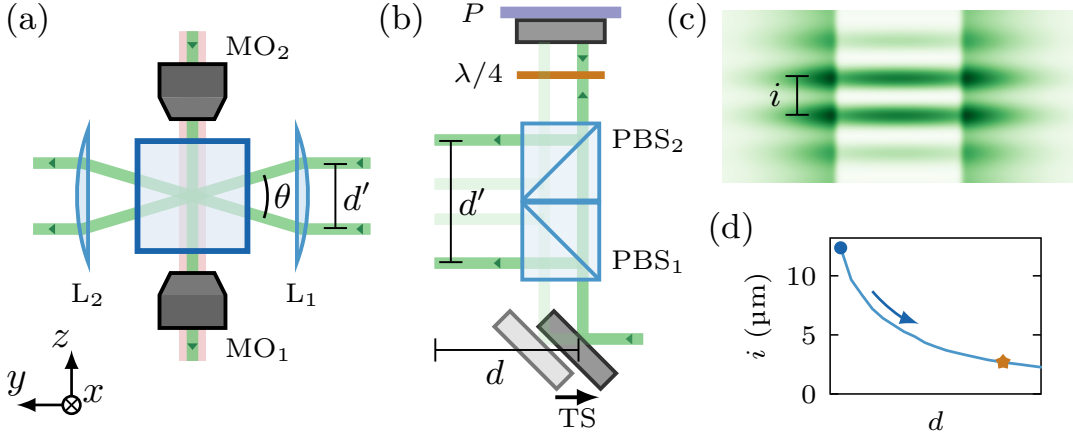


Figure 1.3: Loading into the final trap. (a) Front view: box trap formed from repulsive horizontal walls (green light propagating vertically) and a repulsive optical lattice produced by the interference of the two beams after being focused by the lens  $L_1$ . In-situ absorption imaging is performed using the red light propagating downwards through the two microscope objectives  $MO_x$ . The lens  $L_2$  is used for monitoring the vertical lattice position. (b) Varying the position  $d$  of a translation stage  $TS$  modifies the spacing  $d'$ , the angle  $\theta$  and thus the fringe spacing  $i = \lambda / [2 \sin(\theta/2)]$ . The relative phase of the two beams is corrected by controlling the piezo-electric transducer  $P$ . (c) The cloud is loaded in the most contrasted fringe (white = no intensity). (d) The spacing  $i$  is finally tuned from a large (circle) to a smaller (star) value in order to reach the quasi-2D regime.

### Loading into the final trap

For loading the final trap, we first rise the horizontal confinement, see Fig 1.3(a-d). This repulsive optical potential is produced by a 532 nm laser whose intensity profile is shaped thanks to a digital micro-mirror device<sup>1</sup>. Shortly after, the power of one dipole arm is ramped up to its maximal value to reduce the cloud's vertical size, and the atomic cloud is loaded into a single node of a vertical optical lattice, initially with  $i = 13 \mu\text{m}$  fringe spacing. This lattice – produced from the same 532 nm laser – results from the interference of two beams that intersect onto the atoms with a small angle  $\theta$ . The lenses  $L_x$  shown in Fig 1.3(a) are aspherical to limit spherical aberrations which could lead a displacement of the beam during the compression. After loading this green box, atoms are transferred to the magnetic-insensitive state  $|F = 1, m_F = 0\rangle$  using a succession of micro-wave pulses.

### Compression of the accordion

For atoms lying deep in a well of the optical lattice, one can approximate the vertical potential by a harmonic potential with angular frequency  $\omega_z$ . The population of the vertically excited states then depends on the thermal energy  $k_B T$  and the interaction energy per particle  $E_i/N$ . The so-called *quasi-2D regime* is reached when  $k_B T$  and  $E_i/N \ll \hbar \omega_z$ . For such a tight confinement, the cloud is effectively 2D and has a Gaussian density distribution of thickness  $\ell_z = \sqrt{\hbar/m\omega_z}$  along the vertical direction. In practice, the fringe spacing is adiabatically reduced down to  $3 \mu\text{m}$  thanks to an optical accordion [50, 59, 60]

<sup>1</sup>More precision is given in the next subsection.

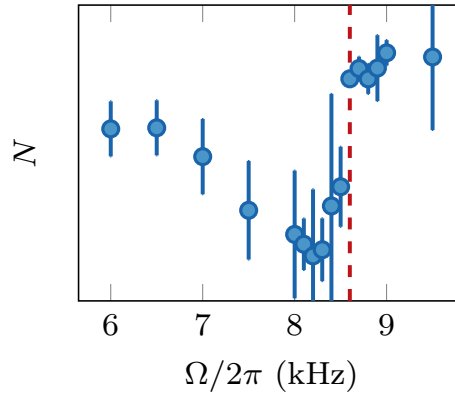


Figure 1.4: Calibration of the vertical accordion frequency via parametric heating. The depth of the trap is modulated at a frequency  $\Omega/2\pi$ , with an amplitude  $\lesssim 1\%$ , during 400 ms. The edge of the resonance at  $\Omega_0 = 2\pi \cdot 8.6$  kHz (red dashed line) corresponds to twice the vertical frequency  $\omega_z$ .

before forcing optical evaporation, so that the quasi-2D regime is reached with typically  $\gtrsim 1 \cdot 10^5$  atoms. The angular frequency of the vertical optical lattice is typically set to  $\omega_z = 2\pi \cdot 4$  kHz, and can be adjusted by modifying the power of the accordion beams. This allows us to estimate the thickness  $\ell_z \simeq 180$  nm of the cloud for all experiments reported here.

We calibrate  $\omega_z$  by inducing parametric resonance along the vertical direction [61, 62]. More precisely, we modulate  $\omega_z$  with a small amplitude. The loss rate is maximum when the modulation frequency  $\Omega$  satisfies the resonance condition  $\Omega = 2\omega_z$ . The asymmetric profile of the loss curve shown in Fig 1.4 is related to the anharmonicity of the vertical confinement. The harmonic frequency  $\omega_z$  is obtained at the high-frequency edge of the resonance. Indeed, atoms with a sufficiently high energy explore a larger portion of the vertical well. Henceforth, they experience a curvature of the potential which is lower than deeply trapped atoms do, and some atoms can thus be excited even when  $\Omega \lesssim 2\omega_z$ . Additionally, the spatial phase of the interference pattern is stabilized by adjusting the difference of optical path between the two beams. To do so, a picture of the lattice is taken at the beginning of each sequence. The optical path difference is adjusted thanks to piezo-electric transducer placed inside an arm to keep constant the fringe position over long time scales.

### Magnetic field control

The quantization axis is defined by a static magnetic field  $\mathbf{B}$ . Its direction can be tuned arbitrarily thanks to a set of coils mounted around the glass cell. The magnitude of this magnetic field is kept sufficiently high – on the order of 1 G, up to 10 G – to lift the degeneracy between the different Zeeman states. This also limits spin-changing collisions in the ground state and thus avoids redistribution of the Zeeman populations. We compensate for the magnetic field fluctuations along the vertical direction – mainly due to the subway traffic – to maintain a sufficient magnetic field stability. We measure less than 1 mG peak-to-peak fluctuations over the day when the magnetic field is vertical. Fluctuations can reach up to a few mG when the magnetic field lies in the horizontal plane.

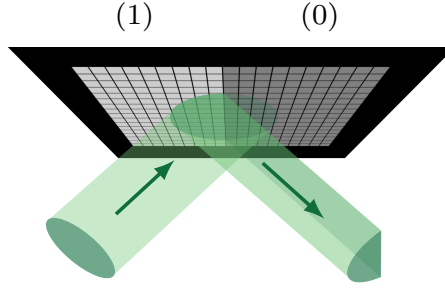


Figure 1.5: Beam shaping with a DMD. The light impinging on (1)-mirrors is deflected toward the atoms, the rest of the beam is lost.

Using the magnetic trap coils, we can create an additional in-plane harmonic potential. While this technique is much less flexible than the one described in Subsec 1.1.2, it provides us with a less rough potential, with frequencies of a few tens of Hz. Note that only magnetic field-sensitive states (e.g.  $|F = 1, \pm 1\rangle$ ) can experience this potential. This technique has allowed us to study the dynamical symmetry present in our system, see [49, 50] and Subsec 2.1.3.

### Final atom number and temperature

Optionally, we can tune the final atom number by transferring a fraction of them from state  $|F = 1, m_F = 0\rangle$  to state  $|F = 2, m_F = 0\rangle$ . This fraction – which is then resonant with the 780 nm laser light – is expelled from the trap by sending a short light pulse. The temperature of the cloud can also be tuned by adjusting the final level of evaporation. Finally, the system is hold during 0.5 s to reach thermal equilibrium.

#### 1.1.2 A tunable horizontal confinement

We now describe with greater detail our final horizontal potential. By using a digital micromirror device (DMD), we are able to tailor the light potential felt by the atoms and to produce a large variety of geometries, with sizes ranging from 5 to 50  $\mu\text{m}$  and densities ranging from 5 to 100 atoms/ $\mu\text{m}^2$ . Our DMD (DLP7000 from Texas Instrument interfaced by Vialux GmbH) is an array of  $1024 \times 784$  square mirrors of side 13.7  $\mu\text{m}$ . Each mirror can be set in one of the two following positions: on position (1), light of the incoming laser beam is reflected toward the atoms; on position (0), light is deflected to another direction, such that it is not perceived by the atoms. The potential can thus locally be turned ON or OFF by programming the position of each mirror using a binary image, see Fig 1.5 for an illustration.

The DMD plane is imaged onto the atoms with a magnification 1/70, through a high numerical aperture microscope ( $\text{NA} = 0.45$ ). Each mirror has an effective size of 0.2  $\mu\text{m}$  on the atomic plane, and the Gaussian beam reflecting on the DMD has a waist of 40  $\mu\text{m}$  at the same position. The steepness of the optical potential is limited by the optical resolution of  $\sim 1 \mu\text{m}$ . Since the potential is repulsive, atoms are trapped in the low-intensity regions which are disconnected from free-space. Images displaying the 2D column density of a few samples are shown in Fig 1.6. The inset of Fig 1.6(a) gives a side-view of the same sample loaded in a single node of the vertical lattice. It is also possible to display a movie of binary images on the DMD, with a refresh rate as large as 10 kHz. This is useful e.g. for

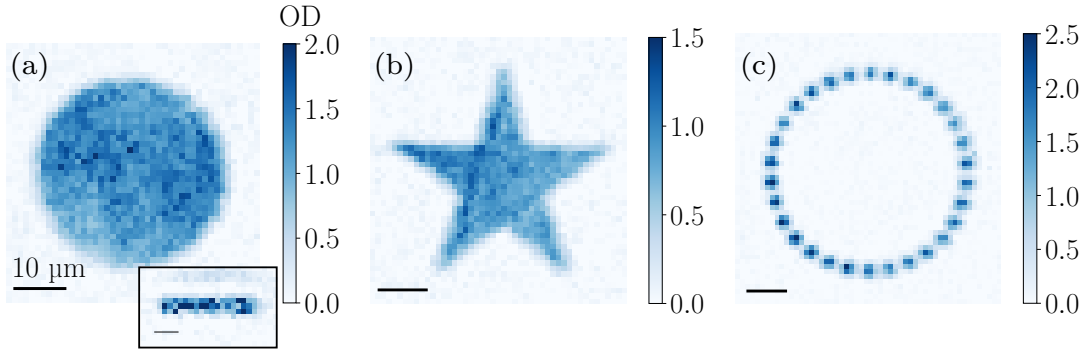


Figure 1.6: In-situ images of 2D samples. The effective pixel size on the atomic plane is  $1.15 \mu\text{m}$ , the optical resolution is limited to  $\sim 1 \mu\text{m}$ . The inset of (a) corresponds to a side view of the same sample before compression of the accordion. Because of the limited resolution along this imaging axis, the undesirable loading of two dark fringes can only be detected in this uncompressed configuration.

loading a complicated box from a larger (and more regular) one, or for exciting the cloud with a time-dependent potential.

### Arbitrary control of the in-plane geometry

During this thesis, we have developed a new method for the generation of optical potentials with a controllable intensity, as reported in [48, 53]. The use of a binary pattern for intensity modulation has been demonstrated for flattening a beam profile in direct imaging [63], as well as for holographic beam shaping when working in Fourier space [64]. These techniques rely on the averaging of the light reflected by many adjacent DMD pixels whose separation is smaller than the optical resolution.

The realization of grey-levels of intensity using a DMD requires a *dithering* operation for converting a continuous map into a binary image made of (0)'s and (1)'s. Here, this operation is achieved using the so-called *error diffusion technique*, motivated by the good performances of this algorithm [65]. Additionally, precise generation of the optical potential is made possible thanks to a feedback loop. A related approach has also been recently demonstrated for a 1D Bose gas by Tajik et al [66].

### Atomic response

Besides the sharp horizontal confinement described earlier, we use an additional DMD projected onto the atoms (same model, Vialux DLP7000). The corresponding beam has a waist of  $\sim 55 \mu\text{m}$  in the atomic plane. Since the effective pixel size of this extra-DMD is also of  $\sim 0.2 \mu\text{m}$ , the area defined by the diffraction spot of the imaging system – with an optical resolution of  $\sim 1 \mu\text{m}$  – contains approximately  $5 \times 5$  pixels. The combination of this DMD with the optical system can be thought as a spatially-varying reflectance for the impinging beam. Hence, this allows us to modulate the incoming intensity among about 25 levels.

In practice, we characterize this supplementary optical potential  $V_2(\mathbf{r})$  by looking directly at the modification of the atomic density distribution. The potential is added after

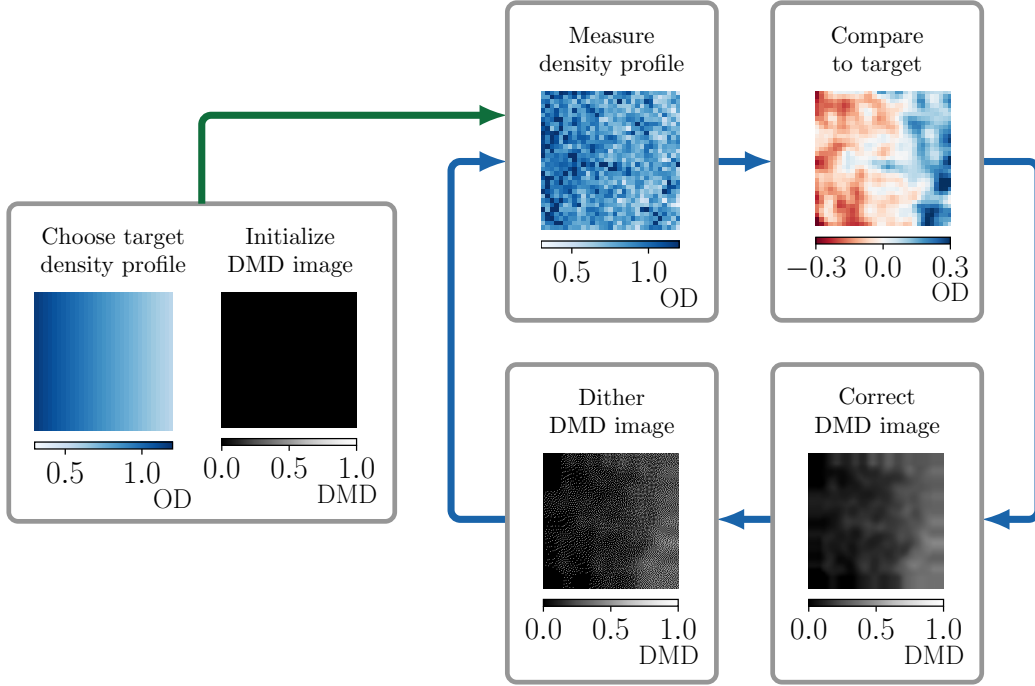


Figure 1.7: Feedback loop for intensity modulation. Here we chose a target profile which varies linearly along the  $x$ -direction, and a uniform (0)-configuration for the initial DMD pattern. The density profile (top left) was obtained after the first three turns in the loop and by averaging 5 independent shots. The error signal (top right) is simply the difference between the measured and the target density profiles. The result of the feedback loop after 15 turns is illustrated on Fig 1.8(a, e).

compression of the accordion, before the last evaporation stage. We work in a regime where the cloud is well described by the Thomas-Fermi approximation presented in Subsec 2.1.2. This simply means that the local density  $n(\mathbf{r})$  at position  $\mathbf{r}$  can be written

$$n(\mathbf{r}) \propto \mu - V(\mathbf{r}), \quad (1.2)$$

with  $\mu$  the (global) chemical potential, and a proportionality factor which is not essential at this stage. The full potential  $V(\mathbf{r}) = V_1(\mathbf{r}) + V_2(\mathbf{r})$  also accounts for the overall box potential  $V_1(\mathbf{r})$  with possible optical defects. Because of the simple relation between  $n(\mathbf{r})$  and  $V(\mathbf{r})$ , generating a particular optical potential is equivalent to preparing a specific density profile – our *target profile*. This is achieved by displaying the suitable image on the device.

### Feedback loop

The feedback loop we implemented is shown in Fig 1.7. Starting from a simple image on the DMD – e.g. a uniform image made of (0)s – we measure the initial density profile. We compute the difference between the measured and the target density profile at each point  $\mathbf{r}$  of the atomic plane. This error map, convoluted with a Gaussian function for filtering high-frequency noise, is then projected back onto the DMD plane. Up to a conversion factor, the error is added to the continuous DMD map for adapting the local intensity.

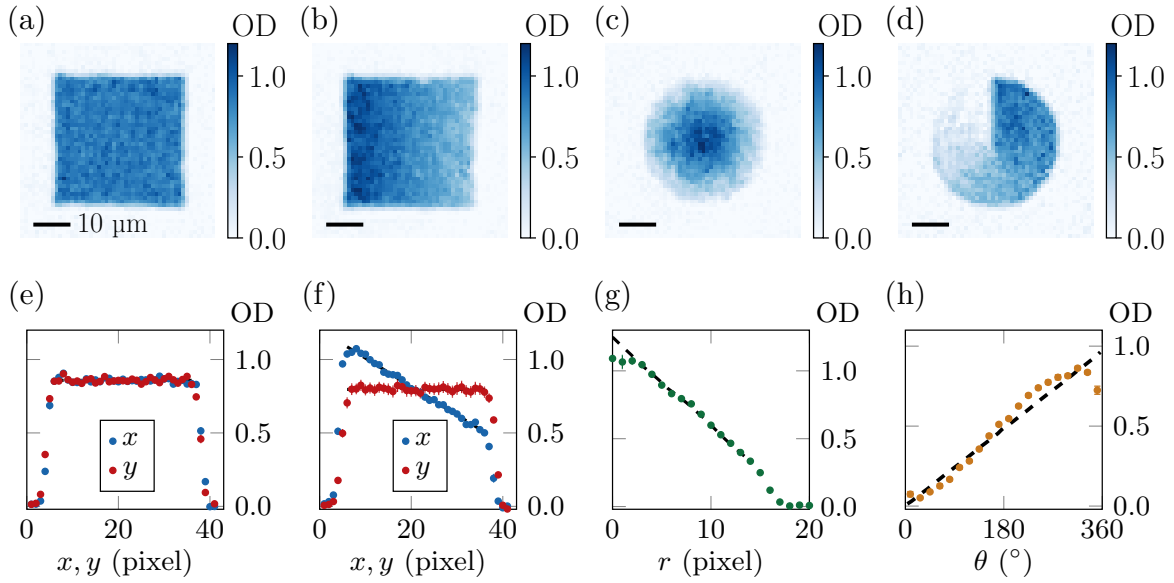


Figure 1.8: Samples with arbitrary potential. (a-d) are example density profiles measured after applying the feedback loop for various target profiles. (e,f) give the profiles integrated along the  $x$ - and  $y$ -directions for samples (a,b). (g) shows the radial profile of sample (c), and (h) shows the azimuthal profile of sample (d). Figure adapted from [48].

The latter is dithered using the error diffusion algorithm. The updated binary image is then displayed on the DMD, and the correction loop goes on until the procedure converges.

### Performances

Fig 1.8 presents a few density profiles obtained thanks to this method, which provides us with an enhanced control of the optical potential. The convergence of the loop is hindered by various noise sources contributing to the measured density profile: thermal fluctuations of the atomic cloud, quantum projection noise due to the partial transfer before imaging, photonic shot noise associated to the imaging. While thermal fluctuations are expected to have little influence deep in the superfluid regime, the two other contributions can be mitigated by averaging more images to determine the density distribution. In practice, this number of images per turn is the main factor limiting the quality of the correction, as discussed in [48]. In practice, we limit ourselves to reasonable optimization times and typically take 10 to 30 images on each turn. However, the above procedure is less efficient for preparing potentials varying over a short distance. In particular, it requires a very good knowledge of the mapping between the DMD and the atomic plane. Both can drift in the course of a day because of mechanical relaxation on the optical table. In some cases, we thus choose a slightly different approach to circumvent this issue.

### Azimuthal correction

We illustrate this last remark in Fig 1.9. Here, the goal is to produce a thin ring of atoms with a flat azimuthal density profile. Experimentally, we find that the method presented above can seriously damage the initial density profile by producing small-scale potential defects, essentially due to the vicinity to the box boundaries. In this case, it

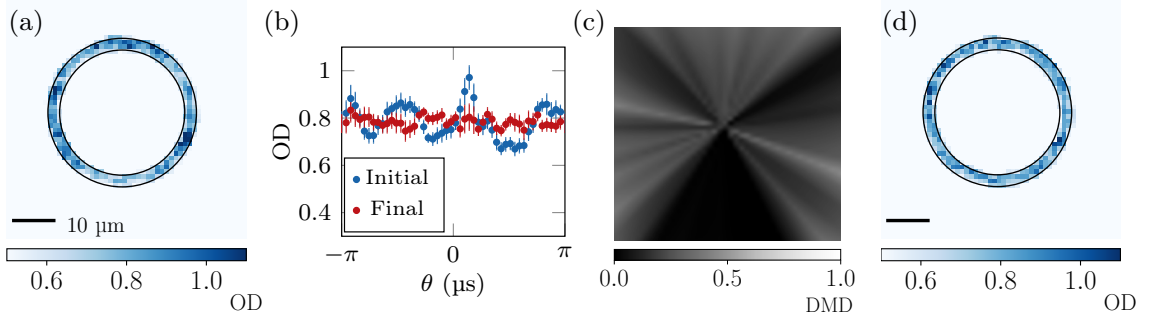


Figure 1.9: Azimuthal correction. (a) Initial density profile trapped in a ring of inner radius  $15\text{ }\mu\text{m}$  and outer radius  $20\text{ }\mu\text{m}$ . (b) The corresponding azimuthal density profile (in blue) presents large fluctuations. (c) The feedback loop produces a DMD image which does not vary along the radial direction. (d) Final density profile, together with the azimuthal profile represented as red dots in (b). Although the improvement is not very apparent on the images, the dispersion of the red dots in (b) is only 2% of their mean value (versus 9% for the blue dots).

is more efficient to produce a correcting potential which varies only along the azimuthal coordinate, as shown in Fig 1.9(c).

### 1.1.3 Some calibrations

#### Detection

In-situ density distributions like the ones shown in Fig 1.6 are obtained using *absorption imaging* along the vertical axis, see also Fig 1.3(a). To do so, we first transfer a certain fraction of atoms from state  $|F = 1, m_F = 0\rangle$  to state  $|F = 2, m_F = 0\rangle$ . The latter is resonant with our imaging beam. We then measure the optical depth of the sample, i.e. the attenuation of the laser intensity in the forward direction due to light scattering. The optical depth (OD) is defined such that the transmitted intensity  $I_{\text{out}}$  links to the incident intensity  $I_{\text{in}}$  through the relation

$$I_{\text{out}} = e^{-\text{OD}} I_{\text{in}}. \quad (1.3)$$

We use vertically propagating light, resonant with the  $(F = 2 \rightarrow F' = 3)$  cycling transition at  $780\text{ nm}$ , in the low intensity-saturation regime. Thanks to a high numerical aperture microscope ( $\text{NA} = 0.45$ ), we get an optical resolution of  $\sim 1\text{ }\mu\text{m}$ . The transmitted light is imaged on a CCD camera (Princeton - Pixis 1024 Excelon), with an effective pixel size of  $1.15\text{ }\mu\text{m}$  on the atomic plane.

#### Temperature calibration

The temperature of the cloud is estimated using the equation of state of a 2D Bose gas. An important simplification of this equation arises from the so-called scale invariance discussed later in Subsec 2.1.3. Thanks to this, the phase-space density  $\mathcal{D}$  can be expressed in a reduced form

$$\mathcal{D} = \mathcal{D} \left( \frac{\mu}{k_B T}, \tilde{g} \right), \quad (1.4)$$

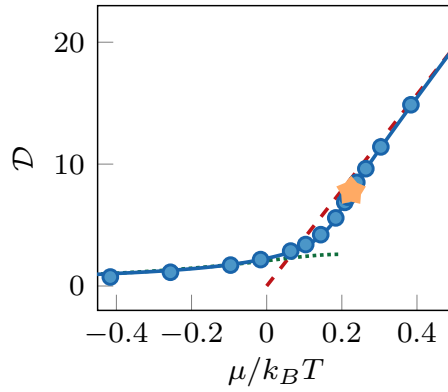


Figure 1.10: Equation of state (1.4) for a coupling strength  $\tilde{g} = 0.16$  provided by Prokof'ev & Svistunov [67] (blue dots), together with the Thomas-Fermi (green dotted line) and Hartree-Fock (red dashed line) predictions. We use an interpolating function (solid blue line) for calibrating the temperature. The star indicates the critical point for the superfluid transition.

where  $\mu$  and  $k_B T$  appear only through their ratio. In this equation, we also introduced the dimensionless parameter  $\tilde{g}$  defined by

$$\tilde{g} = \sqrt{8\pi} \frac{a}{\ell_z} \quad (1.5)$$

which characterizes the interactions in 2D,  $a$  being the 3D scattering length<sup>2</sup>. There is no analytic form for Eq (1.4) that links the thermal to the deeply degenerate regime. However, Prokof'ev & Svistunov [67] could determine numerically (1.4) using Monte-Carlo simulations. Their results were verified experimentally by Hung et al. [68] and Yefsah et al. [69] on trapped systems.

In this thesis, we work with uniform samples and we wish to determine their temperature  $T$  and chemical potential  $\mu$ . Inspired from [70], we locally modify the effective chemical potential felt by the atoms by adding a small and flat repulsive potential, assuming it does not alter the temperature significantly. This picture applies within the local density approximation (LDA). In practice, the extra-potential is imposed using a second DMD and an adjustable light intensity. We measure the density in this region for various potential heights, and extract  $(T, \mu)$  by fitting these data to an analytical version of (1.4) plotted on Fig 1.10.

### Density calibration with Ramsey sequence

The relation between the 2D density and the optical depth is linear for sufficiently small densities [71, 72], with a proportionality factor given by the light-scattering cross-section  $\sigma_l$ . In practice, the visible density is kept low by transferring only a small fraction of atoms into state  $|F = 2, m_F = 0\rangle$ . Currently,  $\sigma_l$  is determined using Ramsey spectroscopy, which we now briefly present. In the experiment, atoms can occupy the two internal states  $|F = 1, m_F = 0\rangle \equiv |1\rangle$  and  $|F = 2, m_F = 0\rangle \equiv |2\rangle$  which can be coupled through microwave pulses (see Subsec 1.2.1). These states are characterized by intra-species and inter-

<sup>2</sup>See Subsec 2.1.1 for more details



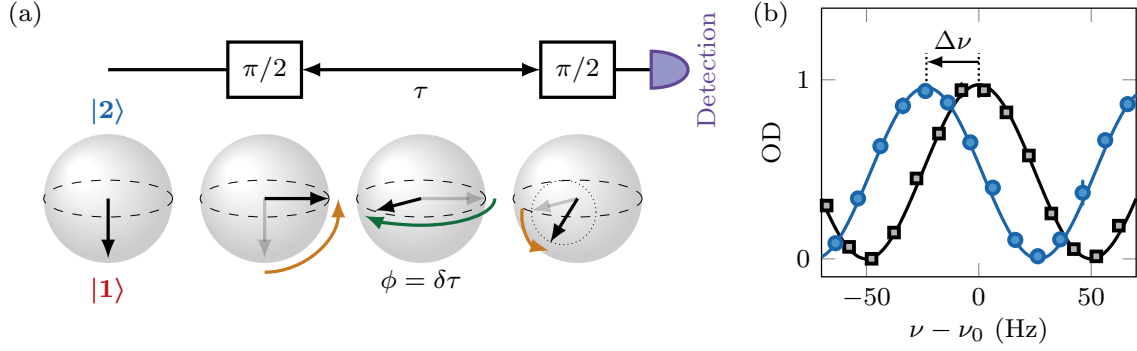


Figure 1.11: (a) Ramsey sequence on the Bloch sphere. (b) In the absence of interactions, the population of atoms detected in state  $|2\rangle$  exhibits oscillation centered on  $\nu_0$  (black points), which are shifted by an amount  $\Delta\nu$  in the presence of interactions (blue points). Figure adapted from [51].

species scattering lengths  $a_{11}, a_{22}, a_{12}$ , or equivalently by the corresponding 2D coupling strengths  $\tilde{g}_{ij}$ .

Let us first neglect interactions and consider a two-level atom with a Bohr frequency  $\nu_0$ . Initially, the atom is in state  $|1\rangle$ . On the Bloch sphere of Fig 1.11(a), this is represented by a Bloch vector pointing downwards. At time  $t = 0$ , we apply the following Ramsey sequence. A first pulse with frequency  $\nu$  creates a coherent superposition of states  $|1\rangle$  and  $|2\rangle$  with equal weights ( $\pi/2$ -pulse). The corresponding vector now lies in the equatorial plane of the Bloch sphere and is let evolving freely during a time  $\tau$ . During this waiting time, atoms get dephased at a rate  $\delta = 2\pi(\nu - \nu_0)$  and the corresponding vector rotates in the equatorial plane at the same angular velocity<sup>3</sup>. A second identical pulse is applied before measuring the total population transferred into state  $|2\rangle$ . When the experiment is repeated for several values of  $\nu$ , the population in  $|2\rangle$  exhibits oscillations<sup>4</sup> centered on  $\nu = \nu_0$ , with a period  $(2\pi/\tau)$ , as shown in Fig 1.11(b). In practice, this reference Ramsey sequence is performed after releasing the atoms from the trap for a 2 ms time-of-flight, such that the cloud's density gets low enough and interactions can be neglected<sup>5</sup>.

Now we consider the effect of interactions on the Ramsey signal. In the supplemental material of [51] (see also [73]), it is shown that weak interactions solely induce a shift of the resonant frequency, as indicated in Fig 1.11(b). For atoms deeply in the superfluid regime, the resonant frequency shift associated to mean-field effects can be written as

$$\Delta\nu = \mu_1 - \mu_2 \quad \mu_i = \frac{\hbar^2}{m} (\tilde{g}_{11}n_1 + \tilde{g}_{12}n_2), \quad (1.6)$$

where  $\mu_i$  is the chemical potential in state  $|i\rangle$ , with density  $n_i$  after the first pulse. In the present case,  $n_1 = n_2 = n/2$ ,  $n$  being the total density to be determined. Henceforth, one

<sup>3</sup>This is valid within the rotating-wave approximation (RWA).

<sup>4</sup>The waiting time  $\tau = 10$  ms limits the uncertainty on the frequency measurements to  $\sim 1$  Hz. The duration of the pulses (typically  $\tau' = 100$   $\mu$ s) is much shorter than the time-scale for any spatial dynamics ( $\gtrsim 1$  ms) and the waiting time  $\tau$ , so that they can be considered as instantaneous. When  $|\nu - \nu_0|$  becomes of the order of  $\pi/(2\tau')$  (the Rabi-frequency), the first pulse cannot bring the Bloch vector onto the equatorial plane, and the amplitude of the oscillations is reduced (not visible on Fig 1.11(b)).

<sup>5</sup>We calibrated the magnetic field gradient experienced during free-fall to subtract the effect of this magnetic field change on the atomic energy levels.

obtains

$$\Delta\nu = \frac{\hbar}{m} \frac{\Delta a}{\sqrt{2\pi}\ell_z} n \quad \Delta a = a_{22} - a_{11}. \quad (1.7)$$

Knowing the scattering length difference  $\Delta a$  [74], this frequency shift allows us to estimate the 2D density.  $\sigma_l$  can then be deduced by comparing this density to the optical depth measured on the same sample. This method is more easily implemented than the one based on the triangle periodic evolution, already described in [50, 53]. Moreover, we can measure  $\ell_z$  with great accuracy and  $\Delta a$  is fixed although known with limited accuracy. Hence, this method is much less sensitive to statistical noise than the triangle method.

## 1.2 Preparation of binary mixtures

We now turn to the preparation of binary mixtures. In Subsec 1.2.1, we show how to create linear superpositions of two different states. Importantly, we are able to modify the inter-species scattering length through magnetic dipole-dipole interactions (Subsec 1.2.2).

### 1.2.1 Internal degrees of freedom

We consider the electronic ground-state manifold of  $^{87}\text{Rb}$ , spanned by the states  $|F, m_F\rangle$  with total angular momentum  $F = 1, 2$  ( $m_F = -F, \dots, F$ ). In most of this work, we manipulate the two states  $|F = 1, m_F = 0\rangle \equiv |1\rangle$  and  $|F = 2, m_F = 0\rangle \equiv |2\rangle$  which will form the basis of a pseudo-spin [26]. One advantage of using these states is their insensitivity to magnetic fields. If one neglects the quadratic Zeeman shift, the energy splitting between these two states is not altered by magnetic field fluctuations and defines the clock-transition frequency  $\nu_0 \simeq 6.8683 \text{ GHz}$ . Furthermore, magnetic field inhomogeneities do not modify the potential felt by the atoms.

### Coherent coupling

A coherent field nearly resonant with the energy splitting  $|1\rangle \leftrightarrow |2\rangle$  can induce Rabi oscillations between these states, in the absence of interactions. For example, starting with all atoms in state  $|1\rangle$ , the probabilities  $(\Pi_1, \Pi_2)$  to find the atoms in each state after a driving time  $t$  are given by

$$\Pi_1(t) = \frac{\Omega^2}{\delta^2 + \Omega^2} \sin^2 \left( \sqrt{\delta^2 + \Omega^2} \frac{t}{2} \right) \quad \Pi_2(t) = 1 - \Pi_1(t), \quad (1.8)$$

where  $\delta = 2\pi(\nu - \nu_0)$  is the detuning of the field's frequency  $\nu$  with respect to the hyperfine frequency, and  $\Omega$  is the corresponding Rabi frequency. At resonance  $\delta = 0$ , one can exchange the populations of  $(|1\rangle, |2\rangle)$  by applying a pulse with duration  $t$  such that  $\Omega t = \pi$  ( $\pi$ -pulse). For  $\Omega t = \pi/2$  ( $\pi/2$ -pulse), an atom in state  $|1\rangle$  is put in the coherent superposition  $(|1\rangle + |2\rangle)/\sqrt{2}$ . For  $N$  atoms initially in state  $|1\rangle$ , the corresponding state thus writes

$$\left( \frac{|1\rangle + |2\rangle}{\sqrt{2}} \right)^N = \frac{1}{2^{N/2}} \sum_{j=0}^N \sqrt{\binom{N}{j}} |1 : j, 2 : N - j\rangle \quad (1.9)$$

where  $|1 : j_1, 2 : j_2\rangle$  is the fully symmetric state with  $j_i$  atoms in  $|i\rangle$ ,  $i = 1, 2$ . The population of atoms in state  $|2\rangle$  is thus given by a binomial law. In the large  $N$  limit which we consider in most cases, one can neglect the so-called *quantum projection noise*, i.e. the fluctuations of the two populations in state (1.9) which scale as  $1/\sqrt{N}$ . This holds

also for other pulse durations. We can then replace such a superposition by a product state  $|1 : N_1, 2 : N_2\rangle$  with well-defined atom numbers, in particular when writing the coupled equations describing our binary mixtures. In practice, we use two techniques for coherently coupling states  $|1\rangle$  and  $|2\rangle$ , which we now describe.

### Micro-wave for homogeneous addressing

In many situations, we use an antenna located near the glass cell to produce a micro-wave field driving a magnetic dipole transition<sup>6</sup>. When doing so, we address the cloud homogeneously since the radiation's wavelength is of a few cm. We reach Rabi frequencies on the order of  $\Omega = 2\pi \cdot 10$  kHz. As a consequence, magnetic field fluctuations of  $\sim 1$  mG have little impact on magnetic field-sensitive transitions<sup>7</sup>. Furthermore, these transfers occur much faster than any spatial dynamics studied here, whose typical timescales are  $\gtrsim 1$  ms.

### Raman transfer with spatial resolution

We now present the optical setup used to perform Raman transitions between states  $|1\rangle$  and  $|2\rangle$ . A simplified scheme is shown in Fig 1.12 and many implementation details can be found in [50, 53]. To summarize, we use two co-propagating laser beams with almost equal wavelength  $\lambda \simeq 790$  nm. These two beams, denoted  $R_1$  and  $R_2$  hereafter, are frequency-shifted by an amount  $\delta\nu_R$  close to the hyperfine splitting  $\nu_0$  between states  $|1\rangle$  and  $|2\rangle$ , so that they can induce resonant two-photon transitions. Both beams have waists of  $\sim 40$   $\mu\text{m}$  and carry a total power of a few 10 mW. As exemplified on Fig 1.13(a), we reach Rabi frequencies larger than 25 kHz. Note that the Raman beams are not flat. Indeed, both beams have a finite waist and surface defects on the DMD might also deform this intensity profile. This induces significant intensity gradients on the atomic plane. This is confirmed by measuring the local Rabi-frequency on the cloud, as reported in Fig 1.13(b).

The chosen wavelength  $\lambda$  lies in between the  $D_1$  and  $D_2$  lines. It is detuned enough such that spontaneous emission can be neglected for the characteristic experimental times. Moreover, the light-shifts associated to the coupling to the two upper manifolds exactly cancel each other for this *tune-out wavelength*. This is crucial since, because of intensity gradients, the Raman beams could otherwise print a non-uniform phase on the atomic states over the cloud size. Furthermore, since the two beams have identical trajectories after the optical fibers, spatial phase fluctuations over the beam profiles exactly compensate in the two-photon Rabi-frequency  $\Omega_R \propto \Omega_1 \Omega_2^*$ . From this, we can safely assume that the Raman process yields no spatial phase gradients.

---

<sup>6</sup>The corresponding field is generated by a Rohde & Schwarz SMB100AV synthesizer providing a 6.8 GHz source, mixed with a signal around 34 MHz produced by a generator (Rigol DG1062Z) controlled by USB. The frequency of the 6.8 GHz source is stabilized using a 10 MHz reference oscillator. The two signals are mixed using an I-Q mixer (Pulsar IMOH 03-458), the output of which is amplified (Kuhne KU PA 700, maximum output 10 W) before radiating through the antenna. More details can be found in [50, 53]. A second micro-wave chain has recently been mounted: it is composed of a Rohde & Schwarz SMB100AV synthesizer controlled by GPIB, an amplifier (maximum output 50 W) and a one-loop antenna mounted as close as possible to the glass-cell.

<sup>7</sup>As presented in Subsec 1.1.1, atoms are initially polarized in state  $|1, -1\rangle$  when being transferred into the box potential. We apply two successive micro-wave pulses driving the transitions  $|1, -1\rangle \leftrightarrow |2, 0\rangle$  and  $|2, 0\rangle \leftrightarrow |1, 0\rangle$  to transfer atoms into state  $|1, 0\rangle$  before starting most experiments. The first frequency is affected by the linear Zeeman effect and hence much more sensitive to magnetic field fluctuations (1 mG fluctuations correspond to 0.7 kHz frequency fluctuations).

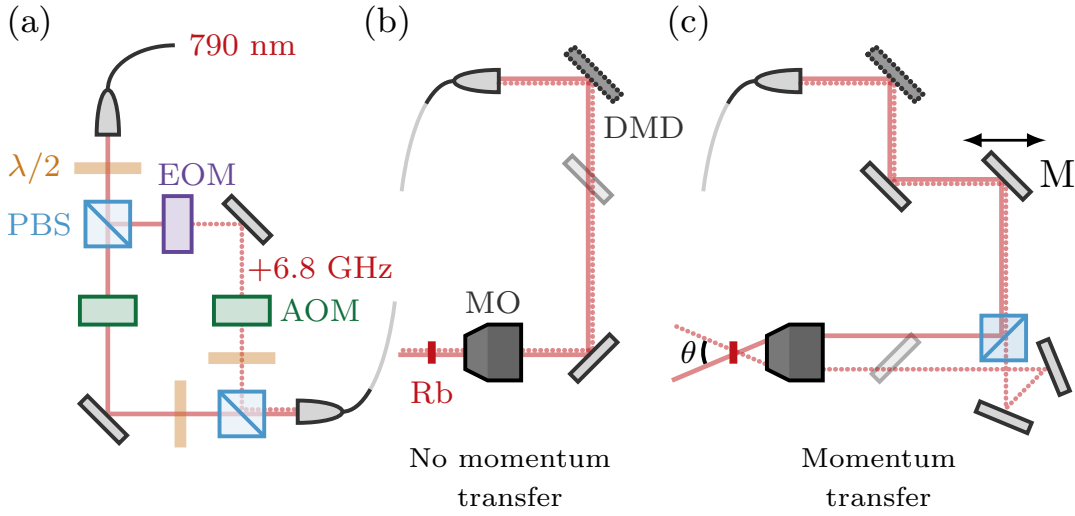


Figure 1.12: Raman beam setup. (a) Laser light is split into two paths with frequency shifts controlled using an electro-optical modulator (EOM) and acousto-optical modulators (AOM). The beams are then recombined with orthogonal polarization and sent to the main table. (b) On the main table, the two overlapping beams impinge on a DMD for intensity modulation before shining onto the atomic plane. (c) The optical path can be modified to create a relative angle between the two beams on the atomic plane, yielding a non-zero momentum transfer. This is achieved using a motorized mirror M and a polarizing beam-splitter (PBS) which separates again the two frequency components.

Importantly, the two beams can also be splitted and recombined on the atoms making a non-zero angle  $\theta$ , see Fig 1.12(c). In this Bragg configuration, the atoms which are transferred to state  $|2\rangle$  undergo a kick with momentum  $p = 2\hbar k / \sin(\theta/2)$  to ensure momentum conservation. This way, we can imprint a phase gradient corresponding to velocities  $v = p/m$  ranging from 0 to  $3.5 \mu\text{m/ms}$ , a value larger than the sound velocity written in Eq (2.19). Conservation of energy, accounting for the kinetic energy of a non zero-momentum state, yields the following relation for the resonant frequency  $\nu_R$

$$h\nu_R = h\nu_0 + \frac{1}{2}mv^2. \quad (1.10)$$

The corresponding shift equals 1.3 kHz for the largest velocity, which could be determined by spectroscopy. In a near future, we intend to study the propagation of spin bubbles and binary collisions in a bath at rest. A preliminary study of these problems is given in Chapter 6.

### Arbitrary spin distributions

One advantage of this method comes from the small wavelength of the corresponding field, compared to the micro-wave coupling considered above. This allows us to perform spatially-resolved transitions. On the atomic plane, the local Rabi-frequency is proportional to the total intensity<sup>8</sup>. For a given illumination time  $t$ , the population transfer

<sup>8</sup>More precisely, this Rabi-frequency scales as  $\Omega_R \propto \Omega_1 \Omega_2^*$  where  $\Omega_i$  is related to the reduced matrix elements between state  $|i\rangle$  and upper-lying states, induced by the beam  $R_i$ . Since  $\Omega_i$  is proportional to

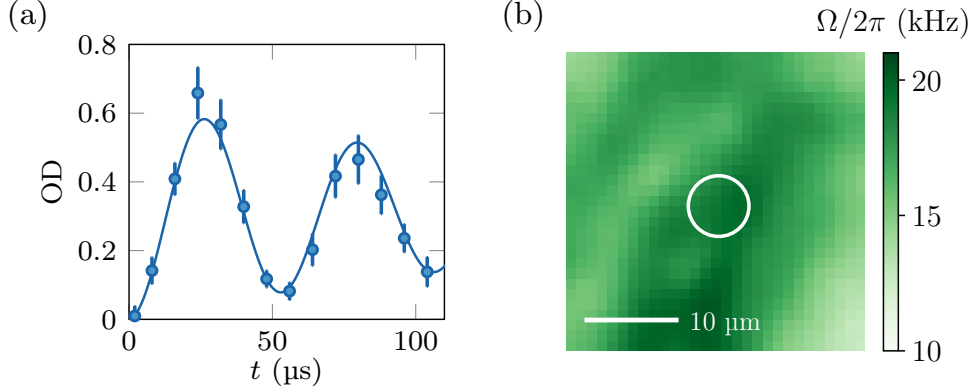


Figure 1.13: (a) Mean OD versus exposure time  $t$ , measured inside the circle depicted in (b). The oscillations have a two-photon Rabi frequency  $\Omega_r = 2\pi \cdot 19\text{kHz}$  and are damped ( $\tau_R = 200(50) \mu\text{s}$ ) because of intensity dispersion in this region. (b) Two-photon Rabi-frequency on the atomic plane.

given in Eq (1.8) thus depends on the local intensity. Before reaching the atoms, the two overlapping beams impinge on a third DMD for intensity modulation<sup>9</sup>. They are mixed with the 780 nm and 532 nm beams – respectively used for imaging and for the horizontal confinement – and sent vertically, passing through the two microscope objectives. The DMD is imaged with a magnification 1/37.5, so that each pixel has an effective size of  $0.4 \mu\text{m}$ . In Chapter 4, we will adapt the grey-level feedback loop presented in Subsec 1.1.2 in order to realize a Townes soliton.

### Hyperfine relaxation

A drawback of using state  $|2\rangle$  is the possibility for hyperfine-changing two-body collisions. These are induced by dipole-dipole interactions [75, 76]. Such collisions involve transitions from states in  $F = 2$  to  $F = 1$  and lead to immediate loss of the collision partners on very short timescales, due to the amount of energy released in kinetic energy during the process. While the lifetime  $\tau$  of the sample composed of  $|1\rangle$  is typically  $\gtrsim 10$  s and essentially determined by one-body losses, hyperfine relaxation limits the duration of experiments involving state  $|2\rangle$  to a few tens of milliseconds. More quantitatively, we measured the loss dynamics of an initially homogeneous sample in  $|2\rangle$  with density  $n$  and fit it to the following (one + two-body) loss model

$$\frac{dn}{dt} = -\frac{1}{\tau}n - \beta_{2D}n^2 \quad n(t) = \frac{n_0 e^{-t/\tau}}{1 + \beta_{2D} n_0 \tau (1 - e^{-t/\tau})}. \quad (1.11)$$

with fit parameters  $(n_0, \beta_{2D})$ . By repeating the experiment for various initial densities, we estimate  $\beta_{2D} = 140(30) \text{ ms} \cdot \mu\text{m}^2$ . For a 2D sample, this quantity is integrated

---

the square-root of  $R_i$ 's intensity, we find that  $\Omega_R$  scales as the total intensity when the two beams undergo the same intensity modulation through the DMD.

<sup>9</sup>In the Bragg configuration, the two beams follow different paths and do not reflect on the same number of mirrors. The corresponding images on the atoms are symmetric to one another with respect to the  $y$ -axis of the camera. The DMD image thus needs to be symmetric as well to be correctly imprinted on the atoms.

along the column density, and one can form a three-dimensional two-body loss coefficient  $\beta_{3D} = \sqrt{2\pi}\ell_z \beta_{2D}$ , yielding a value  $\beta_{3D} = 5(1) \times 10^{-14} \text{ cm}^3 \cdot \text{s}^{-1}$ . We note that this quantity is significantly smaller than the value  $\beta_{3D} = 10.2(1.3) \times 10^{-14} \text{ cm}^3 \cdot \text{s}^{-1}$  reported by Schmaljohann et al. [75] who studied a 3D BEC. This discrepancy might be explained by the lower magnetic field,  $B = 340(20) \text{ mG}$ , imposed in [75], which allows for spin dynamics in the  $F = 2$  manifold, and thus modifies the decay channels for a cloud initially in  $|F = 2, m_F = 0\rangle$ .

### 1.2.2 Magnetic dipole-dipole interactions

In the low-temperature regime, interactions involving states  $|1\rangle$  and  $|2\rangle$  are characterized by the set of scattering lengths  $(a_{11}, a_{12}, a_{22})$ . In this thesis, we use the values given by Altin et al. [74]

$$a_{11} = 100.9 a_0 \quad a_{12} = 98.9 a_0 \quad a_{22} = 94.9 a_0, \quad (1.12)$$

$a_0$  being the Bohr radius. In 3D, a description in terms of scattering lengths hold as long as one can neglect long-range interactions, such as dipole-dipole interactions which scale as  $1/r^3$ . These are characterized by the so-called *dipolar length*  $a_{dd}$ . Since magnetic moments of alkali-metal atoms are limited to  $\lesssim 1$  Bohr magneton ( $\mu_B$ ), long-range magnetic dipole-dipole interactions (MDDI) have no sizable effect in most cases. For  $^{87}\text{Rb}$ ,  $a_{dd} = 0.7 a_0$  which is two orders of magnitude smaller than the values reported in Eq (1.12). Moreover, their averaged contribution to the mean-field energy vanishes when integrated over full 3D space ( $\langle \cos^3 \theta - 1 \rangle = 0$ ), so that they do not contribute to the values of the different scattering lengths.

This reasoning might be mitigated when setting the scattering length to zero by using a Feshbach resonance [29] as exemplified in [77, 78], or when working with spinor gases where many scattering lengths coincide and MDDI can have a significant effect [79, 80]. In this subsection, we summarize our recent findings concerning MDDI in 2D [52] and show that the effective inter-species interaction parameter depends on the orientation of the guiding magnetic field with respect to the atomic plane.

#### Modification of the scattering length $a_{12}$

Consider two atoms ( $A, B$ ) separated by a vector  $\mathbf{r}$ . Their electronic spin operators are denoted  $\hat{\mathbf{s}}_A$  and  $\hat{\mathbf{s}}_B$ . For this two-particle system, the MDDI Hamiltonian writes

$$\hat{U}(\mathbf{r}) = \frac{\mu_0 \mu_B^2}{\pi r^3} [\hat{\mathbf{s}}_A \cdot \hat{\mathbf{s}}_B - 3(\hat{\mathbf{s}}_A \cdot \mathbf{u})(\hat{\mathbf{s}}_B \cdot \mathbf{u})], \quad (1.13)$$

with  $\mathbf{u} = \mathbf{r}/r$  the unit vector connecting these two atoms, and  $\mu_0$  the magnetic permeability. This Hamiltonian does not modify the scattering properties of atoms in the same state. However, it does play a role for pairs of particles occupying the two different states  $|1\rangle, |2\rangle$  and can be seen as an additional inter-species potential

$$U(\mathbf{r}) = \frac{\mu_0 \mu_B^2}{\pi r^3} (1 - 3 \cos^2 \theta), \quad (1.14)$$

where  $\theta$  is the angle between  $\mathbf{u}$  and the (arbitrary) quantization axis. To evaluate the effect of (1.14), we consider the Fourier transform  $\tilde{U}(\mathbf{k})$  of the potential  $U(\mathbf{r})$  in a quasi-

2D geometry as derived by Fisher [81]

$$\tilde{U}(\mathbf{k}) = \frac{\hbar^2}{m} \frac{\sqrt{8\pi} a_{\text{dd}}}{\ell_z} \left[ \cos^2 \Theta \left( 2 - 3\sqrt{\frac{2}{\pi}} \bar{k} e^{\bar{k}^2/2} \text{erfc}(\bar{k}/\sqrt{2}) \right) + \sin^2 \Theta \left( -1 + 3\sqrt{\frac{2}{\pi}} \frac{\bar{k}_x^2}{\bar{k}} e^{\bar{k}^2/2} \text{erfc}(\bar{k}/\sqrt{2}) \right) \right], \quad (1.15)$$

where  $\text{erfc}(x) = 1 - \text{erf}(x)$  is the complementary error function,  $a_{\text{dd}} = \mu_0 \mu_B^2 m / 12\pi \hbar^2 = 0.7 a_0$  is the dipolar length,  $\Theta$  is the angle between the magnetic field and the normal to the atomic plane, and  $\bar{\mathbf{k}} = \mathbf{k} \ell_z$ . The anisotropy of the potential is signaled by the factor  $\bar{k}_x$  in the second term of (1.15). This expression has a simple limit for values of  $k \ll 1/\ell_z$

$$\tilde{U}(0) = \frac{\hbar^2}{m} \sqrt{8\pi} \frac{a_{\text{dd}}}{\ell_z} (3 \cos^2 \Theta - 1), \quad (1.16)$$

which corresponds to the spatial average of the MDDI potential. An analogous calculation in 3D yields an infinite value due to the long-range character of the potential [82]. An additional difference with the 3D case [83] is that MDDI does not induce any dynamical instability in a single-component planar system of bosons, as shown by Fisher [81]. By considering the spatial average of the contact potential (2.6) in the quasi-2D regime, one can interpret Eq (1.16) as a modification of the scattering length  $a_{12}$  with respect to its 3D bare value  $a_{12}^0$  by an amount

$$\delta a_{12}(\Theta) = a_{\text{dd}} (3 \cos^2 \Theta - 1). \quad (1.17)$$

### Can one add up the scattering lengths $a_{12}^0$ and $\delta a_{12}(\Theta)$ ?

In general, the scattering length associated to a pair-wise potential cannot be decomposed as the sum of the scattering lengths computed for each term appearing in the potential. In other words, the scattering length is not a linear function of the potential. Yet, this is true within the Born approximation. One condition of applicability of the Born approximation is the fact that the potential does not contain any bound state. However, this is absolutely not the case of the inter-atomic potentials from which  $a_{12}^0$  can be deduced, which contains tens of bound states. At this stage and contrary to Eq (1.17), there is no reason to conclude that the effective scattering length accounting for MDDI can be written as  $a_{12} = a_{12}^0 + \delta a_{12}(\Theta)$ .

In fact, this is still authorized and we now briefly explain why. The reasoning is made of two steps. First, the length scale associated to the interatomic potential – with a van der Waals tail in  $1/r^6$  – is different from the length scale associated the MDDI, since the first dominates at a short distance. For this reason, one can use the asymptotic form of the zero-energy wave function associated to  $a_{12}^0$  when treating the effect of MDDI, for instance through the Bethe-Peierls prescription [84, 85]. Second, the potential associated to MDDI is weak, and can be treated at the Born approximation level in a region where the van der Waals potential can be neglected. Eventually, one finds that the modified scattering length indeed writes as  $a_{12} = a_{12}^0 + \delta a_{12}(\Theta)$ .

### Ramsey spectroscopy

We characterize the effect of MDDI using Ramsey spectroscopy, as presented in Subsec 1.1.3. Here, the two identical pulses do not necessarily create equal-weight superpositions of the basis state ( $|1\rangle, |2\rangle$ ). These pulses are parametrized by the population



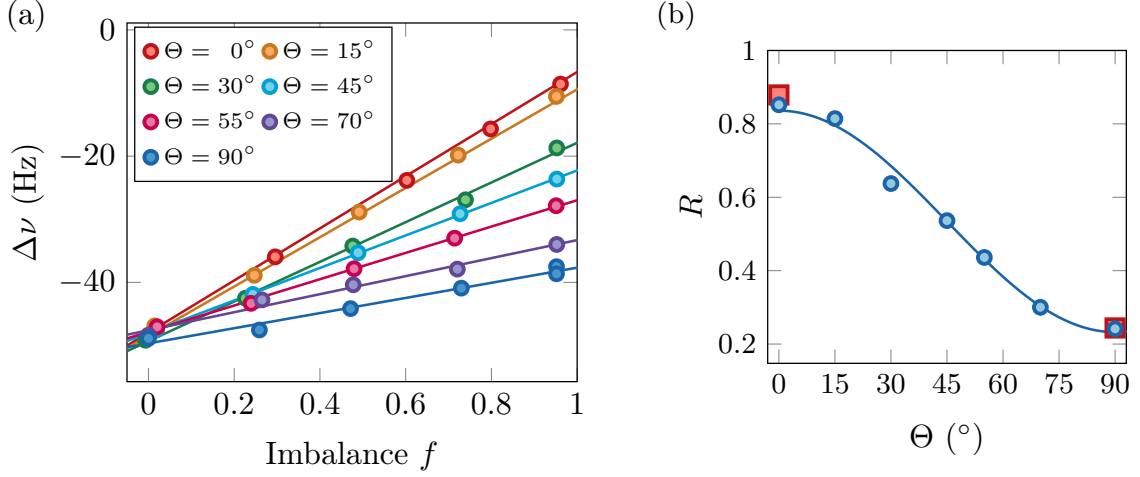


Figure 1.14: Magnetic dipole-dipole interactions in 2D. (a) Clock shift versus imbalance parameter  $f$  for various orientations of the magnetic field. (b) Ratio  $R$  defined in Eq (1.19), showing the variation of  $a_{12}$  when varying the orientation of the magnetic field. The sine fit furnishes a calibration of the various interaction parameters. Blue dots correspond to the maximum density, while red squares are obtained at half density. Figure adapted from [52].

imbalance  $f = (n_1 - n_2)/(n_1 + n_2)$  after the first transfer. For instance,  $f = 0$  for a balanced mixture,  $f = 1$  for a pulse of area  $\Omega t \ll \pi$ . We work in the deeply degenerate regime. Applying Eq(1.6) in this imbalanced case, one deduces that the resonant frequency shift writes

$$\Delta\nu = \frac{\hbar}{m} \frac{n}{\sqrt{2\pi}\ell_z} [a_{22} - a_{11} + (2a_{12} - a_{11} - a_{22}) f] \quad (1.18)$$

for an initial 2D density  $n$ . For a given orientation  $\Theta$  of the magnetic field, we measure the variation of  $\Delta\nu$  with respect to the imbalance  $f$ , and observe the expected affine behavior (1.18), as shown in Fig 1.14(a). The change of slope observed when changing  $\Theta$  (with a fixed  $y$ -intercept) reflects the modification of  $a_{12}$ . Up to an irrelevant minus-sign, the ratio of the slope to the intercept of this line

$$R(\Theta) = \frac{2a_{12}(\Theta) - a_{22} - a_{11}}{a_{11} - a_{22}} \quad (1.19)$$

should be independent of the density and is thus a robust observable. We plot the variation of the measured ratio for different angles  $\Theta$  in Fig 1.14(b) and confirm its insensitivity to density. From a sinusoidal fit of  $R(\Theta)$ , we determine the values of  $a_{22} - a_{11} = -7.0(2) a_0$  and  $a_{12}^0 - a_{11} = -2.0(1) a_0$ . These are in fair agreement with the values (1.12). Furthermore, we checked that contrary to the 3D case, the effect of MDDI does not depend on the size nor on the shape of the sample. This result holds as long as the horizontal size of the system is much larger than the vertical confinement length  $\ell_z$ .



### 1.3 Conclusion

In this chapter, we have presented our experimental platform for preparing two-dimensional Bose gases. We created a single slab of atoms from a 3D cloud using an optical accordion. We also demonstrated our ability to prepare a system with an arbitrary geometry, thanks to a digital micromirror device and grey-levels of intensity. Emphasis was then placed on the two states which we manipulate in the rest of this work. In particular, we are able to create spin superpositions by using spatially-resolved Raman transitions. The effect of magnetic dipole-dipole interactions was also investigated. Although weak, these can drastically modify the properties of our mixture due to the vicinity to the miscibility-threshold. In particular, tuning  $a_{12}$  will allow us to test important properties of soliton physics in Chapter 4.

## Chapter 2

# Description of a two-dimensional Bose gas

In the previous chapter, we showed how to prepare a homogeneous planar Bose gas deep in the quantum regime. The next step is to describe its main properties. For a large phase-space density, Einstein [4] predicted that a non-interacting 3D bosonic system experiences a phase transition characterized by the accumulation of particles in the state of lowest energy. This is the celebrated Bose-Einstein condensation (BEC). Remarkably, the addition of sufficiently weak interactions does not dramatically modify this picture and can be captured in a mean-field approximation.

In Sec 2.1, we apply this mean-field approximation to describe the ground state of a weakly-interacting 2D Bose gas. This allows us to introduce the celebrated nonlinear Schrödinger equation (NLSE), also known as the Gross-Pitaevskii equation (GPE) in the context of superfluids. This equation is a standard model of nonlinear physics and will be considered throughout this thesis. The dimensionality of a system can dramatically affect its macroscopic behavior, especially the occurrence and the characteristics of phase transitions. In Sec 2.2, we show that BEC does not occur in 2D at a non zero temperature, but that a transition to a superfluid state still exists. In particular, this justifies the use of a mean-field formalism even at low (but finite) temperature. The reader will find a more exhaustive account in the review article [86] and the lecture notes [87].

### 2.1 Description at zero temperature

In this section, we describe the ground state of a weakly-interacting 2D Bose fluid at zero temperature. We first derive the nonlinear Schrödinger equation (Subsec 2.1.1) and discuss some properties that hold in any dimension (Subsec 2.1.2). Interestingly, there are other features specific to the 2D case. In particular, extra symmetries come into play and constrain the dynamics as well as the equilibrium properties, as shown in Subsec 2.1.3.

#### 2.1.1 The nonlinear Schrödinger equation

##### The quantum problem

We consider a system of  $N \gg 1$  bosons of mass  $m$ , in two dimensions. In this section, we ignore any internal degree of freedom. The particles feel a trapping potential  $V(\mathbf{r})$  and interact through a pairwise potential  $U(\mathbf{r} - \mathbf{r}')$ . In the language of first quantization, the

corresponding Hamiltonian is given by

$$\hat{H} = \sum_{i=1}^N \left[ \frac{\hat{\mathbf{p}}_i^2}{2m} + V(\hat{\mathbf{r}}_i) \right] + \frac{1}{2} \sum_{i \neq j} U(\hat{\mathbf{r}}_i - \hat{\mathbf{r}}_j) \quad (2.1)$$

where  $\hat{\mathbf{r}}_i$  and  $\hat{\mathbf{p}}_i$  are the operators representing the position and the momentum of particle  $i$ . Equivalently, one can switch to the second quantization formulation and write

$$\begin{aligned} \hat{H} = \int d^2r \left[ \frac{\hbar^2}{2m} \nabla \hat{\Psi}^\dagger(\mathbf{r}) \cdot \nabla \hat{\Psi}(\mathbf{r}) + V(\mathbf{r}) \hat{\Psi}^\dagger(\mathbf{r}) \hat{\Psi}(\mathbf{r}) \right. \\ \left. + \frac{1}{2} \int d^2r' \hat{\Psi}^\dagger(\mathbf{r}) \hat{\Psi}^\dagger(\mathbf{r}') U(\mathbf{r} - \mathbf{r}') \hat{\Psi}(\mathbf{r}') \hat{\Psi}(\mathbf{r}) \right]. \quad (2.2) \end{aligned}$$

In this expression,  $\hat{\Psi}(\mathbf{r})$  (resp.  $\hat{\Psi}^\dagger(\mathbf{r})$ ) is the field operator annihilating (resp. creating) a particle at position  $\mathbf{r}$ . Our goal is to describe the ground state  $|\Phi_N\rangle$  of the Hamiltonian (2.2), under the constraint that  $|\Phi_N\rangle$  contains exactly  $N$  particles.

### Weakly-interacting regime

In the following, the interaction potential  $U(\mathbf{r} - \mathbf{r}')$  is assumed to be short-ranged and will eventually be replaced by an effective potential accounting for the low-energy scattering properties [85]. This substitution is possible when working in the *low-temperature regime* in which collisions only affect particles with zero relative angular momentum, through the so-called *s-wave* channel. This regime is reached when the thermal wavelength  $\lambda_{\text{th}}$  is much larger than the characteristic range of the interactions. For  $^{87}\text{Rb}$ , this is given by the van der Waals radius  $R_{\text{vdW}} = 99.4 a_0$ ,  $a_0$  being the Bohr radius.

In a 3D situation, it is relevant in this low-temperature regime to substitute the full inter-atomic potential by a pseudo-potential  $U_{\text{pp}}$  with zero range, which acts on a wave function  $\psi$  as

$$U_{\text{pp}}[\psi(\mathbf{r})] = g \delta(\mathbf{r}) \frac{\partial}{\partial r} [r \psi(\mathbf{r})] \Big|_{r=0}. \quad (2.3)$$

In this expression, the coupling parameter  $g = 4\pi\hbar^2 a/m$  is set precisely to recover the 3D scattering length  $a$  of the full inter-atomic potential. The latter is related to the 3D scattering cross-section through  $\sigma_c = 8\pi a^2$ . Note that for the ground state levels of  $^{87}\text{Rb}$  and at low magnetic field, the scattering length  $a \simeq R_{\text{vdW}}$  is positive and the corresponding interactions are effectively repulsive ( $g > 0$ ). Importantly, the derivative term in Eq (2.3) is useful only when wave functions present a singularity at the origin. It does not yield any difference with respect to a pure contact potential in the case of functions regular at the origin.

In 2D, there exists no such zero-range potential for quantum scattering problems. We will discuss some consequences of this statement at the end of Subsec 2.1.3. Still, it is allowed to use a 2D contact potential when studying the classical field problem associated to Eq (2.2)

$$E[\phi] = \int d^2r \left[ \frac{\hbar^2}{2m} |\nabla \phi|^2 + V(\mathbf{r}) |\phi(\mathbf{r})|^2 + \int d^2r' U(\mathbf{r} - \mathbf{r}') |\phi(\mathbf{r})'|^2 |\phi(\mathbf{r})|^2 \right], \quad (2.4)$$

i.e. when one can neglect the operatorial nature of the field. This is the approach we will follow in the next paragraph. We now explain which coupling parameter to choose in this

case. We saw in the previous chapter that an effective 2D system is realized by imposing a tight confinement along one direction of space, here the vertical direction  $z$ . The motion along that direction is then frozen and occurs only in the perpendicular  $(x, y)$ -plane. For deeply trapped atoms, the vertical confinement can be approximately described by a harmonic potential, with angular frequency  $\omega_z$ . The tight-confinement condition then writes

$$k_B T \text{ and } E_i/N \ll \hbar\omega_z \quad (2.5)$$

with  $E_i/N$  the interaction energy per particle. In other words, the characteristic energies at play should not allow the particles to populate the excited states of the vertical potential. Note that most experiments work in the regime  $\mu < k_B T$ . When condition (2.5) is fulfilled, the vertical state of the system is a Gaussian density distribution of extension  $\ell_z = \sqrt{\hbar/(m\omega_z)}$ . In a situation where a mean-field treatment is possible, the macroscopic wave function is regular everywhere and one can forget about the derivative term in Eq (2.3). Integrating the resulting contact potential along  $z$  yields the following effective 2D contact potential

$$U(\mathbf{r}) = \frac{\hbar^2}{m} \tilde{g} \delta(\mathbf{r}) \quad \tilde{g} = \sqrt{8\pi} \frac{a}{\ell_z}. \quad (2.6)$$

associated to the dimensionless coupling strength  $\tilde{g}$ . We insist on the fact that this expression makes sense only for a classical field problem like (2.4). The *weakly-interacting regime* in 2D corresponds to  $\tilde{g} \ll 1$  [86]. With our experimental parameters ( $a \simeq R_{\text{vdW}}$ ,  $\omega_z/2\pi \simeq 4$  kHz), one obtains  $\tilde{g} \simeq 0.16$ . While the cloud is kinematically 2D, as expressed by Eq (2.5), collisions conserve their 3D character since  $a \ll \ell_z$ , hence the name of *quasi-2D regime*.

### Hartree ansatz

As discussed by Petrov et al. [88], the ground state of a weakly-interacting 2D system is a true condensate. This means that, at  $T = 0$ , a majority of the particles described by  $|\Phi_N\rangle$  are in the same quantum state, described by a single-particle wave-function  $\phi(\mathbf{r})$ . We get a good description of  $|\Phi_N\rangle$  by using the so-called *Hartree ansatz*

$$\langle \mathbf{r}_1, \dots, \mathbf{r}_N | \Phi_N \rangle \propto \phi(\mathbf{r}_1) \cdots \phi(\mathbf{r}_N), \quad (2.7)$$

i.e. by assuming that *all* particles are in the same state. In particular, this prescription amounts to neglecting all spatial correlations between particles. The *macroscopic wave-function*  $\phi$  will be normalized in the following way

$$\int d^2r |\phi(\mathbf{r})|^2 = N, \quad (2.8)$$

such that  $|\phi(\mathbf{r})|^2$  represents the particle density. We emphasize that the validity of (2.7) holds for the ground state description valid at  $T = 0$ , and not at temperatures  $T > 0$  *a priori*. By computing the total energy  $\langle \Phi_N | \hat{H} | \Phi_N \rangle$  with the Hartree ansatz, one obtains the energy functional

$$E[\phi] = \int d^2r \left[ \frac{\hbar^2}{2m} |\nabla \phi|^2 + V(\mathbf{r}) |\phi(\mathbf{r})|^2 + \frac{\hbar^2}{2m} \tilde{g} |\phi(\mathbf{r})|^4 \right], \quad (2.9)$$

where we used the expression of the potential given in Eq (2.6). In this expression, the term  $\int d^2r |\phi|^4$  does not yield any singularity. Note that we also used the following approximate

relation  $N - 1 \simeq N$  assuming  $N \gg 1$ . The three terms in Eq (2.9) respectively give the kinetic energy  $E_k$ , the potential energy  $E_p$  and the interaction energy  $E_i$  of the system. We can now minimize (2.9) with respect to  $\phi$  to get a description of the ground state. To satisfy condition (2.8), we introduce a Lagrange multiplier  $\mu$  and we add the following term

$$-\mu N = -\mu \int d^2r |\phi(\mathbf{r})|^2 \quad (2.10)$$

to the expression defining (2.9).  $\mu$  represents the chemical potential  $\partial E / \partial N$  of the system. The modified functional can now be minimized in the standard manner and one gets the stationary *nonlinear Schrödinger equation*

$$-\frac{\hbar^2}{2m} \nabla^2 \phi + V(\mathbf{r}) \phi + \frac{\hbar^2}{m} \tilde{g} |\phi|^2 \phi = \mu \phi. \quad (2.11)$$

Multiplying Eq(2.11) by  $\phi^*(\mathbf{r})$  and integrating over the full plane leads to the following remarkable relation, valid in any dimension

$$-\mu N = E_k + E_p + 2E_i = E + E_i. \quad (2.12)$$

### Time-dependent formulation

We now derive the equation describing the dynamics of the macroscopic wave-function. We change notation for this time-dependent field  $\psi(\mathbf{r}, t)$ . An evolution equation generalizing (2.11) can be obtained by considering the following Lagrangian

$$\mathcal{L}[\psi] = \int d^2r \frac{i\hbar}{2} \left( \psi^* \frac{\partial \psi}{\partial t} - \psi \frac{\partial \psi^*}{\partial t} \right) - E[\psi], \quad (2.13)$$

where  $\psi^*$  represents the complex conjugate of  $\psi$ . Looking for the minimum of the action  $\mathcal{S}[\psi] = \int dt \mathcal{L}[\psi]$  with given initial and final configurations, this leads to the time-dependent NLSE

$$i\hbar \frac{\partial \psi}{\partial t} = -\frac{\hbar^2}{2m} \nabla^2 \psi + V(\mathbf{r}) \psi + \frac{\hbar^2}{m} \tilde{g} |\psi|^2 \psi. \quad (2.14)$$

Importantly, the evolution under Eq (2.14) conserves both the energy  $E$  and the atom number  $N$ . As usual, from a solution  $\phi(\mathbf{r})$  of the stationary equation (2.11), one can form a time-dependent function  $\psi(\mathbf{r}, t) = \phi(\mathbf{r}) e^{-\frac{i\mu t}{\hbar}}$  solution of Eq (2.14),  $\mu$  playing the same role as the energy for the linear Schrödinger equation.

#### 2.1.2 Ground state and dynamics

Hereafter, we present various properties of the NLSE solutions. These can be generalized in any dimension  $D$ , and a more exhaustive account can be found in [89]. We focus on the 2D homogeneous case which is relevant for our experiments. In practice, this is achieved by considering a system confined in a large and flat potential  $V(\mathbf{r})$  with sharp edges (vanishing boundary conditions). Alternatively, it is often easier to consider periodic boundary conditions for theoretical or numerical calculations, as long as one focuses on properties not sensitive to the presence of edges.

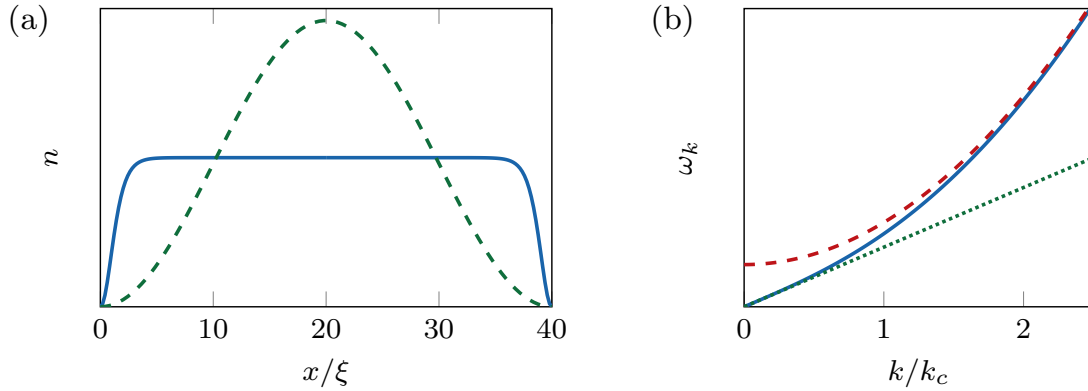


Figure 2.1: (a) Density profile in the Thomas-Fermi regime (blue solid line) compared to the ground-state density profile in the absence of interactions (green dashed line). (b) Bogoliubov dispersion relation (blue solid line), together with the phonon regime at low  $k$ 's (green dotted line) and the regime of large  $k$ 's (red dashed line) which resembles the free particle spectrum (up to an additive constant). Momenta are expressed in units of  $k_c = 1/\xi$ .

### Thomas-Fermi regime

Let us determine the equilibrium properties of the system in a box potential. Deep in the bulk, we study the situation in which one can neglect the kinetic term of Eq (2.11) with respect to the nonlinear term. This leads to the important relation

$$\mu = \frac{\hbar^2}{m} \tilde{g} n, \quad (2.15)$$

and the density  $n = |\phi|^2$  is thus uniform far from the edges. This is the so-called *Thomas-Fermi* approximation. Close to the boundaries, one cannot neglect the kinetic term and the density  $|\phi|^2$  varies from  $n$  to zero over a characteristic distance

$$\xi \equiv \frac{1}{\sqrt{2\tilde{g}n}}, \quad (2.16)$$

called the *healing length*, obtained by balancing the kinetic and interaction energy cost in the transition region. With our typical experimental parameters ( $\tilde{g} \simeq 0.16$ ,  $n \simeq 100/\mu\text{m}^2$ ) one can estimate  $\xi \simeq 0.2 \mu\text{m}$ . In Fig 2.1, we show a density-cut obtained after solving Eq (2.11) in a rectangular system with vanishing boundary conditions. The profile is almost uniform except when approaching the box edges. For comparison, we also represented the ground state of the system in the absence of interactions – i.e. a sine square vanishing at both edges.

There exist other stationary solutions to Eq (2.11) with an energy strictly larger than the ground state, thus being metastable. In 2D and in 3D, important examples are the vortex states and ring solitons in a disk box potential with axial symmetry [90]. Vortex states feature a phase winding (multiple of  $2\pi$ ) around the origin, and ring solitons combine this vorticity with alternating rings of high and low densities. In 2D, these solutions take the following form using polar coordinates

$$\phi(r, \theta) = R(r) e^{is\theta}, \quad (2.17)$$

where  $s \in \mathbb{Z}^*$ . The radial part  $R(r)$  of the wave-function must vanish at  $r = 0$  since the phase is ill-defined at this position, and the healing length gives the characteristic radius of the corresponding density depletion.

### Bogoliubov excitations

Elementary excitations above the ground state can be determined via a linear stability analysis of Eq (2.14). In the uniform case, this leads to the celebrated Bogoliubov equations [91] involving complex frequencies  $\bar{\omega}_k = \omega_k + i\gamma_k$  and associated to plane waves with wave vector  $\mathbf{k}$  of norm  $k$ . In the case of repulsive interactions, one obtains only real frequencies ( $\gamma_k = 0$ ) which satisfy the following dispersion relation

$$\hbar\omega_k = \frac{\hbar^2}{2m} \sqrt{k^2 (k^2 + 4\tilde{g}n)}. \quad (2.18)$$

In this expression, the healing length provides a typical momentum separating the free-particle excitations ( $k \gg k_c \equiv 1/\xi$ ), for which the dispersion relation (2.18) is quadratic, from the phonon excitations ( $k \ll k_c$ ), for which it is linear. The corresponding phonons propagate at the Bogoliubov speed of sound  $c_0$  defined such that  $\omega_k \simeq c_0 k$ , yielding

$$c_0 = \frac{\hbar}{m} \sqrt{\tilde{g}n} = \frac{\hbar}{\sqrt{2m\xi}}. \quad (2.19)$$

With our experimental parameters, one can estimate  $c_0 \simeq 3 \text{ mm}\cdot\text{s}^{-1}$ . Note that  $c_0$  gives an upper bound to the critical velocity for a superfluid flow, based on Landau's criterion [92]. These sound modes were observed experimentally in a 2D configuration by several groups [93–95]. In the finite temperature case, however, the generalization of Bogoliubov's theory in two dimensions is not straightforward, as explained by Mora & Castin [96].

### Hydrodynamic formulation

We reformulate the time-dependent equation (2.14). Using the density-phase representation  $\psi = \sqrt{n(\mathbf{r})} e^{i\theta(\mathbf{r})}$ , we consider the two variables

$$n(\mathbf{r}) \quad \mathbf{v}(\mathbf{r}) = \frac{\hbar}{m} \nabla \theta, \quad (2.20)$$

where  $\mathbf{v}$  can be seen as an irrotational velocity field. Due to the gradient term in (2.20) and the fact that  $\theta$  is single-valued, the circulation of  $\mathbf{v}$  along any closed contour  $\Gamma$  must be quantized

$$\int_{\Gamma} d\ell \cdot \mathbf{v} = \frac{h}{m} s, \quad s \in \mathbb{Z} \quad (2.21)$$

Using the so-called Madelung transform (2.20), Eq (2.14) can be re-expressed as

$$\begin{cases} \frac{\partial n}{\partial t} = -\nabla \cdot (n\mathbf{v}) \\ \frac{\partial \mathbf{v}}{\partial t} = \nabla \left[ -\frac{1}{2}\mathbf{v}^2 - V(\mathbf{r}) - \frac{\hbar^2}{m^2} \tilde{g} n + \frac{\hbar^2}{2m^2} \frac{\Delta \sqrt{n}}{\sqrt{n}} \right] \end{cases} \quad (2.22)$$

where the first line is simply a continuity equation ensuring the conservation of the atom number. The second equation can be seen as a modified Euler equation. These hydrodynamic equations further simplify in the Thomas-Fermi regime where the last term of the second equation – known as the quantum pressure – can be neglected. In this case, the motion of a condensate can be described by classical, irrotational hydrodynamics.

### 2.1.3 Symmetries in two dimensions

In general, physical models come with a certain number of symmetries. These symmetries usually constrain the possible behaviors and can greatly simplify the study of the associated physical phenomena. For example, the celebrated theorem established by Noether [97] shows that a Hamiltonian system with a continuous symmetry features a corresponding conserved quantity. In the context of partial differential equations, these symmetries formally correspond to transformations linking different solutions of the same equation. As simple examples, one can derive the conservation of energy from the invariance of Eq (2.14) with respect to a time translation, while the conservation of the norm (2.8) is associated to the invariance of Eq (2.14) under the transformation  $\psi \mapsto e^{i\varphi}\psi$  with phase  $\varphi$ .

Symmetries of the 2D NLSE are well-known and were studied extensively during the thesis of Raphaël Saint-Jalm [50]. In the free-space case or in a harmonic potential, the NLSEs written in various dimensions  $D$  all share a certain group of symmetries. However, the two-dimensional case is particular as it comes with an additional set of transformations whose group is isomorphic to  $SL(2, \mathbb{R})$  [98]. In the following, we discuss the origin and some consequences of this dynamical – or hidden – symmetry. We first focus in the free-space case (with an external potential  $V = 0$ ) which is easier to grasp and relevant for our experiments. For the presentation to be self-contained, the corresponding transformations are also listed and briefly described in Appendix A.

#### Scale invariance

Among these transformations, the most important of them is certainly the following *dilation* by a factor  $\lambda$ , which we rewrite hereafter

$$\mathcal{D}_\lambda[\psi](\mathbf{r}, t) = \frac{1}{\lambda} \psi\left(\frac{\mathbf{r}}{\lambda}, \frac{t}{\lambda^2}\right). \quad (2.23)$$

Using this transformation, one can deduce a new solution  $\mathcal{D}_\lambda[\psi]$  of Eq (2.14) from a previously known one  $\psi$ . This procedure can also be applied to the stationary solutions obtained from Eq (2.11), for which the transformation (2.23) only affects space. The corresponding property is called *scale invariance*, since the dynamics do not depend on the scale over which it happens (up to a simple rescaling of time). This phenomenon arises because of the particular form of the “contact-potential” in 2D, which scales exactly like the kinetic operator  $\nabla^2$  in a dilation operation. In more precise terms, this happens because the interaction energy  $\propto \int d^2r |\phi|^4$  and the kinetic energy  $\propto \int d^2r |\nabla\phi|^2$  for a classical field scale in the same way under (2.23), both being multiplied by a factor  $1/\lambda^2$ . For the same reason, one cannot form a quantity homogeneous to a length scale based on the model (2.14) solely<sup>1</sup> when  $V = 0$ .

These conclusions hold also for a  $1/r^2$ -interaction potential, a model known as the Calogero-Sutherland model [99]. This model is well-known for being exactly solvable in 1D, e.g. using the Bethe-ansatz [100]. Finally, the spin-1/2 unitary Fermi gas in 3D is another realization of a scale invariant system [101, 102]. In this important case, the  $s$ -wave scattering length  $a$  is infinite and does not appear anymore in the description of the system. Note that this does not apply to the 3D unitary Bose gas as three-body physics – the existence of Efimovian states with universal properties – then come into play [103, 104].

---

<sup>1</sup>There is no contradiction between this statement and the introduction of a healing length  $\xi$  in Eq (2.16) as the latter is related to a particular system (a homogeneous system with density  $n$ ).



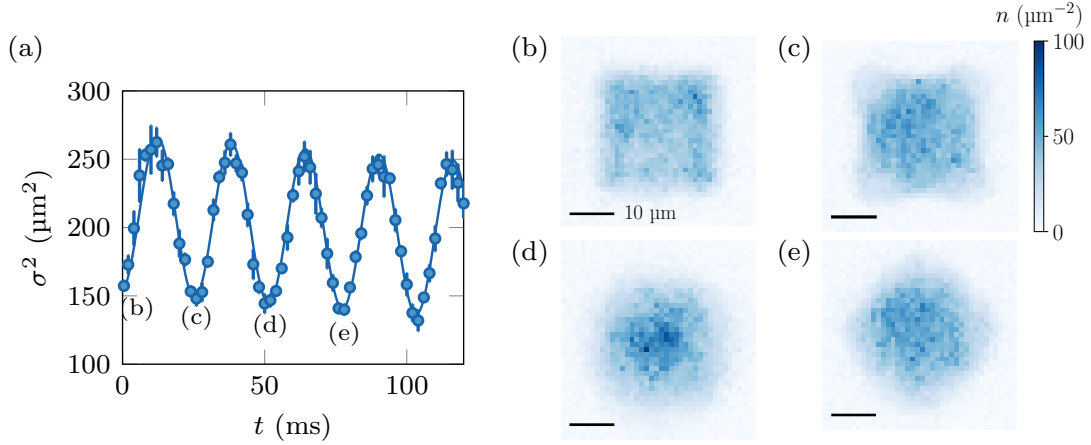


Figure 2.2: Dynamical symmetry. (a) Evolution of the RMS size  $\sigma^2$  in a harmonic trap with angular frequency  $\omega = 2\pi \cdot 19.3(1)$  rad/s, starting from a homogeneous square (b). The oscillations are fitted with a cosine function and an additional linear slope to account for losses. The fitted frequency  $\omega' = 2\pi \cdot 38.5(1)$  rad/s agrees well with the frequency  $2\omega$  deduced from Eq (2.25). The density profiles corresponding to the times indexed by (b, c, d, e) are shown on the right. Figure adapted from [49].

### Variance identity

An important consequence of the dynamical symmetry described by the  $\text{SL}(2, \mathbb{R})$  group is the *variance identity*, also known as the *virial theorem*. In the absence of an external potential, this identity relates the evolution of the root-mean-square (RMS) size  $\sigma$  to the total energy  $E$

$$\frac{d^2\sigma^2}{dt^2} = \frac{4E}{m} \quad \sigma^2 \equiv \frac{1}{N} \int d^2r n(\mathbf{r}, t) r^2. \quad (2.24)$$

In two dimensions and in free space, a stationary state is thus a zero-energy state. Note that when interactions are repulsive ( $\tilde{g} > 0$ ), there exists no stationary and normalizable state for which the definition of  $\sigma$  makes sense. Stationary states can only be realized with the help of an external potential. Actually, the relation (2.24) is always true for the linear Schrödinger equation in any dimension  $D$ , but it is maintained in the nonlinear case only for  $D = 2$ . The variance identity will be our main test-bed of scale invariance in Chapter 4.

### Dynamics in a harmonic trap

In the presence of a harmonic potential with angular frequency  $\omega$ , scale invariance is violated. However, there is still a symmetry group isomorphic to  $\text{SL}(2, \mathbb{R})$  which has distinctive consequences on the dynamics [105, 106]. For example, the variance identity (2.24) is modified and one can verify that

$$\frac{d^2\sigma^2}{dt^2} + 4\omega^2\sigma^2 = \frac{4E}{m}. \quad (2.25)$$

The size  $\sigma^2$  thus oscillates at angular frequency  $2\omega$  [106] – or with a period  $T/2$ , where  $T = 2\pi/\omega$  is the period of the classical motion in the trap<sup>2</sup>. This *breathing mode* was observed

<sup>2</sup>This is also the period for the center-of-mass motion, according to Kohn's theorem [107].

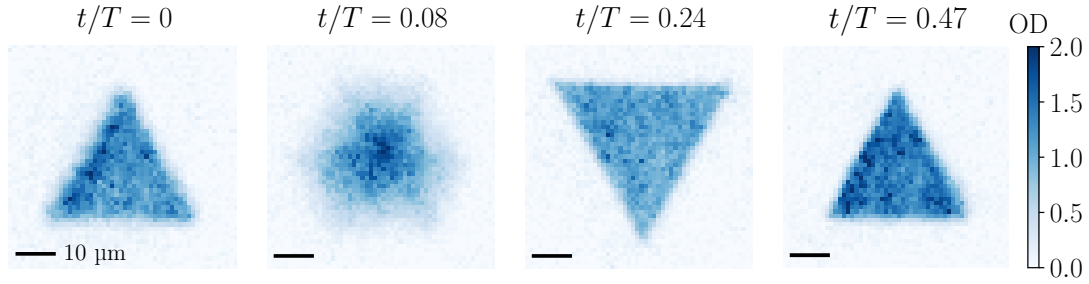


Figure 2.3: Breather of the 2D NLSE. Evolution of an equilateral triangle (from the left, first picture) in a harmonic trap. The triangle is inverted after a quarter of period of the trap (third picture). It is very close to the initial distribution after half a period (fourth picture). Figure adapted from [49].

experimentally using an elongated 3D Bose gas [108] and a 2D Fermi gas [109], and also recently using a multitude of initial states on our setup [49], see Fig 2.2. Importantly, one can also relate the dynamics in a harmonic trap with the one happening in free space through the transformation (A.9) reported in Appendix A, as tested by Saint-Jalm et al. [49].

### Breathers

These well-established facts do not constrain all the possible behaviors of a system described by the 2D NLSE. In [49], we found that the evolution of certain wave packets in a harmonic trap is periodic. Such periodic solutions of a nonlinear wave equations are called *breathers*. These findings concern the uniform equilateral triangle<sup>3</sup> featuring a motion of period  $T/2$ . The evolution of a triangle is shown on Fig 2.3. The periodicity was confirmed by numerical simulations of the 2D NLSE. Note that the evolution of an initially uniform disk was also explored in [49]. However, refined numerical simulations seem to show that the uniform disk is not a breather of the 2D NLSE, although it features a nearly periodic evolution at short times. This situation was studied recently by Torrents et al. [110].

The periodicity of the triangular wave-packet in a harmonic trap has been rigorously elucidated by Shi et al. [111], thanks to a mapping between the non-interacting (hence linear) Boltzmann equation and hydrodynamical equations<sup>4</sup>. Such a mapping is usually possible under local thermal equilibrium, i.e. when the collision rate is high-enough. However, it may also be accidentally valid despite the absence of interactions. Shi et al. [111] explicitly showed that the triangle dynamics fall into that category. Olshanii et al. [112] have interpreted this dynamics as the periodic formation of Damski shock-waves [113].

### Quantum anomaly

As claimed earlier, the use of a contact potential for describing interactions in 2D must be limited to the weakly-interacting regime  $\tilde{g} \ll 1$ . In this case, the mean-field approximation

<sup>3</sup>Experimentally, such a system is prepared by reaching equilibrium in a uniform box potential, deep in the Thomas-Fermi regime (i.e. with a healing length  $\xi$  negligibly small with respect to the size of the system).

<sup>4</sup>As recalled after introducing Eqs (2.22), the NLSE can be mapped to classical hydrodynamical equations for an irrotational flow in the Thomas-Fermi regime.

can describe the ground state with good accuracy. However, while the formulation of the NLSE (2.14) is always mathematically acceptable, the quantum treatment of scattering is ill-defined for such a contact potential. Indeed, one can show that the low-energy limit for the scattering in 2D introduces a length scale, the so-called 2D scattering length  $a_{2D}$  [87, 114, 115]. How does this translate in a geometry with reduced dimension? Petrov & Shlyapnikov [115] could relate this quantity to the parameters of the full 3D problem

$$a_{2D} \sim \ell_z \exp\left(-\frac{2\pi}{\tilde{g}}\right) \quad \tilde{g} = \sqrt{8\pi} \frac{a_{3D}}{\ell_z}. \quad (2.26)$$

The introduction of  $a_{2D}$  is in direct contradiction with the scale invariance discussed above, and the symmetry initially present in the classical theory is thus broken by quantum mechanics. Such a situation is known as a *quantum anomaly* [116]. In practice, due to the exponential term, the weakly-interacting regime associated to  $\tilde{g} \ll 1$  implies that  $a_{2D}$  is so small (with respect to any realistic atomic length scale) that  $a_{2D}$  has no concrete physical meaning. Scale invariance is then effectively realized in this regime.

How can one investigate the possible breaking of scale invariance for larger values of  $\tilde{g}$ ? Experimentally, this regime can be reached using a Feshbach resonance, for instance. Olshanii et al. [117] have proposed an experimental scheme for evidencing this phenomenon as a shift of the breathing mode frequency predicted to be equal to  $2\omega$  by the scale-invariant theory (see Eq (2.25)). Related experiments have been performed since then, allowing the observation of this anomalous shift in the case of a 2D-Fermi gas [118], as well as in the 2D-3D crossover with a unitary Fermi gas [119].

In this section, we have shown how to describe a weakly interacting two-dimensional Bose gas at zero temperature through the nonlinear Schrödinger equation. In the following, we treat the case relevant experimentally of a non-zero temperature.

## 2.2 Description at finite temperature

We now account for a finite temperature in the description of a two-dimensional Bose gas. Our main question is the following: is the mean-field theory developed in the previous section still relevant when  $T > 0$ , i.e. when the system is not in its ground state but may present fluctuations? It is well-known that the accumulation of particles in a single state, i.e. Bose-Einstein condensation, allows for such a simplification. However, it is also well-known that BEC cannot occur in an ideal two-dimensional system at  $T > 0$ . It is thus necessary to study the effect of interactions on the thermodynamics of the 2D Bose gas.

To give a simple insight over this vast program, we extend the concept of classical field theory to a finite temperature situation and formulate the question of Bose-Einstein condensation in this formalism (Subsec 2.2.1). Although BEC does not occur in the 2D interacting case, we show that both phase and density fluctuations are still strongly reduced for large phase-space densities, allowing for the presence of a superfluid fraction (Subsec 2.2.2). Finally, we remind that the appearance of this superfluid fraction is linked to a particular phase transition, the so-called Berezinski-Kosterlitz-Thouless mechanism (Subsec 2.2.3).

### 2.2.1 Classical field formalism

#### Description of thermal equilibrium

In general, a system at thermal equilibrium is described by a density matrix  $\hat{\rho}$  in which the populations of eigen-states depend only on the temperature  $T$ . For example, if one uses the grand-canonical ensemble, this density matrix can be expressed as

$$\hat{\rho} = \mathcal{Z}^{-1} \exp \left( -\frac{\hat{H} - \mu \hat{N}}{k_B T} \right) \quad \mathcal{Z} = \text{Tr} \left[ \exp \left( -\frac{\hat{H} - \mu \hat{N}}{k_B T} \right) \right], \quad (2.27)$$

where  $\hat{H}$  is the quantum Hamiltonian written in (2.2),  $\mu$  is the chemical potential and  $\hat{N}$  is the atom number operator. Formally, one could solve the problem by diagonalizing the argument in the exponential of (2.27) to deduce the corresponding populations  $\propto \exp \left( -(E_N^{(i)} - \mu N)/k_B T \right)$ . Because of the interaction term in (2.2), however, the eigen-states of  $\hat{\rho}$  involve *a priori* entangled many-body states living in a huge Hilbert space, precluding any analytical (even numerical) resolution in most cases.

The *classical field* formalism relies on a two-fold assumption [120–122]. First, similarly to Sec 2.1, most atoms occupy a same single-particle state  $\phi$ . In other words, each eigen-state of  $\hat{\rho}$  writes like Eq (2.7) for various  $\phi$ 's. Second, one can neglect the granularity of the quantum field – associated to the number of particles, excitations – and adopt classical equations for the fluctuating field  $\phi$ . The problem of thermal equilibrium is thus reduced to the determination of the probability distribution  $\mathcal{P}[\phi]$  of observing the field  $\phi$ . Physical quantities can then be evaluated through expressions of the type

$$\langle \hat{\mathcal{O}} \rangle = \text{Tr} \left( \hat{\mathcal{O}} \hat{\rho} \right) \simeq \int \mathcal{D}[\phi] \mathcal{P}[\phi] \mathcal{O}[\phi], \quad (2.28)$$

where  $\mathcal{O}$  is the classical counterpart of some quantum observable  $\hat{\mathcal{O}}$ , and  $\int \mathcal{D}[\phi]$  indicates an integral over all configurations  $\phi$ .

Note that in most cases, classical field theories suffer from divergences when accounting for short-scale modes, a problem analogous to the ultra-violet (UV) catastrophe for the black-body radiation. Such ultra-violet (UV) divergences come from high-energy degrees of freedom not being quantized. In practice, these divergences can often be cured by introducing some UV-cutoff at short scales. A natural choice for this cutoff is the thermal wavelength  $\lambda_{\text{th}}$ . Indeed, modes with an energy lower than the thermal energy have appreciable populations and satisfy condition (2), while this becomes less and less true for higher-energy modes. However, physical quantities should not be sensitive to the precise choice of the cutoff, as long as one is not interested in physical properties at the corresponding scale.

In the following, we thus forget about the density matrix  $\hat{\rho}$  given in Eq (2.27) and use a description based on a classical fluctuating field  $\phi(\mathbf{r})$ . At thermal equilibrium, the behavior of the system is then fully determined by the energy functional

$$E[\phi] = \int d^2r \left[ \frac{\hbar^2}{2m} |\nabla \phi|^2 + V(\mathbf{r}) |\phi(\mathbf{r})|^2 + \frac{\hbar^2}{2m} \tilde{g} |\phi(\mathbf{r})|^4 \right], \quad (2.29)$$

and the temperature  $T$  for the modes of length scale  $\gtrsim \lambda_{\text{th}}$ .

### BEC as a spontaneous symmetry breaking

We discuss how to translate the notion of Bose-Einstein condensate in the vocabulary of classical field theory. In the density-phase representation already considered in Eq (2.20), one writes the fluctuating field as

$$\phi = \sqrt{n} e^{i\theta}. \quad (2.30)$$

As originally formulated by Bogoliubov [91], the presence of a BEC (e.g. in dimension  $D = 3$ ) is associated to a density distribution with strongly reduced density fluctuations, together with a spatially-locked phase field  $\theta(\mathbf{r})$  which does not fluctuate even over large distances. This prescription – i.e. the choice of a particular phase  $\theta$  – breaks the  $U(1)$ -symmetry of the model, associated to the transformation  $\phi \mapsto e^{i\theta} \phi$  [123]. Moreover, the chosen phase (defined with respect to some arbitrary convention) will differ randomly from shot to shot.

### Long-range order

The property discussed above defines the onset of *long-range order* (LRO) for the *order parameter*  $\phi$ . To be more quantitative, let us introduce the (reduced) first-order correlation function for a homogeneous system<sup>5</sup>

$$g_1(\mathbf{r}_1, \mathbf{r}_2) \equiv \frac{1}{n} \langle \phi^*(\mathbf{r}_1) \phi(\mathbf{r}_2) \rangle, \quad (2.32)$$

In reality,  $g_1$  is only a function of the distance  $r = |\mathbf{r}_1 - \mathbf{r}_2|$  because of homogeneity and isotropy, so that we write  $g_1(r)$  in the following. What is the physical meaning of  $g_1(r)$ ? Since the system is homogeneous, the modulus of  $\phi$  will be the same everywhere, on average. Knowing a value of  $\phi$  at position  $\mathbf{r}_1$ ,  $g_1(r)$  measures the relative values taken by  $\phi$  at the distant point  $\mathbf{r}_2$ . Anticipating the next discussions, we see that, if one forgets about density fluctuations,  $g_1(r)$  is a convenient tool for quantifying the phase fluctuations between two distant points.  $g_1$  should thus take very small values whenever the quantities  $\phi(\mathbf{r}_1)$  and  $\phi(\mathbf{r}_2)$  are statistically independent. On the contrary, the classical field is spatially-coherent when  $g_1$  takes values of order unity [124, 125]. Like in optics, the presence of spatial coherence allows the observation of interference effects.

As formulated by Penrose & Onsager in 1956 [126], the presence of a BEC in an infinite medium is indicated by a non-zero limit of  $g_1$  for large separations, a property known as *off-diagonal LRO*<sup>6</sup>. This is for example realized in the 3D-case below the critical temperature for BEC.

## 2.2.2 Description at low temperature

### Freezing of density fluctuations

In any dimension, the interaction energy becomes dominant for large phase-space densities. Density fluctuations then come with a high cost and are strongly reduced [127–129], as

---

<sup>5</sup>In the quantum formalism,  $g_1$  is defined as

$$g_1(\mathbf{r}_1, \mathbf{r}_2) \equiv \frac{1}{n} \langle \hat{\Psi}^\dagger(\mathbf{r}_1) \hat{\Psi}(\mathbf{r}_2) \rangle, \quad (2.31)$$

where the field operators  $\hat{\Psi}, \hat{\Psi}^\dagger$  were introduced in Subsec 2.1.1.

<sup>6</sup>In fact, an equivalent definition of  $g_1$  is based on the off-diagonal elements of the density matrix  $\langle \mathbf{r}' | \hat{\rho} | \mathbf{r} \rangle$ .

observed experimentally in non-uniform systems [68, 130, 131]. This *quasi-condensate* or *pre-superfluid regime* can be understood as a state with a fixed density smaller than  $n$  and a fluctuating phase  $\theta$ . Traditionally, density fluctuations are characterized using the density-density correlation function

$$g_2(\mathbf{r}_1, \mathbf{r}_2) \equiv \frac{1}{n^2} \langle n(\mathbf{r}_1) n(\mathbf{r}_2) \rangle, \quad (2.33)$$

which depends on  $r = |\mathbf{r}_1 - \mathbf{r}_2|$  only, and quantifies the probability to detect a particle at position  $\mathbf{r}_1$  knowing that another particle has been detected at position<sup>7</sup>  $\mathbf{r}_2$ . In particular,  $g_2(0)$  measures the probability to detect simultaneously two particles at the same position. For a random (Poissonian) distribution of particles, one can show that  $g_2(0) = 1$ . A value of  $g_2(0) > 1$  (resp.  $g_2(0) < 1$ ) thus indicates a bunching (resp. an antibunching) tendency of these particles. The ideal thermal Bose gas is characterized by a value  $g_2(0) = 2$  (obtained using the quantum definition (2.34)), while a quasi-condensate should exhibit reduced density fluctuations associated to  $g_2(0) = 1$ , the results being the same for a true BEC.

Importantly,  $g_2(0)$  is generically ill-defined for an interacting quantum fluid. Indeed,  $g_2(r)$  is expected to diverge as  $\ln^2 r$  at short distance, in 2D [132]. A more rigorous way to study density fluctuation relies on the so-called Tan's contact, first introduced by Tan [133–135] as a proxy for characterizing the tails in the momentum distribution of an interacting two-component Fermi gas. Tan's contact also gives information on pair correlations. During this thesis, we measured the two-body contact of a weakly-interacting 2D Bose gas across the superfluid phase transition [51]. This work has been reported in Appendix H, and confirms that density fluctuations are strongly reduced at low temperature in our system. Our next concern is thus the freezing of phase fluctuations quantified by the first-order correlation function  $g_1$

### Mermin-Wagner-Hohenberg theorem

In 2D and without interactions,  $g_1$  decays fast and vanishes at a large distance whatever the temperature  $T > 0$ , in line with the absence of BEC reminded above. The characteristic decay length  $\ell$  of  $g_1$  – or coherence length – is given by  $\lambda_{\text{th}}$  in the classical regime  $\mathcal{D} \ll 1$ . For a system in dimension  $D < 3$ , Peierls [136] pointed out in 1935 that self-ordering is seriously hindered by thermal fluctuations. He was then studying the physics of crystallization. Following the work of Bogoliubov [137] and his famous  $k^{-2}$ -theorem, Hohenberg [138] and Mermin & Wagner [139] simultaneously established the following theorem: for a system of dimension  $D < 3$  with short-range interactions, there cannot be any phase transition involving the spontaneous breaking of a continuous symmetry at  $T > 0$ . The Mermin-Wagner-Hohenberg (MWH) theorem thus forbids genuine BEC in the weakly-interacting 2D Bose fluid. Nevertheless, one should keep in mind that, even in the ideal case, coherence can still establish over a finite size sample for a large enough degeneracy [86, 87].

---

<sup>7</sup>When considering classical fields, there is no need for normal-ordering in Eq (2.33) since all quantities commute. In the quantum case,  $g_2$  is defined as

$$g_2(\mathbf{r}_1, \mathbf{r}_2) \equiv \frac{1}{n^2} \langle \hat{\Psi}^\dagger(\mathbf{r}_2) \hat{\Psi}^\dagger(\mathbf{r}_1) \hat{\Psi}(\mathbf{r}_1) \hat{\Psi}(\mathbf{r}_2) \rangle, \quad (2.34)$$

where normal ordering allows us to get rid of a  $\delta(\mathbf{r}_1 - \mathbf{r}_2)$  term appearing when writing directly Eq (2.33) with quantum operators. The latter is the expression of quantum shot-noise.

The MWH theorem not only concerns the weakly-interacting 2D Bose fluid, and we now list a few other models with similar interactions and symmetries. For example, the XY-model in 2D describes planar ferromagnets composed of rigid magnetic moments  $\mathbf{S}$  disposed on a regular lattice. The corresponding Hamiltonian includes only nearest-neighbor interactions of the form  $\mathbf{S} \cdot \mathbf{S}'$ . This model clearly features a  $U(1)$ -symmetry associated to a simultaneous rotation of the spins in the lattice plane. The ground state of the system is obtained when all spins are parallel to each other. However, the MWH theorem precludes any long-range ordering at finite temperatures, and thus the existence of true 2D ferromagnets. The concepts developed below, in particular in Subsec 2.2.3, are also relevant to the study of quasi-crystals in 2D [140], the 2D Coulomb gas [141], thin liquid Helium films [142], exciton-polariton fluids [143] and 2D arrays of Josephson-coupled BECs [144].

### Quasi-long-range order

In the low-temperature phase, only long-wavelength phase perturbations (phonons) are significant [86]. In this regime, Bogoliubov's theory can be applied and leads to the following form for the first-order correlation function

$$g_1(r) = \langle \exp [i (\theta(\mathbf{r}_2) - \theta(\mathbf{r}_1))] \rangle \simeq \exp [-\langle \theta(\mathbf{r}_2) - \theta(\mathbf{r}_1) \rangle^2] . \quad (2.35)$$

Evaluating the quantity  $\langle \theta(\mathbf{r}_2) - \theta(\mathbf{r}_1) \rangle^2$  (which requires a UV cut-off, typically at  $\lambda_{\text{th}}$ ) shows that the behavior of  $g_1$  is very different from the high-temperature case, in which we expect  $g_1$  to decay exponentially. Indeed, for  $T < T_c$ ,  $g_1$  is found to decay as a power-law

$$g_1(r) \sim \left( \frac{\lambda_{\text{th}}}{r} \right)^\alpha \quad \alpha = \frac{1}{\mathcal{D}_s} \quad (2.36)$$

Such a slow decay of correlations is the defining feature of *quasi-long-range order* (QLRO). It allows phase coherence to establish over macroscopic distances, without contradicting the MWH theorem. This phenomena, which can be seen as a manifestation of *phase stiffness*, allows the appearance of a superfluid fraction [145]. This shows that the 2D weakly-interacting Bose gas is indeed superfluid at low temperature, in spite of MWH theorem.

### 2.2.3 Berezinskii-Kosterlitz-Thouless transition

What is the main mechanism limiting phase ordering? And how does the weakly-interacting 2D Bose gas evolves from a normal fluid at low phase-space densities to a superfluid system at high phase-space densities? Indeed, we have seen that there is no Bose-Einstein condensation in this case. The answers to these questions were given by Thouless & Kosterlitz [146] and Berezinskii [147] in 1972, through the so-called Berezinski-Kosterlitz-Thouless (BKT) mechanism.

#### A topological phase transition

We start by explaining which mechanism limits phase ordering in the system. Vortices have been introduced in Subsec 2.1.2. For any contour rounding the center of a vortex, the phase field smoothly changes by an integer multiple of  $2\pi$ . This is an intrinsic property of the topology of the phase field  $\theta(\mathbf{r})$ , hence the name of *topological defects*. Because of the phase winding, isolated vortices induce large variations of the phase field over small



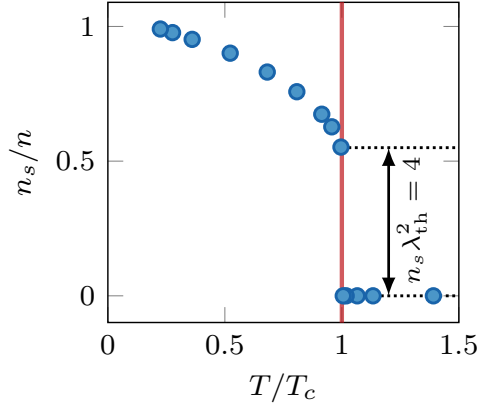


Figure 2.4: Superfluid fraction  $n_s/n$  determined by Prokof'ev & Svistunov [148] for  $\tilde{g} = 0.16$ . The universal jump of  $n_s$  at the critical point is indicated by the red line.

distances. Strictly speaking, a vortex is also associated to a zero of the density field where the velocity field gets ill-defined. This density depletion is limited to the vortex core and extends approximately over a size given by the healing length  $\xi$ .

Remarkably, there exists a critical temperature  $T_c$  below which isolated vortices are not thermodynamically favored in the system. While these isolated vortices proliferate in the high-temperature phase and destroy phase ordering, they can only survive in the form of bound vortex-antivortex pairs below  $T_c$ . Such pairs do not perturb significantly the phase field on large distances. In this case, the thermodynamic properties of the system are essentially determined by phonon modes, and lead to the quasi-long-range order presented in Subsec 2.2.2. This example of *topological phase transition* allows the appearance of a superfluid fraction  $n_s$ . Across this transition, all thermodynamic quantities are regular, but the superfluid phase-space density  $\mathcal{D}_s = n_s \lambda_{\text{th}}^2$  exhibits a universal jump from 0 to 4 at the critical point. In particular, this means that the exponent  $\alpha$  introduced in Eq (2.36) and characterizing the decay of  $g_1$  is comprised between 0 and 1/4.

This last universal relation does not provide the value of  $T_c$  in terms of  $n$  and  $\tilde{g}$  since the superfluid density  $n_s$  is not easily accessed. Using Monte-Carlo simulations, Prokof'ev & Svistunov [148] have established a quantitative connection between the critical value  $\mathcal{D}_c$  of the total phase-space density  $\mathcal{D}$ , and the coupling strength  $\tilde{g}$ . Their result writes

$$\mathcal{D}_c = \ln \left( \frac{\xi_{\mathcal{D}}}{\tilde{g}} \right), \quad (2.37)$$

where  $\xi_{\mathcal{D}} = 380(3)$  is a number determined numerically. They also provided the superfluid fraction  $n_s/n$  across the BKT transition, see Fig 2.4. Note that for temperatures  $T/T_c < 0.2$  relevant for this work, the system is almost entirely superfluid.

### Some experimental investigations

The BKT mechanism was first demonstrated experimentally by Bishop & Reppy [142] in 1978 during their study of two-dimensional liquid  $^4\text{He}$  films with torsion pendula. In this pioneering work, Bishop & Reppy indirectly determined  $n_s$  through the reduction of the moment of inertia of a torsion pendulum under the critical temperature. In cold atom



physics, Hadzibabic et al. [149] were first to observe quasi-coherence on a trapped 2D Bose gas at low temperature together with the onset of proliferation of free vortices. There has been a proposal to determine  $n_s$  by measuring the response of the system to a rotation simulated using an artificial gauge field [150, 151], though not implemented yet. Besides, Christodoulou et al. [95] determined the superfluid density through their measurement of the sound velocity across the BKT transition.

A robust characterization of the decay of  $g_1$  across the BKT transition should discriminate between an exponential and an algebraic behavior when crossing the critical point, and should also test the value for the exponent  $\alpha$  defined in (2.36). Despite remarkable attempts using various platforms (e.g. [152, 153]), such a characterization has been elusive until the very recent work of Sumami et al. [154]. Indeed, Sumami et al. indirectly determined the behavior of  $g_1$  in the homogeneous case by performing matter-wave interferometry on a system of two independent and harmonically trapped Bose gases. An analogous study with a homogeneous system has been reported in the thesis of Raphaël Saint-Jalm [50], although not published. This protocol might provide an even more stringent test of the BKT theory.

## 2.3 Conclusion

We have introduced the nonlinear Schrödinger equation describing the ground state of a two-dimensional Bose gas in the weakly-interacting regime. While some properties of this equation are relevant in any dimension, there are features specific to the 2D case due to an additional dynamical symmetry. This leads to spectacular phenomena such as the existence of breathing solutions in spite of the nonlinear character of the equation. We also presented some features going beyond the mean-field description. In the second section, we briefly discussed the main arguments justifying the use of the NLSE even at finite temperature. In the next chapter we will see which interesting properties emerge from the 2D NLSE with attractive interactions.

## Chapter 3

# Physics of Townes soliton

Solitons are fundamental objects in the study of nonlinear phenomena. They are encountered in a broad range of fields, including photonics, hydrodynamics, condensed matter, cosmology and high-energy physics [13]. For our purpose, solitons – or solitary waves<sup>1</sup> – can be defined as localized stationary solutions of nonlinear wave equations.

Why considering nonlinear models? As long as a linear description is adequate, wave propagation is generically affected by *dispersion*, i.e. the fact that the phase velocity depends on the wave’s frequency. In a more intuitive fashion, dispersion ultimately provokes the spreading of a wave packet in time or space. In some cases, however, nonlinearities cannot be neglected. A nonlinear contracting effect may then compete with the dispersive behavior. When these two mechanisms exactly compensate each other, one obtains a self-bound solution – a soliton – often with fascinating properties. Solitons were first introduced in the study of one-dimensional problems where some exact analytical solutions could be exhibited. They were found to be easily created and remarkably stable. Extensions to higher dimension soon revealed dramatically different behaviors, such as instabilities and wave collapse.

In this chapter, we discuss the existence and the stability of solitons, laying the foundations for the results of Chapter 4. The nonlinear Schrödinger equation (NLSE) with repulsive interactions was presented in Chapter 2. In the following, we will study the case of attractive interactions and its solitonic solutions (Sec 3.1), in particular in two dimensions. The 2D NLSE is known to host the celebrated Townes soliton (Sec 3.2), a stationary but unstable solution of this equation. In fact, we show that under certain circumstances, solutions of the 2D NLSE dynamics can collapse in a finite time (Sec 3.3). Finally, we discuss a recent series of experiments performed by Chen & Hung [46, 47] which show the appearance of solitary waves in an attractive 2D Bose gas (Sec 3.4).

### 3.1 Solitons of the nonlinear Schrödinger equation

In this section, we introduce the various NLSE solitons. We do not dig too much into the mathematical details and rather give some phenomenological arguments. One-dimensional solitons were first discovered in the context of the Korteweg-de Vries equation, before being exhibited for the 1D NLSE (Subsec 3.1.1). In higher dimension, stationary solutions are more fragile than in 1D, as discussed in Subsec 3.1.2.

---

<sup>1</sup>The distinction between the notions of soliton and solitary wave is discussed in Subsec 3.1.2. Somewhat imprecisely, we will often use these two expressions indifferently.

### 3.1.1 Solitons in one dimension

#### Historical background

The first detailed report of a solitonic behavior dates back to the nineteenth century. In 1845, Russell [11] described the course of a *wave of translation* or *large solitary elevation* in a narrow and shallow channel, over a few kilometers. This discovery also brought some controversies about the possibility of such a phenomenon. In particular, the soliton celerity was claimed to be larger than the one of gravity waves  $c_0$  obtained in the linear regime. At the end of the nineteenth century, Korteweg & de Vries [155] derived the model equation (KdV) for the propagation of small deformations in a shallow channel

$$\frac{1}{c_0} \frac{\partial \eta}{\partial t} + \frac{\partial \eta}{\partial x} + \frac{3}{2h} \eta \frac{\partial \eta}{\partial x} + \frac{h^2}{6} \frac{\partial^3 \eta}{\partial x^3} = 0. \quad (3.1)$$

In this nonlinear partial differential equation,  $\eta(x, t)$  stands for the elevation of the surface with respect to its rest value  $h$ ,  $x$  counts the position along the canal, and  $t$  is the time<sup>2</sup>. The linear gravity-wave celerity writes  $c_0 = \sqrt{gh}$ , with  $g$  the acceleration of gravity. The first three terms of Eq (3.1) represent convection in 1D, while the last term has a dispersive character.

Remarkably, Eq (3.1) admits the following exact solution

$$\eta(x, t) = \eta_0 \left[ \cosh \left( \sqrt{\frac{3\eta_0}{h}} \frac{x - vt}{2h} \right) \right]^{-2} \quad v = c_0 \left( 1 + \frac{\eta_0}{2h} \right) \quad (3.3)$$

which describes the propagation of a localized elevation of maximum height  $\eta_0$  at a constant velocity  $v > c_0$ . Solution (3.3) is thus a supersonic excitation of Eq (3.1). For this reason, it is intrinsically a nonlinear phenomenon, i.e. it cannot be obtained as a solution of the corresponding linear theory. Tidal bores (*marescaux* in French) and tsunamis are concrete illustrations of solitonic propagation.

The special status of the KdV equation and its shape-maintaining solution (3.3) was uncovered in 1965. A decade earlier, Fermi et al. [156] numerically simulated the evolution of a 1D-chain of particles, where nearest neighbor interactions were imposed by a harmonic plus a simple perturbing potential (e.g. linear, cubic). The harmonic case is exactly solvable. Indeed, the evolution can then be decomposed into independent modes oscillating with a well-defined frequency. However, the perturbed cases are not. By tracking the spatial Fourier components of this chain under simple initial conditions, Fermi et al. did not observe the equipartition of energy between modes which was expected at long times, a characteristic of thermal equilibrium. Quite the contrary, the system showed an almost periodic evolution. This became known as the Fermi-Pasta-Ulam (FPU) problem.

In 1965, Zabusky & Kruskal [12] re-derived KdV as an effective description for small amplitude waves in the FPU problem. Through numerical simulations, they noticed that a large class of initial conditions led Eq (3.1) to the formation of multiple pulses similar to

---

<sup>2</sup>Note that under the proper change of variable and some rescaling, Eq (3.1) can be expressed in the more standard and dimensionless form

$$\frac{\partial \eta}{\partial t} + \frac{\partial}{\partial x} \left( \frac{\partial^2 \eta}{\partial x^2} + \eta^2 \right) = 0, \quad (3.2)$$

in which we kept the same notations for simplicity.

(3.3). They were first to coin the term *solitons* for these peaks. The solitons were found to propagate at a constant velocity when far from each other, and to emerge roughly unaffected from successive collisions. This was a crucial step to explain the recurrence phenomenon observed in [156]. In 1967, the *inverse scattering method* was discovered by Gardner et al. [157] as a powerful technique for solving KdV.

Actually, the KdV equation is a particular instance of an *integrable model*. This holds also for the 1D NLSE whose solitonic solutions are presented in the next paragraph. For both examples, the existence of a large number of conservation laws constrains the dynamics to a regular (and solvable) behavior. Such systems do not feature *ergodicity*: they can only visit a tiny portion of phase-space during the dynamics, as illustrated by the recurrence phenomenon observed by Fermi et al. [156]. In particular, thermal equilibrium is never reached. This is to be opposed to chaotic systems, where slightly differing initial conditions can lead to arbitrary large deviations at long times.

### Nonlinear Schrödinger equation

We now remind the nonlinear Schrödinger equation describing the evolution of a matter-wave  $\psi$ . In dimension  $D$ , we choose to write the NLSE

$$i\hbar \frac{\partial \psi}{\partial t} = -\frac{\hbar^2}{2m} \nabla^2 \psi + \frac{\hbar^2}{2m} \tilde{g} |\psi|^2 \psi. \quad (3.4)$$

In this expression, the quantity  $\tilde{g}$  has the dimension of a length to the power  $(D - 2)$ . It is dimensionless only for  $D = 2$ . As reminded earlier, the *cubic nonlinearity*  $|\psi|^2 \psi$  stems from our choice of a contact potential. In reality, the NLSE is a very general model as it often emerges when describing the envelope dynamics of a quasi-monochromatic plane wave propagating in a dispersive medium with a weak nonlinearity [158].

In the context of nonlinear optics, Eq (3.23) describes the propagation of a light beam within the paraxial approximation, inside a medium with a focusing Kerr effect. For a *spatial soliton*,  $\psi$  represents the complex envelop of the electric field. The beam profile is then supposed to be stationary in time:  $t$  represents the distance on the optical axis, while the spatial coordinates represent the transverse directions. In this case, dispersion is due to diffraction. In dimension  $D = 1$ , it is also possible to obtain *temporal solitons*, i.e. a beam localized in time, a pulse. In that case,  $t$  still represents the distance on the optical axis, while the spatial direction is a local time. The NLSE also applies to some cases of non-linear wave propagation in plasmas, such as small-amplitude Langmuir waves [13, 159, 160].

### Reduced notations

To avoid the heaviness of standard physical units, we define a system of reduced notations where all physical quantities are expressed in units of length. In some cases, we will also incorporate the absolute value of the parameter  $\tilde{g}$  in the norm of the wave function  $\phi$ , such that  $\int d^2r |\phi|^2 = |\tilde{g}|N$ . This way, it gets clearer that the strength of the nonlinearity is solely determined by the *nonlinear parameter*  $\mathcal{N} \equiv \tilde{g}N$ . To help switching from one convention to another, we list the correspondence between the standard and the reduced notations in Table 3.1, with a symbol  $\prime$  over the reduced quantities. In practice, we do not use these primed notations for simplicity and solely mention the convention beforehand.

Quantity	In physical units	Reduced quantity
Position	$\mathbf{r}$	$\mathbf{r}'$
Spatial derivative	$\nabla$	$\nabla'$
Time	$t$	$\frac{m}{\hbar}t'$
Velocity	$(c_0, \mathbf{v})$	$\frac{\hbar}{m}(c'_0, \mathbf{v}')$
Angular frequency	$\omega$	$\frac{\hbar}{m}\omega'$
Energy	$(E, \mu)$	$\frac{\hbar^2}{m}(E', \mu')$
Wave function	$(\phi, \psi)$	$(\phi', \psi')$

Table 3.1: Correspondence between the quantities expressed in physical units and reduced quantities. The notations of the two right-hand columns facing each other are defined to be equal. In some cases, we choose a different normalization for the wave function such that  $\int d^2r |\phi|^2 = |\tilde{g}|N$ .

### Solitons of the 1D NLSE

The pioneering works [12, 157] raised interest in solvable models with an infinite number of degrees of freedom. In 1972, Zakharov & Shabat [161] extended the inverse scattering method to the 1D attractive NLSE. Using our reduced notations, this equation writes

$$i\frac{\partial\psi}{\partial t} = -\frac{\partial^2\psi}{\partial x^2} - |\psi|^2\psi. \quad (3.5)$$

with  $\int d^2r |\psi|^2 = |\tilde{g}|N$ . Similarly to KdV, the evolution under (3.5) is also nearly periodic, see Fig 3.1 for an illustration starting from a Gaussian distribution. A well-known stationary solution of Eq (3.5) is the following *bright soliton*

$$\psi(x, t) = \sqrt{2|\mu|} \frac{1}{\cosh\left(\sqrt{|\mu|x}\right)} e^{-i\mu t} \quad (3.6)$$

which only depends on a parameter  $\mu < 0$  analogous to a chemical potential. Note that the analytical form (3.6) is surprisingly similar to the Eq (3.3) describing the KdV soliton. An extended family of moving solutions can also be obtained from (3.6) using Galilean invariance. Alike KdV solitons, solitons of the 1D NLSE can collide and retrieve their original shape afterwards, up to a phase jump [161]. This stability is also reminiscent of particles undergoing elastic collisions. These properties suggest that a fine tuning of the initial conditions is not required for the observation of 1D NLSE solitons.

Let us stress that the bright soliton (3.6) is not the only remarkable solution of the attractive NLSE (3.5). The Peregrine soliton is another example both localized in time and space [162], which is reminiscent of the rapid formation and disappearance of freak waves in the ocean. Shape-preserving solutions also exist for the repulsive NLSE – corresponding to a nonlinear term with a positive sign in Eq (3.5). Since they correspond to a hole in an infinite system, they are called *grey solitons* [163]. If the asymptotic  $|\psi|^2$  is taken to be equal to 1 (hence the chemical potential equals  $\kappa$ ), they can be expressed as

$$\psi(x, t) = (\nu \tanh[\nu\sqrt{\kappa}(x - \sqrt{\kappa}\chi t)] + i\chi) e^{-i\kappa t} \quad \nu^2 + \chi^2 = 1 \quad (3.7)$$

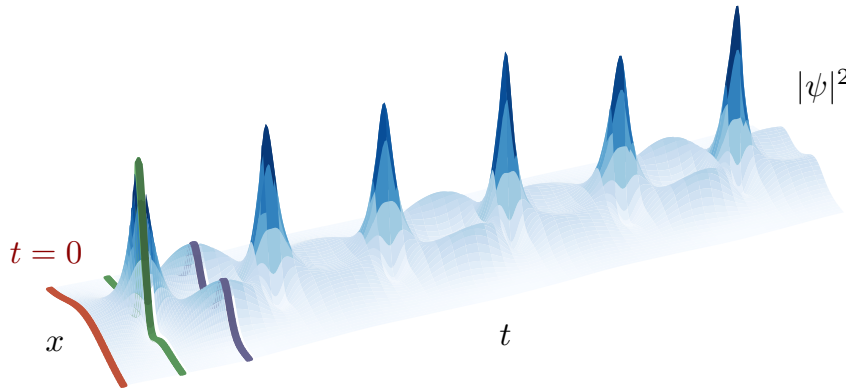


Figure 3.1: Evolution under the 1D NLSE. Example with Gaussian initial conditions (red curve at the left). The time of evolution  $t$  increases from left to right. The density profile  $|\psi(x,t)|^2$  first shows one bright peak (green curve) before it splits into two peaks (purple curve). The subsequent evolution is almost periodic.

with real numbers  $-1 < \nu, \chi < 1$ . Such a wavefunction cannot be normalized but still corresponds to a localized excitation. More precisely, (3.7) can be interpreted as a density hole with depth  $\nu^2$  moving at a constant velocity  $\sqrt{\kappa}\chi$ . For a 1D BEC, the limit ( $\nu = 0, |\chi| = 1$ ) gives a velocity equal to the Bogoliubov speed<sup>3</sup>, meaning that a grey soliton is always subsonic. In the other limiting case  $|\nu| = 1, |\chi| = 0$ , the density profile is stationary and vanishes for  $x = 0$ , with a phase jump of  $\pi$  across its center, hence the name of *dark soliton*. Note that a solution analogous to this dark soliton is the vortex in dimension  $D = 2$ , as presented in Subsec 2.1.2.

### Some observations of 1D solitons

In nonlinear optics, the experimental study of NLSE solitons started soon after the invention of intense and monochromatic laser sources. Self-trapping of laser light in a nonlinear medium was predicted in the early 1960s [16]. However, this situation involving two transverse dimensions is qualitatively different from the 1D case, as we will show in the next subsection. Henceforth, diffraction needed to be inhibited along one or two directions to realize a genuine 1D soliton, be it a temporal or a spatial soliton.

The first realization of a 1D (temporal) soliton in optics was described by Mollenauer et al. [20], following the earlier proposal of Hasegawa & Tappert [164]. Dynamics in the transverse directions was frozen thanks to a tight confinement using an optical fiber. The first observation of temporal dark solitons was reported by Weiner et al. [165]. The optical generation of spatial solitons in a 1D configuration was demonstrated a bit later than its temporal counterpart, using liquid carbon disulphide  $\text{CS}_2$  [21]. In this case, the beam was strongly elliptical so that diffraction along the major axis was essentially suppressed. Other realizations and extensions of the NLSE paradigm for the study of optical solitons can be found in the lecture notes of Zakharov et al. [166]. Note that solitonic pulses were proposed as promising platforms for the implementation of ultra-fast optical communications [167].

Regarding matter-wave solitons, two series of experiments performed in 2002 reported the production of bright solitons using attractive Bose gases confined in a quasi-1D ge-

<sup>3</sup>See Subsec 2.1.2.



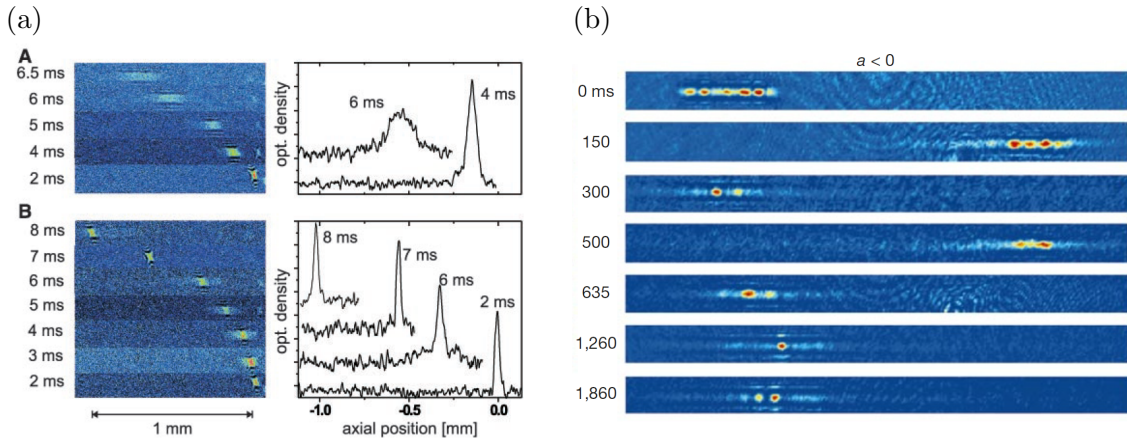


Figure 3.2: One-dimensional matter-wave solitons. (a) Atomic cloud in an anti-confining cigar-shaped trap. In (A), the interactions are repulsive and the systems gets more dilute as it drifts when time goes one (from bottom to top). In (B), attractive interactions allow a self-bound soliton to propagate through the optical wave-guide. The integrated density profiles are shown on the left. Figure taken from [23]. (b) Example of soliton train. The atom number in the initial BEC is one order of magnitude larger than in (a), facilitating the formation of multiple solitons. Figure taken from [24].

ometry [23, 24], see Fig 3.2. Both groups used ultracold  $^7\text{Li}$  initially at equilibrium with a positive scattering length in a cylindrical trap. The scattering length could then be tuned from positive to negative thanks to a magnetic Feshbach resonance. Khaykovich et al [23] obtained a single soliton, while a train composed of a few solitons was observed by Strecker et al [24]. In the second case, the axial confinement allowed them to observe the solitons on a longer timescale.

Following these pioneering experiments, subsequent studies observed the reflection of a soliton on a potential barrier [168], binary collisions [15], long-lived excitation (breathing) modes<sup>4</sup> [169]. Bright solitons could also be used for implementing a Mach-Zender interferometer [170]. Note that dark solitons in a repulsive Bose gas have been produced earlier using a phase imprinting method [22, 172]. Finally, matter-wave magnetic solitons – spin solitary waves in a multi-component superfluid system – were proposed by Qu et al. [173] and observed very recently [27, 28].

### 3.1.2 Multidimensional solitons

For a given nonlinear problem, supplementary dimensions can substantially enrich the observable behaviors. For instance, topologically non-trivial configurations like 2D vortices with embedded vorticity, or 3D magnetic textures alike skyrmions can be realized [174]. However, unlike 1D solitons which are usually stable objects, integrability is generically lost in 2D and 3D settings – in particular, the inverse scattering method cannot be applied – and stability becomes a major concern. This is the origin of the distinction between *solitary waves* and solitons, the first ones being stationary waves which do not share the stability properties of 1D solitons.

<sup>4</sup>Note that the existence of a localized breathing mode in this experiment is a signature of physics beyond the standard 1D NLSE. Indeed, this soliton does not support localized excited states [171].

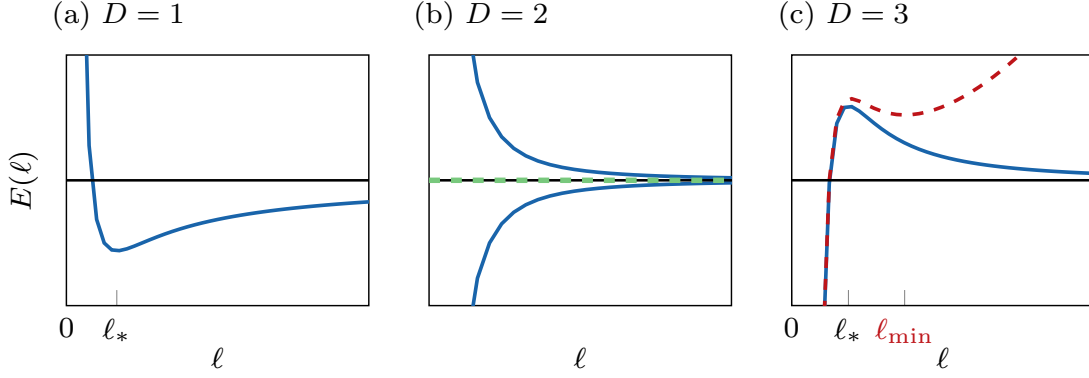


Figure 3.3: Scaling analysis. The function  $E(\ell)$  defined in (3.9) is represented for  $D = 1, 2, 3$  (blue solid line in each case). While it presents a clear minimum (resp. maximum) for  $D = 1$  (resp.  $D = 3$ ), it is monotonic for  $D = 2$ . An extremum can be obtained only for a particular value of the nonlinear parameter  $\mathcal{N}$ , and any  $\ell$  due to scale invariance (green dashed line). In (c), we also plot the analogous scaling in the presence of a harmonic potential (red dashed line), in the case where a local minimum exists at  $\ell = \ell_{\min}$ .

As an illustration, the immersion of a 1D soliton in higher dimension is likely to suffer from *transverse instabilities*, also known as snake instabilities. Indeed, a system with a solitonic profile in one direction and an almost uniform distribution along the others fragments into small pieces along the uniform direction, as shown by Zakharov & Rubenchik [175].

### Scaling analysis

A simple scaling argument can bring insight onto the existence of stationary localized wave packets  $\phi(\mathbf{r})$  in dimension  $D$ . We first rewrite the energy functional (2.9) in the case of a focusing nonlinearity using our reduced notations

$$E[\phi] = \frac{1}{2} \int d^D r (|\nabla \phi|^2 - |\phi|^4), \quad (3.8)$$

where  $\phi$  has been normalized such that  $\int d^2 r |\phi|^2 = |\tilde{g}|N = \mathcal{N}$ . To proceed further, let us introduce a family of self-similar wave functions, each being described by its characteristic size  $\ell$ . Then, the energy functional (3.8) should scale with  $\ell$  as

$$E(\ell) \propto \frac{1}{\ell^2} - \kappa \frac{\mathcal{N}}{\ell^D}, \quad (3.9)$$

where the number  $\kappa > 0$  depends on the shape of the chosen wave function. This dependence is shown in Fig 3.3 for  $D = 1, 2, 3$ . For  $D = 1$ , one finds a global minimum for a certain size  $\ell_* \sim 1/\mathcal{N}$ , a signature of the bright solitons introduced earlier. When  $D = 3$ , a global maximum is reached for  $\ell_* \sim \mathcal{N}$ , indicating a dynamical instability. For  $D = 2$ , the two terms of Eq (3.9) have the same scaling with  $\ell$  as a consequence of scale invariance (see Subsec 2.1.3). An extremum of  $E[\phi]$  can only be found for a particular value of  $\mathcal{N}$  and whatever size  $\ell$ .



### Some observations of multidimensional solitary waves

A fundamental realization of 2D NLSE solitary waves is the so-called *self-trapping* of optical beams, i.e. the equilibration between 2D diffraction and nonlinear Kerr focusing of an intense laser beam. *Self-focusing* was predicted by Askar'yan in 1962 [16], while the self-trapped mode was first described by Chiao et al. [17] and Talanov [18]. This mode is the celebrated *Townes soliton* which we study in detail in Sec 3.2.1.

Historically, a first attempt to demonstrate self-trapping was reported by Garmire et al [176]. Using a pulsed laser propagating in CS<sub>2</sub>, the authors observed the formation of a bright filament. With a modified setup and an enhanced optical resolution, the same team found a few months later that the filament was in reality formed of multiple small-scale filaments [177]. In all experiments performed at that time, the use of nano-second lasers induced time-dependent effects which were not captured by the simple 2D NLSE, as discussed by Shen [178]. The first robust observation of self-trapping using a continuous-wave laser was reported by Bjorkholm & Ashkin [19]. In this case, the propagating medium was a sodium vapor characterized by a saturating nonlinearity which provided a stabilization mechanism.

Remarkably, the formation of 2D solitary waves has been observed with other types of nonlinearities, including the photorefractive effect [179], quadratic or second-order optical nonlinearity [180], combination of fifth-seventh order ( $\sim$  focusing-defocusing) nonlinearity [181]. Let us also mention the formation of discrete solitons in photonic lattices [182] and gap solitons in two-dimensional lattices [183]. In another vein, 3D *light bullets*<sup>5</sup> in arrays of waveguides have been reported by Minardi et al. [184]. However, despite long-term efforts (e.g. the recent experiment of Falcaõ-Filho et al. [185]), a robust observation of the soliton profile associated to the focusing 2D NLSE has been only qualitative.

In the tightly-confined geometries associated to BECs, an external potential can also stabilize a 3D solitary wave. As shown in Fig 3.3(c), a local energy minimum may emerge in a harmonic potential, provided the BEC atom number does exceed a critical value. It is then in a metastable state which may decay by tunnelling effect [187]. Such a 3D system was observed by Cornish et al. [188] as shown in Fig 3.4. The measured atom number was then significantly larger than the theoretical prediction because multiple solitons were formed [189]. In [190], Meyer et al. generated the previously unobserved Jones-Roberts dark solitons in a three-dimensional atomic Bose-Einstein condensate using a phase-imprinting method. More recently, Chen & Hung [46, 47] performed a quench of a homogeneous 2D Bose gas from repulsive to attractive interactions and observed the formation of multiple solitary waves. The properties of these wave packets were found to be in good agreement with the Townes soliton, as we discuss in Sec 3.4.

### Quantum droplets

*Quantum droplets* form another important class of multidimensional self-bound objects, although their nature is fundamentally different. Originally proposed by Petrov [30], they were considered first in a 3D binary system with intra-species repulsion and inter-species attraction, in a regime where a mean-field theory predicts no stable state. Petrov suggested that quantum fluctuations [191] could stabilize the system and give it liquid-like properties. This approach was subsequently generalized to situations in low dimension [192].

---

<sup>5</sup>Light bullets refer to solitons which are localized both along the propagation axis and in transverse directions [186].

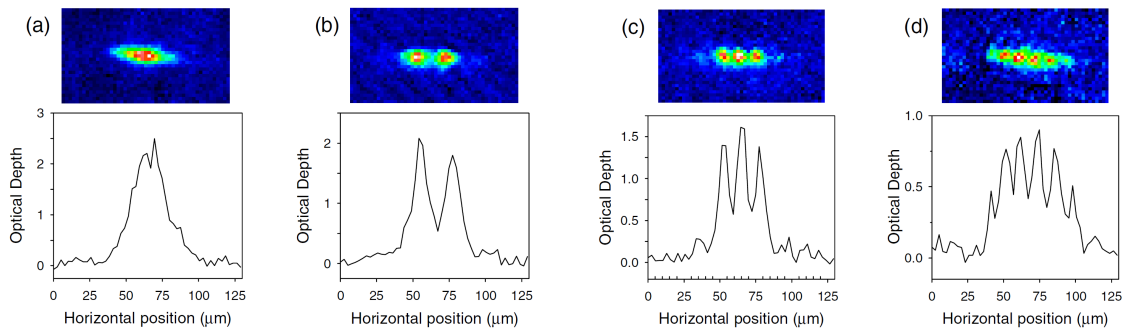


Figure 3.4: Formation of 3D matter-wave solitons in a harmonic trap. Images and integrated profiles of remnant condensates after the collapse of a 3D cloud with attractive interactions. When the interaction are sufficiently weak, a single peak is observed like in (a), while multiple peaks form for stronger interactions and/or a larger initial condensate (b-d). Figure taken from [188]

The proposal of Petrov [30] was experimentally demonstrated shortly after [31, 32]. Moreover, the transition from quantum droplets to bright solitons in a BEC mixture was studied by Cheiney et al. [193]. A few month before, quantum droplets were also observed using highly-magnetic atoms where quantum fluctuations also stabilized the otherwise unstable system [33, 34]. Hot topics on multidimensional solitary waves and related objects were recently reviewed by Kartashov et al. [14].

### Wave collapse

The energy scaling (3.9) allows some wave packets to reach arbitrary small sizes  $\ell$  during the dynamics, in dimension  $D = 3$ . It is also true in dimension  $D = 2$  for some values of the nonlinear parameter  $\mathcal{N}$ . This can have dramatic consequences on the dynamics, as for example it may allow for the collapse of the wave packet. This brings also some new questions: Can this collapse be observed? Can one predict the corresponding dynamics? Can one stabilize these solitary waves?

Such a sudden contraction was predicted numerically by Kelley [194] in 1965 for a laser beam with a sufficiently high input power. It was soon invoked to explain the anomalous onset of stimulated Raman scattering in liquids and solids observed in the sixties [195]. Self-focusing is not only a fundamental but also a technical problem, as it is often responsible for the damage caused by high-power lasers [196]. In particular, the control of nonlinear effects is one key point of the chirped-pulse amplification technique [197].

The rigorous analysis of this singular behavior triggered a lot of research in mathematics from the late seventies [158, 198]. In the (marginal) 2D case where the nonlinearity has exactly the same scaling as the dispersive term, the situation is said to be *critical*. In this case, the collapse is shown to be *strong*, i.e. a finite amount of mass concentrates in the collapsing core<sup>6</sup>. In 3D or higher dimensions, the situation is called *super-critical* and the collapse is *weak*, i.e. the mass of the collapsing core tends to zero as one approaches the collapse time. This distinction is important as it determines the efficiency of the collapse as a mechanism for energy dissipation.

<sup>6</sup>See Subsec 3.3.2.

In atomic systems, a strong increase of the density usually leads to enhanced inelastic processes which at least partially destroy the sample. In 3D BECs confined in a harmonic trap, wave collapse occurs when the atom number exceeds a critical value and leads to the celebrated *Bose-nova*. This was experimentally demonstrated by Donley et al. [199]. In the experiment performed by Eigen et al. [200], collapse was triggered in an initially homogeneous system trapped in a 3D box potential. In this case, the authors confirmed the scaling laws associated to weak collapse, in particular the counter-intuitive fact that stronger instability leads to reduced losses.

## 3.2 Properties of the Townes soliton

In this section, we study the stationary states of the 2D NLSE, in particular the celebrated Townes soliton. Various solutions are presented in Subsec 3.2.1, and the stability of the Townes soliton is discussed in 3.2.2.

### 3.2.1 Stationary states of the 2D NLSE

#### Fundamental solutions

Our goal is to determine the localized stationary solutions  $\phi(\mathbf{r})$  of the 2D NLSE. By localization, we mean that  $|\phi|$  and its derivatives should go to zero sufficiently fast at a large distance. Using polar coordinates  $(r, \theta)$  and the reduced notations of Subsec 3.1.1,  $\phi$  should thus satisfy the following equation

$$\mu \phi = -\frac{1}{2} \nabla^2 \phi - |\phi|^2 \phi \quad \nabla^2 = \frac{\partial^2}{\partial r^2} + \frac{1}{r} \frac{\partial}{\partial r} + \frac{1}{r^2} \frac{\partial^2}{\partial \theta^2}. \quad (3.10)$$

with  $\int d^2r |\phi|^2 = |\tilde{g}|N = \mathcal{N}$ . If we consider solutions with a rotational symmetry,  $\phi$  can be written as

$$\phi(r, \theta) = e^{is\theta} R(r), \quad (3.11)$$

with a phase winding  $s \in \mathbb{Z}$ . Functions (3.11) have an angular momentum of  $L_z = Ns\hbar$ . Using this ansatz, Eq (3.10) rewrites as an ordinary differential equation on  $R(r)$

$$\mu R = -\frac{1}{2} \left( \frac{d^2}{dr^2} + \frac{1}{r} \frac{d}{dr} - \frac{s^2}{r^2} \right) R - R^3, \quad (3.12)$$

where the phase term is responsible for the centrifugal barrier term  $s^2/r^2$ . If one assumes a power-law behavior at the origin, i.e.  $R(r) \sim r^\alpha$ , then Eq (3.12) leads automatically to<sup>7</sup>  $\alpha = |s|$ . As expected, a phase singularity is associated to a vanishing density for the vortex modes with  $s \neq 0$ . Solutions with  $s \neq 0$  are of great interest, in particular for their topological properties [174]. However, we restrict in the following to the *fundamental solutions* with no embedded vorticity. For  $s = 0$ , we rewrite Eq (3.12) in a slightly different manner

$$\frac{d^2 R}{dr^2} = -\frac{1}{r} \frac{dR}{dr} - 2R^3 - 2\mu R, \quad (3.13)$$

with boundary conditions  $R(r) \rightarrow 0$  when  $r \rightarrow +\infty$ , and  $dR/dr(0) = 0$ . In fact, this last condition on  $dR/dr(0)$  is automatically verified by the fundamental solutions [158], but here we take it as a regularity assumption. Eq (3.13) is a second-order differential equation. Knowing  $dR/dr(0) = 0$ , one only needs to specify  $R(0)$  to determine  $R$  on the whole axis. However, an arbitrary choice of  $R(0)$  does not guarantee the desired asymptotic behavior.

<sup>7</sup>A solution with  $\alpha = -|s| \neq 0$  cannot be normalized.

### Asymptotic behavior

For a localized state, the nonlinear term becomes negligible at sufficiently large distances. Eq (3.13) then reduces to the linear problem

$$\frac{d^2 R}{dr^2} = -\frac{1}{r} \frac{dR}{dr} - 2\mu R. \quad (3.14)$$

A localized solution of the nonlinear problem should thus approach a solution of Eq (3.14) asymptotically. For  $\mu > 0$  and up to a rescaling, the solutions of (3.13) are the zeroth-order Bessel functions  $(J_0, Y_0)$  with asymptotic behavior

$$J_0(r) \sim \sqrt{\frac{2}{\pi r}} \cos\left(r - \frac{\pi}{4}\right) \quad Y_0(r) \sim \sqrt{\frac{2}{\pi r}} \sin\left(r - \frac{\pi}{4}\right). \quad (3.15)$$

Since these functions cannot be normalized, the values of  $\mu > 0$  will be disqualified from now on. For  $\mu < 0$ , the solutions of (3.14) are the zeroth-order *modified* Bessel functions  $(I_0, K_0)$  with asymptotic behavior

$$I_0(r) \sim \sqrt{\frac{\pi}{2r}} \exp(+r) \quad K_0(r) \sim \sqrt{\frac{\pi}{2r}} \exp(-r). \quad (3.16)$$

Because of the divergent behavior of  $I_0(r)$ , our solution should behave like the zeroth-order modified Bessel function of the second kind,  $K_0$ . More precisely, we expect that

$$R(r) \sim \frac{C}{\sqrt{r/\ell}} e^{-\sqrt{2}r/\ell} \quad \ell \equiv \frac{1}{\sqrt{|\mu|}}, \quad (3.17)$$

with a characteristic extension  $\ell$ , and a solution-dependent number  $C$ .

### Scale invariance

Importantly, one can further restrict the parameter space and only study the case  $\mu = -1$  for which Eq (3.13) rewrites as

$$\frac{d^2 R}{dr^2} = -\frac{1}{r} \frac{dR}{dr} - 2R^3 + 2R. \quad (3.18)$$

Indeed, solutions  $R^{(\ell)}$  of (3.13) corresponding to  $\mu \neq -1$  can be deduced from a solution  $R$  of (3.18) through the rescaling

$$R^{(\ell)}(r) = \frac{1}{\ell} R\left(\frac{r}{\ell}\right). \quad (3.19)$$

The mapping between different  $\mu$ 's is a direct consequence of the scale invariance of the 2D NLSE (3.10), already discussed in the previous chapter. To summarize, finding a single stationary state  $R$  gives access to a family of stationary solutions containing the same atom number, obtained by dilation operations.

### Mechanical analogy, shooting method

To show the existence and to determine the shape of the localized solutions of Eq (3.18), we now propose a mechanical analogy in which  $R$  represents the position of a particle, and  $r$  is the time [201, 202]. The left-hand-side of Eq (3.13) stands for the acceleration of

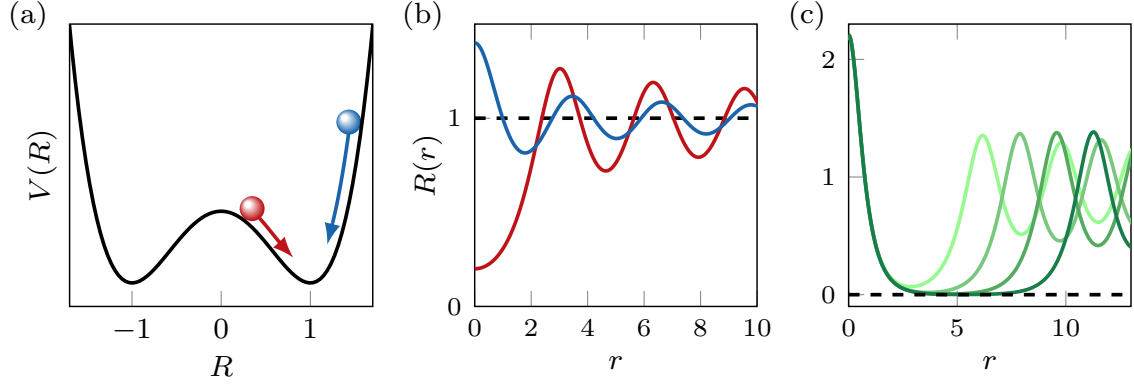


Figure 3.5: Mechanical analogy. (a) Double-well associated to Eq (3.18). We show the initial trajectories of two particles starting from a position slightly smaller (red ball) and larger (blue ball) than the local equilibrium position  $R = +1$ . (b) The corresponding wavefunctions  $R(r)$  with the same color code. These solutions do not respect the constrain of localization. (c) Various trajectories for increasing  $R(0)$  while getting closer and closer to the Townes value  $R(0) \simeq 2.21$ . From light to dark green, the initial values  $R(0)$  differ respectively by  $10^{-2}$ ,  $10^{-3}$ ,  $10^{-4}$  and  $10^{-5}$  from the Townes value.

the particle, while its right-hand-side is the associated force. More precisely, the first term on the right-hand-side of Eq (3.13) is a time-dependent friction  $\propto -dR/dr$ , while the two last ones derive from the potential

$$V(R) = \frac{1}{2}R^4 - R^2. \quad (3.20)$$

As shown in Fig 3.5(a),  $V(R)$  is a double-well potential. The *shooting method* consists in tuning precisely  $R(0)$  to fulfill the asymptotic constrain  $R(r) \rightarrow 0$  for large  $r$ , noting that  $R = 0$  is an unstable equilibrium position. Starting from an initial position  $R(0) > 0$ , the particle should first roll down the slope. If  $R(0)$  is small, it will go to the right. Due to the friction term, the mechanical energy is not conserved and the particle will undergo damped oscillations around  $R = 1$ , see Fig 3.5(b). If  $R(0)$  is large enough, the particle will go to the left and eventually cross the central hill. It will maybe come back and most probably finish its course around one of the stable equilibrium positions,  $R = \pm 1$ .

### Townes soliton

In Fig 3.5(c), we observe that starting from a low value of  $R(0)$  and increasing it progressively, the strictly positive solution that we obtain will approach more and more the value  $R = 0$  at infinite time, eventually finishing its course at  $R = 1$ . Remarkably, there exists a specific value  $R(0) \simeq 2.21$  for which the particle goes to the position  $R = 0$  at infinite time ( $r \rightarrow +\infty$ ) without ever crossing the hill, thus fulfilling the desired asymptotic condition. This solution  $R_0(r)$  which is positive and monotonically decreasing to zero is nothing but the Townes soliton [17]. It is shown in Fig 3.6(a), and we now summarize some of its properties. Coming back to physical units, the atom number contained in the soliton verifies

$$N_T |\tilde{g}| = \int d^2r R_0(r)^2 \equiv \mathcal{N}_T = 5.85 \dots \quad (3.21)$$

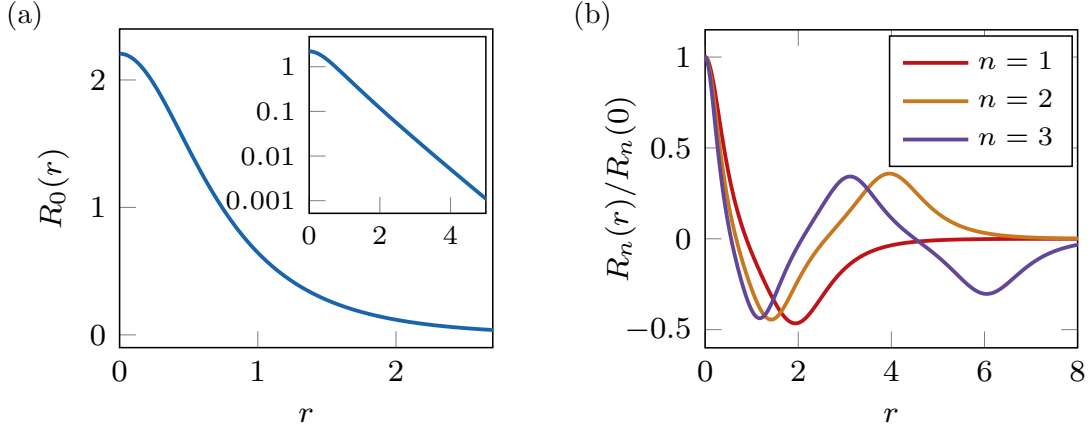


Figure 3.6: Fundamental solutions. (a) Townes soliton radial profile  $R_0(r)$ , with its quasi-exponential tails represented in logarithmic-linear scale in the inset. (b) Higher-order solutions  $R_n(r)$  with  $n = 1, 2, 3$  (resp. in red, orange, purple) have exactly  $n$  nodes.

	$\int d^2r R_n(r)^2$	$R_n(0)$
$n = 0$	5.85	2.21
$n = 1$	38.58	3.33
$n = 2$	97.89	4.15
$n = 3$	183.66	4.83

Table 3.2: Norm and value at the origin of the four first fundamental solutions of Eq (3.18).

which can be determined only numerically. Alternatively, an approximate value  $\mathcal{N}_T \simeq 2\pi$  can be obtained analytically through a Gaussian ansatz (see Desaix et al. [203] and Appendix B) with an error of only  $\simeq 7\%$ . For this specific value of  $\mathcal{N}$ , the family of Townes profiles are minimizers of the energy functional (3.8) with exactly  $E = 0$ . This is a necessary condition for stationarity, as we immediately deduce from the variance identity (2.24). From this fact combined with Eq (2.12) expressed for  $\mu = -1$ , we also deduce the following relation

$$\mathcal{N}_T = E_k = -E_i. \quad (3.22)$$

For  $N < N_T$ , the energy functional  $E[\phi]$  is always strictly larger than 0. This lower bound is approached from above by dilating infinitely any wave function. For  $N > N_T$ , there exist functions with arbitrary negative energy.

### Higher-order solutions with zero vorticity

Higher-order solutions of Eq (3.13) were first considered by Haus [201] and Yankauskas [202]. If we carry on with the mechanical analogy, the corresponding trajectories start from a position higher than for the Townes soliton value  $R(0) \simeq 2.21$ , cross a finite number of times  $n$  the central hill and finally approach  $R = 0$  at infinite time. These solutions  $R_n(r)$  can thus be indexed by their number of nodes  $n$ . The solutions corresponding to  $n = 1, 2, 3$  are shown in Fig 3.6(b).

Alike the Townes soliton, all stationary states need to satisfy  $E = 0$  to fulfill the variance identity (2.24), and thus also verify Eq (3.22). Table 3.2 gives the corresponding norms and values at the origin – which is also the maximum in absolute value [201, 204]. Analogous spherical shell solutions exist also in dimension  $D = 3$ . Finally, note that such oscillating solutions have no equivalent in dimension  $D = 1$ , the only localized stationary state being (3.6). This difference is due to the singular behavior of the Laplacian at the origin  $r = 0$  in dimension  $D > 1$ , as written in Eq (3.10).

### 3.2.2 Stability of the Townes soliton

#### Linear stability analysis

Now that we have determined the shape of the Townes soliton, we discuss its stability with respect to small perturbations when evolving under the time-dependent NLSE

$$i\frac{\partial\psi}{\partial t} = -\frac{1}{2}\nabla^2\psi - |\psi|^2\psi. \quad (3.23)$$

Here, we used reduced notations of Subsec 3.1.1 with  $\int d^2r |\psi|^2 = |\tilde{g}|N = \mathcal{N}$ . Stability and elementary excitations of the 2D NLSE around the Townes soliton have been investigated in various works [171, 205–207]. The analysis can be worked out in a way similar to the Bogoliubov formalism, as shown in Appendix A. In this paragraph, we only summarize the main steps and results of this analysis.

Starting from a small perturbation  $R_0(r) + \epsilon(\mathbf{r}, 0)$  around the stationary solution  $R_0(r)$ , one linearizes Eq (3.23) and obtains a linear operator describing the evolution of the perturbation. Determining the spectrum of this operator allows one to decompose the perturbation into normal modes evolving independently, with a complex frequency  $\bar{\omega}$ . For the Townes soliton, Malkin & Shapiro [171] showed that there is no dynamical instability, i.e. no eigen-frequency with a non-zero imaginary part. On the one hand, there is a continuous spectrum of real frequencies which correspond to delocalized excitations. In practice, a localized superposition of such excitations would eventually spread and leave the soliton unaffected. Henceforth, modes belonging to the continuous part of the spectrum do not induce any instability.

#### Instability by collapse

On the other hand, Malkin & Shapiro exhibit eight discrete modes corresponding to the value  $\omega = 0$ . These so-called *neutral modes* are all generated by one of the 2D NLSE symmetries. In other words, each of these modes can be obtained by applying one of the symmetries listed in Sec A.1 to a previously known solution. One can say that the Townes soliton has no genuine excitation modes. Moreover, these modes cannot grow faster than a power of  $t$ , i.e. the difference between the wave function  $\psi(\mathbf{r}, t)$  obtained at time  $t$  and the Townes soliton can be expressed as

$$\psi(\mathbf{r}, t) - R_0(r)e^{it} \simeq \left[ \sum_{j=0}^n \epsilon_j(\mathbf{r})t^j \right] e^{it}, \quad (3.24)$$

with an integer  $n \leq 3$ , as long as the corresponding deviation is not too large. However, all this does not guarantee the orbital stability of the soliton. Indeed, using the lens



transformation written in Eq (A.8) and applied to the Townes soliton  $R_0$ , one can consider the evolution under Eq (3.23) of the following initial condition

$$\psi(\mathbf{r}, t = 0) = R_0(r) \exp\left(-\frac{\beta r^2}{2}\right), \quad (3.25)$$

for a real parameter  $\beta$ . For  $\beta > 0$  (resp.  $\beta < 0$ ), this corresponds to a situation of focusing (resp. defocusing), where the velocity field  $\mathbf{v}$  associated to  $\psi$  and the radius vector  $\mathbf{r}$  are anti-parallel (resp. parallel) everywhere. The solution of the 2D NLSE with initial condition (3.25) can be written exactly as

$$\psi(\mathbf{r}, t) = \frac{1}{1 - \beta t} R_0\left(\frac{r}{1 - \beta t}\right) \exp\left[i\left(\frac{t}{1 - \beta t} - \frac{\beta}{2} \frac{r^2}{1 - \beta t}\right)\right]. \quad (3.26)$$

The evolution of the corresponding density profile will thus be self-similar. Importantly, for  $\beta > 0$ , this solution will become singular exactly at time  $t_* = 1/\beta$ . Choosing a small  $\beta > 0$ , we have found a solution of the 2D NLSE initially close to the Townes soliton and which collapses in a finite time. This shows that the Townes soliton is subject to an *instability by collapse*, despite the absence of a standard dynamical instability. Importantly, the other symmetry-generated mode given in Eq (A.19) may also induce a collapse in a finite time. In this case, it corresponds to a solution having slightly more atoms than the Townes soliton. Note that the same conclusion applies to all the stationary solutions of the 2D NLSE 3.10.

### Beyond the cubic equation

Let us outline a few strategies that were proposed for stabilizing the Townes soliton, i.e. to suppress the instability by collapse and to make it linearly stable. The simplest cure consists in adding a harmonic potential to the nonlinear equation [208, 209]. This is sufficient to stabilize all solutions with azimuthal number  $s = 0$  (no embedded vorticity) introduced in Subsec 3.2.1, and a subset of the  $s = \pm 1$  solutions (vortex solutions). Alternatively, one may consider discrete models in two-dimensional lattices [210, 211], or impose a periodic modulation of the coupling strength  $\tilde{g}$  in the free-case [212].

Another strategy consists in introducing higher-order nonlinearities, besides the standard  $-|\psi|^2\psi$  cubic term of Eq (3.10). NLSEs with nonlinear terms of the form

$$(-|\psi|^2 + |\psi|^4) \psi \quad \left(e^{-|\psi|^2} - 1\right) \psi \quad - \frac{|\psi|^2}{1 + |\psi|^2} \psi \quad (3.27)$$

were studied for example by Malkin [213], Zakharov et al. [204] and Vakhitov & Kolokolov [206] respectively. All these nonlinear functionals are dominated by the cubic term  $-|\psi|^2\psi$  for small  $|\psi|$ , and the last two terms exhibit *saturation* of the nonlinearity. More exotic nonlinear models might involve spatial derivatives like the expression

$$-(|\psi|^2 + \nabla^2 |\psi|^2) \psi, \quad (3.28)$$

originally considered by Rosanov et al. [214] as a weakly nonlocal nonlinearity. Note that the last term is indeed stabilizing, since the two terms have opposite sign around a maximum of  $|\psi|^2$ , the Laplacian being negative around a maximum.

Note that in all these cases, scale invariance is broken. In particular, solitons with different chemical potentials  $\mu < 0$  have generically different norms  $\mathcal{N} = |\tilde{g}|N$  and different shapes. However, in the limit where the stationary solution has a very small density



$|\psi|^2$  everywhere, higher-order nonlinearities can be neglected and the solutions tend to the Townes soliton profile, with an atom number  $N \simeq \mathcal{N}_T/|\tilde{g}|$ . In most cases, this limit is given by  $\mu \rightarrow 0^-$  since  $1/\sqrt{|\mu|}$  sets the typical scale of the stationary solution. Protection against collapse in a saturating non-linear medium was demonstrated numerically by Dawes & Marburger in 1969 [215]. Interestingly, a necessary – though not always sufficient – condition for guaranteeing the linear stability of the fundamental positive solution in such models is given by the Vakhitov-Kolokolov criterion [206]

$$\frac{d\mathcal{N}}{d\mu} < 0. \quad (3.29)$$

Intuitively, this condition ensures that the system cannot decay spontaneously by emitting particles towards infinity.

In this section, we have studied the properties and the stability of the Townes soliton. We now propose to discuss a fundamental aspect of the 2D NLSE (3.23) where the Townes soliton will appear again.

### 3.3 Wave-packet collapse

We study the phenomenon of wave-packet collapse associated to the time-dependent 2D NLSE. This will allow us to highlight the universality of the Townes profile, even in such a catastrophic situation. We first discuss in which conditions collapse can occur (Subsec 3.3.1). Special emphasis is placed on the consequences of the variance identity. As a second step, we briefly describe the behavior of collapsing solutions, just before the collapse occurs (Subsec 3.3.2).

#### 3.3.1 Conditions for collapse

As seen earlier, the 2D NLSE may lead to a singularity in finite time, in the sense that one (or more) points of space are associated to a diverging density. In real experiments, the 2D NLSE is never appropriate when the wave amplitude has increased so dramatically. Indeed, other effects (higher-order nonlinearities, dissipative processes, physical damage) then need to be taken into account. However, understanding the conditions for the onset of such phenomena is still relevant for the applications. In parallel, grasping the nature of the singularity has triggered a lot of research in mathematics [158, 198, 216]. In this section, we examine if one can predict the occurrence of collapse from the knowledge of the initial conditions.

#### A sufficient (but not necessary) condition for collapse

For convenience, we rewrite and integrate the variance identity (2.24) using the reduced notations of Subsec 3.1.1

$$\frac{d\sigma^2}{dt^2} = 4E \quad \sigma^2(t) = \sigma_0^2 + t\langle \mathbf{r} \cdot \mathbf{v} \rangle_0 + 2Et^2, \quad (3.30)$$

where  $\sigma$  is the RMS size of the cloud,  $\mathbf{v}$  is the velocity field defined in Eq 2.20, and the index  $\cdot_0$  stands for the averaged value taken at time  $t = 0$ . In the case of a real initial state, the initial velocity field vanishes everywhere and thus  $\langle \mathbf{r} \cdot \mathbf{v} \rangle_0 = 0$ . In this case, one finds that  $\sigma$  will reach zero at a time  $t_\sigma = \sqrt{\sigma_0^2/2|E|}$  if and only if  $E < 0$ . For a real wave function, an energy  $E < 0$  is thus a *sufficient condition* for collapse. Note that

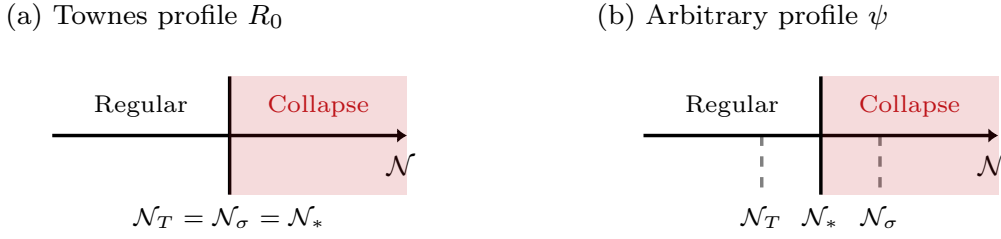


Figure 3.7: Condition for collapse. (a) For a profile with a Townes shape  $\propto R_0$ , the condition for collapse  $\mathcal{N} = \mathcal{N}_*$  coincides exactly with the upper bound given by the variance identity  $\mathcal{N}_\sigma$ . (b) For an arbitrary profile  $\psi(\mathbf{r})$ , the solution will be regular for  $\mathcal{N} < \mathcal{N}_T$  and singular for  $\mathcal{N} > \mathcal{N}_\sigma$ . However, there is no analytical criterion to determine the regularity for  $\mathcal{N}_T < \mathcal{N} < \mathcal{N}_\sigma$ .

collapse might happen at an earlier time  $t_* < t_\sigma$ , and it is the case in general. Besides, if one considers an arbitrary profile  $\psi(\mathbf{r}, t = 0)$ , it is always possible to multiply  $\psi$  by a sufficiently large number – thus modifying the product  $\mathcal{N} = |\tilde{g}|N$  – to compel  $\sigma^2$  to vanish in a finite time. Indeed, the energy can be made arbitrarily negative in this way, while the first two terms on the right-hand-side of Eq (3.30) are left unaffected.

However, let us stress that  $E < 0$  is not a *necessary condition* for wave-collapse. For example,  $\sigma^2$  might vanish in spite of  $E > 0$ , for example if the term  $\langle \mathbf{r} \cdot \mathbf{v} \rangle_0$  is negative and sufficiently large in absolute value. This corresponds to a situation of strong focusing, as exemplified by the solution explicitly given in Eq (3.25). This solution has indeed a positive energy: the initial kinetic energy increases due to the phase term, while the interaction energy stays the same (the density is unchanged). In this case, the evolution toward collapse is rigorously self-similar. Conversely, Fibich & Papanicolaou [217] show that for a given profile and a defined atom number, it is always possible to modify its phase field to avoid collapse, using a sufficiently “exploding” velocity field directed outwards.

### A gap in the theory

We just saw that a given profile can be made collapsing by adjusting the nonlinear parameter  $\mathcal{N}$ . It can also be made regular at all times by defocusing it sufficiently. A natural question thus rises: is it possible to focus enough a given profile with a given atom number – i.e. to find the adequate phase field for a given real wave function – to make it collapse in a finite time? An important result was obtained by Weinstein in 1983 [218] who showed that any solution of the 2D NLSE with regular initial conditions and  $\mathcal{N} < \mathcal{N}_T$  is regular at all times. Below this threshold, solutions disperse to zero in a way similar to solutions of the linear Schrödinger equation. Moreover, example (3.25) shows that this is a sharp condition, in the sense that one can exhibit a singular evolution for any value of  $\mathcal{N} \geq \mathcal{N}_T$ <sup>8</sup>. To summarize, for a given real profile  $\psi(\mathbf{r}, t = 0)$ , the nonlinear parameter  $\mathcal{N}$  must be larger than  $\mathcal{N}_T$  to authorize a possible collapse. Moreover, there always exists a value of  $\mathcal{N} = \mathcal{N}_\sigma$  above which  $E < 0$  and such that collapse is certain.

The regularity of solutions should thus be questioned only in the range  $\mathcal{N}_T \leq \mathcal{N} \leq \mathcal{N}_\sigma$ , and it is indeed a subtle issue. These two values coincide only for the Townes profile. For

<sup>8</sup>For examples with  $\mathcal{N} > G_T$ , it is sufficient to multiply the Townes profile by the correct factor  $c > 1$  to obtain a negative energy and thus a collapse.

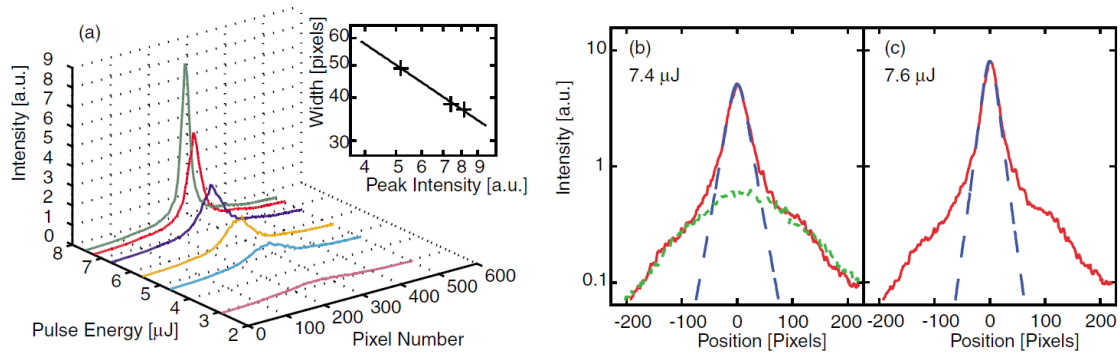


Figure 3.8: Observation of the Townes profile after partial collapse of an optical pulse. (a) Output intensity profile of a laser beam after propagating in a nonlinear medium, for various powers. The beams shrinks more and more when the total power increases. (b-c) For a large enough power, the central part of the intensity profile is consistent with the one of a Townes wave-packet. Figures taken from [221].

an arbitrary profile  $\psi(\mathbf{r})$ , it is probable that there exists a third value  $\mathcal{N}_*$  separating the domain of regular and singular solutions. On the particular case of a Gaussian profile, Fibich & Gaeta [219] have estimated numerically this threshold to be  $\mathcal{N}_* \simeq 5.96$ , which is strictly lower than  $\mathcal{N}_\sigma = 2\pi$  (see Appendix B). The case of a radial profile decreasing like  $e^{-r^4}$  is also considered. However, there is no systematic way of determining if a solution with  $\mathcal{N}_T \leq \mathcal{N} \leq \mathcal{N}_\sigma$  will undergo collapse or not.

### 3.3.2 Collapse dynamics

The numerical study of Kelley [194] was the first to report singular behaviors from smooth initial conditions. Kelley was then considering cylindrical beams with an initial Gaussian profile. This was the starting point of intense research on wave collapse. The large amplitudes and steep gradients which are reached before the formation of the singularity require very precise simulations, particularly challenging in the early days of numerical computation. In particular, accurate simulations of the collapse dynamics require a very high and adaptative resolution around the singular point.

On the analytical side, early studies of the collapse dynamics assumed that an initial Gaussian beam evolved essentially in a self-similar manner. Under this assumption, a variational method can reduce the 2D NLSE to a simple ordinary differential equation describing the evolution of the amplitude, see [220] and Appendix B. In this framework, the threshold for collapse on  $\mathcal{N} = |\tilde{g}|N$  is found to coincide with the sufficient condition of zero energy. However, we claimed in the last paragraph that this is not verified numerically. More advanced methods, like the so-called adiabatic approach of Malkin [213], were developed since and helped estimate the collapse point with good accuracy.

#### Self-similar collapse

Using the lens transformation (3.25), it is possible to exhibit a solution of (3.23) which collapses exactly at a given time and position of space, while conserving its Townes profile through a self-similar evolution. Interestingly, it is also possible to exhibit solutions

which collapse on a finite number of positions simultaneously [198]. It was soon realized numerically that any collapsing solution eventually concentrates a finite mass toward the collapse point, this atom number being at least equal to the Townes soliton one [222]. If the RMS size is still strictly positive at the time of collapse, it means that only a fraction and not all the mass concentrate around toward the singular point. This applies to the Gaussian profile for instance.

In fact, it can be shown that the collapse dynamics is asymptotically quasi-self-similar close to the singular point. More precisely, most collapsing solutions are well approached by a profile given by

$$\psi(\mathbf{r}, t) \simeq \frac{1}{\lambda(t)} R_0 \left( \frac{r}{\lambda(t)} \right) \exp \left[ i r(t) + i \frac{\dot{\lambda}(t) r^2}{2\lambda(t)} \right] \quad \lambda(t) \sim (t - t_*)^{1/2} \quad (3.31)$$

for  $t < t_*$ , plus corrections associated to a lack of exact self-similarity, the rest of the distribution forming a background [213, 223, 224]. In particular, the peak density should thus increase approximately as  $(t - t_*)^{-1}$ . As shown in Fig 3.8, a signature of the self-similar evolution toward a Townes-profile (3.31) during collapse was obtained experimentally by Moll et al. [221]. To do so, they studied the intensity profiles of laser pulses after propagating in a nonlinear medium. The Townes profile has thus a universal character, even for out-of-equilibrium dynamics.

## 3.4 A recent experiment

In this last section, we discuss a series of experiments recently realized by Chen & Hung [46, 47]. We start from their experimental observations (Subsec 3.4.1) and then discuss their interpretation of the phenomena as a modulational instability, yielding a novel insight on Townes soliton physics (Subsec 3.4.2).

### 3.4.1 Quench of a 2D Bose gas

In the experiments reported by Chen & Hung [46, 47], uniform quasi-2D samples of cesium atoms at equilibrium undergo a quench from repulsive to attractive interactions, using a Feshbach resonance. In [46], a preliminary universal dynamics was followed by the formation of long-lived solitary waves of size  $\lambda_c$  containing approximately the Townes atom number  $N_T$ . It is likely that blobs with an excess atom number underwent collapse, being subject to atom losses when reaching high densities. An alternative protocol using two successive quenches suggested that blobs with an atom number  $N > N_T$  could still form a quasi-stationary state after losing this excess. On the contrary, blobs with a too low atom number generically spread and form a background in the density distribution.

In [47], Chen & Hung confirmed the scale invariance of the underlying physics as well as the scaling (3.21) of  $N_T$  with the coupling strength  $\tilde{g}$ . As reported in Fig 3.9(a), the observed solitary waves were in good agreement with the Townes soliton profile. This was confirmed over a broad range of experimental parameters, by varying the initial density and the final interaction parameter.

### 3.4.2 Modulational instability

How can one interpret the results of Chen & Hung [46, 47]? The uniform state is the simplest stationary solution of the 2D NLSE (3.10) in a infinite medium. This holds indeed

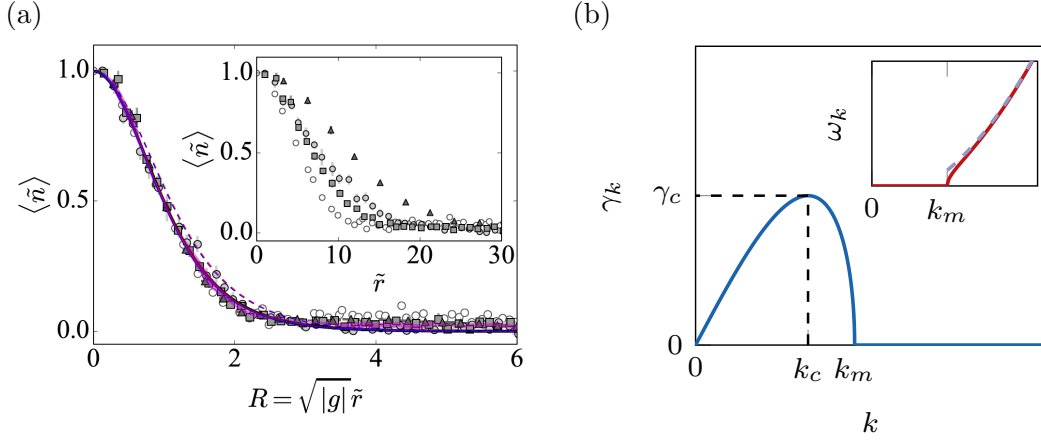


Figure 3.9: (a) Radial profile of the remnant blobs following the quench of a 2D Bose gas from repulsive to attractive interactions. Over a broad range of parameters, the bare data (inset) can be rescaled and collapsed onto a single curve, showing good agreement with the expected Townes soliton (solid line). Figure taken from [47]. (b) Complex frequencies  $\bar{\omega}_k = \omega_k + i\gamma_k$  from a Bogoliubov analysis in the attractive case. Contrary to the repulsive case (2.18), low  $k$  modes have an imaginary part and are therefore unstable, with a largest growing rate at  $(k_c, \gamma_c)$ .

both for a positive *and* a negative coupling strength. In the positive case, this solution is the ground state of the system as it minimizes both the kinetic and the interaction energy. By contrast, we have seen that the energy functional (3.9) is not bounded in the negative case whenever the atom number is larger than the Townes one. We thus anticipate that the uniform solution will be subject to a dynamical instability in the presence of a weak modulation.

### Bogoliubov analysis

Let us understand the effect of a tiny modulation above a homogeneous system. For an atomic system with density  $n$ , the Bogoliubov analysis presented in Subsec 2.1.2 can be directly extended to the attractive case, yielding a set of complex frequencies  $\bar{\omega}_k = \omega_k + i\gamma_k$  associated to a wave vector of norm  $k$ . In the limit of small  $k$ , the free-particle term of Eq (2.18) becomes negligible. As a consequence,  $(\hbar\bar{\omega}_k)^2$  becomes negative for  $k \leq k_m = 2\sqrt{|\tilde{g}|n}$ . Such an imaginary frequency can lead to the exponential growth of modes  $k \in ]0, k_m[$  with a rate

$$\gamma_k = \frac{\hbar}{2m} \sqrt{k^2 (k_m^2 - k^2)} \quad (3.32)$$

which we represent in Fig 3.9(b). Unstable modes thus correspond to long wavelengths  $\lambda \equiv 2\pi/k \geq 2\pi/k_m$ . For a system with a finite extension, the corresponding infrared cut-off might suppress the instability. For instance, consider a square of side  $L$  with periodic boundary conditions, the initial uniform density then writes  $n = N/L^2$ , with  $N$  is the atom number. This system can only host discrete modes with wave-vector  $\mathbf{k} = (2\pi/L) \mathbf{n}$  indexed by a pair  $\mathbf{n} \in \mathbb{Z}^2$ . Unstable modes are not present when  $\lambda_m \equiv 2\pi/k_m > \sqrt{2}L$

(longest wavelength along the diagonal), which leads to the condition

$$N < N_c \equiv \frac{\pi^2}{\sqrt{2}|\tilde{g}|} \simeq \frac{7}{|\tilde{g}|}. \quad (3.33)$$

This critical atom number  $N_c$  is similar to the Townes atom number  $N_T$  defined in Eq (3.21). This naive analysis suggests that a finite uniform system is stable below the threshold for the formation of a Townes soliton, a prediction supported numerically [219].

### Fastest-growing mode

In a very large system, one expects self-modulation to be initially dominated by the most unstable mode, i.e. the mode with largest growth rate  $\gamma_k$ . This maximum is easily determined for  $k$  and  $\gamma_k$  respectively equal to

$$k_c = \sqrt{2|\tilde{g}|n} \quad \gamma_c = \frac{1}{2} \frac{\hbar}{m} |\tilde{g}|n. \quad (3.34)$$

Let us consider the case relevant here of an interaction parameter quenched from positive to negative values, starting with a system at thermal equilibrium. We then expect modes of low energy (long wavelength) to have initially an appreciable population. Moreover, even if this dominant mode is not initially populated but other modes are, small nonlinear couplings from the populated modes to this fastest-growing mode might trigger its rapid growth. In most practical situations, we thus expect the formation of structures whose size is approximately given by the wavelength  $\lambda_c = 2\pi/k_c$ . Chen & Hung [46, 47] exploited the fact that this dynamics leads to the formation of blobs of size  $\lambda_c$  which contain typically  $\simeq \pi\lambda_c^2 n = N_c$  atoms. As noted above, this number is close to the Townes atom number  $N_T$ .

This so-called *modulational instability* (MI) – also known as self-modulation or side-band instability – is a hallmark of many phenomena encountered in nonlinear physics, including hydrodynamics, electrodynamics, optics, or matter-wave physics [225]. The phenomenon of *filamentation*, observed in the early experiments on self-focusing, can be seen as a particular manifestation of this instability [178]. The formation of matter-wave soliton trains by Strecker et al [24] already mentioned in Subsec 3.1.1 was also interpreted in this manner [226]. In the series of experiments [46, 47], solitons were thus formed in a stochastic fashion. This is complementary to our protocol detailed in Chapter 4 which allows the deterministic realization of Townes solitons.

## 3.5 Conclusion

In this chapter, we presented the solitary waves associated to the nonlinear Schrödinger equation. The absence of integrability and the collapse instabilities in 2D suggest the physics is very different from the one-dimensional case. These also make solitary waves in higher dimensions less easy to probe. The amount of experimental works on this topic, especially in nonlinear optics and matter-wave physics, show the broad interest that were risen by these issues.

We then focused on the Townes soliton, historically the first solution considered in the problem of self-trapping of optical beams. Its stability and elementary excitations were discussed, as well as stabilization mechanisms which can facilitate the observation of the soliton profile. The Townes soliton also emerges as a universal profile for the collapse

dynamics. The recent demonstration of Chen & Hung [46, 47] confirms this universal character.

As an outlook, note that spatial light modulators could be useful for the deterministic preparation of solitary waves propagating in optical media, for example in atomic vapors with large nonlinear parameters and good transparency. In parallel to this, the high versatility of cold-atomic platforms make them ideal candidates to study the existence and the stability of solitary waves for multidimensional fields. In the next chapter, we present our recent deterministic realization of a Townes profile using a novel experimental approach, namely a two-component planar Bose gas which mimics the physics of a single-component attractive system.

## Chapter 4

# Realization of a Townes soliton

In this chapter, we discuss our realization of a matter-wave Townes soliton. This solitary wave arises in a two-dimensional homogeneous system described by the nonlinear Schrödinger equation, in the presence of attractive interactions. Under that condition, the soliton may exist with any size, provided it has the correct shape and the correct atom number. In cold atom physics, this can be achieved by considering an assembly of bosons in a two-dimensional box, described by contact interactions. At low magnetic fields, interactions between the  $^{87}\text{Rb}$  atoms which we use are repulsive.

To circumvent this limitation, we use a novel approach based on a two-component planar Bose gas. Starting from a uniform bath of atoms in a given internal state, we imprint the soliton wave function using an optical transfer to another state. In Sec 4.1, we illustrate the dynamics of strongly imbalanced binary mixtures under our experimental conditions. As a first test, we observe contraction behaviors which are compatible with the physics described by the attractive NLSE. A rigorous study of the underlying physics is postponed to Chapter 5. The realization of a Townes soliton is demonstrated in Sec 4.2. In particular, we check the scale invariance of the solitonic behavior for the well defined atom number  $N_T = \mathcal{N}_T/|\tilde{g}_e|$ , where  $\mathcal{N}_T \simeq 5.85$  and  $\tilde{g}_e$  the effective coupling strength in our two-component system.

*Most of the material presented in this chapter has been taken from [45]. Some complementary data were also added.*

### 4.1 Effective one-component dynamics

In the following, we show that under appropriate experimental conditions, the dynamics of a two-component system can mimic the physics of a single-component matter-wave, evolving according to the nonlinear Schrödinger equation (3.23). This naturally arises in a weak depletion limit presented in Subsec 4.1.1. Our experimental protocol for preparing such mixtures is detailed in Subsec 4.1.2, and an example dynamics is given in Subsec 4.1.3.

#### 4.1.1 Weak depletion regime

##### Effective equation at equilibrium

We first present the main ingredient of this chapter, i.e. the mapping to a single-component NLSE description for our binary mixture and its domain of validity. To do so, we consider a two-component planar superfluid at zero temperature and described by the macroscopic



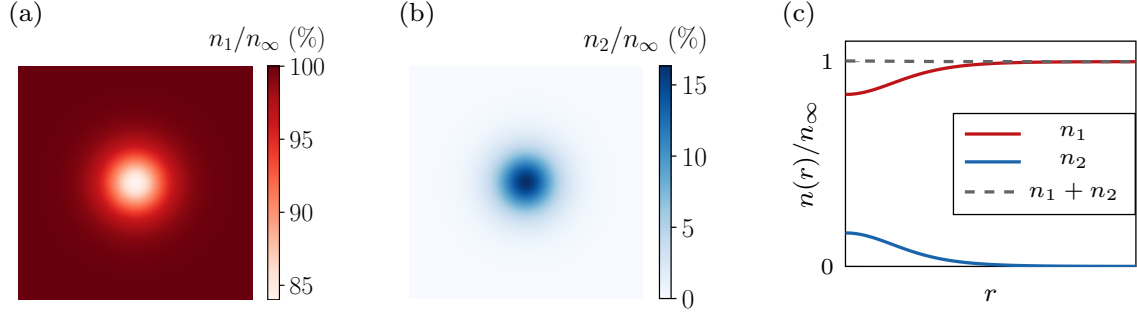


Figure 4.1: Equilibrium configuration of a strongly imbalanced mixture in the weak depletion regime. The in-plane density distribution of the majority component  $|1\rangle$  (resp. the minority component  $|2\rangle$ ) is depicted in (a) (resp. in (b)). The minority component forms a bubble, and digs a small hole in the bath of atoms in state  $|1\rangle$  which has asymptotic density  $n_\infty$ . The corresponding radial profiles are shown in (c), together with the almost constant total density. Profiles were obtained through imaginary time evolution of the coupled NLSEs, as described in the next chapter, for parameters similar to the ones explored in this chapter.

wave-functions  $(\phi_1(\mathbf{r}), \phi_2(\mathbf{r}))$ . Each component  $i = 1, 2$  describes the external state of an atom with mass  $m$  in a given internal state  $|i\rangle$ . The dimensionless coupling strength  $(\tilde{g}_{11}, \tilde{g}_{22}, \tilde{g}_{12})$  characterizing the intra- and inter-component interactions are assumed to be all positive.

Most importantly, we consider a situation in which the density of component  $|1\rangle$  is everywhere much larger than in state  $|2\rangle$ , see Fig 4.1 for an example. In the following, we refer to this as the *weak depletion regime*, and component  $|2\rangle$  will be called the minority component. In this configuration, the equilibrium state of component  $|2\rangle$  can be determined using an equation for a single component only. The corresponding (stationary) cubic NLSE

$$\mu'_2 \phi_2 = -\frac{\hbar^2}{2m} \nabla^2 \phi_2 + \frac{\hbar^2}{m} \tilde{g}_e |\phi_2|^2 \phi_2 \quad \tilde{g}_e = \tilde{g}_{22} - \frac{\tilde{g}_{12}^2}{\tilde{g}_{11}} \quad (4.1)$$

is characterized by an effective (composite) coupling strength  $\tilde{g}_e$ , a modified chemical potential  $\mu'_2$ , and the same mass  $m$ . In the following, we give simple physical arguments supporting this mapping, whereas a rigorous justification will be given in Chapter 5.

### An immiscible mixture

For the states we consider hereafter, the interaction parameters are such that  $\tilde{g}_{12}^2 > \tilde{g}_{11} \tilde{g}_{22}$ . As a consequence, our mixture is immiscible [53, 227] (see also Subsec 5.1.1). The effective coupling strength  $\tilde{g}_e$  is then negative, and the corresponding single-component equation (4.1) can host a Townes soliton. At a large distance away the soliton, the bath of atoms in state  $|1\rangle$  is essentially unaffected by the minority component and has asymptotic density  $n_\infty$ . In practice, this is relevant when the soliton size is much smaller than the bath container, and the density is approximately uniform in the intermediate region, far from the box edges.

### The total density is frozen

We will show in the next chapter that, when the interaction parameters  $\tilde{g}_{ij}$  are all close to each other, the total density of the mixture is almost constant over the full system's extent

$$n_1 + n_2 \simeq n_\infty, \quad (4.2)$$

and component  $|1\rangle$  forms a negative pattern of the  $n_2$ -distribution, as illustrated in Fig 4.1(c). This remark applies beyond the weak depletion regime. For example, if the two states were to occupy separate domains, then mechanical equilibrium imposes  $\tilde{g}_{11}n_1^2 = \tilde{g}_{22}n_2^2$ , as we show in Subsec 5.1.1. If  $\tilde{g}_{11} \simeq \tilde{g}_{22}$ , one finds that the total density changes very little (in relative value) from one domain to the other. Eq (4.2) is approximately realized in our experiment, since the interaction parameters given in Eq (1.12) all differ by less than 6%. The effective interaction parameter  $\tilde{g}_e$  is then always one order of magnitude smaller than the bare  $\tilde{g}_{ij}$ 's.

### Physical justification

Let us give some physical insights on the use of Eq (4.1) for the minority component, in the immiscible case. The mapping from an all-repulsive to an effectively-attractive system may seem exotic at first glance. It was already considered by Dutton & Clark [228]. Actually, Eq (4.1) can be qualitatively understood by analyzing the behavior of a very dilute bubble of atoms in state  $|2\rangle$  in a bath of the other species.

Since the two components are immiscible, it might be energetically favorable for the bubble to contract and to push away the other component in order to reduce their reciprocal overlap. Equilibrium is reached when the decrease of total interaction energy is exactly balanced by the increase of kinetic energy, which rises when the spatial extension gets smaller. When the atom number in  $|2\rangle$  is large enough, the two species segregate and form spin domains, with a significant overlap restricted to the frontier between the domains [53].

### Minority component dynamics

An important issue is the promotion of the stationary description (4.1) to its time-dependent version

$$i\hbar \frac{\partial \psi_2}{\partial t} = -\frac{\hbar^2}{2m} \nabla^2 \psi_2 + \frac{\hbar^2}{m} \tilde{g}_e |\psi_2|^2 \psi_2. \quad (4.3)$$

In the weak depletion regime, one can assume that the dynamics of the dense bath of atoms in state  $|1\rangle$  with density  $n_\infty$  occurs on a short time scale ( $\propto m/(\hbar^2 \tilde{g}_{11} n_\infty)$ ) compared to the minority component dynamics. The bath is then always at equilibrium on the time scale of the evolution of the minority component, and Eq (4.3) can be deduced from this *adiabatic approximation* [228].

The effective interaction parameter  $\tilde{g}_e$  corresponds to a dressing of the interactions for component  $|2\rangle$  by the atoms of the bath [76]. In this limit, the dynamics of the particles in state  $|2\rangle$  remain scale invariant since the characteristic length of the bath, i.e. its healing length  $\xi_1 = 1/\sqrt{2\tilde{g}_{11}n_1}$ , does not play any role. However, Eq (4.3) fails reproducing the dynamics of density waves which occur on a faster time scale. Nevertheless, we will show in the following that this equation still well captures the dynamics considered in this work. In particular, we will test the important properties associated to Eq (4.3), e.g. the variance identity (2.24).

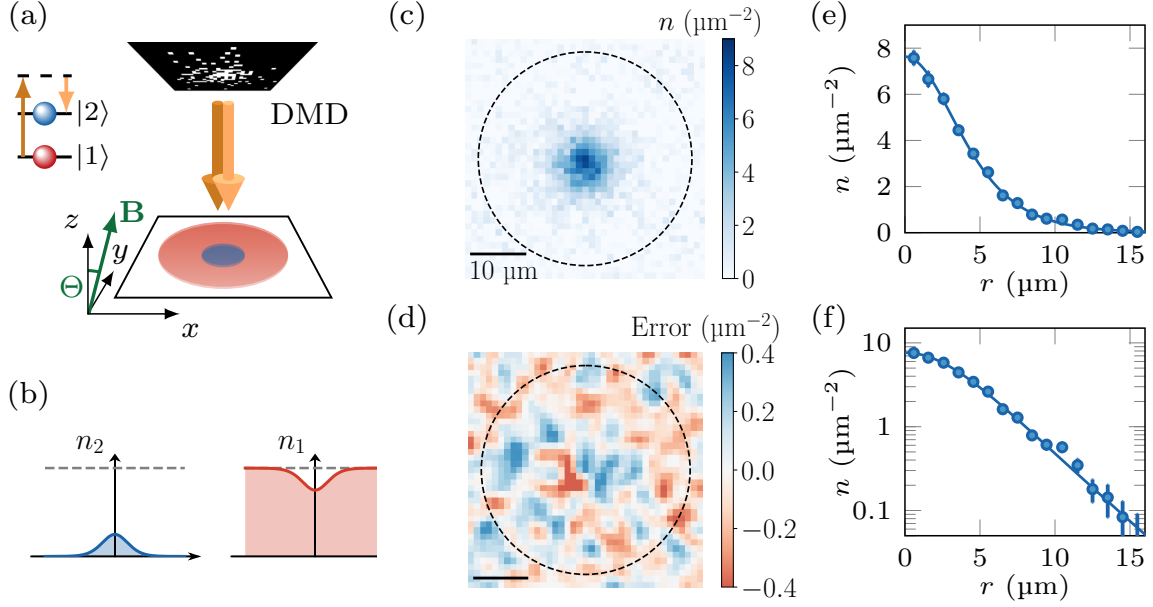


Figure 4.2: Preparation of a spin distribution. (a) A uniform disk of atoms in  $|1\rangle$  undergoes a Raman transition using a pair of co-propagating beams. The in-plane intensity profile of these beams is shaped using a DMD, allowing us to tailor arbitrary intensity patterns on the atomic cloud. (b) Density cuts of the cloud immediately after exposure, with a constant total density (grey dashed line). (c) CCD picture of an example Townes profile in  $|2\rangle$  at  $t = 0$ . The box edge is indicated as a black dashed circle. 20 pictures have been averaged. (d) Corresponding error signal at the end of the feedback loop. The amplitude of the error is less than 10% of the peak density. Radial density profiles for the same data are shown on (e) using lin-lin scale, and (f) using log-lin scale.

#### 4.1.2 Preparation and detection

We now present our experimental protocol for preparing a system close to equilibrium, in the weak depletion regime. The experiment starts with a homogeneous system of atoms in the hyperfine state  $|1\rangle \equiv |F = 1, m_F = 0\rangle$  and density  $n_\infty \simeq 100 \mu\text{m}^{-2}$ . The cloud is contained in a disk box-potential with sharp edges and radius  $R = 20 \mu\text{m}$ . Before preparing the binary mixture, the system is deeply in the superfluid regime with a temperature  $T \simeq 50 \text{ nK}$ ,  $T/T_c \simeq 0.1$  with  $T_c$  the critical temperature for the superfluid transition (see Subsec 2.2.3).

An external magnetic field  $\mathbf{B}$  of magnitude  $B = 0.7 \text{ G}$  with tunable orientation is applied, allowing us to tune the intra-species interactions as explained in Subsec 1.2.2. Unless explicitly mentioned, the magnetic field is kept normal to the atomic plane. The interaction parameters are defined as  $\tilde{g}_{ij} = \sqrt{8\pi}a_{ij}/\ell_z$ , where  $a_{ij}$  are the scattering lengths between  $|i\rangle$  and  $|j\rangle$  given in Eq (1.12), and  $\ell_z = \sqrt{\hbar/m\omega_z}$  is the harmonic oscillator length associated to the confinement along the vertical direction of frequency  $\omega_z = 2\pi \cdot 4 \text{ kHz}$ . Here, we find  $\tilde{g}_{11} = 0.16$ .

### Spin distribution imprinting

As expressed by Eq (4.2), equilibrium configurations have approximately a uniform total density. We thus only have to tune properly the spin distribution. The use of Raman beams allows us to prepare arbitrary spin distributions, see Subsec 1.2.1. Using co-propagating Raman beams, we induce a spatially-resolved transfer from state  $|1\rangle$  to state  $|2\rangle \equiv |F = 2, m_F = 0\rangle$  via a resonant two-photon transition, without any momentum transfer. Thanks to an extra DMD and a dithering algorithm, the local intensity and thus the local Rabi-frequency  $\Omega_R(\mathbf{r})$  can be tuned arbitrarily from 0 to a maximum value  $\gtrsim 10$  kHz, with a spatial resolution of  $\sim 1$   $\mu\text{m}$ , see Fig 4.2(a-b). For a given exposure time  $t_R$ , the total density is kept constant everywhere. One obtains a system whose initial wave functions can be written as

$$\psi_1 = \sqrt{n_\infty} \sqrt{1 - p(\mathbf{r})} \quad \psi_2 = \sqrt{n_\infty} \sqrt{p(\mathbf{r})} \quad p(\mathbf{r}) = \sin^2 \left( \frac{\Omega_R(\mathbf{r}) t_R}{2} \right) \quad (4.4)$$

in the bulk. As reminded in Subsec 1.2.1, the light shifts associated to the Raman beams cancel each other, and the Raman beams do not induce any phase gradient on the wave-functions  $\psi_i$ ,  $i = 1, 2$ . The Raman pulse duration is short enough ( $t_R < 25$   $\mu\text{s}$  for all data studied in this chapter) so that no dynamics occur during the transfer.

Our protocol for preparing well-defined spin patterns is based on an iterative algorithm which minimizes the difference between the measured spin distribution and the target one [51]. In Fig 4.2(c), we show an example realization of a Townes density profile, i.e. a density distribution  $n_2(\mathbf{r}) \propto R_0^2(r)$  where  $R_0$  is the Townes soliton already represented in Fig 3.6. The bubble is imprinted at the center of the box to minimize edge effects, and to preserve the rotational symmetry of the system. In the feedback loop, we typically average 20 pictures for computing the error signal at each turn, see Fig 4.2(d). This rather large number of pictures is required as the signal-to-noise is particularly low in the weak depletion regime.

### Detection

After imprinting a given spin distribution, we let the system evolve for a variable time  $t$  and measure the *in situ* density distribution via absorption imaging. We systematically wait for a minimum delay of 0.8 ms before taking the image. Indeed, a shorter delay may let the Raman beams shine onto the CCD chip during the first imaging pulse. We checked numerically that this technical delay leads to negligible modifications of the density distributions, and we take this time as an initial condition.

In the weak depletion regime, the density  $n_1$  is by definition much larger than  $n_2$ . For that reason, it is not possible to image this component with resonant light, since it would lead to a too large optical depth. For such dense samples, resonant dipole-dipole interactions induced by the probing laser beam make the relation between the optical depth and the density nonlinear, and prevent us from determining the density accurately. Imaging with detuned light could reduce the optical depth, but would also blur the patterns present in the density distribution due to refraction index gradients. For these reasons, we do not image neither consider component  $|1\rangle$  in the following. As we now focus only on component  $|2\rangle$ , we also drop the index 2 ( $\psi_2, n_2 \rightarrow \psi, n$ , etc).

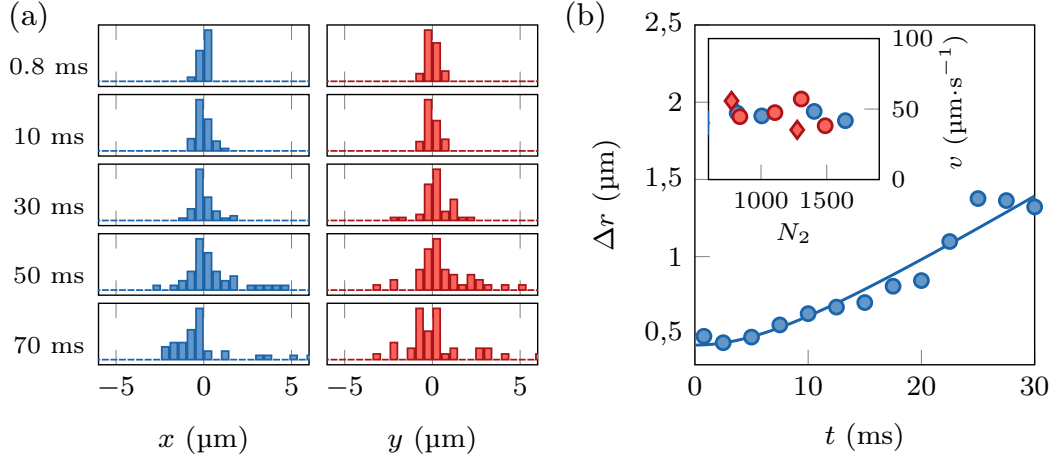


Figure 4.3: Fluctuations of the center of mass position on independent realizations. (a) The coordinate histograms at various times reveal a spreading of the center of mass from shot-to-shot. Data for an initial density distribution varying like  $\propto \exp[-(r/\ell)^4]$ , with RMS size  $\sigma_0 = 8.5 \mu\text{m}$  and  $N = 1050$ . (b) Center of mass dispersion as a function of time (blue dots). The fit (blue line) yields a spreading velocity  $v = 45(2) \mu\text{m}\cdot\text{s}^{-1}$ . The inset shows the velocity  $v$  extracted from various datasets, using initial Townes profiles (red dots) and profiles in  $\propto \exp[-(r/\ell)^4]$  (blue dots). Circles correspond to RMS size  $\sigma = 8.5 \mu\text{m}$  and diamonds to  $\sigma = 5.7 \mu\text{m}$ .

### Radial profiles

The evolutions studied in the following all start with radially symmetric profiles. We checked that this symmetry is approximately preserved during the dynamics, up to small preparation and detection imperfections. For better visualization and for increasing the signal-to-noise, it is thus relevant to work with radial profiles. These radial profiles are defined with respect to the center of mass of the wave packet

$$\mathbf{r}_0 = \frac{1}{N} \int d^2r n(\mathbf{r}) \mathbf{r} \quad N = \int d^2r n(\mathbf{r}), \quad (4.5)$$

where  $N$  is the total atom number of the bubble.  $N$  is estimated by simply summing the measured density distribution pixel-by-pixel. Experimentally, we observe small random drifts of the wave-packet from one shot to another. We attribute this motion to thermal fluctuations of the bath of atoms in state  $|1\rangle$ , before inducing the Raman transfer. Averaging blindly absorption images taken after the same evolution time would then lead to an artificial broadening of the distribution. To get rid of this effect, we determine the center of mass of each individual image.

*A priori*, this step could be achieved by using the standard definition for the center of mass (4.5). Because of the small densities studied here, we checked by eye that this method leads to large errors in some cases. We find it more robust to extract the center of mass using a 2D fit to the data, with the (initial) target density distribution as a fitting model. For a given evolution time, we finally bin the data with respect to their distance  $r$  to the center, with a one-pixel bin size. At this stage, we are left with a 1D radial density profile

$n(r)$ , as shown in Fig 4.2(e-f). This shows an excellent control of the density distribution of component  $|2\rangle$  over almost two decades in density.

### Center of mass fluctuations

Choosing an arbitrary dataset, we show in Fig 4.3(a) the histograms of the center of mass position for various evolution times. This clearly reveals the spreading of the centers aforementioned, although a more accurate description of the statistics would necessitate a larger sampling. A global drift is also observed in some cases, probably caused by a residual inhomogeneity of the trapping potential. We plot in Fig 4.3(b) the center of mass dispersion  $\Delta r$  for  $t < 30$  ms, where the evolution is well captured by a model in  $\sqrt{\Delta r_0^2 + (vt)^2}$ , typical of a ballistic expansion.

Reproducing the analysis for various datasets yields an approximately constant spreading velocity  $v \sim 50 \mu\text{m}\cdot\text{s}^{-1}$ , seemingly independent of the shape, size or atom number, as shown on the inset of Fig 4.3(b). Note that the corresponding velocity is low compared to other velocity scales considered throughout this work (Bogoliubov velocity, expansion velocity in the absence of interactions). Preliminary data do not show a clear dependence of this spreading velocity with temperature neither.

### Finite size

Since we restrict to the weak depletion regime, all the profiles studied here have a density  $n$  which does not exceed 20% of the bath density  $n_\infty = 100 \mu\text{m}^{-2}$ . Moreover, the bath itself has a finite size (20  $\mu\text{m}$  radius), and should always be larger than the soliton size. This restricts the range of sizes we can explore for the soliton preparation, since the latter has a well defined atom number. On the other side, we will show in Subsec 5.2.2 that the soliton should necessarily have a size  $\sigma$  much larger than the bath healing length  $\xi_1 \simeq 0.2 \mu\text{m}$ . In fact, one can show that this condition is immediately satisfied in the case of a small depletion  $n \ll n_\infty$ , provided  $|\tilde{g}_e| \ll \tilde{g}_{11}$  as verified here.

### Losses

We restrict the evolution to short times to limit the amount of losses in state  $|2\rangle$  to typically  $< 10\%$ . Such losses occur mainly in this state because of the two-body hyperfine-changing collisions already discussed in Subsec 1.2.1. This is especially important for the contracting bubbles which undergo strong losses when the density has increased significantly. In practice, the explored evolution times are  $\lesssim 50$  ms.

#### 4.1.3 An example dynamics

We now illustrate our approach with an example dynamics and motivate the use of the time-dependent NLSE (4.3) for our binary mixture. In Fig 4.4, we follow the evolution of a Gaussian density profile  $\propto \exp[-(r/\ell)^2]$  with an atom number  $N = 950(50)$  and an initial RMS size  $\sigma_0 = 5.7 \mu\text{m}$ . The density distributions in 4.4(a) show an increase of the central density from 10 to 16 atoms per  $\mu\text{m}^2$  over 30 ms, and an apparent contraction of the full distribution. This is made clearer by looking at the corresponding radial profiles in Fig 4.4(b, c).

The various lines shown in Fig 4.4(b-e) enable a direct comparison to the one-component NLSE. Indeed, these were obtained from a numerical simulation of Eq (4.3) with parame-

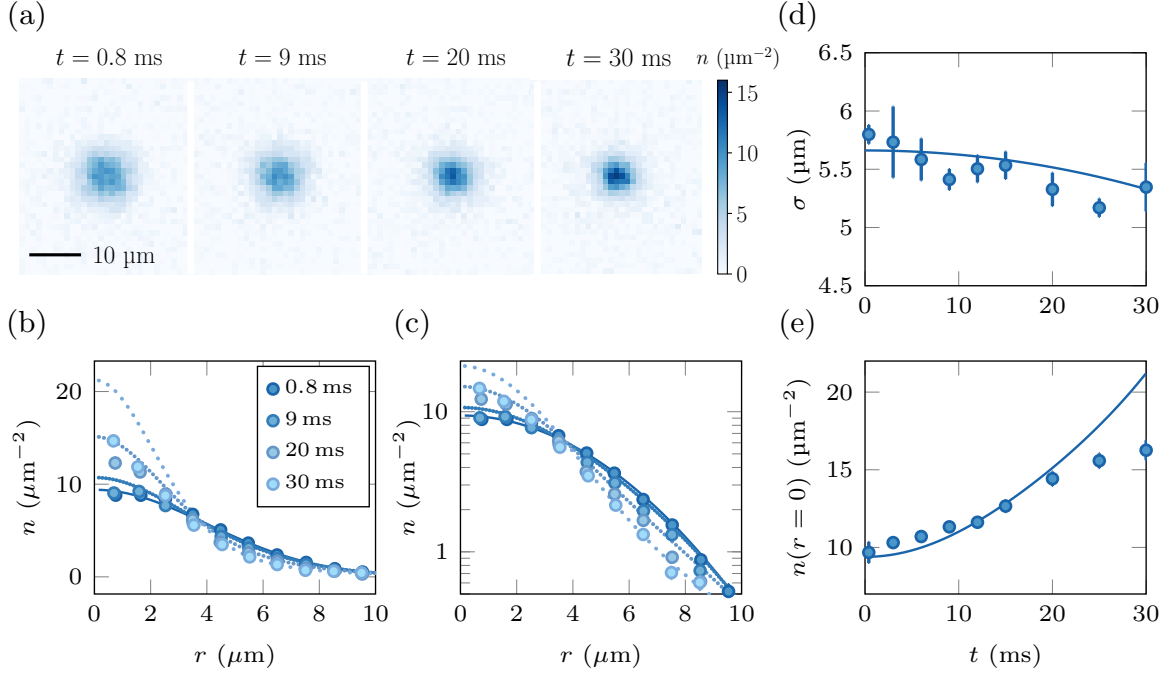


Figure 4.4: Evolution of a Gaussian wave packet, with atom number  $N = 950(50)$  and initial RMS size  $\sigma_0 = 5.7 \mu\text{m}$ . The density distributions at various times are shown in (a), together with the radial profiles in lin-lin (resp. log-lin) scale on (b) [resp. (c)]. The solid lines are numerical simulations of the one-component NLSE with similar parameters and sampled at the same times (more sparsely dotted lines correspond to longer times). The finite imaging resolution was taken into account by convolving the numerical profiles with a 2D-Gaussian kernel of standard deviation  $1.1 \mu\text{m}$ . The density profile is clearly not Gaussian anymore at  $t = 30$  ms. The RMS size  $\sigma$  and the central density  $n(r = 0)$  are shown on (d, e).

ters matching the initial target distribution<sup>1</sup>. In particular, we observe a decrease of the RMS size<sup>2</sup>  $\sigma$  compatible with the one expected from the variance identity 2.24. Note that  $\sigma$  decreases only slightly while the central density increases significantly. This indicates that, contrary to the non-interacting case, the evolution of a Gaussian is not self-similar and  $n(r = 0)\sigma^2$  is not a conserved quantity. At times  $t > 20$  ms, we observe a large deviation of the measured central density with respect to the numerics, which we attribute to the saturation of the optical depth for high density. We find that this affects very little the determination of the RMS size.

## 4.2 Dynamics of a Townes profile

In this section, we demonstrate our ability to prepare a Townes soliton. We prepare a Townes profile and explore various atom numbers in Subsec 4.2.1. We then consider various sizes and interaction strengths in 4.2.2. We confirm the existence of a solitonic behavior for a specific value of  $|\tilde{g}_e|N_T$  and arbitrary sizes, a hallmark of scale invariance.

<sup>1</sup>Numerical methods are described in Appendix E .

<sup>2</sup>See Subsec 4.2.1 and Appendix D for more details about the determination of the RMS size.



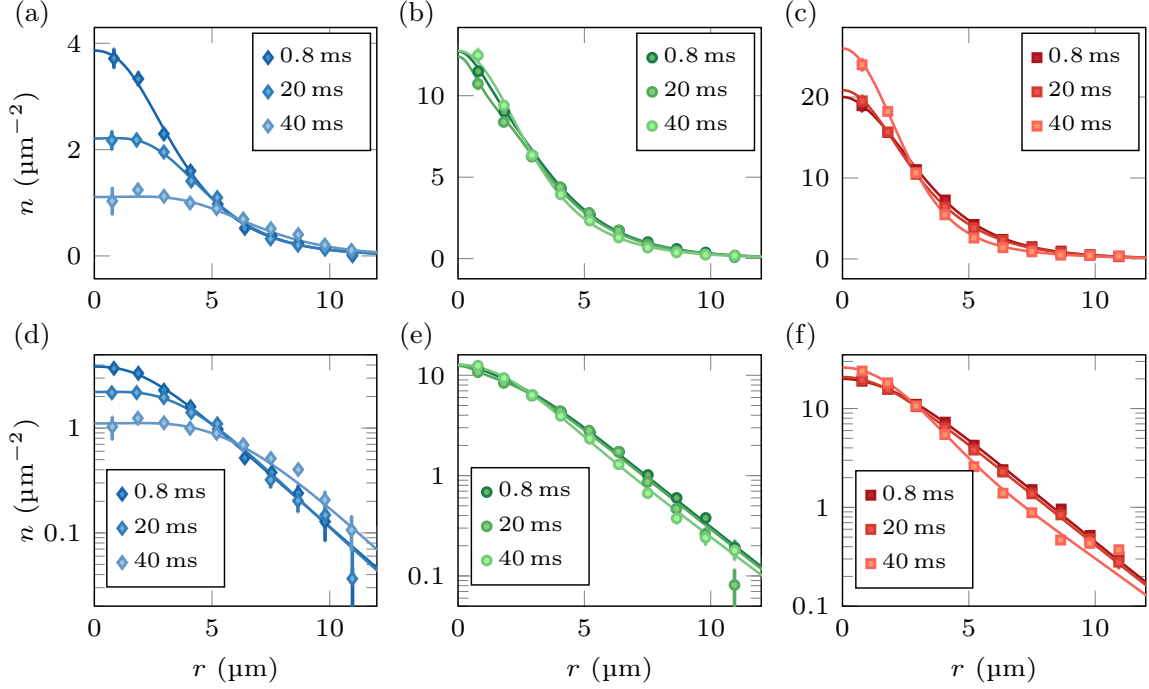


Figure 4.5: Evolution of a Townes profile. (a-c) Radial profiles at different times for imprinted Townes profiles with (a)  $N = 250(40)$ , (b)  $N = 720(20)$  and (c)  $N = 1200(50)$  atoms. The initial RMS sizes  $\sigma_0$  are similar. The solid lines are fits to the data used for the determination of the RMS size  $\sigma(t)$ , as explained in the main text. (d-f) Same data reported in log-lin scale. Similarly to Fig 4.4, note that for  $N$  notably different from  $N_T$ , the functional form of the density distribution  $n(r)$  changes significantly during the evolution. Therefore, the product  $n(0)\sigma^2$  is not a constant of motion in spite of the atom number conservation.

We finally discuss some effects beyond the weak depletion regime in Subsec 4.2.3.

#### 4.2.1 Various atom numbers

We first study the evolution of a Townes profile for a fixed initial RMS size and various atom numbers  $N$ . Here, the external magnetic field is set perpendicular to the atomic plane, yielding a value of  $\tilde{g}_e = -7.6 \times 10^{-3}$ . We focus on data corresponding to an initial value of  $\sigma_0 = 5.7 \mu\text{m}$ . The corresponding radial density profiles are shown in Fig 4.5. We observe an almost stationary time evolution for  $N = 720(20)$  whereas the central density of the cloud decreases for  $N = 250(40)$  and increases for  $N = 1200(50)$ .

#### Determination of the RMS size

To be more quantitative, we measure the RMS size  $\sigma$  of the system at each time  $t$ . Direct determination of the RMS size is challenging experimentally. Indeed, the contribution of points at large  $r$  is important for a 2D integral and our signal-to-noise ratio is poor in this region. As a remedy, we use a fit to the data to determine  $\sigma(t)$ . The choice of the fitting function relies on a time-dependent perturbation theory of the one-component NLSE.



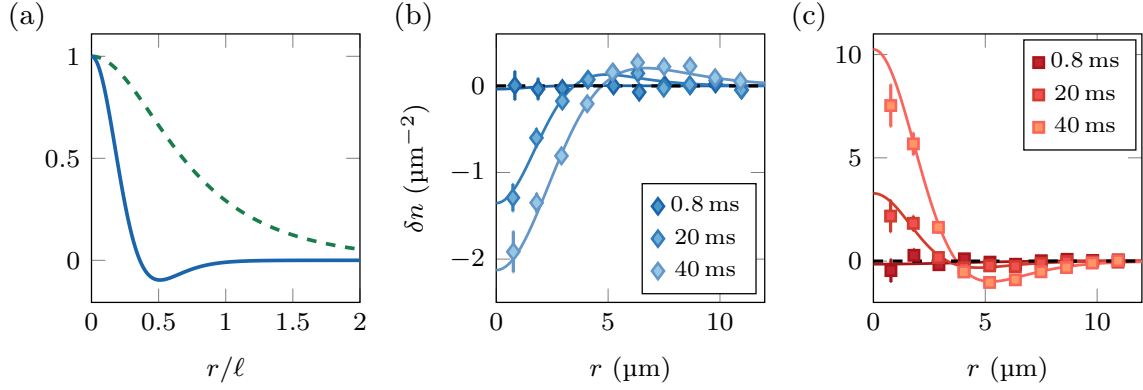


Figure 4.6: Determination of the RMS size, fitting procedure. (a) Fitting function  $\chi(r)/\chi(0)$  deduced from time-dependent perturbation theory (blue dashed line), together with a Townes profile (dashed line). Deformation  $\delta n(r, t)$  as defined in Eq (4.7), for various times  $t$  of the experimental runs presented in Fig 4.5(a) for ( $N = 250$ ) (a), and Fig 4.5(c) ( $N = 1200$ ) (b). We also plot the best fit of  $\chi(r)$  to the data.

Technical details have been gathered in Appendix D. Using this perturbation theory, we predict the deformation of the density profile  $n(r, t)$  at short times and close to the critical atom number  $N_T$

$$\delta n(r, t) = n(r, t) - n(r, 0) \simeq \eta \chi(r) t^2, \quad (4.6)$$

which is expected to be quadratic in time. In this expression,  $\eta$  is a small parameter measuring the deviation from the critical atom number, and  $\chi(r)$  is the shape of the deformation reported in Fig 4.6(a), overlaid with a Townes profile. An explicit expression of  $\chi(r)$  in terms of the Townes profile and its first radial derivative is given in Eq (D.6). We checked that the 2D integral of  $\chi(r)$  is zero, as the integral of the density should be conserved by the evolution under the NLSE.

In practice, we first fit the initial profile to a Townes density profile with a free amplitude and size, which we denote  $n^0(r)$ . For each time of the evolution, we compute the deformation of the density profile with respect to the fitted initial one

$$\delta n(r, t) = n(r, t) - \Lambda n^0(r) \quad (4.7)$$

where  $\Lambda$  is a correction factor to make the two terms of the right-hand-side of Eq (4.7) have the same atom number. The second step consists in fitting this profile with the function  $\chi(r)$  with a free amplitude and size. This fit is performed on a radial region that extends from 0 to  $1.75\sigma_0$ , with  $\sigma_0$  the initial RMS size (obtained from the Townes fit). Examples of such fits are reported in Fig 4.6(b,c). Finally, we compute  $\sigma_0$  using the initial Townes fit of Eq (4.7) and this fitting function, which we integrate over the full plane. The corresponding profiles are shown in Fig 4.5 as solid lines. Additionally, we estimate the error on  $\sigma$  by performing a bootstrap analysis. We confirmed the validity of this method by applying it to the results of numerical simulations of the two-component NLSEs and by checking the overall quality of the fits.

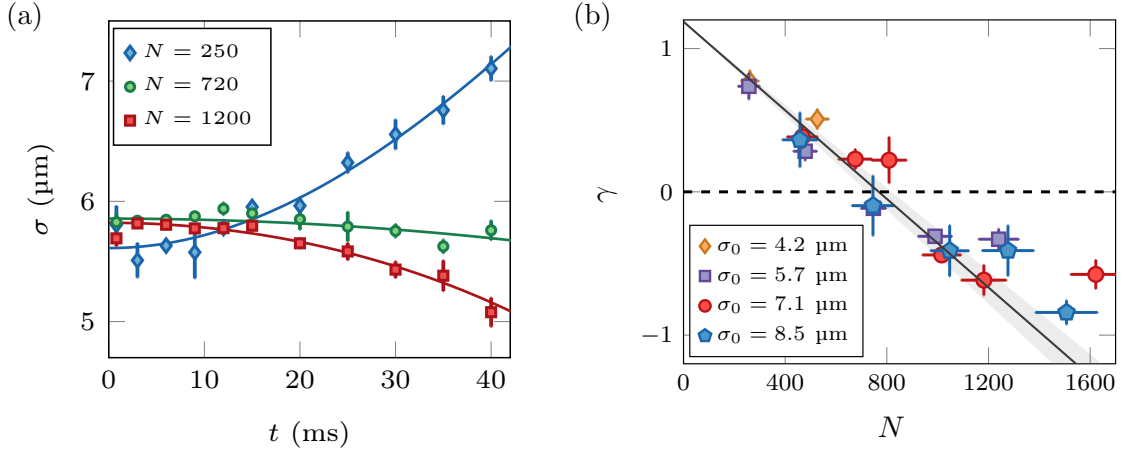


Figure 4.7: Variance identity and scale invariance. (a) Time evolution of the fitted RMS size for the three configurations considered in Fig 4.5 with  $\sigma_0 \simeq 5.7 \mu\text{m}$ . The solid lines are a fit to the data with Eq (4.8), following the variance identity. (b) Expansion coefficient as a function of the atom number of the imprinted wave packet for a magnetic field perpendicular to the atomic plane. All data for different initial sizes collapse onto a single curve. The solid line is the theory prediction computed for  $\tilde{g}_e = -7.6 \times 10^{-3}$  without any adjustable parameter. The shaded area around this line represents our estimated uncertainty on the calibration of  $\tilde{g}_e$ .

### Variance identity, expansion coefficient

Using the previous method, we extract the RMS size  $\sigma(t)$  of the cloud for each time  $t$  and study its time evolution, as shown in Fig 4.7. Qualitatively, the variation of  $\sigma$  for each atom number confirms our initial intuition of an expansion (resp. a contraction) for the data represented in Fig 4.5(a) (resp. Fig 4.5(b)), while the size measured for  $N = 720$  varies only slightly over 40 ms. We further analyze these data using the variance identity (2.24) which provides the time evolution of the RMS size of the density profile for the one-component NLSE. More precisely, we fit the time evolution of  $\sigma$  to the function resulting from the integration of Eq (2.24)

$$\sigma^2(t) = \sigma_0^2 + \left( \frac{\hbar}{m\sigma_0} \right)^2 \gamma t^2, \quad (4.8)$$

with fitting parameters  $\sigma_0$  and  $\gamma$ . Here, we assumed that the imprinted state is a real wave function and thus  $d\sigma/dt = 0$  at  $t = 0$ . The *expansion coefficient*  $\gamma$  we just defined is a dimensionless quantity. It can be written as  $\gamma = 2m\sigma_0^2 E/\hbar^2$ , where  $E$  is the (conserved) total energy for the effective single-component NLSE (4.3).

For a family of real wave functions with a given shape, the expansion coefficient does not depend on the size of the wave function due to scale invariance. Moreover, it should vary as an affine function with the atom number  $N$ , according to the form of  $E$ . In the specific case of a Townes profile, one can show that the expressions of the kinetic and interaction energy integrals (3.22) lead to

$$\gamma(N) = \alpha \left( 1 - \frac{N}{N_T} \right) \quad \alpha \simeq 1.19, \quad (4.9)$$

where the coefficient  $\alpha$  is determined numerically. Consistently,  $\gamma$  cancels for the Townes soliton which contains precisely  $N = N_T$  atoms. The fits shown in Fig 4.7 as solid lines indicate that the evolution of  $\sigma$  is well-captured by the law (4.8), again confirming the validity of the attractive NLSE description.

### 4.2.2 Check of scale invariance

#### Townes profiles with various sizes

The expansion coefficient  $\gamma$  should not depend on the size of the wave packet and thus allows us to test scale invariance in our system. We repeat the experiments described above for various initial sizes  $\sigma_0$  and various atom numbers  $N$ . We report in Fig 4.7(b) the fitted expansion coefficient  $\gamma$  as a function of the atom number  $N$  for these different values of  $\sigma_0$ . All data collapse onto a single curve  $\gamma(N)$  which experimentally confirms the scale invariance of the system.

The stationary state, obtained for  $\gamma = 0$ , contains an atom number equal to  $N_T^{\text{exp}} = 790(40)$ . We determined  $N_T^{\text{exp}}$  using a linear fit of  $\gamma$  with  $\gamma(N = 0) = 1.19$  fixed at the expected value. In Fig 4.7(b), we also show as a solid line the prediction for  $\gamma$  of Eq (4.9), where  $N_T = 770(50)$  is fixed by the independently estimated value of  $\tilde{g}_e$ <sup>3</sup>. It shows a very good agreement for lower values of  $N$ . The small deviation at large  $N$  is likely due to the larger density of the minority component wave packet, which leads to increased losses and deviation from the low depletion regime.

#### Gaussian profiles

What is the particular status of the Townes profile in the above experiment? As shown in Subsec 3.3.1, for an arbitrary density profile there always exists an atom number such that the energy of Eq (3.8) is zero and hence, from the variance identity (2.24), the RMS size is stationary. Of course, this is not sufficient to achieve a fully stationary profile. To show this, we reproduce the previous analysis starting from a family of Gaussian density distributions.

The determination of the RMS size is also done through a fit to the radial density profiles whose details have been gathered in Appendix D. We extract a new series of expansion coefficients  $\gamma$  for various sizes and atom numbers, which we plot in Fig 4.8(a). The data also collapse onto a single curve. The solid line gives the theoretical prediction for  $\gamma(N)$  analogous to (4.9). In the case of Gaussian wave-packets,  $\gamma = 1$  in the non-interacting case ( $N = 0$ ), and intercepts the  $x$ -axis for  $N = N_G \equiv 2\pi/|\tilde{g}_e|$ , which is only 7% larger than  $N_T$  (see Appendix B). Again, we observe good agreement of the experimental data with theory<sup>4</sup>.

We find however that even when  $\gamma = 0$ , the corresponding profile is not stationary. We illustrate this point in Fig 4.8(b) where we compare the deformation over time of two

<sup>3</sup>Note that in all data reported here, the uncertainties on the measured atom number are associated to the statistical variations of the cloud over the different repetitions of the experiment. Systematic errors on the atom number calibration are estimated to be on the order of 10%. The determination of  $N_T$  is sensitive to the knowledge of the scattering length differences. A variation of these two differences by  $0.1 a_0$  corresponds to a variation of  $N_T$  by  $\approx 50$  atoms for our experimental parameters.

<sup>4</sup>We indicate that these data were collected at an early stage of the project. In particular, the feedback loop for the Raman beam-shaping was not implemented yet. The choice of grey-level images projected on the DMD was done by inverting the relation between the local target transferred fraction and the local Rabi frequency for the two-photon transition.

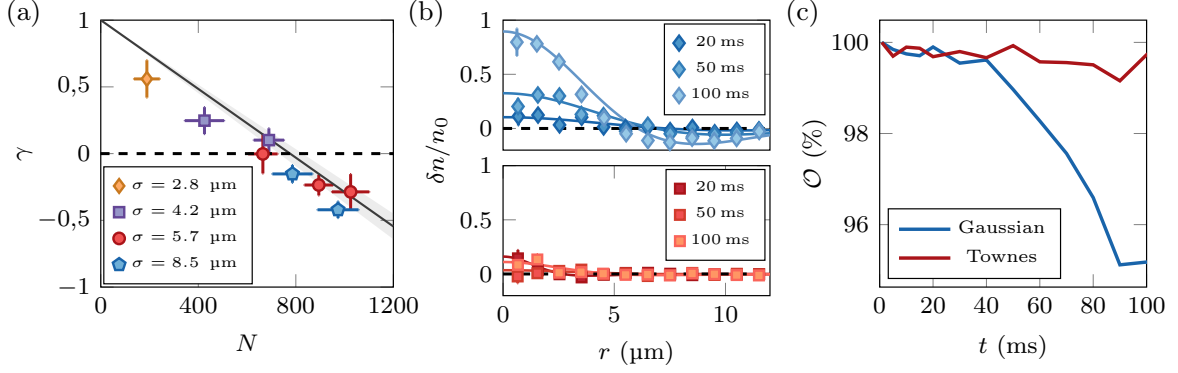


Figure 4.8: Gaussian initial states. (a) Expansion coefficients for the evolution of Gaussian initial states. As in Fig 4.7(b), the solid line is the theory prediction computed for  $\tilde{g}_e = -7.6 \times 10^{-3}$  without any adjustable parameter. It crosses the  $x$ -axis for  $N = N_G \gtrsim N_T$ . (b) Deformation of an initial Gaussian profile in blue (resp. an initial Townes profile in red) computed from Eq (4.7) and normalized by the initial peak density  $n_0$ . For both data-sets, the initial peak density are very close to each other,  $\sigma_0 = 8.5 \mu\text{m}$ ,  $N = 800 \simeq N_G \simeq N_T$  leading to a almost constant RMS size ( $\gamma \simeq -0.2$ ). However the Gaussian profile undergoes much larger deformations over the represented time-scale. (c) Overlap of the radial profiles with the initial ones for the same data.

wave packets, a Gaussian and a Townes profile, with the same atom number  $N = 800$  and same initial RMS size  $\sigma_0 = 8.5 \mu\text{m}$ . In Fig 4.8(a) and 4.7(b) these correspond to the blue pentagons with slightly negative  $\gamma$  values ( $\simeq -0.2$ ), thus having both an almost stationary RMS size. However, the observed density distributions is clearly not stationary in the Gaussian case, as shown in the upper panel of Fig 4.8(b), while the corresponding Townes profiles has almost not evolved for the selected profiles (lower panel of Fig 4.8(b)).

To consolidate this argument, we study the overlap  $\mathcal{O}(t)$  between the profiles at time  $t$  and  $t = 0$  for each distribution, which we define as

$$\mathcal{O}(t) = \frac{\langle n(0)|n(t) \rangle}{\|n(0)\| \|n(t)\|}, \quad \langle n_1|n_2 \rangle = \int dr n_1(r) n_2(r) \quad \|n\|^2 = \langle n|n \rangle. \quad (4.10)$$

The evolution of  $\mathcal{O}(t)$  is shown in Fig 4.8(c) and confirms our initial observation. This highlights the specific status of the Townes profiles in our experiment<sup>5</sup>

### Control of $N_T$

Thanks to the existence of magnetic dipole-dipole interactions in a mixture of the two components, the value of the inter-species scattering length  $a_{12}$  can be shifted, for a 2D cloud, by an amount varying from  $-0.7 a_0$  to  $+1.4 a_0$  around its 3D bare value  $a_{12}^0 = 98.9 a_0$ , see Subsec 1.2.2 and [52]. This is achieved by changing the angle  $\Theta$  of the applied magnetic field with respect to the atomic plane, as represented in Fig 4.2(a). In all cases, we have  $a_{22} - a_{12}^2/a_{11} < 0$  and thus a similar inequality for the interaction parameters  $\tilde{g}_{ij}$ . This

<sup>5</sup>Note that in Eq (4.10), the integral does not comprise the Jacobian factor expected from an azimuthal integration. Indeed, the low signal-to-noise ratio of our data leads to aberrant values when using this definition. We also notice that the values of  $\mathcal{O}(t)$  do not deviate strongly from one in all our data. Indeed, the density profiles have not dramatically changed and must take positive values everywhere.

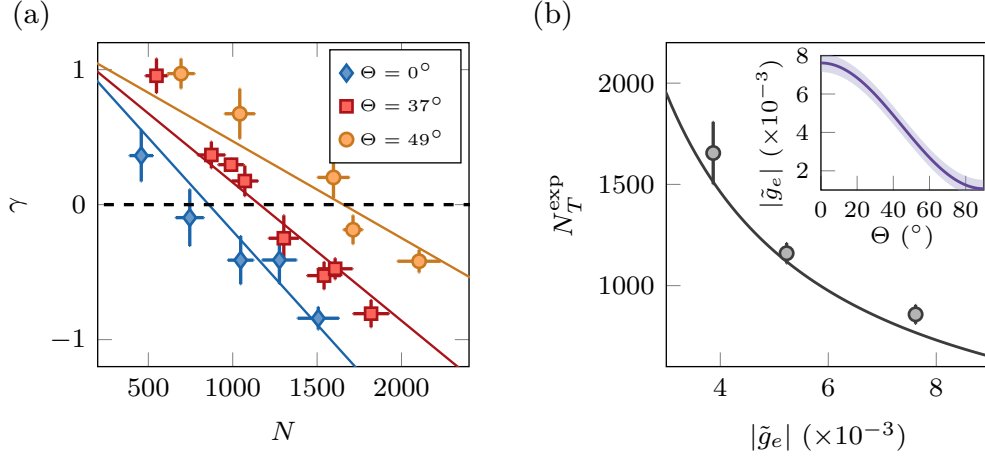


Figure 4.9: Control of  $N_T$ . (a) Expansion coefficient as a function of the atom number  $N$  for various orientations of the magnetic field. The RMS size of the imprinted cloud is set to  $\sigma_0 = 8.6 \mu\text{m}$  for all data considered here, and the bath density is  $n_\infty = 90$  atoms per  $\mu\text{m}^2$ . For each set of points we also plot the linear fit of  $\gamma(N)$  from which we deduce  $N_T^{\text{exp}}$ . (b) Variation of  $N_T^{\text{exp}}$  for different values of  $\tilde{g}_e$ . The solid line is the prediction  $N_T = \mathcal{N}_T / |\tilde{g}_e|$ . (Inset) The experimentally accessible values of  $|\tilde{g}_e|$  are plotted with respect to the angle  $\Theta$ . The shaded area around this line represents our estimated uncertainty on the calibration of  $\tilde{g}_e$ .

implies that  $\tilde{g}_e < 0$ , such that we cannot cross the miscibility threshold using this trick. The inset of Fig 4.9(b) shows the experimentally accessible values of  $|\tilde{g}_e|$ . Despite the smallness of the shift on  $a_{12}$  compared to  $a_{12}^0$ , it has a strong influence on the effective critical atom number  $N_T = \mathcal{N}_T / |\tilde{g}_e|$ , which varies from  $N_T(\Theta = 0^\circ) = 770$  to  $N_T(\Theta = 90^\circ) = 5600$  with our experimental parameters.

In Fig 4.9(a), we report our measurements of the expansion coefficient  $\gamma(N)$  for various orientations  $\Theta$  of the magnetic field. We restrict ourselves to atom numbers  $N < 2200$  to ensure the bath stays in the weak depletion limit for the sizes  $\sigma < 9 \mu\text{m}$  imposed by the geometry of the experiment. From a linear fit of  $\gamma$  with  $\gamma(N = 0) = 1.19$  fixed at the expected value, we deduce the stationary atom number  $N_T^{\text{exp}}$  at which this expansion coefficient vanishes. We show in Fig 4.9(b) the measured variation of  $N_T^{\text{exp}}$  when varying  $\Theta$ . We confirm the prediction  $N_T = \mathcal{N}_T / |\tilde{g}_e|$  with  $\tilde{g}_e$  varying from  $-3.9 \times 10^{-3}$  to  $-7.6 \times 10^{-3}$ . Anisotropic effects due to magnetic dipole-dipole interactions are not expected to modify the properties of the system as long as  $\sigma \gg \ell_z$ , where  $\ell_z$  is the vertical confinement length [52]. In Appendix C, we show that the modification of  $N_T$  should remain smaller than 10% for all data presented here. We have thus observed the main properties of a Townes soliton in our experimental setup.

### 4.2.3 Finite-depletion regime

Our approach using a two-component gas raises new specific questions. For instance, for a wave packet with large enough  $|\tilde{g}_e|N$ , the central density can diverge in a finite time in the single-component case whereas such a collapsing behaviour cannot occur in

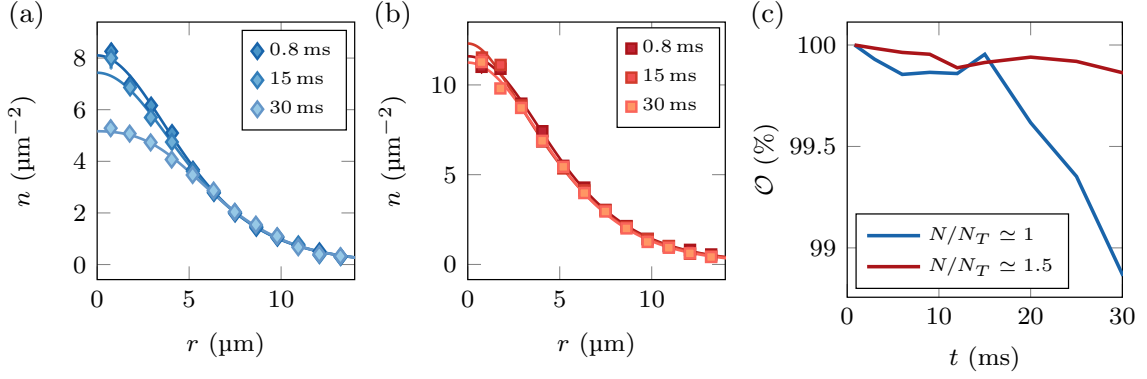


Figure 4.10: Dynamics with finite depletion. Radial profiles for a Townes density profile with  $N/N_T \approx 1$  in (a) and  $N/N_T \approx 1.5$  in (b), both with an initial RMS size  $\sigma_0 \approx 8.5 \mu\text{m}$ . The bath density is set to  $n_\infty \approx 30$  atoms per  $\mu\text{m}^2$ , and the angle of the magnetic field with the atomic plane is  $\Theta = 39^\circ$ , leading to a value of  $N_T = 1100(50)$ . (c) Overlap with the initial profile for the same data.

the two-component case with repulsive interactions (all  $\tilde{g}_{ij} > 0$ ). Indeed, as the minority component density becomes comparable to the bath one, the bath brings a new length scale to the effective one-component description, thus breaking scale invariance. As discussed in the next chapter, such corrections act as a stabilization mechanism and modify the equilibrium properties of the system. In particular, they lead for any atom number  $N > N_T$  to a localized ground state solution with a well-defined size  $\sigma_N$ . We checked that for all data reported in Fig. 4.7(b) and 4.9(b), the shift of the stationary atom number due to the additional stabilizing terms remains small ( $\lesssim 10\%$ ).

In Fig 4.10, we show some preliminary data signaling physics beyond the standard cubic NLSE. To reach the finite-depletion regime while maintaining a small density in state  $|2\rangle$ , we prepare a bath with a much lower density than previously ( $n_\infty \approx 30$  atoms per  $\mu\text{m}^2$ ). We then consider two initial Townes density profiles with atom numbers  $N/N_T \approx 1$  and  $1.5$  respectively. The corresponding initial depletions are 27% and 37%, respectively. While the bubble with  $N/N_T \approx 1$  undergoes large changes of its amplitude over the first 30 ms of evolution, the system with  $N/N_T \approx 1.5$  seems close to equilibrium. This is further confirmed by extracting the overlap  $\mathcal{O}$  of the radial profiles with the initial ones for the same data, as shown in Fig 4.10(c). These results suggest a modification of the equilibrium atom number for such depletions and sizes. In particular, the increase of size for case (a) indicates that the stationary state for such an atom number has a larger size than what we imprinted.

### 4.3 Conclusion

In this chapter, we have presented a novel approach for the exploration of matter-wave solitons using a two-component planar Bose gas. The mapping to a single-component attractive system was possible because of the immiscible character of the mixture. We have shown our excellent control for the preparation of arbitrary spin distributions using intensity modulation of Raman laser beams. Experimentally, we showed that the single-

component NLSE gives a fairly accurate description of our system.

Most importantly, we could prepare a Townes soliton in a deterministic fashion. To our knowledge, this has not been achieved previously. We tested scale invariance of the underlying physics by observing the solitonic behavior for various sizes. We also confirmed the universal scaling  $|\tilde{g}_e|N_T = \mathcal{N}_T \simeq 5.85$  that holds between the nonlinear coupling strength  $\tilde{g}_e$  and the atom number  $N$  of the soliton. The next chapter complements this experimental study with various theoretical considerations and numerical verification. In particular, we will explore physics beyond the weak depletion regime.

As an outlook, note that similar methods could allow us to investigate higher-order solutions of the 2D NLSE, with nodes in the density profile as depicted in Fig 3.6(b), or even vortex solitons. For the first category, the wave function changes sign across each node. This can be implemented by adjusting the duration of the Raman pulse. Imprinting a phase winding is more subtle, and could be achieved by imposing a light shift for a certain time  $t$  to induce a dynamical phase  $e^{-itE/\hbar}$  with a well-chosen spatial dependence of  $E$ . However, a phase winding imposes a discontinuity in the laser intensity profile for connecting the regions that have a  $2\pi$  phase difference.

There is another recipe for doing so in the weak depletion regime. It consists in applying four consecutive pulses of duration  $t_R$ , with alternating phases  $\Phi_j = j\pi/2$ ,  $j = 0, 1, 2, 3$ <sup>6</sup>. If we denote  $\Omega_j(\mathbf{r})$  the corresponding positive Rabi frequency at position  $\mathbf{r}$  for the pulse  $j$ , the wavefunction in state  $|2\rangle$  will be given in the perturbative regime by

$$\psi_2(\mathbf{r}, 4t_R) \simeq t_R \sum_{j=0}^3 \Omega_j(\mathbf{r}) e^{i\Phi_j} = t_R [(\Omega_0(\mathbf{r}) - \Omega_2(\mathbf{r})) + i(\Omega_1(\mathbf{r}) - \Omega_3(\mathbf{r}))]. \quad (4.11)$$

By properly choosing the values of  $\Omega_j(\mathbf{r})$  across the sample for each pulse, one can design the appropriate phase field. In particular, using two instead of four pulses (for example  $\Omega_0, \Omega_1$ ) does not allow to tune the real and imaginary parts of  $\psi_2$  from positive to negative. For example, an ( $s = +1$ ) vortex profile  $F(r)e^{i\theta}$  with polar coordinates  $(r, \theta)$  could be realized by choosing

$$\Omega_j(\mathbf{r}) = F(r) \cos^2 \left( \frac{\theta(\mathbf{r})}{2} - j\frac{\pi}{4} \right). \quad (4.12)$$

The large refresh rate of our spatial light modulator allows for a sufficiently fast modification of  $\Omega$ . The phase jump  $\Phi_j$  can be imposed by sweeping the phase of the generator used for driving the Raman laser AOMs. In practice, it takes  $\lesssim 40 \mu\text{s}$  for a  $2\pi$ -shift and should not be limiting considering the typical timescale for the mixture. Interestingly, this method would avoid the discontinuous intensity profile imposed by the dynamical phase method aforementioned.

---

<sup>6</sup>Phases  $\Phi_j$  are defined here in the frame rotating with the effective micro-wave coupling induced by the pair of Raman beams.



## Chapter 5

# Single-component description of a binary mixture

In the previous chapter, we demonstrated experimentally that the equilibrium configuration of a dilute superfluid immersed in a bath of another component is well-described by a single-component attractive nonlinear Schrödinger equation. Supported by direct comparisons of the experimental data with the behavior predicted by the NLSE, this allowed us to observe a Townes soliton. We interpreted the attractive interactions as the manifestation of the immiscible character of the mixture. We also noticed that the cubic NLSE could not capture the physics of the system when the density of the minority component gets comparable to the bath density.

In this chapter, we provide some theoretical foundations to the results of Chapter 4. We start by studying the equilibrium state of an immiscible binary mixture (Sec 5.1). Using these results, we justify rigorously the approach of Chapter 4 by reducing the coupled equations which describe the immiscible mixture to a single equation for the minority component, without assuming a weak depletion of the bath (Sec 5.2). We also complement this result by adopting a microscopic point-of-view on the problem, yielding a complementary insight on the weak depletion regime. Finally, we discuss some effects going beyond the NLSE formalism in Sec 5.3.

### 5.1 Two-component description

In this section, we describe the equilibrium state of an immiscible mixture, in the strongly imbalanced regime. In Subsec 5.1.1, we remind a simple condition which determines whether a binary superfluid is miscible or immiscible, in the absence of trapping potential. Focusing on the immiscible case, we use numerical simulations to determine the equilibrium state of a minority component immersed in a large bath (Subsec 5.1.2).

#### 5.1.1 An immiscible mixture

##### Immiscibility criterion

We first revisit some concepts relevant for our experiment and already developed in the thesis of Edouard Le Cerf [53]. Here, we consider a 2D system, but these results do not depend on the dimension of space. At zero temperature, the two wave functions



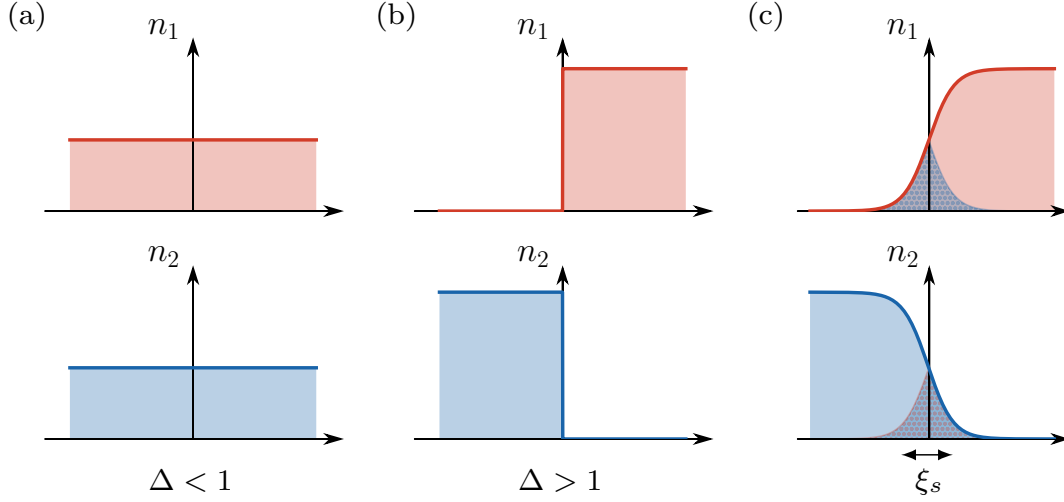


Figure 5.1: Immiscibility criterion. The energy balance between a fully overlapping (a) and a fully segregating (b) configuration is determined by the parameter  $\Delta$  defined in Eq (5.3). (c) In our case, the frontier is smooth and the density profiles partially overlap inside a region of width  $\xi_s \sim$  a few  $\mu\text{m}$ .

$(\phi_1(\mathbf{r}), \phi_2(\mathbf{r}))$  describing our mixture satisfy a set of coupled NLSEs generalizing Eq (2.11)

$$\mu_1 \phi_1 = -\frac{\hbar^2}{2m} \nabla^2 \phi_1 + \frac{\hbar^2}{m} \tilde{g}_{11} |\phi_1|^2 \phi_1 + \frac{\hbar^2}{m} \tilde{g}_{12} |\phi_2|^2 \phi_1 \quad (5.1)$$

$$\mu_2 \phi_2 = -\frac{\hbar^2}{2m} \nabla^2 \phi_2 + \frac{\hbar^2}{m} \tilde{g}_{22} |\phi_2|^2 \phi_2 + \frac{\hbar^2}{m} \tilde{g}_{12} |\phi_1|^2 \phi_2 \quad (5.2)$$

with  $\int d^2r |\phi_i|^2 = N_i$  the total atom number in component  $|i\rangle$ , and with dimensionless coupling strengths  $\tilde{g}_{ij} > 0$  between component  $|i\rangle$  and  $|j\rangle$ . Since the interactions are all repulsive, the chemical potentials  $\mu_i$ 's are positive numbers. Let us compare the total energy of two overlapping condensates to the energy of fully segregating components, neglecting the kinetic energy cost of such a frontier – see Fig 5.1(a,b) and Timmermans [229] for instance. One deduces that, if the interaction parameters satisfy the *immiscibility criterion*

$$\Delta = \frac{\tilde{g}_{12}^2}{\tilde{g}_{11} \tilde{g}_{22}} > 1, \quad (5.3)$$

then it is energetically favorable for the two species to segregate, like oil and water would do. In this case, the density  $n_i$  of each component is homogeneous inside the corresponding *spin domain*, while the other component is completely absent. By computing the pressure in each domain, one deduces that mechanical equilibrium is possible provided that

$$\tilde{g}_{11} n_1^2 = \tilde{g}_{22} n_2^2. \quad (5.4)$$

As depicted in Fig 5.1(c), the frontier between the domains is smooth when the parameter  $\Delta$  takes moderate values above 1. On the other hand, one would expect the two components to fully separate when  $\Delta \gg 1$ . More quantitatively, Ao & Chui [230] and Barankov [231] show that, perpendicularly to the frontier, the density profiles rise from

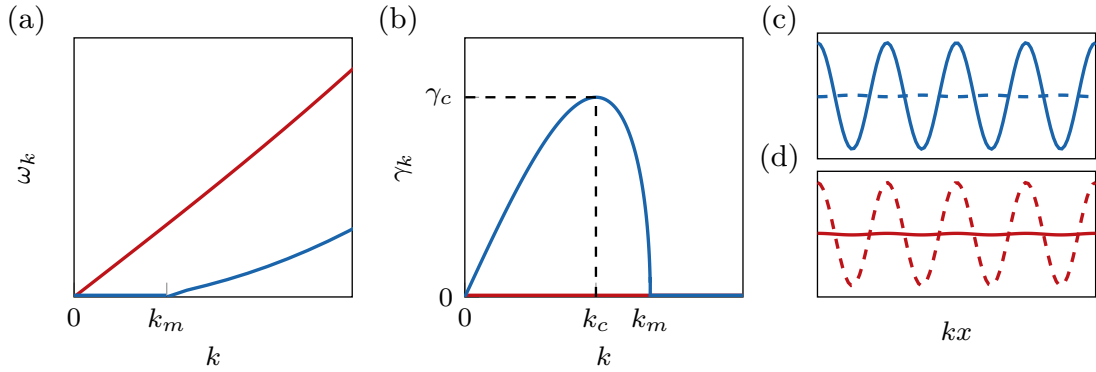


Figure 5.2: Bogoliubov analysis of a balanced mixture with our experimental parameters. (a) Real part  $\omega_k^\pm$  of the Bogoliubov frequencies associated to modes (+) (red line) and (−) (blue line). (b) Same convention for the imaginary  $\gamma_k^\pm$ : only the lower branch (−) induces a dynamical instability, with a maximum rate  $\gamma_c = mc_-^2/2\hbar$  obtained for a wave-vector  $k_c = k_m/\sqrt{2} = 2mc_-/\hbar$ . For better visualization, the span of the vertical axis in (b) is 50 times smaller than in (a). (c) Spatial variation of  $\delta n_1 - \delta n_2$  (solid line) and  $\delta n_1 + \delta n_2$  (dotted line) for the lower-branch excitation with the same wave-vector. These modes are essentially associated to spin modulations. The same for the upper branch is shown in (d), associated to total density modulations.

zero to their bulk value over a typical width called the *spin healing length*

$$\xi_s \equiv \frac{1}{(\sqrt{\Delta} - 1)^{1/2}} \frac{\xi_1 + \xi_2}{2} \quad \xi_i = \frac{1}{\sqrt{2\tilde{g}_{ii}n_i}}, \quad (5.5)$$

where the  $\xi_i$ 's are the individual healing lengths [230]. With our typical experimental parameters, one obtains  $1.005 < \Delta < 1.05$ , for any orientation of the magnetic field (see Subsec 1.2.2). For a balance mixture ( $n_1 = n_2 = 50$  atoms/ $\mu\text{m}^2$ ), one always finds  $\xi_s \gtrsim 1.5$   $\mu\text{m}$ , i.e. a length scale significantly larger than the healing length  $\xi_i \simeq 0.25$   $\mu\text{m}$  of each component. In the intermediate region, the two components thus partially mix. Note that there is a kinetic energy cost in forming a frontier. Hence, we anticipate that when reducing the atom number of one component, it might become favorable to fully mix with the other component.

### Bogoliubov analysis

We now adopt a dynamical point of view and perform a Bogoliubov analysis of the coupled equations (5.1, 5.2), starting from an initially homogeneous configuration with densities  $n_i$  ( $i = 1, 2$ ). Following Timmermans [229], this yields two branches of excitations ( $\pm$ ) with dispersion relations  $\hbar\bar{\omega}_k^\pm(k)$ , associated to a modulation with wave vector  $k$ . These can be written as

$$(\hbar\bar{\omega}_k^\pm)^2 = \hbar^2 c_\pm^2 k^2 + \left( \frac{\hbar^2 k^2}{2m} \right)^2 \quad c_\pm^2 = \frac{1}{2} \left( c_1^2 + c_2^2 \pm \sqrt{(c_1^2 - c_2^2)^2 + 4\Delta c_1^2 c_2^2} \right), \quad (5.6)$$

with  $c_i^2 = (\hbar/m)^2 \tilde{g}_{ii} n_i$  the sound velocity of each component taken separately. As usual,  $\bar{\omega}_k = \omega_k + i\gamma_k$  is *a priori* a complex number. We show the two branches in Fig 5.2 for

a balanced mixture using our typical experimental parameters. While the upper branch has the same form as the standard Bogoliubov spectrum written in Eq (2.18),  $(\hbar\omega_k^-)^2$  can take negative values for low values of  $k$ , if and only if  $(c_-)^2 < 0$ . More precisely, one finds  $(c_-)^2 < 0$  if and only if the immiscibility criterion (5.3) is satisfied.

As a consequence, a homogeneous and immiscible binary mixture is unstable with respect to some small modulations with large wavelengths. The subsequent dynamics, called *demixion phenomenon*, has been extensively studied by our team [53]. In the immiscible case, the dispersion relation of the lower branch  $(-)$  is formally equivalent to the Bogoliubov spectrum of an attractive Bose gas which we discussed in Subsec 3.4.2. Moreover, the eigen-vectors associated to (5.6) are associated to a density modulation  $\delta n_i$  above  $n_i$  in each component. The latter are related to each other through

$$\delta n_1 = \pm \frac{mc_-^2 - (\hbar^2/m)\tilde{g}_{11}n_1}{(\hbar^2/m)\tilde{g}_{12}n_1} \delta n_2 \simeq \pm \delta n_2. \quad (5.7)$$

The last inequality holds for nearby interaction parameters  $\tilde{g}_{ij}$ , and thus  $\Delta$  slightly differing from one. In this case, the soft modes  $(-)$  correspond essentially to spin modulations for which the difference  $\delta n_1 - \delta n_2$  varies appreciably, i.e. the two density fields oscillate out of phase (see Fig 5.2(c)). On the contrary, the upper branch  $(+)$  corresponds to density modulations where the total density  $\delta n_1 + \delta n_2$  oscillates, see Fig 5.2(d). Since  $|c_-| \ll |c_+|$ , we find that the characteristic time scales for large wavelength spin modulations is significantly larger than for density modulations, with inverted conclusions for the energies at play. Hence, we anticipate that the equilibrium state of an inhomogeneous configuration will be dominated by spin modulations, while the total density should be approximately frozen.

### Strong imbalance limit

To further connect the attractive Bose gas case to the physics studied in Chapter 4, we consider the case of a strongly imbalanced mixture where the initially homogeneous densities verify  $n_2 \ll n_1$ . In this situation, the expansion of Eq (5.6) with respect to the small parameter  $n_2/n_1$  yields the following expression at first order

$$\gamma_k^- \simeq \frac{\hbar}{2m} \sqrt{k^2 \left[ k^2 + 4 \left( \tilde{g}_{22} - \frac{\tilde{g}_{12}^2}{\tilde{g}_{11}} \right) n_2 \right]}, \quad (5.8)$$

for the growth rate of the lower branch in the unstable region. A direct comparison to the analogous results for an attractive Bose gas (Subsec 3.4.2) allows us to identify the effective coupling strength  $\tilde{g}_e = \tilde{g}_{22} - \tilde{g}_{12}^2/\tilde{g}_{11}$  associated to the component  $|2\rangle$ . This is precisely the parameter considered in Chapter 4 for describing the weak depletion regime. We will now describe more precisely the spatial structure of the ground state for such an imbalanced mixture.

#### 5.1.2 Spin bubbles

##### Formulation of the problem

We are interested in localized wave functions of component  $|2\rangle$  immersed in a bath of atoms in state  $|1\rangle$ , this bath extending to infinity with asymptotic density  $n_\infty$ . In the rest of this manuscript, we refer to this object as a *spin bubble*. In this case, the chemical potential  $\mu_1$  of component  $|1\rangle$  equals the mean-field energy shift  $(\hbar^2/m)\tilde{g}_{11}n_\infty$ . For symmetry reasons,

such a stationary state has a rotational symmetry around its center. In practice, one needs to enclose the system in a box potential with sharp edges. We thus assume that the box is significantly larger than the spin bubble lying at its center.

An important simplification comes from the scale invariance of the binary system, arising because all interactions are given by “contact potentials” in the mean-field description (see Subsec 2.1.3). Starting from a known equilibrium configuration, we can generate an extended family of spin bubbles by rescaling simultaneously both components with the same factor. In particular, the value of the asymptotic density  $n_\infty$  – and thus of the chemical potential  $\mu_1$  – merely sets a length scale for the system. As a consequence, one only needs to study the problem for one value of  $n_\infty$ , other solutions being deduced from the simultaneous dilation operation. With such a prescription, the system is fully determined by the value of the other chemical potential  $\mu_2$ . In other words, the only meaningful quantity is the ratio  $\mu_2/\mu_1$ .

### Radial NLSE resolution

We now determine the spin bubble distributions for various<sup>1</sup> $\mu_2/\mu_1$ . To determine the ground state configuration, we evolve the two coupled equations (5.1, 5.2) in imaginary time through a time split-step algorithm, as explained in Appendix E. In this approach, the inputs of the numerical calculation are the atom numbers of each component, chosen such that  $N_1 \gg N_2$ . We initialize the wave function with a Gaussian distribution containing  $N_2$  atoms for component  $|2\rangle$ , and its “negative” for component  $|1\rangle$ , with density  $n_\infty$  at large distance. The chemical potentials  $\mu_i$ ’s are deduced afterwards. Due to the vicinity of the interaction parameters in our case, we expect  $\mu_2$  and  $\mu_1$  to be almost equal in whatever equilibrium configuration. Because the energy scales at play in the ground state are small, this method requires extremely long evolution times. These long times can be limiting in a fully 2D geometry as one also desires good spatial resolution.

We developed a new method for evolving Eqs (5.1, 5.2) using only the radial coordinate  $r$ , enforcing rotational invariance around the origin  $\mathbf{r} = 0$  and reducing the full 2D problem to a less involved 1D problem along the radial axis. Note that this method also enforces vanishing boundary conditions at the edges, since periodic boundary conditions would not make sense for a radial problem. As claimed earlier, the presence of edges does not perturb the spin bubble state as long as it lies deeply in the bulk. The generalization of the standard split-step method from Cartesian to radial coordinates is not straightforward. Implementation details have thus been gathered in Appendix E. Using this method, we observe significant acceleration of the calculation with respect to the full 2D algorithm, allowing us to determine the spin bubble states with a good accuracy.

---

<sup>1</sup>In principle, the determination of the equilibrium state could be achieved using the shooting method introduced in the single-component case (see Subsec 3.2.1). Extending the mechanical analogy to the coupled equations (5.1, 5.2) and assuming real-valued wave-functions, the mechanical system is now a particle with position  $(\phi_1, \phi_2)$  moving in a 2D potential

$$V(\phi_1, \phi_2) = \mu_1 \phi_1^2 + \mu_2 \phi_2^2 - \frac{1}{2} (\tilde{g}_{11} \phi_1^4 + \tilde{g}_{22} \phi_2^4 + 2\tilde{g}_{12} \phi_1^2 \phi_2^2). \quad (5.9)$$

The shooting method then consists in fine-tuning the initial conditions in order to approach asymptotically the equilibrium position given by  $(\phi_1 = \sqrt{n_\infty}, \phi_2 = 0)$ . Because the spatial scale associated to a spin bubble is at least given by the spin healing-length  $\xi_s \gg \xi_i$ , the shooting method requires precise numerics as one needs to resolve the scales given by the  $\xi_i$ ’s and  $\xi_s$  at the same time. We find that it gives very poor results in realistic calculation times.

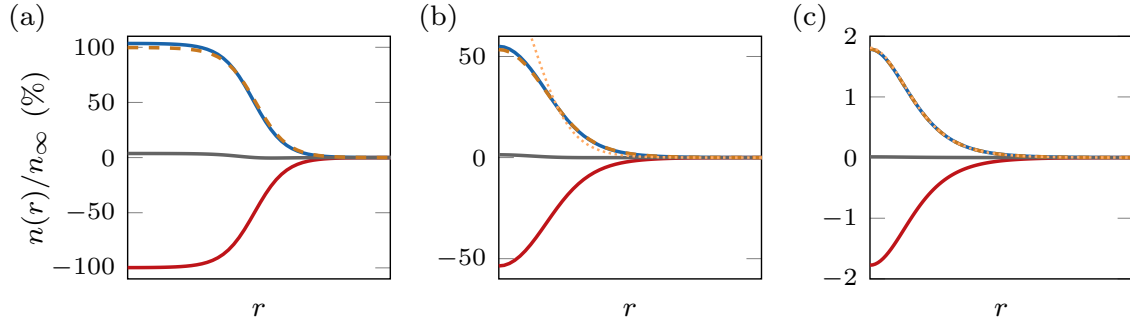


Figure 5.3: Numerical determination of spin bubble states. We show the density distributions  $n_2$  (blue solid lines),  $n_1 - n_\infty$  (red), the excess density  $\delta n$  (grey) for  $N_2/N_T = 10$  (a), 1.5 (b), 1.01 (c). The  $r$ -axis is not fixed between graphs. We also show the profiles predicted from the effective equation (5.13) (orange dashed line) and its moderate depletion limit (5.16) (orange dotted line). Note that the latter overlap almost perfectly with  $n_2$  in (c).

### Determination of spin bubble states

We now determine the spin bubble states for various ratios of the chemical potentials  $\mu_2/\mu_1$  and coupling strengths  $(\tilde{g}_{12}, \tilde{g}_{22}) = (0.99, 0.94) \tilde{g}_{11}$ , similar to the experimental values. We plot a few example distributions in Fig 5.3(a-c) which confirm that the ground state is mainly associated to a spin modulation, the total density varying only slightly.

*A priori*, the atom number  $N_2$  contained in the spin bubble depends on the values of  $\mu_2$  and  $\mu_1$  separately. Using a dimensional argument, one sees that the chemical potentials can only determine  $N_2$  through their ratio  $\mu_2/\mu_1$ . Since we focus on the ground state (which is thus stable),  $N_2$  is a decreasing function of  $\mu_2/\mu_1$ . This is closely related to the Vakhitov-Kolokolov criterion given in Eq (3.29) for a single-component NLSE. Hence, there is a one-to-one correspondence between the authorized values of  $N_2$  and of  $\mu_2/\mu_1$ . In Fig 5.4(a), we plot the variation of  $N_2$  with  $\mu_2/\mu_1$  in the explored region. We normalized  $N_2$  to the Townes atom number  $N_T \simeq 5.85/|\tilde{g}_e|$ , obtained with the effective coupling strength  $\tilde{g}_e$  for the binary mixture.

### The allowed values for $\mu_2/\mu_1$

Let us first determine the extreme values taken by  $\mu_2/\mu_1$ . For a bubble with a large atom number  $N_2$ , we expect component  $|2\rangle$  to form a spin domain with density  $n_2 = \sqrt{\tilde{g}_{11}/\tilde{g}_{22}} n_\infty$  (see Eq (5.4)), rejecting most of the  $|1\rangle$  component out of the central region. This is realized for instance in Fig 5.3(a). Such a spin domain can accommodate any atom number, and  $N_2$  is thus not bounded from above. For an infinite spin domain, the chemical potential of component  $|2\rangle$  simply equals the mean-field energy shift  $(\hbar^2/m)\tilde{g}_{22}n_2 = (\hbar^2/m)\sqrt{\tilde{g}_{22}\tilde{g}_{11}}n_\infty$ . This gives the lower bound for the ratio  $(\mu_2/\mu_1)^{\min} = \sqrt{\tilde{g}_{22}/\tilde{g}_{11}}$ . In Fig 5.4(a), this bound is not reached because the boundary contributes to the chemical potential through kinetic energy. As we will see in Subsec 6.1.3, this correction plays the role of a line tension along the perimeter of the domain. For large  $N_2$ , this correction scales like the fraction of atoms  $\propto 1/\sqrt{N_2}$  contained in the domain boundary.

On the other side, we find numerically that the spin bubble only exists provided its

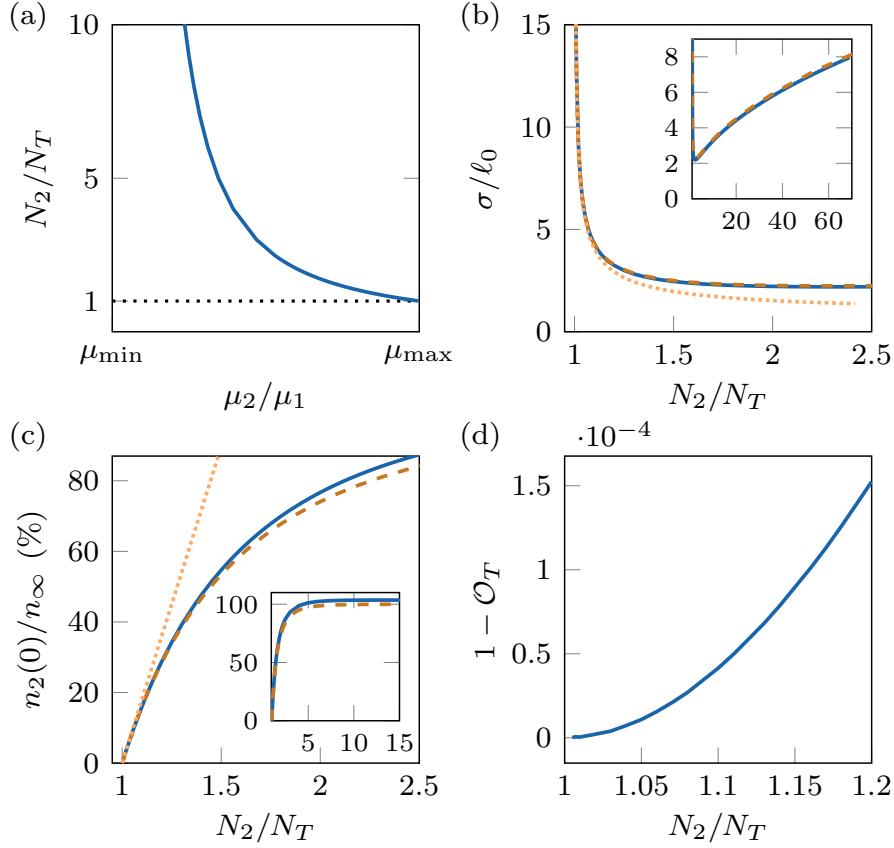


Figure 5.4: Properties of spin bubble states. (a) Atom number as a function of the ratio  $\mu_2/\mu_1$ ,  $(\mu_2/\mu_1)^{\min, \max}$  have been defined in the main text. (b) RMS size  $\sigma$  divide by the natural length scale  $\ell_0 \sim \xi_s$  defined in Eq(5.20). Inset: same data for larger atom numbers. (c) Central density rescaled by  $n_\infty$ . Inset: same data for larger atom numbers. In (b) and (c), we show the same observables obtained from the effective equation (5.13) (orange dashed line) and its moderate depletion limit (5.16) (orange dotted line). (d) The overlap of the spin bubble density with the Townes density profile goes to one when  $N_2/N_T \rightarrow 1$ .

atom number is larger than the Townes atom number  $N_T$ . In the next section, we will show that the profile is indeed determined by a cubic NLSE in this regime. For  $N_2 \leq N_T$ , we obtain two components spreading over the entire box, i.e. not a localized state for component  $|2\rangle$ . For  $N_2 \gtrsim N_T$ , the bubble gets very dilute and the energy cost for adding one particle to the system is simply equal to  $(\hbar^2/m)\tilde{g}_{12}n_\infty$ , such that we obtain the upper limit for<sup>2</sup>  $(\mu_2/\mu_1)^{\max} = \tilde{g}_{12}/\tilde{g}_{11}$ .

<sup>2</sup>One can wonder if these results still hold when considering  $|1\rangle$  instead of  $|2\rangle$  as the minority component, or instead if this depends on our particular choice of  $\tilde{g}_{ij}$ 's. Indeed, in a trapped configuration, it is usually favorable for the component with the largest interaction strength (here  $|1\rangle$ ) to form a shell around the other component. In fact, one finds that  $(\mu_2/\mu_1)^{\min} < (\mu_2/\mu_1)^{\max}$  is equivalent to  $\Delta > 1$ , i.e. only if the immiscibility criterion given in Eq(5.3) is satisfied. Hence, one would find the same behavior if exchanging  $|1\rangle$  and  $|2\rangle$ .

### The shape of the spin bubble

In Fig 5.4(b), we show the non-monotonic variation of the RMS size  $\sigma$  of the bubble as a function of  $N_2/N_T$ . In the spin domain regime, we can approximate the density distribution by a flat-top disk domain with radius  $R = \sqrt{N_2/\pi n_2}$ . In this case, we obtain an RMS size of  $\sigma = R/\sqrt{2}$ . The inset of Fig 5.4(b) shows that the size  $\sigma$  grows indeed like  $\sqrt{N_2}$  when  $N_2/N_T$  gets large. The transition between the small and the large atom number regimes occurs approximately when  $R \sim \xi_s$ , the spin healing length defined in Eq (5.5), or equivalently for  $N_2 \sim N_T$ .

When the atom number  $N_2$  decreases, the kinetic energy and the interaction energy compete for maintaining the  $|2\rangle$ -component together and thus determine the equilibrium shape of the bubble. For  $N_2 \gtrsim N_T$ , we obtain a smooth distribution peaking at the center, see Fig 5.3(b, c) for two different realizations. In Fig 5.4(b), we observe a rapidly increasing size  $\sigma$  when approaching  $N_T$  from above, with a power-law scaling in  $1/\sqrt{N_2 - N_T}$ . Reciprocally, the central density of the bubble decreases to zero as  $n_2(0)/n_\infty \sim (N_2 - N_T)$ .

Importantly, we observe that the wave function  $\phi_2$  tends to a Townes profile when  $N_2$  decreases to  $N_T$ . We confirm this observation by measuring the overlap of  $\phi_2$  with the Townes profile for various  $N_2$ . To do so, we use the definition of the overlap  $\mathcal{O}$  given in Eq (4.10) and determine the overlap  $\mathcal{O}_\ell(N_2)$  between  $|\phi_2|^2$  and a Townes density profile with extension  $\ell$ . We then maximize this quantity to extract  $\mathcal{O}_T(N_2)$ . This is shown in Fig 5.4(d). Our next goal is to justify these results from a theoretical point-of-view, using an effective single component description for the minority component.

## 5.2 Effective one-component description

In this section, we discuss the main result of this chapter, i.e. the determination of a single-component equation for the minority component  $|2\rangle$ . To do so, we present two approaches. In a “top-down” approach, we reduce the coupled NLSEs (5.1, 5.2) to a single-component equation for the minority component (Subsec 5.2.1). This result is valid for any depletion of the bath, provided all interaction parameters are close to each other. In a “bottom-up” approach, we consider spin bubbles from a microscopic point-of-view (Subsec 5.2.2). In particular, we interpret the effective interactions between atoms of the minority component as an exchange of virtual phonons from the underlying condensate.

### 5.2.1 Turning the coupled NLSEs into a single one

#### Derivation

We now justify theoretically the observations made in the previous section. Concretely, we derive an effective single-component description of our binary system described by Eqs (5.1, 5.2), focusing on the ground state wave function<sup>3</sup>. To simplify notations, we use the reduced notations introduced in Subsec 3.1.1 with  $\int d^2r |\psi_2|^2 = N_2$ . The effective single-component description relies on the vicinity of the interaction coupling strengths, i.e.

$$\frac{|\tilde{g}_{12} - \tilde{g}_{11}|}{\tilde{g}_{11}}, \quad \frac{|\tilde{g}_{22} - \tilde{g}_{11}|}{\tilde{g}_{11}} \ll 1, \quad (5.10)$$

<sup>3</sup>Extension of this derivation to vortex states is possible, by separating the radial and azimuthal contributions in the Laplacian written in Eq (5.12).



which allows us to simplify the NLSE at lowest order in these small parameters. The situation in which all parameters are equal correspond to an  $SU(2)$  symmetry point. We remind that for the experiments reported in Chapter 4, the interaction parameters all differ by less than 6%. As discussed above, we expect the low-energy dynamics to be dominated by spin waves, such that the total density

$$n_1 + n_2 = n_\infty + \delta n \quad (5.11)$$

is weakly perturbed, with an excess density  $\delta n$  satisfying  $|\delta n| \ll n_\infty$ . At low energy, the relevant spatial variations occur on the scale of the spin healing length  $\xi_s$ . Using Eq (5.5), the Laplacian operator  $\Delta \sim 1/\xi_s^2$  can itself be considered of order one in the small parameters defined in Eq (5.10), such that the term  $\nabla^2 \phi_1$  in Eq (5.1) can be replaced, at order one, by  $\nabla^2 \sqrt{n_\infty - n_2}$ . This approximation allows one to express the excess density  $\delta n$  in terms of the second component only, as

$$\tilde{g}_{11} \delta n = \frac{\nabla^2 \sqrt{n_\infty - n_2}}{2\sqrt{n_\infty - n_2}} + (\tilde{g}_{11} - \tilde{g}_{12}) \phi_2^2. \quad (5.12)$$

Inserting this expression in Eq (5.2) and keeping terms of order one at most in (5.11), we obtain the following effective single-component equation for component  $|2\rangle$

$$(\mu_2 - \tilde{g}_{12} n_\infty) \phi_2 = -\frac{1}{2} \nabla^2 \phi_2 + \tilde{g}_e \phi_2^3 + \frac{\nabla^2 \sqrt{n_\infty - n_2}}{2\sqrt{n_\infty - n_2}} \phi_2, \quad (5.13)$$

which is the main result of this section. In particular, we recover the effective coupling constant  $\tilde{g}_e = \tilde{g}_{22} - \tilde{g}_{12}^2/\tilde{g}_{11}$ .

### Structure of the effective equation

In Eq (5.13), the prefactor  $\tilde{g}_{12} n_\infty$  corresponds to the interaction energy cost for adding a single particle of component  $|2\rangle$  into the bath. Such a global energy shift plays no role in the following, and we absorb it in the chemical potential  $\mu_2$  hereafter. With this simplification, localized solutions exist only for  $\mu_2 < 0$ . Eq (5.13) is a nonlinear Schrödinger equation with two nonlinear terms. The term  $\tilde{g}_e \phi_2^3$  is the usual cubic nonlinearity, corresponding to an effective system of bosonic particles with contact interactions and coupling constant  $\tilde{g}_e$ , as studied in Chapter 3.

The second term is more complicated and plays a significant role when the density  $n$  becomes comparable to the asymptotic bath density  $n_\infty$ . Moreover, it is not defined for densities larger than  $n_\infty$ . In the limit of large atom numbers the density thus plateaus to this value, describing a spin domain configuration. Note that this plateau density  $n_\infty$  differs from the one deduced from the mechanical equilibrium condition (5.4). This is due to the precision of our derivation, which neglects terms of order larger than one in the small parameters defined in Eq (5.10)<sup>4</sup>. Besides, Eq (5.13) can be derived by adding the supplementary term

$$\frac{1}{2} \int d^2 r (\nabla \sqrt{n_\infty - n_2})^2 \quad (5.14)$$

to the energy functional written in Eq. (3.8). This shows that our effective model inherits from the initial Hamiltonian structure.

<sup>4</sup>This discrepancy could be artificially corrected by defining  $\delta n$  in a slightly different way, for example by writing  $\sqrt{\tilde{g}_{11} n_1} + \sqrt{\tilde{g}_{22} n_2} = \sqrt{\tilde{g}_{11} n_\infty} + \delta n$ . However, this remedy does not ensure better precision far from the top-hat region, or for moderate depletions. We thus prefer to keep a simpler prescription for  $\delta n$ .



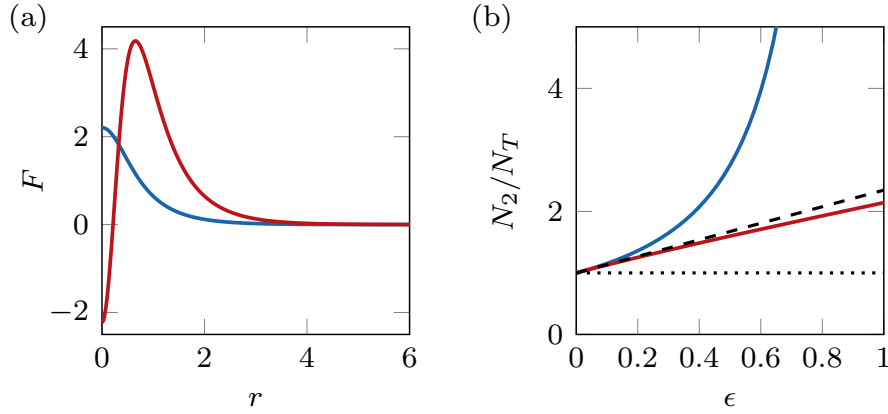


Figure 5.5: (a) Deformation of the Townes soliton in the perturbative regime: function  $F$  introduced by Rosanov & al. [214] and defined in Eq (5.16) (red), together with the non-deformed Townes profile (blue). (b) Atom number for the effective equation (5.13) (blue) and its moderate depletion limit (5.16) (red) as a function of the small parameter of the theory  $\epsilon = |\mu_2|/\tilde{g}_e n_\infty$ . The dashed line gives the perturbative result of Eq (5.19), and the horizontal dotted line indicates the limit  $N_2 = N_T$ .

### Weak depletion

One can expand, in the limit of a large bath density, Eq. (5.13) in powers of the *depletion*  $n_2/n_\infty$ . At minimal order, we obtain the NLSE

$$\mu_2 \phi_2 = -\frac{1}{2} \nabla^2 \phi_2 + \tilde{g}_e \phi_2^2 \phi_2, \quad (5.15)$$

with coupling constant  $\tilde{g}_e$ . We have thus recovered the attractive NLSE introduced empirically in the previous chapter. This result explains the convergence to a Townes soliton for spin bubbles with low depletions, at least with a precision of order one in the small parameters (5.10).

In reality, the numerical results of the previous section suggest that the convergence to a Townes profile when  $N_2 \rightarrow N_T$  holds rigorously, even slightly away from the SU(2) symmetry point. We thus guess that the quantity  $\delta n$  defined in Eq (5.11) goes to zero faster than  $n_2$  when going to the low depletion regime ( $N_2 \rightarrow N_T$ ), such that the replacement of the Laplacian term performed in Eq (5.12) is in fact asymptotically exact when going to zero depletion. This is also revealed by the relative smallness of  $\delta n$  in Fig 5.3(c). While the present derivation does not fully explain this fact, the microscopic picture drawn up in Subsec 5.2.2 will complement the macroscopic model used here.

### A first correction breaking scale invariance

At next order in the perturbation, we obtain the equation

$$\mu_2 \phi_2 = -\frac{1}{2} \nabla^2 \phi_2 + \tilde{g}_e \phi_2^3 - \frac{\nabla^2 n_2}{4n_\infty} \phi_2. \quad (5.16)$$

The additional term, which was considered by Rosanov & al. [214], can be viewed as a weakly non-local interaction. Since this term involves an explicit length scale  $1/\sqrt{n_\infty}$ , it

breaks scale invariance, and we no longer expect self-similarity between stationary states. In a perturbative treatment, the stationary state can be written as a weakly deformed Townes soliton

$$\phi_2(r) = \frac{1}{\ell} R_0(r/\ell) + \frac{1}{2n_\infty |\tilde{g}_e| \ell^3} F(r/\ell), \quad (5.17)$$

where  $\ell = 1/\sqrt{|\mu_2|}$ ,  $R_0$  is the Townes function introduced in Subsec 3.2 and  $F$  is the solution of the linear problem

$$\left( \frac{1}{2} \nabla^2 + 3R_0^2 - 1 \right) F = -\frac{1}{2} R_0 \nabla^2 R_0^2 \quad (5.18)$$

that we show in Fig 5.5(a). In particular, Eq (5.17) allows us to identify the small parameter of the theory  $\epsilon = |\mu_2|/\tilde{g}_e n_\infty$ . In other words,  $\epsilon$  quantifies the importance of the Laplacian term of Eq (5.17) compared to the standard cubic nonlinearity. The atom number contained in the perturbed state is always larger than  $N_T$  and is perturbatively given by

$$N_2 \simeq N_T \left( 1 + 2.72 \frac{|\mu_2|}{|\tilde{g}_e| n_\infty} \right). \quad (5.19)$$

For the effective equation (5.13) and its expansion given by Eq (5.16), we determine the ground state using the shooting method introduced in Subsec 3.2.1. In practice, we solve the models only for  $\tilde{g}_e = -1$  and  $|\tilde{g}_e| n_\infty = 1$  using the proper rescaling. We plot the variation of  $N_2$  with respect to  $\epsilon$  in Fig 5.5(b) and recover the perturbative result given in Eq (5.19).

### Comparison

We now compare the different models studied above, namely the coupled NLSEs (5.1, 5.2), the single-component effective equation (5.13), and the first correction (5.16) breaking scale invariance of the 2D NLSE. To do so, we identify distributions containing the same atom number  $N_2$ . The three different models are shown together in Fig 5.3(a-c), where we observe that the single component effective model gives a faithful description of the two-component system for any atom number. We also checked that we obtain better agreement between the coupled NLSEs and the single component effective equation when the interaction parameters get closer to the SU(2) symmetry point.

We now estimate the RMS size of the deformed Townes soliton in the perturbative regime. The second term inside the parenthesis of Eq (5.19) is assumed to be small, so that it is legitimate to express  $|\mu_2| = 1/\ell^2$  in terms of the RMS size  $\sigma$  of the Townes term of Eq (5.17), yielding  $\sigma = 1.09 \ell$ . Eventually, we obtain the following relation

$$\sigma \simeq \ell_0 \frac{1.26}{\sqrt{N_2/N_T - 1}} \quad \ell_0 \equiv \frac{1}{\sqrt{|g_e| n_\infty}}. \quad (5.20)$$

We thus recover the power-law scaling observed numerically in Subsec 5.1.2. The Townes soliton is asymptotically reached for  $N_2 \rightarrow N_T$ , for an infinite size and zero depletion of the bath. We show the variation of the RMS size  $\sigma$  with the atom number ( $N_2/N_T$ ) for our various models in Fig 5.4(b). All models predict a similar value for  $1 < N_2/N_T < 1.1$ , a regime in which the perturbative prediction (5.20) performs very well. In this interval, we obtain a maximum depletion of the bath of  $\simeq 20\%$  for the coupled NLSEs. This is also the maximum depletion of all data presented in Chapter 4, except for Subsec 4.2.3.

We have shown that the Townes soliton is the ground state of the system in the limit of a weak depletion of the bath. A finite depletion of the bath comes with corrections to the standard cubic NLSE which break scale invariance and imposes an equilibrium size for any atom number  $N_2 > N_T$ . In the previous chapter, we have probed the physics of Townes soliton in a regime in which we are not sensitive to these supplementary terms. Indeed, while the variation of the predicted size is very important for small variations of  $N_2$  (which we cannot resolve anyway), the corresponding energies are small and lead to very slow dynamics.

### An outlook

It would be interesting to prepare any ground state of the system experimentally, without using prior knowledge of the effective coupling strength  $\tilde{g}_e$ . To prepare the ground state in a deterministic way, one could perform an adiabatic evolution of the system under a micro-wave coherent coupling, starting from an initially homogeneous bath of atoms in state  $|1\rangle$ . To do so, one applies micro-wave at a frequency  $\nu$ , initially red-detuned with respect to the clock transition  $|1\rangle \rightarrow |2\rangle$ . In a finite-size bath and choosing a strong-enough detuning, this situation eventually yields a very small transferred population  $N_2 < N_T$ . In this case, one expects the minority component to spread over the entire system. Subsequently, one could slowly ramp up the micro-wave frequency to a final value  $\nu_f$ . The atom number  $N_2$  will rise during the ramp, and can eventually exceed  $N_T$ . If the process is adiabatic, the system will end up with the size and shape expected for the spin bubble. The corresponding atom number will be determined by the final chemical potential  $\mu_2$  of the effective  $|2\rangle$ -system – itself a function of the final frequency  $\nu_f$ . As we will see in Subsec. 6.1.2, the time scale required for an adiabatic preparation would be  $\gtrsim 1$  s. This is currently out of reach using our setup, mainly because of losses in state  $|2\rangle$  (see Subsec. 1.2.1). However, this might be relevant using another system.

## 5.2.2 A microscopic point-of-view

### Induced interactions

Since we can turn the coupled NLSEs into an equation for a single component  $|2\rangle$ , we can think of the bath as an intermediate inducing interactions between atoms of the minority component. Such *induced interactions* are encountered in a broad variety of phenomena in condensed matter physics, from the superconductivity of metals through the exchange of phonons [6], to solutions of Helium 3 in liquid Helium 4 [232]. From a more fundamental point-of-view, the quantum description of the electromagnetic interactions can be pictured in terms of photon exchange [233]. In nuclear physics, the nuclear forces between fermions can be understood in terms of meson exchange through the Yukawa potential.

In cold atom physics, modified interactions between bosons due to the exchange of fermions near the Fermi surface have been observed. These were related to the so-called Ruderman-Kittel-Kasuya-Yosida mechanism [234]. An analog manifestation of this effect is the boson-induced interactions experienced by a polarized – thus non-interacting – Fermi gas, which can trigger collapse [235]. This induced interaction is also described by a Yukawa potential arising from the exchange of phonons in the BEC. In 3D and for increasing couplings, Naidon [236] shows that the Yukawa potential connects to the Efimov potential which also allows two impurities to form a bound state with one BEC atom [103]. However, this is precluded in 2D since the Efimov mechanism is not present.

### The effective potential

In this paragraph, we consider two impurity atoms in state  $|2\rangle$  immersed in a pure BEC in state  $|1\rangle$ , at zero temperature. We temporarily forget about the direct interactions between the atoms in state  $|2\rangle$  and consider solely the impurity-bath interactions. That way, we can determine the modification of the system's energy as a function of the separation  $r$  between the impurities, which we interpret as a potential energy. Within the Bogoliubov approximation and if one neglects the impurity's dynamics (assuming an infinite mass), this energy can be determined using perturbation theory. We report an elementary derivation of this interaction potential in Appendix F. The result of this derivation in two dimensions is the following Yukawa-like potential

$$V_{\text{ind}}(r) = -\frac{2\hbar^2}{\pi m} \tilde{g}_{12}^2 n_0 K_0\left(\frac{1}{\sqrt{2}} \frac{r}{\xi_1}\right), \quad (5.21)$$

where  $\xi_1$  is the BEC healing length, and  $K_0$  is the zeroth-order modified Bessel function of the first kind with the asymptotic behavior  $K_0(r) \sim e^{-r}/\sqrt{r}$ . An important feature of these induced interactions is that the effective potential (5.21) is attractive. It is also short-ranged, with a range provided by  $\xi_1$ .

In the case explored experimentally, the separation between two impurity atoms in state  $|2\rangle$  is of few  $\mu\text{m}$  on average (as given by the size  $\sigma$ ), i.e. much larger than  $\xi_1$ . For that reason, one can approximate this potential by a contact-potential whose coupling strength is given by  $\tilde{g}' = -\tilde{g}_{12}^2/\tilde{g}_{11}$ , see Appendix F. If one sums this contribution to the direct interaction between atoms in state  $|2\rangle$ , one recovers the effective coupling strength

$$\tilde{g}_e = \tilde{g}_{22} - \frac{\tilde{g}_{12}^2}{\tilde{g}_{11}}. \quad (5.22)$$

This provides a microscopic justification to the soliton physics explored in Chapter 4.

### Weakly nonlocal contribution of the effective potential

Importantly, we emphasize that the use of a contact potential in this case is possible only for a bubble whose size is much larger than  $\xi_1$ . This is a much more restricting condition than for using the direct contact potential  $\tilde{g}_{22}$ , whose range is given by  $R_{\text{vdW}}$ . To go beyond this description, we now consider the modified NLSE given by

$$\mu\phi_2(\mathbf{r}) = \left[ -\frac{1}{2}\nabla^2 + \tilde{g}_{22}|\phi_2|^2 + \int d^2r' |\phi_2(\mathbf{r}')|^2 V_{\text{ind}}(\mathbf{r} - \mathbf{r}') \right] \phi_2(\mathbf{r}), \quad (5.23)$$

using the reduced notations introduced in Subsec 3.1.1 with  $\int d^2r |\psi_2|^2 = N_2$ . Following Rosanov et al. [214], we now account for the weakly nonlocal character of the effective potential  $V_{\text{ind}}$ . To do so, we decompose  $\phi_2(\mathbf{r}')$  in a Taylor series and eventually obtain

$$\mu\phi_2(\mathbf{r}) = \left[ -\frac{1}{2}\nabla^2 + \tilde{g}_e n_2 - \left( \frac{\tilde{g}_{12}}{\tilde{g}_{11}} \right)^2 \frac{\nabla^2 n_2}{4n_\infty} \right] \phi_2(\mathbf{r}). \quad (5.24)$$

A direct comparison with Eq (5.16) shows that this model and the one derived from the coupled NLSEs coincide, within a correction in  $(\tilde{g}_{12} - \tilde{g}_{11})/\tilde{g}_{11}$  which we neglected in the derivation of Subsec 5.2.1.

### 5.3 Beyond the nonlinear Schrödinger equation

In this last section, we discuss a few concepts going beyond the NLSE formalism. We first discuss the connection between the behavior of the dilute component  $|2\rangle$  and polaron physics (Subsec 5.3.1). Then, we consider the effect of finite temperature on the solitonic behavior (Subsec 5.3.2). Finally, we go beyond the mean-field formalism and describe the bound states of bosons in 2D with attractive interactions (Subsec 5.3.3).

#### 5.3.1 Polaron physics

In Subsec 5.2.2, we studied the induced interaction between particles whose mass was assumed to be infinite. Does a finite mass  $m$  brings additional physics in this point-of-view? The description of a particle interacting with a bath is a standard problem of quantum mechanics. It was introduced by Landau & Pekar [237] when describing the state of an electron moving through a deformable crystal. As the electron travels through the crystal and deforms it, it excites phonons which in turn may modify the motion of the electron. As a result, the electron gets dressed and screened by the cloud of phonons. The whole thus forms a quasi-particle known as a *polaron*. The properties of polarons have implications on the study of ionic crystals, polar semiconductors or high-temperature superconductors.

The standard model for polaron physics is the so-called Fröhlich Hamiltonian [238]. In particular, this model describes the interaction between an impurity atom and the Bogoliubov modes of a BEC. Just as a phonon-dressing may modify the interactions between particles, it can also modify the dynamical properties of a single polaron. An important question for us concerns the renormalization of the impurity's mass due to the BEC phonons. This renormalized mass  $m^*$  can be defined as the coefficient entering the term in  $\mathbf{p}^2/2m^*$  of the dispersion relation of the impurities. In the weak coupling regime which we define in Appendix F, one can estimate the effective mass of the impurities. By adapting the calculation of Grusdt & Demler [239] to the 2D case, we obtain the following relation

$$m^* = \frac{m}{1 - 0.125 \alpha} > m \quad \alpha = \frac{\tilde{g}_{12}^2}{\tilde{g}_{11}}. \quad (5.25)$$

With our experimental parameters, this corresponds to a relative modification of  $\simeq 2.5\%$ . While this could not be detected with our current setup, it would become feasible by spectroscopic means with slightly stronger interactions.

As an outlook, going further in the limit of uncorrelated impurities could allow us to study the quantum Brownian motion of impurities in a quasi-BEC. Lampo et al. [240] predict a super-diffusive behavior with some memory of the initial conditions. Note that such experiments would necessitate single-particle resolution. In practice, this could be achieved by transferring only a few atoms using our Raman beams. One could then freeze the motion of the particles with a pinning lattice, and detect the position of each impurity using fluorescence imaging.

#### 5.3.2 The influence of finite temperature

A non-zero temperature is usually associated with disorder and tend to destroy fragile structures. In particular, spin bubbles arose in a mean-field picture valid only at zero temperature. What happens to them at finite temperature? In this paragraph, we give an insight on the question of finite temperature through an experimental point-of-view. We

still consider a single-component model for the impurity component with bath-mediated interactions, and we wonder for which atom number  $N_c$  the effective energy of the transferred spin bubble is zero, yielding an expansion factor  $\gamma(N_c) = 0$ .

We have seen that spin bubbles can exist due to the immiscible character of the binary mixture. At finite temperature, a first naive approach consists in using an effective coupling strength

$$\tilde{g}_e(T) = \tilde{g}_{22} + \tilde{g}'(T), \quad (5.26)$$

which depends on the temperature  $T$  through a bath-induced interaction parameter  $\tilde{g}'(T)$ , modified due to thermal fluctuations. As shown by Yu & Pethick [241], this correction can be linked to thermodynamic quantities

$$\tilde{g}'(T) = -\frac{\hbar^2}{m} \tilde{g}_{12}^2 \left( \frac{\partial n_1}{\partial \mu_1} \right)_T \quad (5.27)$$

and  $\tilde{g}'(T)$  can be rewritten in terms of the isothermal compressibility  $\kappa_T = 1/n_1^2 (\partial n_1 / \partial \mu_1)_T$ . Mediated interactions thus get stronger when the underlying bath becomes more compressible. Deep in the superfluid regime, the partial derivative entering Eq (5.27) can be computed using Popov's theory [50, 242], yielding

$$\left( \frac{\partial \mu_1}{\partial n_1} \right)_T = \frac{\hbar^2}{m} \tilde{g}_{11} \left( 1 - \frac{1}{\mathcal{D}} \right). \quad (5.28)$$

One recovers the simple mean-field result when taking  $\mathcal{D} \rightarrow +\infty$ , corresponding to the zero-temperature limit. For finite  $\mathcal{D}$ , one finds that the effective coupling strength  $\tilde{g}'$  is enhanced by a factor  $\mathcal{D}/(\mathcal{D} - 1) > 1$ . In total, we thus expect the effective nonlinear parameter  $\tilde{g}_e(T)$  to become more negative as  $T$  increases. This counter-intuitive effect is due to the rise of compressibility with temperature in the superfluid regime. It is similar to the case studied by Ota et al. [243] who predicted phase separation in a planar mixture even for  $\Delta \lesssim 1$ . In this case, an increase of temperature seems to favor phase separation. For the experiments presented in Chapter 4, we estimate the modification of  $\tilde{g}_e$  to be negligible ( $\lesssim 2\%$  modification of  $N_T$ ).

One could be tempted to deduce from this that the condition  $\gamma(N_c) = 0$  would be shifted to lower values of  $N_c \leq N_T$  at finite temperature. However, while the mediated interactions at large wavelength  $\tilde{g}'(T)$  might be enhanced, a finite temperature also means that the particles can probe more easily the finite range of the effective potential  $V_{\text{ind}}$ . For wavelengths smaller than the healing length  $\xi_1$ , the magnitude of the interactions should be reduced, see Pethick & Smith for example [76]. Moreover, the content in kinetic and interaction energies should be modified by taking into account thermal fluctuations, for instance through the equation of state [244]. Finally, one can simply question the relevance of the simplest single-component model for this problem. Hence, this question seems highly non-trivial but might be approached with numerical calculations. More importantly, this could be experimentally investigated without much difficulty, as we plan to do in a near future. One could then study the effect of the bath thermal excitations and a possible diffusive behavior of the solitons formed in the other component [245, 246].

### 5.3.3 Beyond mean-field effects

Until now, we have described the physics of our binary mixtures through a mean-field approach captured by the coupled equations (5.1, 5.2). This allowed us to exhibit stationary

states with  $N \gtrsim N_T$ , featuring properties similar to the Townes soliton. Contrary to the physics studied in Sec 3.3, these states are protected from wave-packet collapse due to the presence of an effective repulsive term arising from the presence of the bath.

This situation is reminiscent of quantum droplets [30], whose formation results from the competition between a tunable mean-field attractive term and a beyond-mean-field repulsive term. The scaling of these two terms with density is different and leads to a stable equilibrium with a droplet size that depends on the particle number. While our stabilization mechanism here is purely mean-field, we discuss the possibility of beyond mean-field stabilization for 2D bosons with attractive interactions.

### Bound states with universal properties

To proceed, we first forget about the mixture and consider a system of bosons in 2D, with attractive interactions. As noted in Subsec (2.1.3), scale invariance is also broken in the one-component case when one regularizes the contact potential that leads to the interaction energy term  $\int d^2r |\phi|^4$  in Eq. (3.8) [247–249]. Such a regularization is not required as long as one restricts to the classical field approach of Eq (4.3) valid for  $|\tilde{g}| \ll 1$  [145], but it becomes compulsory for larger  $|\tilde{g}|$  where a quantum treatment of atomic interactions is in order. It is thus important to know how this modifies the physics of Townes solitons considered up to now, and if such effects could possibly affect our experimental observations.

Hammer & Son [247] studied the ground state properties of weakly interacting bosons in two dimensions using a classical field formalism with a regularized contact potential. According to Holstein [116], a more accurate description of the system can be obtained by substituting the bare parameter  $\tilde{g}$  by a running coupling constant  $\tilde{g}(k)$

$$\frac{1}{\tilde{g}(k)} = \frac{1}{\tilde{g}} + \frac{1}{2\pi} \ln \left( \frac{k_c}{k} \right), \quad (5.29)$$

which depends on the relative momentum  $k$  of the two particles involved in the collision. The introduction of a cut-off in momentum space  $k_c$  is a signature of an intrinsic length scale  $1/k_c$  of the physical system, here given by the van der Waals radius  $R_{\text{vdW}}$  introduced in Subsec 2.1.1. In the weakly interacting regime, one can neglect the  $k$ -dependent logarithmic correction of Eq (5.29). Hammer & Son [247] determined the properties of the ground state by using a variational approach. One considers trial wave functions with a Townes profile of extension  $\ell$ . The energy per particle of the classical field with  $N$  atoms then writes

$$E_N(\ell) \propto \frac{1}{\ell^2} + \kappa \frac{\tilde{g}(\ell^{-1})N}{\ell^2} \quad (5.30)$$

where  $\kappa > 0$  is a numerical factor and  $\tilde{g}(k)$  is evaluated at the typical momentum  $\ell^{-1}$ . In contrast to Eq (3.9),  $E_N$  has now a non-trivial dependence on  $\ell$  because of the non-constant parameter  $\tilde{g}(\ell^{-1})$ . This term breaks scale invariance and gives rise to an equilibrium size and a binding energy  $(\ell_N, E_N)$  that follow a geometrical law

$$\ell_{N+1} \sim 0.34 \ell_N \quad E_{N+1} \sim \frac{1}{(0.34)^2} E_N. \quad (5.31)$$

Note that  $\ell_N$  and  $E_N$  vary extremely rapidly with  $N$ . For example, one can rewrite  $\ell_N$  as

$$\ell_N \sim R_{\text{vdW}} \exp[-\zeta(N - N_T)], \quad (5.32)$$



with  $\zeta \approx 1$  and  $N_T$  the Townes atom number associated to the bare  $\tilde{g}$ . Observing these universal scalings and the corresponding breaking of scale invariance would be of extreme interest.

### An experimental point-of-view

In practice, the predicted value for  $\ell_N$  is physically reasonable only for  $|N - N_T| \sim \text{few}$  units. For  $N = N_T = \mathcal{N}_T/|\tilde{g}|$ , this size is  $\sim R_{\text{vdW}}$ , which is 3 orders of magnitude smaller than the size of our system. A small shift of only a few atoms, typically from  $N_T$  to  $N_* \equiv N_T - 6$ , gives a size of a few microns, compatible with the extension of our system. Experimentally, we cannot resolve the difference between these two atom numbers, as it would require single-particle resolution. Going further away from  $N_T$ , the corresponding sizes are either much too large or much too small to be experimentally relevant.

Moreover, for  $|\tilde{g}| \ll 1$ , as explored here, the typical evolution time scale of a  $N$ -particle state with a Townes profile of size  $\ell$  slightly different from  $\ell_N$  will be prohibitively long. Indeed, consider a system with  $N = N_*$  atoms. At equilibrium, Hammer & Son [247] predict an energy per particle

$$E_{N_*}(\ell_*) \sim -\frac{\hbar^2}{N_* m \ell_*^2}, \quad (5.33)$$

which can be obtained from Eqs (5.30, 5.29). Interestingly, this energy is  $1/N_*$  smaller than the usual energy associated with the length scale  $\ell_* \equiv \ell_{N_*}$ . Therefore, if the system is prepared in a Townes profile of size  $\ell$  slightly differing from  $\ell_*$ , the typical energy scale governing the dynamics is

$$E_{N_*}(\ell) - E_{N_*}(\ell_*) \sim \frac{1}{N_T} \frac{\Delta \ell}{\ell_*} \frac{\hbar^2}{m \ell_*^2}, \quad (5.34)$$

with  $\Delta \ell = \ell - \ell_*$ . This energy difference  $\propto 1/N_T = |\tilde{g}|/G_T$  is thus negligible for  $|\tilde{g}| \ll 1$  and the typical time scale considered in Chapter 4. In the case  $|\tilde{g}| \sim 1$ , a realistic droplet size would be achieved for only a few atoms and one could observe the predicted scaling of  $\ell_N$  with  $N$ .

This reasoning brings additional questions: is it relevant to go beyond a mean-field description in our case? Do the above arguments hold for such an imbalanced mixture, where the interactions are composite and part of them are mediated by the bath? We saw in Sec 5.1 that the mean-field formalism predicts stable states only for  $N_2 > N_T$ . It is thus an open question if one can predict bound states also for  $N_2 < N_T$ . As shown above, one should go to a regime of stronger interactions to be able to characterize the corresponding states and scalings. Note that beyond-mean-field effects are predicted to play a role in otherwise immiscible mixtures. For instance, Naidon & Petrov [250] expect that bubbles of the mixed phase could coexist with a pure phase of one of the components, provided masses or intraspecies interactions are unequal.

## 5.4 Conclusion

In this chapter, we theoretically and numerically determined the ground state of a strongly imbalanced mixture. We confirmed the mapping to an effective single-component NLSE in a regime of weak depletion where the density of the minority component is much smaller



than the surrounding bath density. We also introduced an effective equation which connects the regime of weak depletion to the physics of spin domains. The rest of the discussion was devoted to a description of the few-particle case through a microscopic point-of-view. We showed that the attractive character of the effective description was linked to supplementary attractive interactions mediated by the bath phonons. We also rose important questions about the case of finite temperature and effects going beyond our mean-field description.

## Chapter 6

# Perspectives on spin bubbles dynamics

In most of this manuscript, we considered spin bubbles – localized states of one superfluid component immersed in a delocalized state of another component – from a static point-of-view. In Chapter 4, we determined experimentally the conditions of existence of such states. This approach was justified theoretically in Chapter 5. A natural extension of this work consists in exploring their dynamical behavior. In this last chapter, we propose a few paths for further characterizations of spin bubbles, through two independent topics.

Given a many-body system at equilibrium, it is fruitful to probe its collective behavior by analyzing its response to a perturbation. For a sufficiently weak perturbation, this response can usually be understood in a linear approach, yielding eigen-frequencies and eigen-modes of the system. Such an approach has been successful in domains as diverse as the study of liquid Helium droplets [35–37], helio-sismology [251], and hydrodynamics in general. For quantum gases, the determination of BECs internal modes has helped gain insight on many-body states since the first experimental achievement of Bose-Einstein condensation [89]. In Sec 6.1, we study the stability and the elementary excitations of spin bubbles, from low to large depletions of the bath.

Another widespread technique to probe the properties and the internal structure of many-body systems consists in studying binary collisions, as is often done in high energy physics. While the phenomenology of soliton binary collisions under the 1D NLSE is well understood [12], much less is known about situations involving higher-dimensional fields. Importantly, these situations can yield a richer phenomenology than in 1D [252–254]. Experiments have allowed to observe collisions of bright solitons in 3D [188] and quasi-1D geometries [15], of vector solitons [255], or quantum droplets [256]. As a preliminary step for exploring 2D spin bubble collisions, we study the collisions of Townes solitons in Sec 6.2.

### 6.1 Stability and elementary excitations

In this section, we determine the elementary excitations of spin bubbles and compare the different models considered in Chapter 5. After presenting our methods (Subsec 6.1.1), we focus on two extreme regimes. In Subsec 6.1.2, we determine the breathing mode of the deformed Townes soliton, in the weak depletion regime. Then, we show that the surface modes of spin bubbles, deep in the spin-domain regime, are closely linked to

the deformations of incompressible 2D droplets (Subsec 6.1.3). We finally discuss the applicability of these results from an experimental point-of-view (Subsec 6.1.4).

### 6.1.1 Methods

#### Models

In the following, we compare the various models introduced in the previous chapter. Using the reduced notations of Subsec 3.1.1, we first remind the coupled NLSEs describing our binary mixture

$$i\frac{\partial\psi_1}{\partial t} = -\frac{1}{2}\nabla^2\psi_1 + (\tilde{g}_{11}|\psi_1|^2 + \tilde{g}_{12}|\psi_2|^2)\psi_1 \quad (6.1)$$

$$i\frac{\partial\psi_2}{\partial t} = -\frac{1}{2}\nabla^2\psi_2 + (\tilde{g}_{22}|\psi_2|^2 + \tilde{g}_{12}|\psi_1|^2)\psi_2, \quad (6.2)$$

with wave functions  $\psi_i$  normalized such that  $\int d^2r |\psi_i|^2 = N_i$ ,  $N_i$  being the atom number in component  $|i\rangle$ , and  $\tilde{g}_{ij} > 0$  the various coupling strengths. In parallel, we also consider the single-component effective models. In Subsec 5.2.1, these were derived when describing the equilibrium state of the bubble. One of our goal in this section is to test whether their time-dependent version can faithfully describe the spin-bubble dynamics. Let us first consider the effective NLSE

$$i\frac{\partial\psi_2}{\partial t} = -\frac{1}{2}\nabla^2\psi_2 - \tilde{g}_e|\psi_2|^2\psi_2 + \frac{1}{2}\frac{\nabla^2\sqrt{n_\infty - |\psi_2|^2}}{\sqrt{n_\infty - |\psi_2|^2}}\psi_2, \quad (6.3)$$

where the wave function  $\psi_2$  is normalized such that  $\int d^2r |\psi_2|^2 = N_2$ ,  $N_2$  being the atom number in the minority component  $|2\rangle$ . In this expression,  $\tilde{g}_e < 0$  is the effective coupling strength for our binary mixture, as written in Eq (5.22), and  $n_\infty$  represents the density of the bath component  $|1\rangle$ , far from the spin bubble. Importantly, Eq (6.3) is meaningful only when the density  $|\psi_2|^2$  is smaller than  $n_\infty$ . Furthermore, the extreme value  $|\psi_2|^2 = n_\infty$  is reached in the case of a spin domain. In this region, the bath component is then completely absent. In Chapter 5, we also considered the expansion of Eq (6.3) with respect to the depletion  $|\psi_2|^2/n_\infty$ . At zeroth order, this yielded the cubic NLSE, which we studied in detail in Chapter 3. At first order, we obtained the first correction to the cubic NLSE breaking scale invariance

$$i\frac{\partial\psi_2}{\partial t} = -\frac{1}{2}\nabla^2\psi_2 - \tilde{g}_e|\psi_2|^2\psi_2 - \frac{\nabla^2|\psi_2|^2}{4n_\infty}\psi_2. \quad (6.4)$$

For each of the above models, we have determined the localized states for atom numbers  $N_2$  larger than the Townes atom number  $N_T \simeq 5.85/|\tilde{g}_e|$ . These states can be indexed by using their chemical potential  $\mu < 0$ , or equivalently by using their atom number  $N_2$ .

#### Linearization and diagonalization

In the following, we study the stability and determine the eigen-modes of these localized states. To do so, we consider a small perturbation around a given equilibrium state. We linearize the evolution equation and obtain a linear partial differential equation, analogous to the Bogoliubov equations. For convenience, the explicit form of this linear system for these models has been reported in Appendix G. The remaining task consists in determining (numerically) the spectrum of the corresponding linear operator, i.e. the set of eigenvalues  $\bar{\gamma} = \gamma + i\omega$ . As usual, the problem is simplified using polar coordinates<sup>1</sup>. Because

<sup>1</sup>Numerically, the gradient and Laplacian operators appearing in these differential operators were expressed using the Bessel-Fourier transform presented in Appendix E.

of rotational invariance, the linear operator decomposes into invariant subspaces with azimuthal number  $s \in \mathbb{Z}$ , such that the action of the angular part of the Laplacian within each invariant subspace reduces to a multiplication by  $(-s^2/r^2)$ .

If any eigen-frequency  $\bar{\gamma} = \gamma + i\omega$  has a non-zero real part  $\gamma$ , we expect the system to be subject to a dynamical instability, i.e. the exponential growth of the associated eigenmode. As expected for the ground state of the system, we do not obtain any unstable mode and always have  $\gamma = 0$ . Thus, we only need to discuss the allowed values for the angular frequency  $\omega$  associated to a periodic evolution of the perturbation. Importantly, we remind that a stable oscillatory mode is localized if and only if  $|\omega| < |\mu|$ , as discussed by Malkin & Shapiro [171]. In this case, we call it an internal mode (or an elementary excitation) of the system<sup>2</sup>. *A priori*, such an oscillation is long-lived, at least as long as one can restrict to a linear description for the perturbation. Note that, due to nonlinear couplings, an internal mode can generate higher-order harmonics which might fall into the continuum. These generally lead to a slow damping of the oscillations<sup>3</sup>.

### Determination of $\omega$ through real-time evolution

Numerically, the previous method is less easily implemented for the coupled NLSEs (6.1, 6.2) for the following reason. The determination of the ground state is necessary for expressing the linearized evolution operators given in Appendix G, before diagonalization. However, obtaining the ground state is very expensive in terms of computational time, especially for atom numbers slightly above the Townes atom number  $N_T$ . The reason for this last statement will be made clearer in Subsec 6.1.2.

Alternatively, it is possible to directly determine the evolution of a given perturbation by simulating the corresponding NLSE. This is the method we choose in Subsec 6.1.2 regarding the coupled NLSEs, focusing on the radial mode with azimuthal number  $s = 0$ . As a good approximation of the ground state in the regime  $N_2/N_T \gtrsim 1$ , we imprint at  $t = 0$  a Townes profile with the desired atom number and the desired RMS size in the minority component  $|2\rangle$ , along with its negative in component  $|1\rangle$ . We then let the system evolve using real time evolution of the coupled NLSEs, as presented in Appendix E. Finally, we extract the RMS size of component  $|2\rangle$  and the frequency  $\omega$  from its evolution.

In practice, nonlinear terms in the evolution of the perturbation are always present when using this protocol, and contribute to the signal by shifting the oscillation frequency. In all numerical results reported here, we assume that the amplitude of the mode, always smaller than 1% of the initial RMS size, yields only little modification of the bare eigenfrequency. As a cross-check, we also used the same protocol for determining the frequency of the  $s = 0$  mode for the single-component models described in the previous paragraph, yielding excellent agreement with the linearization method.

#### 6.1.2 Weak depletion regime

Using the methods described above, we now determine the spectrum of spin bubbles, focusing on the weak depletion regime. For an infinitely small depletion, we expect the system to be described by the cubic NLSE. The elementary excitations of the corresponding Townes soliton were discussed in Subsec 3.2.2 and in Appendix A. Briefly, we remind

<sup>2</sup>The mode is delocalized if  $|\omega| > |\mu|$ , i.e. it is not attached to the localized wave packet.

<sup>3</sup>We mean by *slow* that the decay is typically not exponential but rather inverse polynomial, as discussed by Pelinovsky et al. [257].

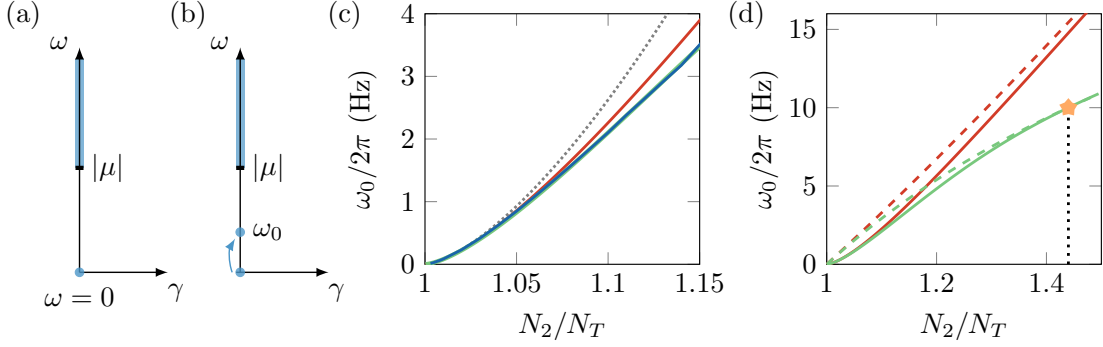


Figure 6.1: Breathing mode. (a) Spectrum of the Townes soliton in the first quarter of the complex plane  $\bar{\gamma} = \gamma + i\omega$ , featuring only neutral ( $\gamma = \omega = 0$ ) and delocalized ( $\gamma = 0, \omega > |\mu|$ ) modes. (b) For the weakly deformed Townes soliton, a breathing mode with angular frequency  $\omega_0$  detaches from the neutral modes. (c) Frequency of the breathing mode for the effective equation (6.3) (green), its weak depletion expansion (6.4) (red), and the coupled NLSEs (6.1, 6.2) (blue). The grey dotted line gives the perturbative result (6.5). We set  $n_\infty = 100$  atoms/ $\mu\text{m}^2$  and  $\tilde{g}_e = -7.6 \cdot 10^{-3}$ , similarly to Chapter 4. (d) Same as (c) for larger  $N_2/N_T$ , only for the single-component models. The limit for the continuum frequencies ( $\omega_0 = |\mu|$ , using reduced notations) is indicated by the dashed line with the same color code. The star indicates the largest value of  $N_2/N_T \simeq 1.45$  for which the breathing mode of the effective equation (6.3) is localized.

that the Townes soliton has only eigen-frequencies inside the continuum spectrum (corresponding to  $|\omega| > |\mu|$ ) and non-oscillating neutral modes ( $\omega = 0$ ). The latter are generated by symmetries and exact solutions of the NLSE. This spectrum is represented in Fig 6.1(a) where we restricted to the first quarter of the complex plane<sup>4</sup>.

For models departing from the cubic NLSE, the situation is modified and genuine elementary excitations can emerge. For example, the elementary excitations of the first correction to the cubic NLSE breaking scale invariance (6.4) were studied by Rosanov et al. [214]. In particular, the authors of [214] exhibit a *breathing mode* with angular frequency  $\omega_0(\mu) \neq 0$ , corresponding to an isotropic deformation with azimuthal number  $s = 0$  and associated to an oscillation of the bubble's size. Rosanov et al. also provide the expression of  $\omega_0(\mu) \neq 0$  in the perturbative limit  $\mu \rightarrow 0^-$ . Using physical units, we express this frequency as a function of  $N_2/N_T$

$$\omega_0(N_2/N_T) = \kappa \frac{\hbar}{m} |\tilde{g}_e| n_\infty (N_2/N_T - 1)^{3/2}, \quad (6.5)$$

with a numerical factor  $\kappa \simeq 0.95$  obtained numerically. To obtain this expression, we used the link between  $\mu$  and  $N_2/N_T$  written in Eq (5.19). In the limit  $N_2 \rightarrow N_T^+$ , higher-order nonlinearities can be neglected. In this case, the Townes soliton and its spectrum are recovered. For  $N_2 > N_T$ , Eq (6.5) shows that this mode detaches from the neutral modes with  $\omega = 0$ , as represented in Fig 6.1(b). As a validation step, we show in Fig 6.1(c) the breathing mode frequency for all three models presented in Subsec 6.1.1, together with the perturbative result given by Eq (6.5). All models overlap for  $N_2/N_T < 1.05$ . In particular,

<sup>4</sup>The rest of the spectrum simply contains  $\bar{\gamma}^*$  and  $-\bar{\gamma}$ , for each value of  $\bar{\gamma}$  shown in Fig 6.1(a), as explained in Appendix A.2.

the perturbative law (6.5) is also verified for the breathing mode of the binary mixture<sup>5</sup>. Henceforth, this result suggests that the models (6.3) and (6.4) not only account for the static properties of spin bubbles, but also for their dynamics.

What about the non-perturbative regime? For  $N_2/N_T > 1.05$ , we observe in Fig 6.1(c) a clear disagreement between the low depletion correction (6.4) and the two others. Rosanov et al. [214] observe numerically that the breathing mode for the NLSE (6.4) exists for any values of  $\mu < 0$ , whereas no other mode seem to detach from the continuum. This is in strong contrast with the situation of Eq (6.3). Intuitively, one does not expect the bubble to breath when the depletion gets maximal, since its central density then cannot increase. We show in Fig 6.1(d) that the breathing mode approximately disappears for  $N_2/N_T \gtrsim 1.45$ , where it reaches the limit of the continuum. This corresponds to a depletion of  $|\psi|^2/n_\infty \simeq 55\%$  at the center of the bubble (see Fig 5.4). Moreover, we show in the next paragraph that other modes emerge for Eq (6.3) for larger atom numbers.

### 6.1.3 Surface modes

We now look for additional modes associated to an azimuthal deformation, i.e. to an azimuthal number  $s \neq 0$ . For the coupled NLSEs in the immiscible case, these elementary excitations have been determined for a trapped immiscible mixture [258], and for a linear interface [259]. For simplicity, here we study only the effective model (6.3). Indeed, we saw that this model gives a fair description of the spin bubbles, even for finite depletion.

As shown in Fig 6.2(b), diagonalisation of the linearized evolution operator show that the first  $s \neq 0$  mode (namely the quadrupolar mode with  $s = 2$ ) appears for  $N_2/N_T \simeq 4$ , i.e. when the depletion of the bath approaches 100% (see Fig 5.4). Using this model, we thus find that surface modes only appear in the spin domain regime. For larger atom numbers, other modes with larger values of  $s$  fall below the continuum. This occurs approximately when the perimeter of the domain equals  $s$ -times the spin healing length  $\simeq 1/\sqrt{n_\infty|\tilde{g}_e|}$ .

### Link with incompressible hydrodynamics

As seen earlier, a spin domain has a fixed density in the bulk. As a consequence, one may expect this system to behave like an incompressible liquid. In reality, this maximum density is fixed by the bath density and can be seen as an external parameter. Hence, the analogy is true only for the effective description of the minority component  $|2\rangle$  but, of course, not without the bath. In particular, the binary system is not self-bound in the absence of potential, since the two components described by repulsive interactions would then expand.

For a 3D spherical droplet shaped by surface tension, one can show that surface modes are quantized, see [260] for example. These *ripplon type* excitations also exist for a 2D incompressible droplet. As depicted in Fig 6.2(a), these excitations correspond to an oscillation of the boundary such that

$$r(\theta, t) = R[1 + \alpha \cos(s\theta - \omega_s t)], \quad (6.6)$$

---

<sup>5</sup>As a consequence,  $\omega_0$  goes to zero faster than the other characteristic frequency  $\propto \mu$ , which fixes the spatial scale of the soliton and thus of our numerical grid. This explains why the evolution in imaginary times used to obtain the ground state gets prohibitively long when  $N_2 \rightarrow N_T$ , as claimed in the previous subsection.

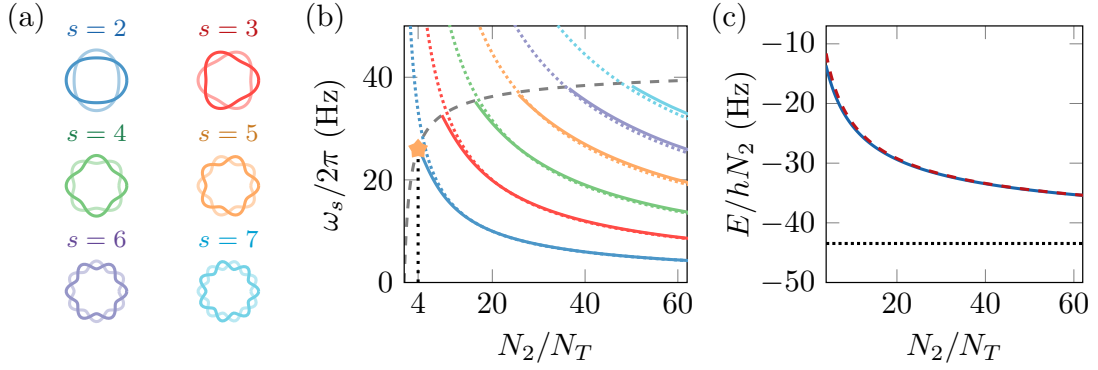


Figure 6.2: Surface modes. We plot in (b) the frequency of each surface mode represented in (a), using the same color code. Similarly to Fig 6.1(d), we expressed the angular frequency in physical units using  $n_\infty = 100 \text{ atoms}/\mu\text{m}^2$  and  $\tilde{g}_e = -7.6 \cdot 10^{-3}$ . Solid lines are deduced from diagonalisation of the linearized operators, while the dotted lines are the predictions written in Eq (6.7) for an incompressible 2D droplet [261]. We only plot the frequencies of localized modes which fall below the continuum line (grey dashed line). The star indicates the smallest value of  $N_2/N_T \simeq 4$  for which the quadrupolar mode ( $s = 2$ ) is localized. (c) Energy per particle computed with the effective NLSE (6.4) (solid blue line) and the hydrodynamical model valid deep in the spin-domain regime (red dashed line).

where  $R$  is the radius of the bubble,  $\theta$  is the polar angle around the bubble,  $r(\theta, t)$  its boundary at an angle  $\theta$  and at time  $t$ , and  $\alpha \ll 1$  the amplitude of the mode. This definition also accounts for a possible breathing mode  $s = 0$ , as described earlier. However, it immediately implies that a breathing mode is forbidden for an incompressible fluid. Furthermore, modes with  $s = \pm 1$  represent a global motion of the bubble (not an internal oscillation) such that we do not consider them in the following. Surface modes with angular frequency  $\omega_s$  ( $|s| > 2$ ) can be obtained following Akulenko & Nesterov [261]

$$\omega_s = \sqrt{\frac{\mathcal{T}}{mn_\infty R^3}} s(s-1)(s+1), \quad (6.7)$$

which also involve the atomic mass  $m$ , the surface density  $n_\infty$  and the linear tension coefficient  $\mathcal{T}$ . In particular, for a large azimuthal number  $s$  and thus a large wave vector  $k_s = 2\pi s/R$ , we recover the well-known dispersion relation  $\omega(k) \propto k^{3/2}$  of capillary waves. In this case, the excitations are not sensitive to the curvature of the droplet.

How to choose the different parameters involved in Eq (6.7) for our single-component effective model? For the radius  $R$ , we will simply use the relation  $N_2 = n_\infty \pi R^2$  applicable to a homogeneous disk, and which become asymptotically exact when  $N_2 \rightarrow +\infty$ . The only missing ingredient is thus the linear tension coefficient which we now determine.

### Linear tension coefficient

To estimate the linear tension coefficient for the single-component effective equation, we use the result of Barankov [231] for a 2D mixture<sup>6</sup>. First, we will assume that the intra-

<sup>6</sup>The difficulty consists in finding a relation which only involves the parameters present in the effective single-component model. Actually, extending the procedure of [231] to our single-component equation should be feasible.



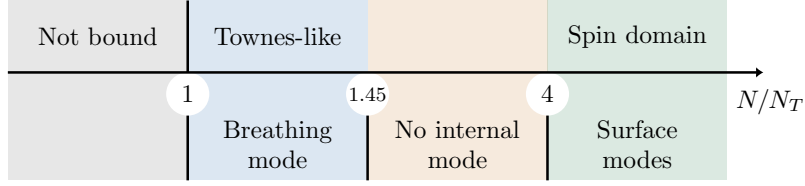


Figure 6.3: Summary of the elementary excitations when varying  $N_2/N_T$ .

species coupling strength are equal, i.e.<sup>7</sup>  $\tilde{g}_{11} = \tilde{g}_{22} \equiv \tilde{g}$ . Since the effective coupling strength  $|\tilde{g}_e| \ll \tilde{g}$ , we can use the following result valid at first order in  $|\tilde{g}_e|/\tilde{g}$

$$\mathcal{T} \simeq \frac{\hbar^2}{2m} \sqrt{|\tilde{g}_e|} n_\infty^{3/2}, \quad (6.8)$$

which only depends on the parameters present in the effective model. To check that this estimate is correct, we compared the total energy obtained numerically to the following estimate  $E \simeq e_0 \mathcal{A} + \mathcal{T} \ell$ , valid in the spin-domain limit. Here,  $\mathcal{A} = \pi R^2$  is the total area,  $e_0 = \tilde{g} n_\infty$  the energy per unit area, and  $\ell = 2\pi R$  the perimeter of the domain. The first term accounts for the bulk contribution, and the second one for the existence of a boundary. We show the result in Fig 6.2(c).

In Fig 6.2(c), we show the frequency of the modes given in Eq (6.7), together with the result of the diagonalization. As expected, we find good agreement between these two. In the previous subsection, we have seen that the breathing mode exists only inside a finite interval of  $|\mu|$ . We deduce that the effective NLSE (6.3) has no localized elementary excitations for  $1.45 \lesssim N_2/N_T \lesssim 4$ . As a consequence, if a domain in this regime of parameters is initially excited, we expect it to self clean by emitting delocalized excitations. This is similar to the situation of 3D quantum droplets, as shown by Petrov [30].

#### 6.1.4 The experimental point-of-view

To conclude this study of spin bubbles' elementary excitations, we discuss the relevance of these features for our experimental setup. We summarized the different results of this section in Fig 6.3. First, the observation of the breathing mode for the weakly deformed Townes soliton – and its scaling given in Eq (6.5) – would be very interesting. In particular, it would yield a new point-of-view on the breaking of scale invariance. However, the experimental time scales required to observe such a scaling for  $N_2/N_T < 1.05$  (typical period of 1 s) are too long compared to the dissipative dynamics associated to two-body losses in state  $|2\rangle$  (see Subsec 1.2.1). For this reason, this study seems currently out of reach.

On the other hand, the frequencies obtained for the surface modes, as shown in Fig 6.2(b), are compatible with realistic experimental time scales. Actually, this study has more to do with (linear) interface phenomena in phase separated mixtures than it is specific to radially symmetric spin bubbles. In particular, there have been various proposals to induce hydrodynamic instabilities using segregated BECs, such as the Rayleigh-Taylor [262], the Kelvin-Helmholtz instability [263] or the Plateau-Rayleigh [264] instabilities. All these proposals start with immiscible components separated by a linear interface.

<sup>7</sup>Since the spin-domain density is equal to  $n_\infty$ , this assumption is already present in the effective model.



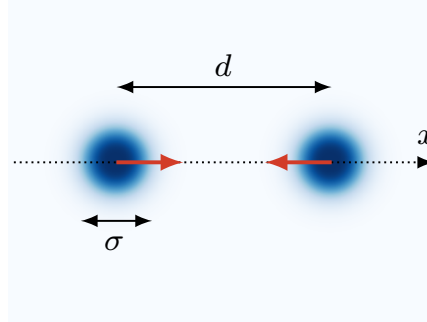


Figure 6.4: Collisions of Townes solitons. Initially, two counter-propagating Townes solitons of size  $\sigma$ , velocity  $v$ , and relative phase  $\varphi$  are separated by a distance  $d$ .

Experimentally, one could wonder how to prepare a quasi-stationary linear interface. Because of the experimental constraint  $\tilde{g}_{22} < \tilde{g}_{11}$ , such domains would feature a density in the region populated by state  $|2\rangle$  larger than in  $|1\rangle$ . Hence, this situation corresponds to a modulation of both the total density and the spin distribution. Our experimental platform allows us to prepare arbitrary density and spin distributions. As an example, one could start from a system in state  $|1\rangle$  with the desired total density obtained using an extra-optical potential, as described in Subsec 1.1.2. From that point, one could use a spatially resolved Raman transition to transfer half of the system in state  $|2\rangle$ , the other half remaining in  $|1\rangle$ . In particular, our optical resolution should allow thus to tailor the smooth density profiles expected at the interface.

## 6.2 Collisions of Townes solitons

In this second part, we describe binary collisions of Townes solitons using numerical simulations. We limit ourselves to the cubic NLSE in Subsec 6.2.1 and determine the stability regime for head-on collisions. As already claimed in Subsec 3.1.1, solitons of the 1D NLSE generically collide and retrieve their original shape afterwards. We will see hereafter that the situation is different in 2D. In Subsec 6.2.2, we point out interesting directions in the case of solitons prepared from a binary mixture.

### 6.2.1 Collisions under the cubic NLSE

We consider the collisions of Townes solitons evolving under the cubic NLSE. Using the reduced notations of Subsec 3.1.1, we write this equation in the attractive case as

$$i\frac{\partial\psi}{\partial t} = -\frac{1}{2}\nabla^2\psi + \tilde{g}|\psi|^2\psi, \quad (6.9)$$

with  $\tilde{g} < 0$  the dimensionless coupling strength. The wave function  $\psi$  is normalized such that  $\int d^2r |\psi|^2 = N$ ,  $N$  being the total atom number. We evolve the initial states described in the next paragraph using real-time evolution of the NLSE in 2D with periodic boundary conditions, as described in Appendix E.

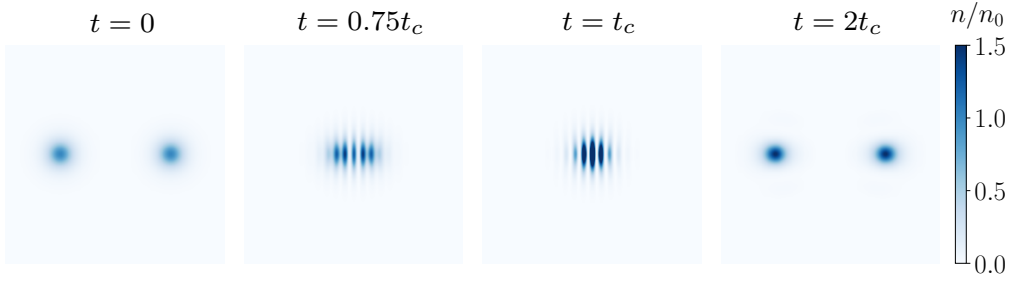


Figure 6.5: Density profiles for head-on collisions taken at various times  $t$ , with relative phase  $\varphi = 0$ , and  $\rho \simeq 1$ . We divided  $n$  by the peak density  $n_0$  obtained at time  $t = 0$ .

### Initial states

We consider initial states given by two counter-propagating Townes solitons, with the same size. Thanks to the Galilean invariance of Eq (6.9), we restrict the analysis to the rest frame for the center of mass, which we set to  $\mathbf{r} = 0$ . We also take the velocities of each solitons aligned with  $(Ox)$ . Finally, we denote the Townes soliton  $R_\sigma(x, y)$ , stationary solution of Eq (6.9) with  $N = N_T$  and RMS size  $\sigma$ . For solitons initially separated by a distance  $d$ , travelling at a velocity  $v$  and with a zero impact parameter, we will thus use as initial conditions

$$\psi(\mathbf{r}, t = 0) = R_\sigma(x + d/2, y)e^{i(kx + \varphi)} + R_\sigma(x - d/2, y)e^{-ikx}. \quad (6.10)$$

In this expression, the wave packet represented by the first term lies essentially in the  $x < 0$  half plane and propagates toward increasing  $x$ , and conversely for the second term, see Fig 6.4(a). The wave vector  $k$  is related to the velocity through the relation  $k = mv/\hbar$ , and it is associated to a de Broglie wavelength  $\lambda_{dB} = 2\pi/k$ . In practice, we choose  $d \gg \sigma$ , so that there is initially negligible overlap between the two wave packets, and the total atom number is approximately given by  $2N_T$ . Numerically, the useful time scale is given by the classical collision time for point-like particles  $t_c = d/2v$ . In the following, we consider a regime in which the initial separation  $d$  does not play any role, except for fixing  $t_c$ . Finally, we also introduced a possible relative phase  $\varphi$ . Such a relative phase will alter the interference pattern made by the two wave packets when overlapping.

### Interaction parameter $\rho = \lambda_{dB}/\sigma$

Contrary to the 1D cubic NLSE, Townes solitons are deformed during the collision and do not conserve their shape after  $t_c$ . However, one can clearly distinguish between qualitatively different behaviors. Because of the scale invariance of Eq (6.9), the two relevant length scales  $\sigma$  and  $\lambda_{dB}$  should determine the dynamics only through their ratio  $\rho = \lambda_{dB}/\sigma$ . Rewriting  $\lambda_{dB}$  in terms of the velocity  $v$ , we see that  $\rho$  is proportional to the duration of the interaction during which the two solitons overlap (if they were to separate afterwards).

### Nearly elastic collisions

A small value of the interaction parameter  $\rho$  corresponds to a very short interaction time. In this case, one expects the collision to be nearly elastic and the solitons to emerge almost unaltered from the process. In other words, kinetic energy dominates over the interaction

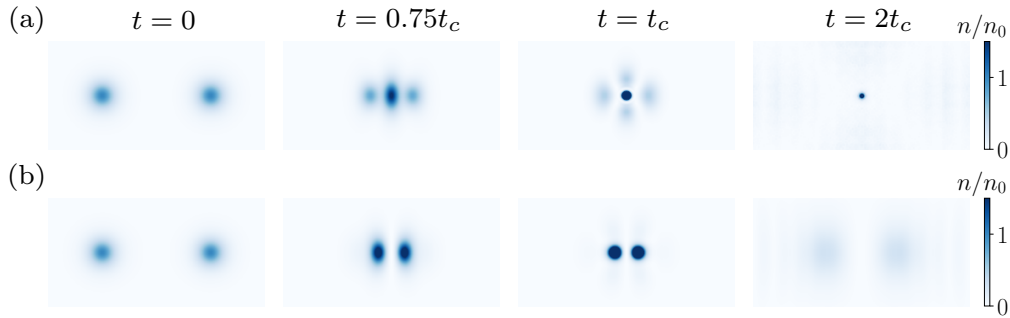


Figure 6.6: Density profiles for head-on collisions taken at various times  $t$ , with  $\rho \simeq 4.3$  and relative phase  $\varphi = 0$  (a),  $\pi$  (b). We divided  $n$  by the peak density  $n_0$  obtained at time  $t = 0$ .

term in Eq(6.9), and the inter-soliton interactions almost play no role. Such a process with small  $\rho$  and relative phase  $\varphi = 0$  is shown in Fig 6.5. After leaving the interaction region indicated by the interference pattern, we indeed observe well defined peaks with constant velocities. After the collision, we observe that the peak density of each wave packet first increases, before decreasing at longer times. Using longer evolution times, we predict numerically that the two separated wave packets will spread and that the evolution will be regular at all times.

As stated above, the relative phase  $\varphi$  determines the position of the interference pattern during the interaction. In this nearly elastic regime, we find that this phase plays essentially no role. Finally, we did not observe any significantly new feature for collisions with non-zero impact parameters in this regime. By measuring the diffusion angle of these well-defined wave packets, we observed a small enhancement of this angle for an impact parameter  $b \simeq \sigma$  of the system, the maximum angle increasing with larger values of  $\rho$ . This is not surprising since we do not expect any deviation for head-on collisions, as well as when the impact parameter is much large than the extent  $\sigma$  of each wave packet.

### Strongly inelastic collisions

For larger values of  $\rho$  corresponding to longer interaction times, the situation is dramatically different. As illustrated in Fig 6.6(a) for a relative phase  $\varphi = 0$ , the central density blows up during the period of overlap, i.e. the system collapses at the origin  $\mathbf{r} = 0$ . Obviously, we do not expect our simulations to properly describe the dynamics just before the collapse<sup>8</sup>. We only assert that they provide a fair estimate of the threshold for collapse at the center, which we observe for  $\rho_c \simeq 3.6$ . For a relative phase  $\varphi \neq 0$ , these conclusions no longer hold. In particular, for  $\varphi = \pi$ , the density at the center is strictly zero at any time and collapse can thus never occur at the center  $\mathbf{r} = 0$ , as shown in in Fig 6.6(b).

### Near-threshold collisions

Interestingly, we observe a remarkable behavior close to the threshold for collapse at the center, as we show in Fig 6.7. In this case, after an initial rise of the density at the

<sup>8</sup>In particular, the image shown in Fig 6.6(a) at  $t = 2t_c$  has been added to show that collapse is indicated by a long-living peak in our simulation.

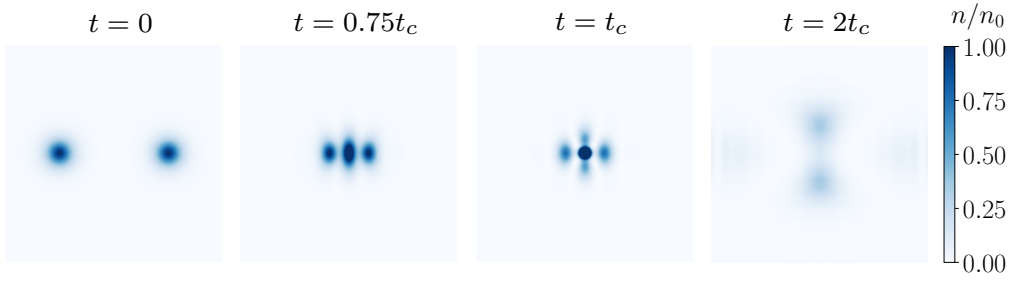


Figure 6.7: Scattering perpendicularly to the propagation axis for  $\rho \simeq 3.4$ , just above the threshold for collapse at the center given by  $\rho_c \simeq 3.6$ . We divided  $n$  by the peak density  $n_0$  obtained at time  $t = 0$ .

center, a large part of the mass is eventually scattered perpendicularly to the propagation axis. We observe that the system is then regular at all times. This situation in which four well-defined momentum states participate to the nonlinear dynamics is reminiscent of four-wave mixing in Bose-Einstein condensates [265]. In particular, one could wonder if this formalism could be useful for understanding this numerical observation. However, contrary to the usual case of four-wave mixing, here the different wave packets overlap notably in momentum space. Finally, it is not excluded that some fine tuning of the parameters could lead to long-lived wave packets propagating along  $y$ .

### 6.2.2 Extension to a binary mixture

#### Propagation in a bath

We now address the question relevant experimentally of binary collisions of solitons obtained from a binary mixture. We insist on the fact that the following discussions are not rigorous. They are rather conjectures which we plan to explore in future work. Our first concern is the description of initial states like (6.10) in the case of spin bubbles. Indeed, these states being immersed in a bath, the naive use of Galilean invariance to describe a moving soliton should impart the same motion to the bath. On the other hand, we observe numerically that launching the soliton with a finite velocity in a bath initially at rest yields nontrivial dynamics, which can even destroy the spin bubble for large velocities.

In practice, one might obtain a shape-maintaining bubble by pushing it gradually. In particular, Sasaki et al. [266] show that a deformed bubble can propagate at a constant velocity in a bath at rest at a large distance. However, Sasaki et al. studied the case of spin domains formed in strongly segregating components, so that our situation necessitates further theoretical investigation. In parallel, one might look for an effective NLSE generalizing Eq (6.3), in the case of a relative motion between the soliton and the bath. This effective equation could describe the state obtained from this gradual launch, going to the frame attached to the bubble. In other words, our protocol could then be understood as an adiabatic evolution of the bubble under this effective model, with a slowly evolving bath velocity. However, the existence of a dynamical instability for large relative velocities of the two components suggested that this adiabatic protocol will not yield a stable soliton above a certain propagation velocity, see the work of Takeuchi et al. [263] for example.

## Collisions

A second question concerns the long time dynamics following the collision. If the limit of short interaction times (small  $\rho$ ) is accessible, it seems reasonable to think that the collisions will still be nearly elastic. After the collision, the deformed solitons would escape from the interaction region. They might be excited and could undergo long living oscillations.

For longer interaction times (i.e.  $\rho \gtrsim$  a few units), we showed earlier that the system described by the cubic NLSE (6.9) can undergo collapse. In the case of a binary mixture, we have seen in Chapter 5.1.1 that the system possesses a well-defined ground state and thus cannot undergo such a collapse. In this regime, do we expect the system to form a bound state, as explored for example by Montesinos et al. [254] in the case of stabilized two-dimensional vector solitons? One could also wonder about the fate of such bound states after long times. In particular, we have seen in Subsec 6.1.3 that the ground state of the system does not possess any localized elementary excitations for a certain range of atom numbers. This situation might lead to a self-cleaning (self-evaporating) of the self-bound system. Finally, it would be interesting to determine if the collision can destroy both solitons, as predicted in the last paragraph of Subsec 6.2.1.

## Experimental implementation

Finally, we briefly discuss the experimental feasibility of such experiments with minimal modifications of our current setup. Using the method described in Subsec 1.2.1, we can transfer two bubbles separated by  $d$  with proper beam shaping. However, the two bubbles would then propagate in the same direction. A collision of one of the solitons on the external box potential could reverse its propagation direction, eventually producing a collision. However, this situation would bring a new difficulty associated to the barrier reflection. In order to circumvent this issue, one could switch the momentum transfer from one direction to the opposite direction, by exchanging the frequencies of the two beams involved in the two-photon transition.

## 6.3 Conclusion

In this chapter, we have discussed a few experimental paths for future characterizations of the spin bubbles explored in this thesis. We first determined the excitation spectrum of the spin bubbles. This allowed us to compare the various equilibrium descriptions introduced in Chapter 5. This suggested that a single-component model could also describe accurately the spin bubbles' dynamics. In the large depletion regime, we draw an analogy between the excitation spectrum of a spin domain and the behavior of an incompressible 2D droplet.

In a second part, we briefly described the binary collisions of Townes solitons. Contrary to the cubic 1D NLSE, the counter-propagating solitons do not survive after a collision, in the case of the 2D NLSE. There is however a possibility for nearly elastic collisions, depending on the effective duration of the interaction between the two solitons. Finally, we discussed the extension of the observed phenomena to the case of solitons prepared from a binary mixture.

# Summary and outlook

In this thesis, I presented our recent realization of a Townes soliton using a two-component planar Bose gas [45]. In Chapters 1, I first explained how to produce two-dimensional samples of Rubidium 87 with fully controllable geometry. I also detailed our techniques for the preparation of binary mixtures, using two different internal states of Rubidium 87. A theoretical description of this two-dimensional weakly-interacting Bose gas with repulsive interactions was given in Chapter 2. This allowed us to derive a nonlinear wave equation – the celebrated nonlinear Schrödinger equation – as a good description for both the equilibrium and the dynamical properties of our system. We discussed the specific dynamical symmetries associated to this equation, which give rise to additional features not present in 1D and 3D geometries.

In Chapter 3, I introduced the Townes soliton. This long-sought solitary wave is a solution of the 2D nonlinear Schrödinger equation with attractive interactions. Because of the specific symmetries of this equation, the Townes soliton has some peculiar properties. It contains an atom number fixed by the strength of the interactions, and it can adopt any size because of the scale invariance of the underlying theory. However, this soliton is also intrinsically unstable and can be subject to collapse for small deviations away from equilibrium. In Chapter 4, we showed our experimental realization of this solution using a novel protocol based on an immiscible mixture of superfluids. The Townes soliton was prepared as the state of one minority component of the system, digging a shallow hole in a bath of the other component. We called this system a spin bubble.

In Chapter 5, I justified rigorously our approach in two complementary ways. Starting from the system of coupled NLSEs describing the mixture, we re-derived the attractive NLSE under the approximation that all interaction parameters were nearly equal. In this case, the total density of the system is approximately frozen. The ground state is then effectively described by a spin modulation which obeys a single-component NLSE with additional nonlinearities. Eventually, the attractive NLSE was recovered in the limit of a small depletion of the bath. From a microscopic point-of-view, we showed that the interactions between atoms of the minority component were modified due to the exchange of virtual phonons through the superfluid bath. Beyond this paradigm, we discussed a few effects not currently observable with our setup, but which could motivate future developments. These concerned the connection of our work to polaron physics, the effect of finite temperature, and the possibility to study bound states of attractive bosons in 2D with universal properties for sufficiently strong interactions.

Chapter 6 was conceived as an outlook. First, we determined the excitation spectrum of spin bubbles. In particular, we showed the appearance of a breathing mode for the deformed Townes soliton, in the case of a finite depletion of the bath. We could also relate the state of this bubble in the spin-domain regime (in which the bath is fully expelled at the center) with the behavior of an incompressible fluid, which can be subject to surface

deformations. In addition, we briefly explored the dynamics of colliding Townes solitons and raised some prospects about analogous experiments using solitons formed from a binary mixture.

As discussed throughout this thesis, there are many possible extensions to this work. Let me recall a few of them. In a very near future, we first plan to understand how the state of the bubble is modified when it has a relative motion with respect to the bath. While one could expect the bubble to be slightly deformed in the low-velocity case, its dynamics could be subject to strong damping mechanisms for larger velocities, such as surface instabilities, vortex generation, etc. This will also lead us to study the interactions between moving bubbles. A second direction concerns the temperature dependence of the solitonic features. In particular, it would be useful to determine how the conditions for quasi-stationarity vary with temperature. Due to the interactions with thermal fluctuations, one could also expect some diffusive motion of the soliton center of mass, and a modification of the soliton lifetime. Another path could consist in studying the effect of disorder on this behavior. Experimentally, a disordered potential could be implemented by applying a supplementary optical potential, using a speckle pattern [267] or by generating random patterns on a digital micromirror device [268]. In particular, the interplay between interactions and disorder could yield new insights on localization phenomena in 2D [269]. Using a single-particle detection scheme, we could study the dynamics of isolated impurity atoms evolving inside a 2D superfluid bath, an instance of quantum brownian motion [240]. Finally, reaching a regime of strong interactions could allow us to study phenomena going beyond the mean-field description applied throughout this work. In consonance with this, we are currently studying the possibility of micro-wave induced Feshbach resonance in our system, as predicted by Papoular et al. [270]. Another long-time prospect in this direction would consist in inducing Rydberg excitations inside the system. The corresponding Rydberg dressing could lead to a greatly enhanced effective interaction potential. This is precisely the goal of the new experiment which is currently built by the next generation of students in the team.

## Appendix A

# Elementary excitations of the Townes soliton

In this appendix, we determine the elementary excitations of a Townes soliton and discuss its stability with respect to small perturbations. Our presentation is mostly inspired from Malkin & Shapiro [171]. As a preliminary step, we recall the list of the continuous symmetries associated to the 2D NLSE (Sec A.1). After linearizing the equation of motion (Sec A.2), we describe the so-called neutral modes of the soliton. Importantly, we show that each of them can be associated to one of the continuous symmetries listed below (Sec A.3). The main conclusion of the analysis is the following: despite there is no dynamical instability in the usual sense, there exist neutral modes which can lead to a collapse of the perturbed soliton in a finite time.

### A.1 Continuous symmetries

For the presentation to be self-contained, we first remind the continuous symmetries associated to the 2D NLSE in the free case ( $V = 0$ ), as detailed by Saint-Jalm [49, 50]. In the context of partial differential equations, a symmetry can be defined as a group of transformations<sup>1</sup> defined on a functional space, which realize a one-to-one correspondence between solutions of the equation. These transformations form a *continuous group* when they are parametrized by a continuous parameter. We rewrite the 2D NLSE for a complex field  $\psi(\mathbf{r}, t)$  with attractive interactions using the reduced notations introduced in Subsec 3.1.1

$$i\frac{\partial\psi}{\partial t} = -\frac{1}{2}\nabla^2\psi - |\psi|^2\psi. \quad (\text{A.1})$$

with  $\int d^2r |\psi|^2 = |\tilde{g}|N \equiv \mathcal{N}$ . All the symmetries described here also apply to the repulsive case.

#### Galilean group

The Galilean group is a symmetry group of the 2D NLSE in any dimension  $D$  [98]. It is composed of the following transformations.

- The translations  $\mathcal{T}_{\mathbf{r}_0}$  by a distance vector  $\mathbf{r}_0$

$$\mathcal{T}_{\mathbf{r}_0}[\psi](\mathbf{r}, t) = \psi(\mathbf{r} - \mathbf{r}_0, t). \quad (\text{A.2})$$

---

<sup>1</sup>The identity operator, the composition of two transformations, and the inverse of any transformation must belong to the group.



- The boosts  $\mathcal{B}_{\mathbf{v}_0}$  with velocity  $\mathbf{v}_0$

$$\mathcal{B}_{\mathbf{v}_0}[\psi](\mathbf{r}, t) = \psi(\mathbf{r} - \mathbf{v}_0 t, t) \exp \left[ i \left( \mathbf{v}_0 \cdot \mathbf{r} - \frac{\mathbf{v}_0^2}{2} t \right) \right]. \quad (\text{A.3})$$

- The rotations in plane  $\mathcal{R}_\theta$  of angle  $\theta$

$$\mathcal{R}_\theta[\psi](\mathbf{r}, t) = \psi(R_{-\theta} \cdot \mathbf{r}, t). \quad R_\theta = \begin{pmatrix} \cos \theta & -\sin \theta \\ \sin \theta & \cos \theta \end{pmatrix}. \quad (\text{A.4})$$

- The time translations  $\mathcal{U}_{t_0}$  of time  $t_0$

$$\mathcal{U}_{t_0}[\psi](\mathbf{r}, t) = \psi(\mathbf{r}, t - t_0). \quad (\text{A.5})$$

In total, the above transformations form a group with 6 generators. The gauge transformation  $\mathcal{P}_\varphi$  with phase  $\varphi$

$$\mathcal{P}_\varphi[\psi](\mathbf{r}, t) = e^{i\varphi} \psi(\mathbf{r}, t). \quad (\text{A.6})$$

is also a symmetry in any dimension.

### Dynamical symmetry

In 2D, the NLSE symmetry group is enlarged thanks to a dynamical symmetry [50, 98] associated to the following transformations

- The *dilations*  $\mathcal{D}_\lambda$  by a factor  $\lambda$

$$\mathcal{D}_\lambda[\psi](\mathbf{r}, t) = \frac{1}{\lambda} \psi \left( \frac{\mathbf{r}}{\lambda}, \frac{t}{\lambda^2} \right), \quad (\text{A.7})$$

hallmark of scale invariance of the 2D NLSE.

- The *lens transformations* or *expansions*  $\mathcal{L}_\beta$  by a factor  $\beta$

$$\mathcal{L}_\beta[\psi](\mathbf{r}, t) = \frac{1}{1 - \beta t} \psi \left( \frac{\mathbf{r}}{1 - \beta t}, \frac{t}{1 - \beta t} \right) \exp \left( -\frac{i}{2} \frac{\beta r^2}{1 - \beta t} \right). \quad (\text{A.8})$$

These last two sets of transformations can be combined with the time translations  $\mathcal{U}_{t_0}$  to form a group isomorphic to  $\text{SL}(2, \mathbb{R})$ .

### Link with the 2D NLSE in a harmonic potential

There also exist transformations  $\mathcal{K}_\alpha$  linking the solutions  $\psi'$  of the 2D NLSE in a harmonic potential  $V(\mathbf{r}) = \alpha r^2/2$  to solutions in the free case  $V(\mathbf{r}) = 0$

$$\mathcal{K}_\alpha[\psi'](\mathbf{r}, t) = \frac{1}{\lambda(t)} \psi' \left( \frac{\mathbf{r}}{\lambda(t)}, \frac{\arctan(\sqrt{|\alpha|}t)}{\sqrt{|\alpha|}} \right) \exp \left( \frac{i}{2} \frac{\dot{\lambda}(t) r^2}{\lambda(t)} \right), \quad (\text{A.9})$$

with  $\lambda(t) = \sqrt{1 + \alpha t^2}$ , and  $\dot{\lambda}$  its derivative [105]. Written that way, we allow the potential  $V$  to be either confining (in which case  $\alpha = m\omega^2 > 0$ , with  $\omega$  the associated angular frequency), or anti-confining ( $\alpha < 0$ ). To be rigorous, these transformations are not symmetries of the 2D NLSE, since they do not link solutions of the free 2D NLSE. Formally, they correspond to Bäcklund transformations between two different partial differential equations, as investigated by Saint-Jalm et al. [49, 50].

## A.2 Stability analysis

We now present a stability analysis for the Townes soliton, analogous to Bogoliubov's formalism [171, 205–207]. Thanks to scale invariance, one can restrict the analysis of stability around the Townes soliton  $R_0$  defined by

$$-R_0 = -\frac{1}{2}\nabla^2 R_0 - R_0^3 \quad \nabla^2 = \frac{d^2}{dr^2} + \frac{1}{r} \frac{d}{dr}. \quad (\text{A.10})$$

### The linear system

We assume initial conditions  $\psi(\mathbf{r}, t = 0)$  slightly departing from the stationary solution  $R_0(r)$ , and write it as  $\psi(\mathbf{r}, t = 0) = R_0(r) + \epsilon(\mathbf{r}, t = 0)$ . The wave function  $\psi(\mathbf{r}, t)$  evolving under Eq (A.1) can then be expressed as

$$\psi(\mathbf{r}, t) = [R_0(r) + \epsilon(\mathbf{r}, t)] e^{it}, \quad (\text{A.11})$$

with  $\epsilon(\mathbf{r}, t)$  a small perturbation with respect to  $R_0(r)$ , at least at short times. Decomposing  $\epsilon(\mathbf{r}, t)$  into real and imaginary parts  $\epsilon(\mathbf{r}, t) = u(\mathbf{r}, t) + iv(\mathbf{r}, t)$ , Eq (A.1) can be linearized around the stationary solution  $R_0(r, t) = R_0(r) e^{it}$ . This leads to the following differential system<sup>2</sup>

$$\frac{\partial}{\partial t} \begin{pmatrix} u \\ v \end{pmatrix} = \begin{pmatrix} 0 & \hat{L}_0 \\ -\hat{L}_1 & 0 \end{pmatrix} \begin{pmatrix} u \\ v \end{pmatrix} = \mathcal{M} \begin{pmatrix} u \\ v \end{pmatrix}, \quad (\text{A.13})$$

where we defined the operator  $\mathcal{M}$  in terms of the self-adjoint differential operators  $\hat{L}_0$  and  $\hat{L}_1$  introduced by Zakharov [205]

$$\hat{L}_0 = 1 - \frac{1}{2}\nabla^2 - R_0^2 \quad \hat{L}_1 = 1 - \frac{1}{2}\nabla^2 - 3R_0^2. \quad (\text{A.14})$$

### Structure of the spectrum of $\mathcal{M}$

A standard way to proceed consists in reducing the operator  $\mathcal{M}$  into its simplest form. One thus wishes to decompose  $\mathcal{M}$  into generalized eigen-functions and eigen-spaces with associated eigen-values<sup>3</sup>  $\bar{\gamma} = \gamma + i\omega \in \mathbb{C}$ . This will allow us to identify modes which evolve independently – *normal modes* – at least as long as the linear perturbation theory remains valid. Contrary to  $\hat{L}_0$  and  $\hat{L}_1$ ,  $\mathcal{M}$  is not self-adjoint itself. Hence, it is *a priori* unclear if this operator can be diagonalized, and where the eigen-values  $\bar{\gamma}$  lie in the complex plane. However, from the definition of  $\mathcal{M}$ , one can show that if  $\bar{\gamma}$  is an eigen-value, then  $-\bar{\gamma}$  and  $\bar{\gamma}^*$  are too.

Malkin & Shapiro [171] show that there is no dynamical instability, i.e. that  $\mathcal{M}$  has no eigen-value  $\bar{\gamma}$  with a real part  $\gamma \neq 0$ . An eigen-value with  $\gamma \neq 0$  would lead to the exponential growth of the amplitude of the corresponding eigen-function. Moreover, the

<sup>2</sup>This is easily obtained by noticing that

$$|\psi|^2 = (R + u)^2 + v^2 \simeq R^2 + 2Ru \quad (\text{A.12})$$

at first order.

<sup>3</sup>This is the analog of the Jordan decomposition for infinite dimension operators. Our choice for the real and imaginary part of  $\bar{\gamma}$  will help identify stable and unstable modes.

operator  $\mathcal{M}$  has a continuous spectrum of imaginary eigen-values  $\bar{\gamma} = i\omega \in i\mathbb{R}$  such that  $|\omega| > 1$ . As shown in [171], these correspond to non-normalizable (delocalized) excitations whose amplitude oscillates in time. In practice, a localized superposition of such excitations would eventually spread and leave the soliton unaffected. Henceforth, these do not induce any instability. Finally, Malkin & Shapiro show that there are otherwise no elementary excitations that can be associated to an eigen-value  $\bar{\gamma} = i\omega \in i\mathbb{R}$  such that  $0 < |\omega| < 1$ .

### A.3 Neutral modes and symmetries

The remaining part of the spectrum is associated to the eigen-value  $\bar{\gamma} = 0$ . The corresponding generalized eigen-functions can be identified by inserting the following ansatz

$$\epsilon(\mathbf{r}, t) = \sum_{j=0}^n \epsilon_j(\mathbf{r}) t^j \quad n \in \mathbb{N}. \quad (\text{A.15})$$

for the perturbation in the evolution equation (A.13). These modes are called *neutral modes* and do not oscillate, but grow like polynomials with the time<sup>4</sup>  $t$ . To proceed, let us decompose the operator  $\mathcal{M}$  within invariant subspaces with well-defined azimuthal quantum number  $s \in \mathbb{Z}$ , such that the angular part of the Laplacian reduces to a multiplication by  $(-s^2/r^2)$  in each invariant subspace. As usual, this simplification arises from the rotational symmetry of the linearized problem.

One can exhibit eight neutral modes in total: four of them are associated to the azimuthal value  $s = 0$  (corresponding to isotropic perturbations), and four others are combinations of  $s = \pm 1$  modes (dipole modes). Moreover, these cannot grow faster than  $t^3$ . Following the analysis of Malkin & Shapiro [171], we now associate each of these neutral modes with a 2D NLSE symmetry. By this, we mean that each of them can be obtained by applying one of the symmetries listed in Sec A.1 to a previously known solution.

#### Six neutral modes are stable

The translations  $\mathcal{T}_{\mathbf{r}_0}$  defined in Sec A.1 generate two independent dipole modes when applied to the trivial solution  $R_0(r, t)$ . These are rigorously time-independent since a displaced soliton is not subject to any dynamics. They are thus obtained by setting  $n = 0$  in Eq (A.15). The boosts  $\mathcal{B}_{\mathbf{v}_y}$  generate another pair of independent dipole modes. Since they correspond to a uniform motion of the soliton without any deformation, these modes grow linearly with time ( $n = 1$  in Eq (A.15)), as immediately deduced from Eq (A.3).

For the isotropic perturbations  $s = 0$ , a first neutral mode is generated by the gauge transformations  $\mathcal{P}_\varphi$  applied to the trivial solution  $R_0(r, t)$ . It is obviously time-independent ( $n = 0$  in Eq (A.15)). A second one is generated by the dilation operation  $\mathcal{D}_\lambda$  arising from scale invariance. Using Eq (A.7) and the fact the Townes soliton has an overall running phase  $R_0(r) e^{it}$ , we find that the only time-dependence in the perturbation comes from the modification of the phase factor, which grows linearly ( $n = 1$  in Eq (A.15)).

---

<sup>4</sup>Remember that, after some evolution time, the linear analysis may break down, as the perturbing terms become non-negligible.

**One unstable mode is generated by  $\mathcal{L}_\beta$** 

A third isotropic mode with  $s = 0$  can be found by applying the lens transformations (A.8) to the Townes soliton  $R_0(r, t)$

$$\mathcal{L}_\beta[R_0](\mathbf{r}, t) = \frac{1}{1 - \beta t} R_0\left(\frac{r}{1 - \beta t}\right) \exp\left[i\left(\frac{t}{1 - \beta t} - \frac{\beta}{2} \frac{r^2}{1 - \beta t}\right)\right], \quad (\text{A.16})$$

with a real parameter  $\beta$ . For a small  $\beta$ , the exact solution (A.16) varies like a polynomial in  $t$  at short times, with a dominant quadratic term ( $n = 2$  in Eq (A.15)). Importantly, for  $\beta > 0$ , this solution will form a singularity exactly at  $t_0 = 1/\beta$ . This shows that the Townes soliton is subject to an *instability by collapse*, despite there is no dynamical instability in the usual sense. Interestingly, all the modes considered above conserve the Townes soliton norm

$$\mathcal{N} = \int d^2r R_0^2(r) \equiv \mathcal{N}_T \simeq 5.85. \quad (\text{A.17})$$

**One unstable mode is generated by  $\mathcal{K}_\alpha$** 

To exhibit the fourth and last mode with azimuthal number  $s = 0$ , we first consider the stationary solutions of the 2D NLSE in a harmonic trap  $V(\mathbf{r}) = \alpha r^2/2$ . For  $\alpha \geq 0$  and a chemical potential  $\mu \in ]-\infty, \sqrt{\alpha}[$ , there exists a unique solution which is radial and monotonically decreasing [209]. We can thus select the particular solution  $R_\alpha$  obtained for  $\mu = -1$  and satisfying the equation

$$-\frac{1}{2} \left( \frac{d^2 R_\alpha}{dr^2} + \frac{1}{r} \frac{dR_\alpha}{dr} \right) - R_\alpha^3 + \frac{1}{2} \alpha r^2 R_\alpha = -R_\alpha. \quad (\text{A.18})$$

Then, using the transformation (A.9), we can form the exact solution

$$\mathcal{K}_\alpha[R_\alpha](\mathbf{r}, t) = \frac{1}{\lambda(t)} R_\alpha\left(\frac{r}{\lambda(t)}\right) \exp\left[i\left(\frac{\arctan(\sqrt{|\alpha|}t)}{\sqrt{|\alpha|}} + \frac{\dot{\lambda}(t)r^2}{2\lambda(t)}\right)\right]. \quad (\text{A.19})$$

with  $\lambda(t) = \sqrt{1 + \alpha t^2}$ . For a small  $\alpha$ , this exact solution generates the last secular mode exhibited by Malkin & Shapiro [171], which grows like a polynomial with a dominant  $t^3$  term ( $n = 3$  in Eq (A.15)). We now wish to describe the long-time behavior of this perturbation for a small  $\alpha$ . To do so, we first develop the solution (A.19) at  $t = 0$  for small  $\alpha > 0$  as  $R_\alpha(r) \simeq R_0(r) + \alpha u(r)$ . Using (A.18), one finds that  $u(r)$  satisfies the following linear differential equation

$$\hat{L}_1 u = -\frac{1}{2} r^2 R_0, \quad (\text{A.20})$$

with  $u(0) \simeq 0.26$ , the operator  $\hat{L}_1$  being defined in Eq (A.14). We can now discuss the fate of the initial wave function  $R_0(r) + \alpha u(r)$  for a small  $\alpha$ . Interestingly, this mode is the only one not to conserve the Townes atom number. More precisely, one finds in the limit of small  $\alpha$

$$\mathcal{N} = \mathcal{N}_T + 2\alpha \underbrace{\int d^2r u(r) R_0(r)}_{<0}. \quad (\text{A.21})$$

For  $\alpha > 0$ , one finds  $\mathcal{N} < \mathcal{N}_T$ , such that the solution will be regular at all times [218]. This is not surprising since the exact solution (A.19) is regular and expands.

The previous reasoning cannot be extended to  $\alpha < 0$  since localized solutions do not exist in an inverted harmonic potential [271]. However, one can still study the behavior of an initial wave function  $R_0(r) + \alpha u(r)$  for a small  $\alpha < 0$ . This corresponds to  $\mathcal{N} > \mathcal{N}_T$  and thus an excess atom number with respect to the Townes soliton. In this case, one can show that the total energy is negative, such that this wave function will eventually collapse in a finite time, as shown by the variance identity (2.24). In fact, it is even easier to exhibit a collapsing solution initially close to the Townes soliton. To do so, one has simply to multiply the Townes soliton by a factor slightly larger than one. The energy of the corresponding profile will then be negative.

## Appendix B

# Variational method

In this appendix, we study the 2D NLSE through a Gaussian ansatz, which leads to analytical calculations and can help one get insight onto the dynamics. We first determine the total energy  $E$  as a function of the atom number  $N$  contained in the wave packet. Using the reduced notations of Subsec 3.1.1, we thus consider the static wave function

$$\phi(\mathbf{r}) = \sqrt{\frac{\mathcal{N}}{2\pi\beta}} \exp\left(-\frac{r^2}{4\beta}\right) \quad (\text{B.1})$$

with nonlinear parameter  $\mathcal{N} = |\tilde{g}|N$ . Inserting this ansatz into the energy functional

$$E[\phi] = \int d^2r \left[ \frac{1}{2} |\nabla \phi|^2 - \frac{1}{2} |\phi(\mathbf{r})|^4 \right], \quad (\text{B.2})$$

we obtain, term-by-term

$$E(\beta) = \frac{\mathcal{N}}{4\beta} - \frac{\mathcal{N}^2}{8\pi\beta}. \quad (\text{B.3})$$

Using this expression, we deduce that  $E = 0$  for a nonlinear parameter  $\mathcal{N} = 2\pi \equiv \mathcal{N}_G$ . For  $\mathcal{N} > \mathcal{N}_G$  (resp.  $\mathcal{N} < \mathcal{N}_G$ ), one deduces from the variance identity (2.24) that the RMS size of the wave packet will increase (resp. decrease). In a situation where the RMS size decreases, the profile eventually becomes singular in a finite time. We now apply a time-dependent variational method to describe approximately the 2D NLSE dynamics [203, 272]. We still consider a Gaussian density distribution, but the wave function is now time-dependent and we choose to write it as

$$\psi(\mathbf{r}, t) = \sqrt{\frac{\mathcal{N}}{2\pi\beta(t)}} \exp\left(-\frac{r^2}{4\beta(t)}\right) \exp(-i\alpha(t)r^2), \quad (\text{B.4})$$

We insert this time dependent ansatz in the Lagrangian

$$\mathcal{L}[\psi] = \int d^2r \frac{i\hbar}{2} \left( \psi^* \frac{\partial \psi}{\partial t} - \psi \frac{\partial \psi^*}{\partial t} \right) - E[\psi], \quad (\text{B.5})$$

from which the NLSE derives. After dividing by  $\mathcal{N}$ , we find

$$\mathcal{L}(\alpha, \dot{\alpha}, \beta, \dot{\beta}) = \dot{\alpha}\beta - 2\alpha^2\beta - \frac{1}{2\beta} \left( 1 - \frac{\mathcal{N}}{\mathcal{N}_G} \right). \quad (\text{B.6})$$

We now write the Euler-Lagrange equations

$$\frac{d}{dt} \left( \frac{\partial \mathcal{L}}{\partial \dot{\alpha}} \right) = \frac{\partial \mathcal{L}}{\partial \alpha} \quad \frac{d}{dt} \left( \frac{\partial \mathcal{L}}{\partial \dot{\beta}} \right) = \frac{\partial \mathcal{L}}{\partial \beta}, \quad (\text{B.7})$$

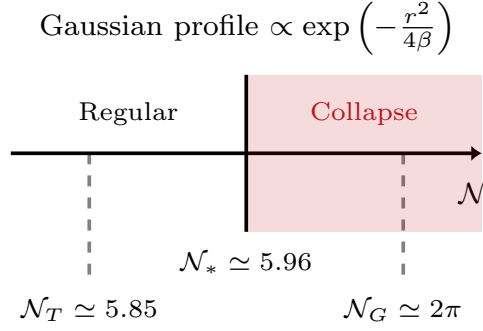


Figure B.1: Regularity domain for Gaussian initial conditions. The collapse threshold  $\mathcal{N}_G = 2\pi$  obtained from the variational method is very close to the more accurate value  $\mathcal{N}_*$ , determined numerically by Fibich & Gaeta [219].

which lead to the following differential equations

$$\dot{\beta} = -4\alpha\beta \quad \dot{\alpha} = 2\alpha^2 - \frac{1}{2} \left(1 - \frac{\mathcal{N}}{\mathcal{N}_G}\right) \frac{1}{\beta^2}. \quad (\text{B.8})$$

If we assume that the wave function is a real Gaussian at  $t = 0$ , then  $\alpha(t = 0) = 0$  and  $\beta(t = 0) = \beta_0 > 0$ . In this case, the solutions of (B.8) can be written explicitly

$$\alpha(t) = -\frac{1}{2} \frac{\gamma t}{\beta_0 + \frac{\gamma}{\beta_0} t^2} \quad \beta(t) = \beta_0 + \frac{\gamma}{\beta_0} t^2, \quad (\text{B.9})$$

with the expansion factor

$$\gamma = 1 - \frac{\mathcal{N}}{\mathcal{N}_G}. \quad (\text{B.10})$$

The evolution of the RMS size  $\sigma^2 = 2\beta$  obtained through the variational method coincides with the exact result given by the variance identity (2.24). Moreover, the variational method predicts a collapse of the wave-function (a diverging density) if and only if  $\gamma < 0$  (i.e.  $\mathcal{N} > \mathcal{N}_G$ ), with a collapse time  $t_* = \beta_0/\sqrt{|\gamma|}$  which coincides with the instant  $t_\sigma$  of zero RMS size. As indicated in Fig B.1, this is very close to the collapse threshold  $\mathcal{N}_* \simeq 5.96$  determined numerically by Fibich & Gaeta [219]. This shows the power of variational methods, even when they consist of minimal ingredients.

## Appendix C

# Anisotropic contribution of MDDI

We study qualitatively the anisotropic contribution of magnetic dipole-dipole interactions (MDDI) to the mixture studied in this thesis. We show that it is sufficient to take the (isotropic) modification of  $a_{12}$  into account for interpreting the experimental results of Chapter 4. As shown in Subsec 1.2.2, MDDI modify the interactions between components  $|1\rangle$  and  $|2\rangle$  through an additional interaction potential  $U(\mathbf{r})$ . In the following, we will consider the Fourier transform of this potential [81]

$$\tilde{U}(\mathbf{k}) = \tilde{g}_{\text{dd}} \left[ \cos^2 \Theta \left( 2 - 3\sqrt{\frac{2}{\pi}} \bar{k} e^{\bar{k}^2/2} \text{erfc}(\bar{k}/\sqrt{2}) \right) + \sin^2 \Theta \left( -1 + 3\sqrt{\frac{2}{\pi}} \frac{\bar{k}_x^2}{\bar{k}} e^{\bar{k}^2/2} \text{erfc}(\bar{k}/\sqrt{2}) \right) \right]. \quad (\text{C.1})$$

In this expression,  $\text{erfc}(x) = 1 - \text{erf}(x)$  is the complementary error function,  $\tilde{g}_{\text{dd}} = \sqrt{8\pi} a_{\text{dd}}/\ell_z$ ,  $a_{\text{dd}} = \mu_0 \mu_B^2 m / 12\pi \hbar^2 = 0.7 a_0$  is the dipolar length ( $a_0$  is the Bohr radius),  $\Theta$  is the angle between the magnetic field (contained in the  $(Oxz)$  plane) and the normal to the atomic plane,  $\ell_z$  is the vertical harmonic oscillator length, and  $\bar{\mathbf{k}} = \mathbf{k} \ell_z$ . As long as momenta  $\bar{k} \ll 1$  are involved, one can limit to the first finite-range correction to  $\tilde{U}(\mathbf{k})$

$$\tilde{U}(\mathbf{k}) \simeq \tilde{g}_{\text{dd}} \left[ 3 \cos^2 \Theta - 1 + 3\sqrt{\frac{\pi}{2}} \left( \cos^2 \Theta \bar{k} - \sin^2 \Theta \frac{\bar{k}_x^2}{\bar{k}} \right) \right]. \quad (\text{C.2})$$

In this last expression, the terms independent of  $k$  simply add to the inter-species coupling strength. The  $k$ -dependent terms break scale invariance, and the term involving  $k_x$  also breaks isotropy. In the following, we determine how much these  $k$ -dependent terms determine the properties of the ground state in our system.

### Single-component effective description

We use an effective single-component description  $\phi$  for component  $|2\rangle$ , with the reduced notations of Subsec 3.1.1 and normalizing  $\phi$  such that  $\int d^2r |\phi|^2 = N$ ,  $N$  being the atom number in state  $|2\rangle$ . Our effective description accounts for the mediated interactions (modified by MDDI) as well as the first correction to the cubic NLSE obtained for a finite depletion of the bath (see Subsec 5.2.1). For taking MDDI into account, we introduce a



momentum-dependent coupling strength  $\tilde{g}_e(\mathbf{k})$  defined as

$$\tilde{g}_e(\mathbf{k}) = \tilde{g}_{22} - \frac{(\tilde{g}_{12}^0 + \tilde{U}(\mathbf{k}))^2}{\tilde{g}_{11}} \quad (\text{C.3})$$

$$\simeq \tilde{g}_{22} - \frac{(\tilde{g}_{12}^0)^2 + 2\tilde{g}_{12}^0\tilde{U}(\mathbf{k})}{\tilde{g}_{11}} \quad (\text{C.4})$$

$$\simeq \tilde{g}_e + \tilde{g}'_e \left( \cos^2 \Theta \bar{k} - \sin^2 \Theta \frac{\bar{k}_x^2}{\bar{k}} \right) \quad (\text{C.5})$$

In this expression,  $\tilde{g}_{12}^0 = \sqrt{8\pi}a_{12}^0/\ell_z$  is defined from the 3D-bare value  $a_{12}^0$  given in Eq (1.12). Note that we assumed  $\tilde{U}(\mathbf{k}) \ll \tilde{g}_{12}^0$  to obtain the second line. Finally, we introduced

$$\tilde{g}_e = \tilde{g}_{22} - \frac{(\tilde{g}_{12}^0)^2 + 2\tilde{g}_{12}^0\tilde{g}_{\text{dd}}(3\cos^2 \Theta - 1)}{\tilde{g}_{11}} \quad \tilde{g}'_e = 3\sqrt{2\pi}\frac{\tilde{g}_{12}^0\tilde{g}_{\text{dd}}}{\tilde{g}_{11}} \quad (\text{C.6})$$

in the last line, with  $\tilde{g}_e$  the  $\Theta$ -dependent effective coupling strength considered in<sup>1</sup> Subsec 4.2.2.

### Gaussian ansatz

We will now use the following anisotropic Gaussian ansatz to describe the ground state

$$\phi(x, y) = \sqrt{\frac{N}{2\pi\sigma_x\sigma_y}} \exp \left[ -\frac{1}{4} \left( \frac{x^2}{\sigma_x^2} + \frac{y^2}{\sigma_y^2} \right) \right], \quad (\text{C.7})$$

with total atom number  $N$  and RMS sizes which we will express as  $\sigma_x = \lambda\sigma$ ,  $\sigma_y = \sigma/\lambda$ ,  $\lambda$  measuring the deviation from isotropy. The corresponding kinetic energy is given by

$$E_0 = \frac{N}{8\sigma^2} \left( \frac{1}{\lambda^2} + \lambda^2 \right). \quad (\text{C.8})$$

The interaction energy associated to Eq C.5 is more easily be computed by going to Fourier space

$$E_1 = \frac{1}{2} \int \frac{d^2k}{(2\pi)^2} \tilde{n}(\mathbf{k}) \tilde{g}_e(\mathbf{k}) \tilde{n}(-\mathbf{k}) \quad (\text{C.9})$$

$$= \frac{N^2}{8\pi\sigma^2} \left( \tilde{g}_e + \tilde{g}'_e \frac{\ell_z}{\sigma} [f_\perp(\lambda) \cos^2 \Theta + f_\parallel(\lambda) \sin^2 \Theta] \right), \quad (\text{C.10})$$

using the Fourier transform  $\tilde{n}(\mathbf{k})$  of the density profile  $n = |\phi|^2$ . In this expression, we introduced the following functions of  $\lambda$

$$f_\perp(\lambda) = \int d^2k k \exp \left[ -\left( \lambda^2 k_x^2 + \frac{k_y^2}{\lambda^2} \right) \right] \simeq \frac{\sqrt{\pi}}{2} \quad (\text{C.11})$$

$$f_\parallel(\lambda) = \int d^2k \frac{k_x^2}{k} \exp \left[ -\left( \lambda^2 k_x^2 + \frac{k_y^2}{\lambda^2} \right) \right] \simeq \frac{\sqrt{\pi}}{4} - \frac{3\sqrt{\pi}}{8} (\lambda - 1). \quad (\text{C.12})$$

<sup>1</sup>Precisely, the expression of  $\tilde{g}_e$  used in Subsec 4.2.2 differs from the quantity considered here by a negligibly small correction  $\propto \tilde{g}_{\text{dd}}^2/\tilde{g}_{11}$ .

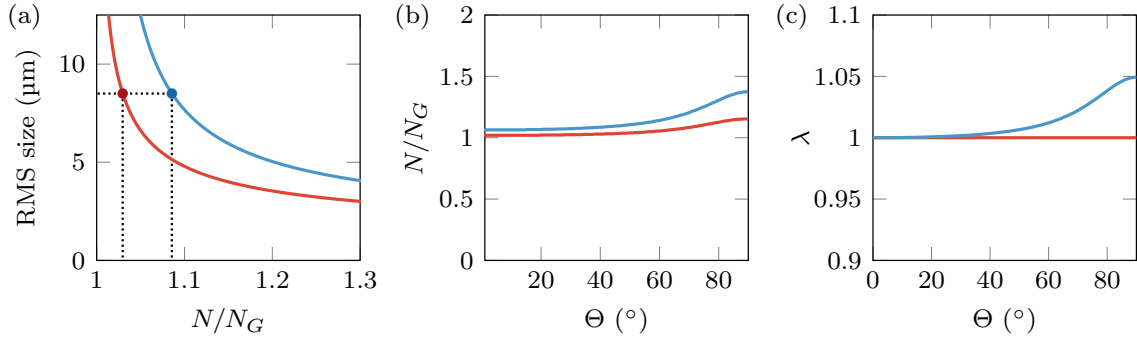


Figure C.1: (a) RMS size as a function of  $N/N_G$  for a tilt of magnetic field of  $\Theta = 37^\circ$ , deduced from minimizing  $E(\sigma, \lambda)$ . (b) Stationary atom number  $N/N_g$  with RMS size = 8.5  $\mu\text{m}$  as a function of  $\Theta$  for models (1) (blue) and (2) (red). (c) Anisotropy parameter  $\lambda$  ( $\lambda = 1$  corresponds to an isotropic Gaussian profile).

For both functions, we also gave the expansion at first order for small anisotropy  $|\lambda - 1| \ll 1$ . For the finite-depletion correction, we have to compute

$$E_2 = \frac{1}{8} \int d^2r \frac{(\nabla n)^2}{n_\infty} \quad (\text{C.13})$$

$$= \frac{N^2}{64\pi n_\infty \sigma^4} \left( \frac{1}{\lambda^2} + \lambda^2 \right). \quad (\text{C.14})$$

### Minimization and discussion

Gathering all the terms, we can now minimize the following energy functional for a given angle  $\Theta$  and an atom number  $N$

$$E(\sigma, \lambda) = E_0 + E_1 + E_2 = \frac{N}{8\sigma^2} \left\{ \left( 1 + \frac{N}{8\pi n_\infty \sigma^2} \right) \left( \frac{1}{\lambda^2} + \lambda^2 \right) + \frac{N}{\pi} \left( \tilde{g}_e + \tilde{g}'_e \frac{\ell_z}{\sigma} \left[ \frac{\sqrt{\pi}}{2} \cos^2 \Theta + \left( \frac{\sqrt{\pi}}{4} - \frac{3\sqrt{\pi}}{8} (\lambda - 1) \right) \sin^2 \Theta \right] \right) \right\}, \quad (\text{C.15})$$

with respect to the two free parameters  $(\sigma, \lambda)$ . In the following, we will compare three models

- Model (1), obtained by taking all the terms of Eq (C.15) into account.
- Model (2), without accounting for the finite-range + anisotropy corrections to  $E_1$ . In other words, by setting  $\tilde{g}'_e = 0$ . This model is analogous to the effective equation considered in Subsec 5.2.1.
- Model (3), without accounting for the finite depletion correction  $E_2$  and the finite-range + anisotropy corrections to  $E_1$ . It thus consists in using a Gaussian ansatz for the 2D NLSE with a modified  $\tilde{g}_e$ , yielding a modified stationary atom number  $N_G = 2\pi/|\tilde{g}_e|$ .

Choosing  $\Theta = 37^\circ$  for illustration, we show in Fig C.1(a) the RMS size of the ground state for the first two models<sup>2</sup>, as a function of the atom number  $N$ . How to relate this point-of-view with the study of Subsec 4.2.2? In Subsec 4.2.2, our goal was to determine the

<sup>2</sup>With our definition of  $\sigma$  in Eq (C.7), the RMS size is given by  $\sqrt{2}\sigma$ .

stationary state of the system, assuming it was approximately given by a Townes profile and had an RMS size  $\simeq 8.6 \mu\text{m}$ , i.e. the typical size we explored in the experiment. To do so, we looked for the atom number  $N$  which canceled the expansion coefficient  $\gamma$ .

Using the variational approach developed here, we can do the same assuming the ground state is approximately given by a Gaussian distribution<sup>3</sup>. In Fig C.1(b), we show the modification of  $N$  with respect to  $N_G$  for the first two models, when imposing an RMS size of  $8.6 \mu\text{m}$ . In Fig C.1(c), we show the corresponding anisotropy parameter  $\lambda$ . From this, we deduce that the deviation of  $N/N_G$  for models (1) and (2) from the simplest effective model (3) is  $\lesssim 10 \%$  for all values of  $\Theta < 50^\circ$  as we explored in Subsec 5.2.1. Even for  $\Theta = 90^\circ$ , the expected anisotropy is  $\lambda \simeq 5 \%$ , which would be challenging to detect experimentally.

## Outlook

Let us mention that the anisotropic contribution of MDDI might be detectable through the adiabatic preparation of the ground state, as proposed at the end of Subsec 5.2.1. Moreover, the isotropic and anisotropic contributions to the spin bubble state could be studied separated by applying a magnetic field rotating around the axis orthogonal to the atomic plane, as recently demonstrated by Tang et al. [273]. This would cancel the anisotropic contribution of MDDI without affecting the correction to the inter-species scattering length. On a broader perspective, it would be interesting to consider such a problem in the case of highly-magnetic atoms, such as Dysprosium or Erbium [83]. In 3D, the shape of a single-component trapped gas of highly-magnetic dipolar atoms has been modified by tuning the orientation of a static magnetic field [274, 275].

---

<sup>3</sup>We remind that the Gaussian profile is not a stationary of the equation of motion, in particular for the simple 2D NLSE. However, as shown in Appendix B and in Fig 4.8, the atom number for which  $\gamma$  cancels gives a good estimate of the Townes atom number.

## Appendix D

# Perturbative expansions for data analysis

In this appendix, we develop perturbatively the nonlinear Schrödinger equation to obtain fitting functions for the data presented in Chapter 4. We study the evolution of initial Townes profiles (Subsec D.1) and Gaussian profiles (Subsec D.2).

### D.1 Dynamics of Townes profiles

We use time-dependent perturbation theory to extract a suitable fitting function for the deformation of the Townes density profile. We use the reduced notations of Subsec 3.1.1 and consider the evolution of a Townes-shaped wave function  $\psi$  with nonlinear parameter  $\mathcal{N}$  under the time-dependent NLSE

$$i\frac{\partial\psi}{\partial t} = -\frac{1}{2}\nabla^2\psi - |\psi|^2\psi. \quad (\text{D.1})$$

From Subsec 3.2.1, we know that the stationary solution of Eq. (D.1) with chemical potential  $\mu = -1$  is given by  $R_0(r)e^{it}$ , with a nonlinear parameter  $\mathcal{N} = \mathcal{N}_T$ <sup>1</sup>. We consider a wave function  $\psi$  proportional to the Townes profile  $R_0(r)$  at  $t = 0$ , but with an interaction parameter  $\mathcal{N}$  that is slightly different from  $\mathcal{N}_T$ . We define the small parameter of the expansion  $\eta$  such that  $\mathcal{N} = (1 + \eta)\mathcal{N}_T$ . At short times, the deformation of the wave function with respect to the Townes profile is expected to be small, and we can expand the solution with respect to  $\eta$

$$\phi(r, t) = [R_0(r) + \eta\epsilon(r, t) + \dots] e^{it}. \quad (\text{D.2})$$

We restrict here to the first-order correction in  $\eta$ , and consider the first terms of the Taylor expansion of  $\epsilon(r, t)$  with respect to  $\tau$

$$\epsilon(r, t) = \epsilon_0(r) + \epsilon_1(r)t + \epsilon_2(r)t^2 + \dots \quad (\text{D.3})$$

The initial condition gives directly  $\epsilon_0(r) = R_0(r)$ , and by injecting the expansion given in Eq. (D.3) in Eq. (D.1), we identify

$$\begin{aligned} \epsilon_1(r) &= iR_0^3(r) \\ \epsilon_2(r) &= \frac{1}{2} \left( 1 - \frac{1}{2}\nabla^2 - R_0^2 \right) R_0^3. \end{aligned} \quad (\text{D.4})$$

---

<sup>1</sup>The results we derive here can be extended to other values of  $\mu$  by dilations, due to the scale invariance of Eq (D.1).

Interestingly, this last identity can be further simplified using the equation (A.10) verified by the Townes soliton  $R_0$ , and we obtain

$$\epsilon_2(r) = \left( R_0^5 - R_0^3 - \frac{3}{2} R_0 R_0'^2 \right). \quad (\text{D.5})$$

When computing the density profile  $n(r, t) = |\psi(r, t)|^2$ , only the real term  $\epsilon_2$  contributes at first order in  $\eta$  (the imaginary term  $\epsilon_1$  contributes to the phase of the wave function). We deduce the expected deformation of the density profile at first order and at short times

$$\begin{aligned} \delta n(r, t) &= n(r, t) - n(r, 0) \\ &\simeq 2\eta R_0(r) \epsilon_2(r) t^2 \equiv \eta \chi(r) t^2, \end{aligned} \quad (\text{D.6})$$

where we have defined  $\chi(r) = 2R_0(r)\epsilon_2(r)$ . We checked that the 2D integral of  $\chi$  is zero, as the norm of  $\psi$  should be conserved by the evolution under Eq. (D.1).

## D.2 Dynamics of Gaussian profiles

For a family of profiles which are not stationary for any  $\mathcal{N}$ , one cannot duplicate the previous method. This applies for instance to the dynamics of Gaussian profiles which we study hereafter. To determine how an initial Gaussian profile

$$\psi(\mathbf{r}, t=0) = G(r) = \sqrt{\frac{\mathcal{N}}{2\pi\sigma^2}} \exp\left(-\frac{r^2}{4\sigma^2}\right) \quad (\text{D.7})$$

is deformed, we expand the evolved density profile at short times  $t$

$$n(\mathbf{r}, t) = |\psi(\mathbf{r}, t)|^2 \simeq n(\mathbf{r}, 0) + \left(\frac{\partial n}{\partial t}\right)_{t=0} t + \left(\frac{\partial^2 n}{\partial t^2}\right)_{t=0} \frac{t^2}{2}. \quad (\text{D.8})$$

Since the initial condition is real, one immediately shows that<sup>2</sup>

$$\left(\frac{\partial n}{\partial t}\right)_{t=0} = 2\text{Re} \left[ \psi(\mathbf{r}, 0) \left(\frac{\partial \psi}{\partial t}\right)_{t=0} \right] = 0 \quad (\text{D.9})$$

using Eq (A.1), with  $\text{Re}(\cdot)$  corresponding to the real part. On the other hand, we obtain

$$\frac{1}{2} \left(\frac{\partial^2 n}{\partial t^2}\right)_{t=0} = \left| \left(\frac{\partial \psi}{\partial t}\right)_{t=0} \right|^2 + \text{Re} \left[ \psi(\mathbf{r}, 0) \left(\frac{\partial^2 \psi}{\partial t^2}\right)_{t=0} \right] \quad (\text{D.10})$$

$$= \frac{\mathcal{N}}{16\pi\sigma^6} \left[ \left(\frac{r^2}{\sigma^2} - 2\right) e^{-\frac{r^2}{2\sigma^2}} - \frac{4\mathcal{N}}{\pi} \left(\frac{r^2}{\sigma^2} - 1\right) e^{-\frac{r^2}{\sigma^2}} \right] \quad (\text{D.11})$$

such that the deformation  $n(\mathbf{r}, t) - n(\mathbf{r}, 0)$  evolves initially quadratically with time. The first term with parenthesis is associated to the linear part of the 2D NLSE, while the second term is generated by the nonlinear cubic term. Eventually, we use the following function for fitting the deformation and determining the RMS size of the data used in Subsec 4.2.2

$$\chi_G(r) = A \left[ \left(\frac{r^2}{\sigma^2} - 2\right) e^{-\frac{r^2}{2\sigma^2}} + B \left(\frac{r^2}{\sigma^2} - 1\right) e^{-\frac{r^2}{\sigma^2}} \right], \quad (\text{D.12})$$

with fitting parameters  $A$ ,  $B$  and  $\sigma$ .

<sup>2</sup>This is obtained from the continuity equation written in Eq (2.22), since the velocity field is then zero.

## Appendix E

# Numerical recipes for the 2D NLSE

### E.1 Resolution in 2D

In this appendix, we summarize the ingredients we used for implementing 2D NLSE simulations [276, 277]. We present the algorithm for a single component, but the generalization to a two-component system is immediate. We consider a time-dependent field  $\psi(x, y, t)$  on a square domain  $\Sigma$  of side  $L$ , normalized to the total atom number such that

$$\int_{\Sigma} d^2r |\psi(x, y, t)|^2 = N. \quad (\text{E.1})$$

For convenience, we use periodic boundary conditions

$$\psi(x + L, y, t) = \psi(x, y + L, t) = \psi(x, y, t). \quad (\text{E.2})$$

The field can be expanded as a Fourier series

$$\psi(\mathbf{r}, t) = \frac{1}{L} \sum_{\mathbf{q} \in \mathbb{Z}^2} \exp\left(i \frac{2\pi}{L} \mathbf{r} \cdot \mathbf{q}\right) \phi_{\mathbf{q}}(t), \quad (\text{E.3})$$

which can be inverted to express the Fourier coefficients  $\phi_{\mathbf{q}}(t)$  as

$$\phi_{\mathbf{q}}(t) = \frac{1}{L} \int_{\Sigma} d^2\mathbf{r} \exp\left(-i \frac{2\pi}{L} \mathbf{r} \cdot \mathbf{q}\right) \psi(\mathbf{r}, t) \quad \mathbf{q} \in \mathbb{Z}^2. \quad (\text{E.4})$$

For completeness, note that the Fourier coefficients of  $\nabla_{\mathbf{r}}\psi$  are given by  $\left[i \frac{2\pi}{L} \mathbf{q} \phi_{\mathbf{q}}(t)\right]_{\mathbf{q} \in \mathbb{Z}^2}$  using this convention, and that the Parseval-Plancherel equality writes

$$\int_{\Sigma} d^2r |\psi(\mathbf{r})|^2 = \sum_{\mathbf{q} \in \mathbb{Z}^2} |\phi_{\mathbf{q}}(t)|^2. \quad (\text{E.5})$$

### Discretization in space and time

For 2D simulations, we sample the fields  $\psi$  on a square lattice with  $N_s^2$  sites. We will use the index  $j_x$  and  $j_y$  (and the vector notation  $\mathbf{j} = (j_x, j_y)$  for compactness) such that

$$x_{j_x} = \frac{L}{N_s} j_x, \quad y_{j_y} = \frac{L}{N_s} j_y, \quad 0 \leq j_x, j_y \leq N_s \quad (\text{E.6})$$

considering that  $x_L = x_0$ ,  $y_L = y_0$  due to periodic boundary conditions. We thus get a physical lattice spacing  $d\ell \equiv L/N_s$ . For a system with typical density  $n$  and dimensionless coupling strength  $\tilde{g}$ , the characteristic length scale associated to the field  $\psi$  is the healing length  $\xi = 1/\sqrt{2\tilde{g}n}$ . Sampling the field  $\psi$  correctly in this region requires maintaining  $d\ell \leq \xi$ . We also discretize the time evolution of the field. Fixing a distance  $d\ell$  brings characteristic time and energy scales given by

$$t_0 \equiv \frac{m(d\ell)^2}{\hbar} \quad E_0 \equiv \hbar \frac{2\pi}{t_0} = \frac{2\pi\hbar^2}{m(d\ell)^2}. \quad (\text{E.7})$$

We will thus express the time  $t$  in the dimensionless form  $\tau = t/t_0$ , with time-step  $d\tau$ . We also express  $\psi$  in a dimensionless form by forming

$$\Psi_{\mathbf{j}} = \frac{1}{\sqrt{n}} \psi(x_{j_x}, y_{j_y}) \quad n \equiv \frac{N}{\ell^2}, \quad (\text{E.8})$$

$n$  being the averaged density. The normalization condition (E.1) now writes

$$\sum_{\mathbf{j} \in \llbracket 0, N_s-1 \rrbracket^2} |\Psi_{\mathbf{j}}|^2 = N_s^2. \quad (\text{E.9})$$

The discrete Fourier transform of  $\Psi_{\mathbf{j}}$  is defined as

$$\Phi_{\mathbf{q}} = \frac{1}{L} \sum_{\mathbf{j} \in \llbracket 0, N_s-1 \rrbracket^2} \exp\left(-i \frac{2\pi}{N_s} \mathbf{j} \cdot \mathbf{q}\right) \Psi_{\mathbf{j}} \simeq \frac{N_s}{\sqrt{N}} \phi_{\mathbf{q}}, \quad (\text{E.10})$$

with  $\mathbf{q} \in \llbracket -N_s/2 + 1, \dots, N_s/2 \rrbracket^2$  for  $N_s$  even, corresponding to the First Brillouin Zone (FBZ)<sup>1</sup>. The inverse transformation writes

$$\Psi_{\mathbf{j}} = \frac{1}{N_s} \sum_{\mathbf{q} \in \text{FBZ}} \exp\left(i \frac{2\pi}{N_s} \mathbf{j} \cdot \mathbf{q}\right) \Phi_{\mathbf{q}}. \quad (\text{E.11})$$

### Split-step method

We solve the NLSE (A.1) using the time split-step algorithm. First, let us have a look at the linear Schrödinger equation

$$i\hbar \frac{\partial \psi}{\partial t} = \hat{H}\psi = \left(-\frac{\hbar^2}{2m} \nabla^2 + V(\mathbf{r})\right) \psi \quad \psi(t=0) = \psi_0 \quad (\text{E.12})$$

whose solutions can be written as

$$\psi(t) = \hat{U}_0(t) \psi_0 \quad \hat{U}_0(t) = \exp\left(-i \frac{\hat{H}t}{\hbar}\right). \quad (\text{E.13})$$

The evolution operator  $\hat{U}_0$  has a simple composition property

$$\hat{U}_0(k dt) = \hat{U}_0(dt)^k \quad k \in \mathbb{Z}. \quad (\text{E.14})$$

---

<sup>1</sup>Why choosing the FBZ? Periodic boundary conditions on  $\psi$  impose an infra-red cut-off and a discretization of  $\mathbf{q}$ -vectors, as expressed in the Fourier series (E.3). All  $\mathbf{q}$ -vectors are defined modulo- $N_s$ , and at this stage all labeling of  $\mathbf{q}$  modulo- $N_s$  are equivalent. For example, one could choose  $\mathbf{q} \in \llbracket 0, \dots, N_s-1 \rrbracket^2$  instead of using the FBZ. However, the best interpolation to the fields derived from  $\psi$  – like its gradient or its laplacian – are given by the FBZ labeling. Choosing the FBZ labelling is thus necessary for computing the kinetic energy, for instance.

The Hamiltonian  $\hat{H}$  is made of two terms which do not commute, so that the exponential cannot be expanded *a priori*. However, for a small enough time interval  $dt$ , one can neglect the error in splitting the two terms and write

$$\hat{U}_0(dt) = \exp \left[ -\frac{i}{\hbar} \left( \frac{\hat{p}^2}{2m} + \hat{V} \right) dt \right] \simeq \exp \left( -\frac{i}{\hbar} \frac{\hat{p}^2}{2m} dt \right) \exp \left( -\frac{i\hat{V}}{\hbar} dt \right), \quad (\text{E.15})$$

using Trotter's product formula. For the NLSE, we extend this time split-step method and apply an infinitesimal time-evolution operator defined by

$$\hat{U}(dt) = \exp \left( -\frac{i}{\hbar} \frac{\hat{p}^2}{2m} dt \right) \exp \left[ -\frac{i}{\hbar} \left( \hat{V} + \frac{\hbar^2}{m} \tilde{g} |\psi|^2 \right) dt \right], \quad (\text{E.16})$$

which depends explicitly on the field  $\psi$  through the last non-linear term.

### Algorithm

We now turn to dimensionless fields and explicitly write the split-step algorithm. Starting from a field  $\Psi_j(\tau_0)$ , we first evolve in real-space for an infinitesimal time  $d\tau$ , using only the potential  $V_j$  (possibly depending on time) and the interaction term. We write the corresponding part of the NLSE in a dimensionless form

$$i \frac{\partial \Psi_j}{\partial \tau} = \left( \tilde{V}_j + G |\Psi_j|^2 \right) \Psi_j \quad \tilde{V}_j \equiv \frac{m(d\ell)^2}{\hbar^2} V_j \quad G \equiv \frac{N}{N_s^2} \tilde{g}. \quad (\text{E.17})$$

and first compute the auxiliary field

$$\Psi'_j = \exp \left[ -i \left( \tilde{V}_j(\tau_0) + G |\Psi_j(\tau_0)|^2 \right) d\tau \right] \Psi_j(\tau_0). \quad (\text{E.18})$$

Then, we write the evolution due to the kinetic term only in Fourier space

$$i \frac{\partial \Phi_{\mathbf{q}}}{\partial \tau} = \frac{1}{2} \left( \frac{2\pi \mathbf{q}}{N_s} \right)^2 \Phi_{\mathbf{q}}, \quad (\text{E.19})$$

and compute the evolved field using the Fourier transform  $\Phi'_{\mathbf{q}}$  of  $\Psi'_j$

$$\Phi_{\mathbf{q}}(\tau_1) = \exp \left[ -\frac{i}{2} \left( \frac{2\pi \mathbf{q}}{N_s} \right)^2 d\tau \right] \Phi'_{\mathbf{q}}, \quad (\text{E.20})$$

before returning to real space to obtain  $\Psi_j(\tau_1)$ . Arbitrary evolution times are performed by iterating the procedure<sup>2</sup>.

In order to compute the ground state of a given NLSE energy functional, we use an *evolution with imaginary time* given by the substitution  $t \rightarrow -it$ . The algorithm is very similar to the real-time evolution. If the initial state used for this evolution has a non-zero overlap with the ground state, then the evolution should converge toward the ground state. However, the evolution not being unitary, the atom number is not conserved by these operations. Therefore, one needs to renormalize the field  $\Psi_j$  after each step, using condition (E.9) in order to maintain a constant atom number.

<sup>2</sup>In order to control the error made by splitting the exponential evolution operation, one should keep the argument of the exponential low enough. Such a condition on  $d\tau$  depends on the potential landscape for the potential energy, but we can express it for the interaction and kinetic energy term, respectively

$$G |\Psi_j|^2 d\tau \sim G d\tau \ll 1 \quad \frac{1}{2} \left( \frac{2\pi}{N_s} \right)^2 \mathbf{q}^2 d\tau \leq \frac{\pi^2}{2} d\tau \ll 1, \quad (\text{E.21})$$

so that we need to satisfy simultaneously  $d\tau \ll 1/G$ , and  $d\tau \ll 2/\pi^2$ .



## E.2 Using radial coordinates

We now turn to the resolution of the NLSE (A.1) using radial coordinates, assuming rotational invariance around the origin  $\mathbf{r} = 0$ . This allows us to map the 2D problem to a 1D problem and should speed up the algorithm. If we use a split-step method, evolving the field with the real space terms of the equation is still straightforward. However, the kinetic term is not as simple to manipulate. Indeed, the evolution in Fourier space (E.19) was easily implemented because the plane waves  $\exp(i\mathbf{q} \cdot \mathbf{r})$  are eigenfunctions of the Laplacian operator in 2D. Thus, the infinitesimal kinetic evolution operator (E.19) was diagonal in the Fourier basis. This is not true when considering only the radial part of the Laplacian.

### Bessel functions and Hankel transform

The eigen-functions of the radial Laplacian operator are obtained using the functions zeroth-order Bessel function of the first kind  $J_0(qr)$ , with  $J_0$  verifying

$$\Delta J_0 = J_0''(r) + \frac{1}{r}J_0'(r) = -J_0(r), \quad (\text{E.22})$$

corresponding to the eigenvalue  $-1$  for the Laplacian. Owing to the spectral theorem, the family  $\{r \mapsto J_0(qr)\}_{q \in \mathbb{R}^+}$  forms a basis of  $r$ -dependent functions that are sufficiently regular. Our approach is based on the work of Baddour [278]. We start by introducing the Hankel transform – or Bessel-Fourier transform – of a function  $f(r)$  defined on  $[0, +\infty[$  and sufficiently regular

$$F(\rho) = \int_0^{+\infty} f(r) J_0(\rho r) r \, dr. \quad (\text{E.23})$$

This transformation can be inverted<sup>3</sup>

$$f(r) = \int_0^{+\infty} F(\rho) J_0(\rho r) \rho \, d\rho, \quad (\text{E.25})$$

which allows us to go from one representation to the other. Our goals are two-fold.

1. Formulate the Hankel transformations for compact support functions.
2. Discretize these transformations.

### Discrete Hankel transform

We start with point (1). We restrict the basis of  $J_0$  functions by limiting to functions  $f$  that are defined on  $[0, R]$ , with  $f(R) = 0$ . In particular, this means that the system is defined on a disk of radius  $R$  with strict boundary conditions at  $r = R$  – using periodic boundary conditions would not make sense for a radial grid. We have the exact series expansion

$$f(r) = \sum_{k=1}^{+\infty} \hat{f}_k J_0\left(\frac{j_k r}{R}\right), \quad (\text{E.26})$$

---

<sup>3</sup>This is readily verified by using the definition of  $J_0(r)$  as an integral

$$J_0(r) = \frac{1}{2\pi} \int_0^{2\pi} e^{ir \cos(\theta)} d\theta. \quad (\text{E.24})$$

where  $j_k$  is the  $k$ -th zero of  $J_0$ . The  $\hat{f}_k$ 's are the coefficients of the decomposition on the discrete basis  $\{r \mapsto J_0(j_k r/R)\}_{k \in \mathbb{N}^*}$ . In terms of the Hankel transform  $F$  of  $f$ , these coefficients write<sup>4</sup>

$$\hat{f}_k = \frac{2}{R^2 J_1^2(j_k)} F\left(\frac{j_k}{R}\right), \quad (\text{E.28})$$

where  $J_1$  is the first-order Bessel function. If we denote  $\rho_k = j_k/R$  the sampling points of the Hankel transform  $F$ , and  $F_k = F(\rho_k)$  its values, then the series expansion (E.26) writes

$$f(r) = \frac{2}{R^2} \sum_{k=1}^{+\infty} \frac{F_k}{J_1^2(j_k)} J_0\left(\frac{j_k r}{R}\right). \quad (\text{E.29})$$

The action of the Laplacian is determined using (E.22)

$$\Delta f = \frac{2}{R^2} \sum_{k=1}^{+\infty} \frac{F_k}{J_1^2(j_k)} \left(-\frac{j_k^2}{R^2}\right) J_0\left(\frac{j_k r}{R}\right). \quad (\text{E.30})$$

such that the coefficients  $F_k$  are multiplied by  $-j_k^2/R^2$ .

### Discrete grid on the radial axis

We now turn to point (2). We need to discretize  $f$  on a grid of size  $N_s \in \mathbb{N}$  lying in  $[0, R]$ . We will choose the following sampling points<sup>5</sup>

$$r_m = \frac{j_m}{\pi}, \quad m \in \llbracket 1, N_s \rrbracket, \quad (\text{E.32})$$

and impose  $R = j_{N_s+1}/\pi$  as a boundary. The series expansion (E.29) at position  $r_m$  writes

$$f_m \equiv f(r_m) = \frac{2}{R^2} \sum_{k=1}^{+\infty} \frac{F_k}{J_1^2(j_k)} J_0\left(\frac{j_k r_m}{R}\right). \quad (\text{E.33})$$

To manipulate such expressions numerically, we restrict this sum to a finite number of  $k$  values (the first  $N_s$  ones). This is legitimate if the function  $f$  varies slowly between successive sampling points  $r_m$ . We thus introduce the approximate expansion

$$f_m = \frac{\pi}{R} \sum_{k=1}^{N_s} Y_{mk} F_k \quad Y_{mk} = \frac{2}{\pi R} \frac{1}{J_1^2(j_k)} J_0\left(\frac{j_k r_m}{R}\right), \quad (\text{E.34})$$

where we introduced the matrix  $Y$  of size  $N_s \times N_s$  [278]. When  $N_s$  goes to infinity,  $Y$  tends to its own inverse. By contrast with the discrete Fourier transform, this is not exact for finite  $N_s$ . However, we will still use the approximate inverse transformation

$$F_k = \frac{R}{\pi} \sum_{m=1}^{N_s} Y_{km} f_m. \quad (\text{E.35})$$

---

<sup>4</sup>This is a consequence of the following relation

$$\int_0^1 J_0(x j_m) J_0(x j_n) x \, dx = \delta_{mn} \frac{J_1^2(j_k)}{2} \quad (\text{E.27})$$

<sup>5</sup>The asymptotic behavior of  $J_0$  being

$$J_0(r) \sim \sqrt{\frac{1}{2\pi r}} \cos\left(r - \frac{\pi}{4}\right), \quad (\text{E.31})$$

its zeros are approximately given by  $j_m \simeq m\pi - \pi/4$ . On thus obtains  $r_m \simeq m - 1/4$ .

### Application to the split-step algorithm

Using these transformations, we determine the action of the kinetic energy evolution term on the field  $\Psi(r)$ . We denote its discretized version  $\Psi_m = \Psi(r_m)$ , and its Fourier-Bessel coefficients  $\Phi_k$ . First, let us notice that

$$e^{i(d\tau/2)\Delta} J_0 \left( \frac{j_k r}{R} \right) = e^{-ij_k^2 d\tau/(2R^2)} J_0 \left( \frac{j_k r}{R} \right), \quad (\text{E.36})$$

so that we can compute

$$e^{i(d\tau/2)\Delta} \Psi(r) \simeq \frac{2}{R^2} \sum_{k=1}^L \frac{\Phi_k}{J_1^2(j_k)} \left[ e^{i(d\tau/2)\Delta} J_0 \left( \frac{j_k r}{R} \right) \right] \quad (\text{E.37a})$$

$$= \frac{2}{R^2} \sum_{k=1}^{N_s} \frac{\Phi_k}{J_1^2(j_k)} J_0 \left( \frac{j_k r}{R} \right) e^{-ij_k^2 d\tau/(2R^2)} \quad (\text{E.37b})$$

$$\simeq \frac{2}{\pi R} \sum_{m=1}^{N_s} \sum_{k=1}^L Y_{km} \frac{\Psi_m}{J_1^2(j_k)} J_0 \left( \frac{j_k r}{R} \right) e^{-ij_k^2 d\tau/(2R^2)}. \quad (\text{E.37c})$$

Using the following relation

$$\frac{2}{\pi R} \frac{1}{J_1^2(j_k)} J_0 \left( \frac{j_k r_{m'}}{R} \right) = Y_{m'k}, \quad (\text{E.38})$$

we evaluate the left-hand side of equation (E.37a) at  $r_{m'}$  and find

$$\left[ e^{i(d\tau/2)\Delta} \Psi \right]_{m'} = \sum_{m=1}^{N_s} \sum_{k=1}^{N_s} Y_{m'k} Y_{km} e^{-ij_k^2 d\tau/(2R^2)} \Psi_m. \quad (\text{E.39})$$

We will thus perform evolution under the kinetic term without going to Bessel-Fourier space. Instead, we will use a matrix multiplication in real-space

$$\Psi_{m'}(t_{n+1}) = \sum_{m=1}^{N_s} K_{m'm} \Psi'_m, \quad (\text{E.40})$$

using the auxiliary field  $\Psi'$  obtained at time  $t_n$  from  $\Psi(t_n)$ , where the matrix  $K$  has been defined as

$$K_{m'm} = \sum_{k=1}^{N_s} Y_{m'k} Y_{km} \exp \left( -i \frac{j_k^2 d\tau}{2R^2} \right). \quad (\text{E.41})$$

Note that the matrices  $Y$  and  $K$  are computed once for all at the beginning of the algorithm. Since this operation involves matrices of size  $N_s \times N_s$ , the corresponding calculation time is still quadratic with the size  $N_s$  of the system, like for the 2D case. Although the scaling with  $N_s$  is *a priori* unchanged, the time need to compute the evolution for a same size is decreased by a factor  $\gtrsim 5$  with respect to the 2D case.

## Appendix F

# Induced interactions

We study the interactions between two impurity atoms induced by a uniform BEC [232]. We consider a 2D geometry at zero temperature, but most results can be generalized to a 3D situation. For simplicity, the impurities do not interact with each other. Still, they interact with the atoms forming the BEC. These interactions are characterized by a coupling strength  $\tilde{g}_{12}$ , whereas interactions among the BEC atoms are characterized by  $\tilde{g}_{11} > 0$ . For a BEC described by the bosonic field operators  $\hat{\Psi}(\mathbf{r})$ ,  $\hat{\Psi}^\dagger(\mathbf{r})$ , the inter-species interaction part of the Hamiltonian writes

$$\hat{H}_{12} = \frac{\hbar^2}{m} \tilde{g}_{12} \left[ \hat{\Psi}^\dagger(\hat{\mathbf{R}}_a) \hat{\Psi}(\hat{\mathbf{R}}_a) + \hat{\Psi}^\dagger(\hat{\mathbf{R}}_b) \hat{\Psi}(\hat{\mathbf{R}}_b) \right]. \quad (\text{F.1})$$

Here, the  $\hat{\mathbf{R}}_{a,b}$  denote the position operators of each impurity. Although the contact potential in Eq (F.1) is generically ill-defined, we will see in the following that it leads to well-defined perturbative calculations. We first determine the perturbation caused by a single impurity immersed in a BEC (Sec F.1), and then compute the effective potential energy of two impurities (Sec F.2).

### F.1 A single impurity

First, let us determine the perturbation on the BEC density distribution caused by the presence of a single impurity. For simplicity, the impurity is assumed to have an infinite mass. As a consequence, it is not subject to any dynamics and remains fixed at a position  $\mathbf{R}_a = 0$ . This impurity thus solely modifies the structure of the underlying BEC through the potential

$$\hat{V}_a = \frac{\hbar^2}{m} \tilde{g}_{12} \hat{n}(\mathbf{0}). \quad (\text{F.2})$$

#### Bogoliubov's approximation

To compute the effect of this perturbation on the BEC, we use Bogoliubov's approximation [89]. We decompose the field operator  $\hat{\Psi}(\mathbf{r})$  as

$$\hat{\Psi}(\mathbf{r}) \simeq \sqrt{n_0} + \delta\hat{\Psi}(\mathbf{r}) = \sqrt{n_0} + \sum_{\mathbf{k} \neq 0} \hat{a}_{\mathbf{k}} \frac{e^{i\mathbf{k} \cdot \mathbf{r}}}{\sqrt{L^2}}, \quad (\text{F.3})$$

where  $n_0$  is the condensate density, and  $\hat{a}_{\mathbf{k}}$  is the operator annihilating a particle in the single-particle state with wave function  $e^{i\mathbf{k} \cdot \mathbf{r}}/\sqrt{L^2}$  ( $L^2$  is the area of the system). Let us

first forget about the interaction with the impurity. Neglecting terms involving more than two  $\hat{a}_{\mathbf{k}}, \hat{a}_{\mathbf{k}}^\dagger$  (with  $\mathbf{k} \neq 0$ ), we diagonalize the Hamiltonian for component  $|1\rangle$  by introducing the new bosonic operators  $\hat{b}_{\mathbf{k}}, \hat{b}_{\mathbf{k}}^\dagger$  such that

$$\hat{a}_{\mathbf{k}} = u_{\mathbf{k}} \hat{b}_{\mathbf{k}} + v_{\mathbf{k}} \hat{b}_{-\mathbf{k}}^\dagger \quad u_{\mathbf{k}}, v_{\mathbf{k}} = \pm \left( \frac{k^2 + 2\tilde{g}_{11}n_0}{2k\sqrt{k^2 + 4\tilde{g}_{11}n_0}} \pm \frac{1}{2} \right)^{1/2}. \quad (\text{F.4})$$

These correspond to quasi-particle excitations carrying an energy quantum  $\hbar\omega_{\mathbf{k}}$  given by

$$\hbar\omega_{\mathbf{k}} = \frac{\hbar^2 k}{2m} \sqrt{k^2 + 4\tilde{g}_{11}n_0}. \quad (\text{F.5})$$

The ground state  $|\Phi_0\rangle$  of the system (with energy  $E_0$ ) is then found as the vacuum of quasi-particles, i.e.  $\hat{b}_{\mathbf{k}}|\Phi_0\rangle$ . We also denote  $|\Phi_{\mathbf{k}}\rangle = \hat{b}_{\mathbf{k}}^\dagger|\Phi_0\rangle$ , the excited state containing a single quasi-particle (with  $\mathbf{k} \neq 0$ ), with energy  $E_{\mathbf{k}} = E_0 + \hbar\omega_{\mathbf{k}}$ .

### Perturbation of the bath

We compute the modified ground state  $|\Phi'_0\rangle$  at first order in perturbation theory. To do so, we only take into account the excited states with at most one elementary excitation. The perturbed ground state then writes

$$|\Phi'_0\rangle = |\Phi_0\rangle + |\delta\Phi_0\rangle = |\Phi_0\rangle + \sum_{\mathbf{k} \neq 0} \frac{\langle \Phi_{\mathbf{k}} | \hat{V}_a | \Phi_0 \rangle}{E_0 - E_{\mathbf{k}}} |\Phi_{\mathbf{k}}\rangle, \quad (\text{F.6})$$

with the following matrix elements

$$\langle \Phi_{\mathbf{k}} | \hat{V}_a | \Phi_0 \rangle = \frac{\hbar^2}{m} \tilde{g}_{12} \sqrt{\frac{n_0}{L^2}} (u_{\mathbf{k}} + v_{\mathbf{k}}). \quad (\text{F.7})$$

We now compute the modified density distribution

$$\langle \hat{n}(\mathbf{r}) \rangle = \langle \Phi'_0 | \hat{n}(\mathbf{r}) | \Phi'_0 \rangle = \|\sqrt{n_0}|\Phi_0\rangle + \delta\Psi^\dagger|\Phi_0\rangle + \sqrt{n_0}|\delta\Phi_0\rangle\|^2 \quad (\text{F.8})$$

By developing the second and third terms of this expression via Eqs (F.4, F.3, F.6) and using Pythagore's theorem, one obtains

$$\langle \hat{n}(\mathbf{r}) \rangle = n_0 + \sum_{\mathbf{k} \neq 0} \left| \langle \Phi_{\mathbf{k}} | \delta\Psi^\dagger | \Phi_0 \rangle + \sqrt{n_0} \langle \Phi_{\mathbf{k}} | \delta\Phi_0 \rangle \right|^2 \quad (\text{F.9})$$

$$= n_0 + \sum_{\mathbf{k} \neq 0} \left| \frac{e^{i\mathbf{k} \cdot \mathbf{r}}}{\sqrt{L^2}} v_{\mathbf{k}} - \frac{\hbar^2}{m} \tilde{g}_{12} \frac{n_0}{\sqrt{L^2}} \frac{u_{\mathbf{k}} + v_{\mathbf{k}}}{\hbar\omega_{\mathbf{k}}} \right|^2. \quad (\text{F.10})$$

In this last expression, developing the modulus square yields three sums. One of them is independent of the perturbation and simply adds a contribution  $n'$  to the condensate density  $n_0$ . This is the celebrated *quantum depletion*. Another is quadratic with respect to the parameter  $\tilde{g}_{12}$  and must be neglected at first order. The interesting term is thus the crossed term. It is also the only one which depends on the position  $\mathbf{r}$ . By taking the continuum limit and substituting the sum on the wave vectors  $\sum_{\mathbf{k} \neq 0}$  by the integral  $\int d^2k \left(\frac{L}{2\pi}\right)^2$ , we can rewrite this defect in the density profile as

$$\delta n(\mathbf{r}) = -\frac{\hbar^2}{m} \tilde{g}_{12} \frac{n_0}{L^2} \int d^2k \left(\frac{L}{2\pi}\right)^2 \frac{v_{\mathbf{k}}(u_{\mathbf{k}} + v_{\mathbf{k}})}{\hbar\omega_{\mathbf{k}}} 2 \cos(\mathbf{k} \cdot \mathbf{r}) \quad (\text{F.11})$$

$$= -\frac{2}{\pi} \tilde{g}_{12} n_0 \int_0^{+\infty} k dk \frac{J_0(kr)}{(1 + u_{\mathbf{k}}/v_{\mathbf{k}})(k^2 + 4\tilde{g}_{11}n_0)}, \quad (\text{F.12})$$

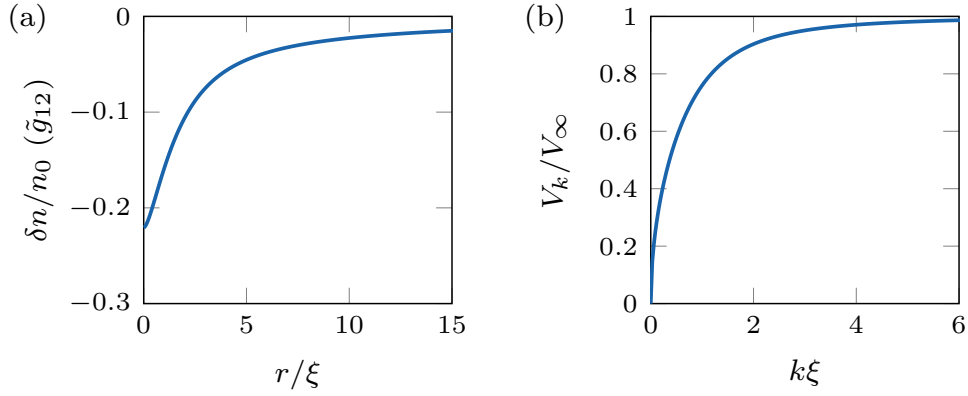


Figure F.1: (a) Density perturbation created by a single impurity, in units of  $\tilde{g}_{12} \ll 1$ . (b) Scattering amplitude  $V_k$  associated to the Fröhlich Hamiltonian of Eq (F.14), as a function of the momentum  $k$ , with  $V_\infty = \frac{\hbar^2}{m}\tilde{g}_{12}\sqrt{n_0/L^2}$ .

where  $J_0$  is the zeroth-order Bessel function of the first kind. The second line was obtained using Eq (F.5) and the algebraic relation

$$(u_k + v_k)^2 = \frac{k}{\sqrt{k^2 + 4\tilde{g}_{11}n_0}}. \quad (\text{F.13})$$

The integral in Eq (F.12) is dimensionless. The factor  $(1 + u_k/v_k)^{-1}$  yields a  $1/k$  divergence, which is compensated by the Jacobian of the integral in polar coordinates. This factor goes to zero like  $1/k^2$  at infinity, and this integral is thus well defined. We can compute this quantity numerically. As shown in Fig F.1(a),  $\delta n(\mathbf{r})/n_0$  varies smoothly from  $\sim -\tilde{g}_{12}$  (which we assume to be small in absolute value) to zero, over a typical distance given by the healing length  $\xi = 1/\sqrt{2\tilde{g}_{11}n_0}$ . As a first conclusion, we find that a single impurity creates a small hole of relative depth  $\tilde{g}_{12}$  and size  $\xi$  in the BEC. Moreover, the energy shift of the system is simply given by  $(\hbar^2/m)\tilde{g}_{12}n_0$ , i.e. the mean-field shift.

### The effective mass

In this paragraph, we consider a single impurity ( $a$ ) with a finite mass – equal to the mass  $m$  of the BEC atoms – and work out the renormalization of this mass through the interactions with the Bogoliubov modes of the BEC. The derivation follows closely Grusdt & Demler [239], adapted to the 2D case. We approximate the impurity-BEC interaction term by

$$\frac{\hbar^2}{m}\tilde{g}_{12}\hat{\Psi}^\dagger(\hat{\mathbf{R}}_a)\hat{\Psi}(\hat{\mathbf{R}}_a) = \frac{\hbar^2}{m}\tilde{g}_{12}n_0 + \sum_{\mathbf{k} \neq 0} V_k \left( \hat{b}_{\mathbf{k}} + \hat{b}_{-\mathbf{k}}^\dagger \right) e^{-i\mathbf{k} \cdot \hat{\mathbf{R}}_a}, \quad (\text{F.14})$$

where we kept only the terms of lowest order in the Bogoliubov operators  $\hat{b}_{\mathbf{k}}, \hat{b}_{\mathbf{k}}^\dagger$ . We also introduced the scattering amplitude

$$V_k = \frac{\hbar^2}{m}\tilde{g}_{12}\sqrt{\frac{n_0}{L^2}}(u_k + v_k) = \frac{\hbar^2}{m}\tilde{g}_{12}\sqrt{\frac{n_0}{L^2}} \left( \frac{k^2}{k^2 + 4\tilde{g}_{11}n_0} \right)^{1/4} \quad (\text{F.15})$$

where the last expression is obtained using Eq (F.13). Physically, this consists in neglecting elementary processes involving the impurity and more than one Bogoliubov quasi-particles,

thus limiting to elementary processes involving the BEC state ( $\mathbf{k} = 0$ ) at least once. Contrary to a contact potential, the amplitude  $V_k$  associated to these processes is not constant but is reduced for low  $k$ 's, as shown in Fig F.1(b). The first term of Eq (F.14) is simply the mean-field shift which we eliminate in the following. Grouping all the terms, we obtain the celebrated Fröhlich Hamiltonian [238].

To proceed, we characterize the importance of the impurity-boson interactions by defining a dimensionless quantity. To do so, we form an energy characteristic of the phonon-impurity interactions  $E_i = (\hbar^2/m)\tilde{g}_{12}\sqrt{n_0/\xi^2}$ . By comparing it to the chemical potential of the condensate  $\mu = (\hbar^2/m)\tilde{g}_{11}n_0$ , we can define the following coupling constant

$$\alpha \equiv \frac{1}{2} \left( \frac{E_i}{\mu} \right)^2 = \frac{\tilde{g}_{12}^2}{\tilde{g}_{11}} \quad (\text{F.16})$$

where the factor  $1/2$  is chosen to follow the usual convention. The so-called weak-coupling regime corresponds to  $\alpha \ll 1$ . Following Grusdt & Demler [239], we determine the renormalized mass of the polaron, defined as the coefficient  $m^*$  which should enter its dispersion relation  $\mathbf{p}^2/2m^*$ . The result, valid only in the weak-coupling regime, writes

$$m^* \simeq \frac{m}{1 - \alpha I} > m, \quad (\text{F.17})$$

where the integral  $I$  is written below and determined numerically

$$I = \pi \int_0^{+\infty} du \frac{u^4}{\sqrt{u^2 + 1} \left( u\sqrt{u^2 + 1} + u^2 \right)^3} \simeq 0.125 \quad (\text{F.18})$$

In the weak coupling regime, the polaron mass is thus always up-shifted with respect to the bare mass. Using our experimental parameters, we find a relative variation of mass given by  $m^*/m - 1 \simeq 2\%$ . This quantity is small with respect to one, as expected from the weak-coupling approximation.

## F.2 The effective potential

We now consider two impurities of infinite mass, separated by  $\mathbf{R} = \mathbf{R}_b - \mathbf{R}_a$ , and the corresponding interaction potential  $\hat{V} = \hat{V}_a + \hat{V}_b$ . We wish to determine the variation of energy of the full system as a function of the separation  $\mathbf{R}$ . Since the impurities do not interact directly, we simply recover (twice) the mean-field energy shift at first order in perturbation theory. We thus apply second order perturbation theory which introduces indirect couplings in the energy correction  $\delta E$ . Limiting again to at most one elementary excitation for the excited states, we obtain

$$\delta E = \sum_{\mathbf{k} \neq 0} \frac{\langle \Phi_0 | \hat{V} | \Phi_{\mathbf{k}} \rangle \langle \Phi_{\mathbf{k}} | \hat{V} | \Phi_0 \rangle}{E_0 - E_{\mathbf{k}}}. \quad (\text{F.19})$$

Similarly to Eq (F.7), we give the expression of the matrix elements

$$\langle \Phi_{\mathbf{k}} | \hat{V} | \Phi_0 \rangle = \frac{\hbar^2}{m} \tilde{g}_{12} \sqrt{\frac{n_0}{L^2}} (u_k + v_k) \left( e^{-i\mathbf{k} \cdot \mathbf{R}_a} + e^{-i\mathbf{k} \cdot \mathbf{R}_b} \right). \quad (\text{F.20})$$

Plugging this in Eq (F.19), we keep only the terms which depend on the separation  $\mathbf{R}$  to extract the interaction potential  $V_{\text{ind}}$ . Taking the continuum limit, this leads to

$$V_{\text{ind}}(\mathbf{R}) = -\frac{\hbar^4}{m^2} \tilde{g}_{12}^2 \frac{n_0}{L^2} \int d^2k \left( \frac{L}{2\pi} \right)^2 \frac{(u_k + v_k)^2}{\hbar\omega_k} 2e^{i\mathbf{k}\cdot\mathbf{R}}. \quad (\text{F.21})$$

Using the relation (F.13), we further simplify this expression into

$$V_{\text{ind}}(\mathbf{R}) = -\frac{\hbar^2}{m} \frac{1}{\pi^2} \tilde{g}_{12}^2 n_0 \int d^2k \frac{e^{i\mathbf{k}\cdot\mathbf{R}}}{k^2 + 4\tilde{g}_{11}n_0} \quad (\text{F.22})$$

$$= -\frac{\hbar^2}{m} \frac{2}{\pi} \tilde{g}_{12}^2 n_0 \int k dk \frac{J_0(kR)}{k^2 + 4\tilde{g}_{11}n_0}. \quad (\text{F.23})$$

In the last integral, one can recognize the Hankel transform of the zeroth-order modified Bessel function of the first kind  $K_0$ , such that we can write

$$V_{\text{ind}}(R) = -\frac{\hbar^2}{m} \frac{2}{\pi} \tilde{g}_{12}^2 n_0 K_0 \left( \frac{1}{\sqrt{2}} \frac{R}{\xi} \right). \quad (\text{F.24})$$

We remind the asymptotic behavior  $K_0(R) \sim e^{-R}/\sqrt{R}$ . In 3D, an analogous calculation yields a Yukawa potential  $\propto e^{-R/\xi}/(R/\xi)$  involving the 3D healing length  $\xi$ . In any case, the potential is attractive. It is also short-ranged with a range provided by the healing length  $\xi$ . For an average distance between atoms  $R \gg \xi$  and in a mean-field treatment, one can approximate this potential by a contact potential whose coupling strength is given by

$$\tilde{g}' = \frac{m}{\hbar^2} \int d^2R V_{\text{ind}}(R) \quad (\text{F.25})$$

$$= -\frac{1}{\pi^2} \tilde{g}_{12}^2 n_0 \int d^2k \frac{1}{k^2 + 4\tilde{g}_{11}n_0} \underbrace{\int d^2R e^{i\mathbf{k}\cdot\mathbf{R}}}_{(2\pi)^2 \delta(\mathbf{k})}, \quad (\text{F.26})$$

so that we obtain eventually

$$\tilde{g}' = -\frac{\tilde{g}_{12}^2}{\tilde{g}_{11}}. \quad (\text{F.27})$$

Importantly, this effective coupling strength is always negative, even though  $\tilde{g}_{12}$  might be positive or negative. Furthermore, this quantity does not depend on the BEC density  $n_0$ .

### Weakly nonlocal contribution of the effective potential

In a mean-field treatment of the impurity component  $\phi_2$ , it might be necessary to account for the nonlocal character of the potential  $V_{\text{ind}}$ . Using the reduced notations introduced in Subsec 3.1.1 with  $\int d^2r |\psi_2|^2 = N_2$ , we rewrite the NLSE as

$$\mu\phi_2(\mathbf{r}) = \left[ -\frac{1}{2}\nabla^2 + \int d^2r' |\phi_2(\mathbf{r}')|^2 V_{\text{ind}}(\mathbf{r} - \mathbf{r}') \right] \phi_2(\mathbf{r}). \quad (\text{F.28})$$

Following Rosanov et al. [214], we now account for the weakly nonlocal character of the effective potential  $V_{\text{ind}}$ . To do so, we decompose  $\phi_2(\mathbf{r}')$  in a Taylor series and eventually obtain

$$\mu\phi_2(\mathbf{r}) = \left[ -\frac{1}{2}\nabla^2 + \tilde{g}'n_2 + \kappa \frac{\nabla^2 n_2}{4} \right] \phi_2(\mathbf{r}), \quad (\text{F.29})$$



with a prefactor  $\kappa$  which can be written as

$$\kappa = \frac{m}{\hbar^2} \int d^2R R^2 V_{\text{ind}}(R) \quad (\text{F.30})$$

$$= - \left( \frac{\tilde{g}_{12}}{\tilde{g}_{11}} \right)^2 \frac{1}{n_0}. \quad (\text{F.31})$$

In this last equality, we used the fact that

$$\int d^2R R^2 e^{i\mathbf{k} \cdot \mathbf{R}} = - (2\pi)^2 \left[ \delta(k_x) \delta''(k_y) + \delta(k_y) \delta''(k_x) \right]. \quad (\text{F.32})$$

## Appendix G

# Elementary excitations of spin bubbles

In this appendix, we provide the equations used to determine the elementary excitations for the various NLSEs encountered in Chapter 5. We will use the reduced notations of Subsec 3.1.1. The procedure can be summarized as follows. For a single-component NLSE, we are given an equilibrium solution  $R(r)$  with chemical potential  $\mu$ , and consider a small perturbation around  $R(r)$ . Similarly to Sec A.2, we write this perturbation as

$$\psi(\mathbf{r}, t) = [R(r) + \epsilon(\mathbf{r}, t)] e^{-i\mu t}, \quad (\text{G.1})$$

with  $\epsilon(\mathbf{r}, t)$  a small perturbation with respect to  $R(r)$ . We decompose  $\epsilon(\mathbf{r}, t)$  into real and imaginary parts  $\epsilon(\mathbf{r}, t) = u(\mathbf{r}, t) + iv(\mathbf{r}, t)$ . We then linearize the evolution equation assuming small  $u$  and  $v$ , and obtain a set of linear partial differential equations. Our goal in this appendix is to write explicitly these equations. Similarly to what we did in Sec A.2, the remaining task consists in determining (numerically) the spectrum of the corresponding linear operator.

### Nonlinear Schrödinger equation with nonlocal correction

We first consider the NLSE studied by Rosanov et al. [214]

$$i\frac{\partial\psi}{\partial t} = -\frac{1}{2}\nabla^2\psi - |\psi|^2\psi - \frac{\nabla^2|\psi|^2}{4}\psi, \quad (\text{G.2})$$

with  $\int d^2r |\psi|^2 = \tilde{g}N$ ,  $\tilde{g} < 0$  being the dimensionless coupling strength in 2D and  $N$  the total atom number. Contrary to Eq (5.16), here we expressed all the lengths in terms of the typical length-scale  $\ell_0 = 1/\sqrt{|\tilde{g}_e|n_\infty}$ . After linearizing the evolution equation (G.2), we obtain the system introduced by [214]

$$\frac{\partial}{\partial t} \begin{pmatrix} u \\ v \end{pmatrix} = \begin{pmatrix} 0 & \hat{L}_0^{\text{nl}} \\ -\hat{L}_1^{\text{nl}} & 0 \end{pmatrix} \begin{pmatrix} u \\ v \end{pmatrix} \quad (\text{G.3})$$

which is analogous to Eq (A.13), except that the differential operators  $(\hat{L}_0^{\text{nl}}, \hat{L}_1^{\text{nl}})$  now write<sup>1</sup>

$$\hat{L}_0^{\text{nl}} = -\mu - \frac{1}{2}\nabla^2 - R^2 - \frac{1}{2}R\nabla^2 R - \frac{1}{2}(\nabla R)^2 \quad (\text{G.5})$$

$$\hat{L}_1^{\text{nl}} = -\mu - \frac{1}{2}(1 + R^2)\nabla^2 - (R\nabla R) \cdot \nabla - 3R^2 - R\nabla^2 R - \frac{1}{2}(\nabla R)^2. \quad (\text{G.6})$$

Note that in this last expression, the scalar product  $(R\nabla R) \cdot \nabla$  acts only on the radial variable.

### Single-component effective equation

We then consider the elementary excitations of the effective equation

$$i\frac{\partial\psi}{\partial t} = -\frac{1}{2}\nabla^2\psi - |\psi|^2\psi + \frac{1}{2}\frac{\nabla^2\sqrt{1-|\psi|^2}}{\sqrt{1-|\psi|^2}}\psi, \quad (\text{G.7})$$

considered in Chapter 5, cf Eq (5.13). For the linearization procedure, we find it easier to rewrite the last term of Eq (G.7) as

$$+\frac{1}{2}\frac{\nabla^2\sqrt{1-|\psi|^2}}{\sqrt{1-|\psi|^2}}\psi = \left[ -\frac{1}{8}\frac{(\nabla|\psi|^2)^2}{(1-|\psi|^2)^2} - \frac{1}{4}\frac{\nabla^2|\psi|^2}{1-|\psi|^2} \right] \psi, \quad (\text{G.8})$$

although this expression seems less easy to interpret physically. The only difference with the previous case is the expression of the operators  $(\hat{L}_0^{\text{eff}}, \hat{L}_1^{\text{eff}})$ , now given by<sup>2</sup>

$$\hat{L}_0^{\text{eff}} = -\mu - \frac{1}{2}\nabla^2 - R^2 - \frac{1}{2}\frac{(\nabla R)^2}{(1-R^2)^2} - \frac{1}{2}\frac{R\nabla^2 R}{1-R^2} \quad (\text{G.10})$$

$$\hat{L}_1^{\text{eff}} = -\mu - \frac{1}{2}\frac{1}{1-R^2}\nabla^2 - 3R^2 - \frac{(R\nabla R) \cdot \nabla}{(1-R^2)^2} - \frac{1}{2}\frac{(3R^2+1)(\nabla R)^2}{(1-R^2)^3} - \frac{R\nabla^2 R}{(1-R^2)^2} \quad (\text{G.11})$$

### Coupled nonlinear Schrödinger equations

Finally, we consider the coupled NLSEs with equal masses

$$i\frac{\partial\psi_1}{\partial t} = -\frac{1}{2}\nabla^2\psi_1 + (\tilde{g}_{11}|\psi_1|^2 + \tilde{g}_{12}|\psi_2|^2)\psi_1 \quad (\text{G.12})$$

$$i\frac{\partial\psi_2}{\partial t} = -\frac{1}{2}\nabla^2\psi_2 + (\tilde{g}_{22}|\psi_2|^2 + \tilde{g}_{12}|\psi_1|^2)\psi_2, \quad (\text{G.13})$$

with  $\int d^2r |\psi_i|^2 = N_i$ ,  $N_i$  being the atom number in component  $|i\rangle$ , and with intra-species and inter-species dimensionless coupling strengths  $\tilde{g}_{11}, \tilde{g}_{22}, \tilde{g}_{12}$ . In this case, we look for

<sup>1</sup>To derive this result, use the relation

$$|\psi|^2 = (R+u)^2 + v^2 \simeq R^2 + 2Ru \quad (\text{G.4})$$

valid at first order, and the identity:  $\nabla^2(fg) = (\nabla^2 f)g + (\nabla^2 g)f + 2(\nabla f) \cdot (\nabla g)$ .

<sup>2</sup>The perturbation must not only be small with respect to  $R$ , but it should also not modify too much the factors like  $1/(1-|\psi|^2)$ . To obtain these expressions, one thus uses the following expansion

$$\frac{1}{1-|\psi|^2} \simeq \frac{1}{1-R^2} \left( 1 + 2\frac{R}{1-R^2}u \right). \quad (\text{G.9})$$

perturbations around the equilibrium configuration  $(R_1, R_2)$ , with chemical potentials  $(\mu_1, \mu_2)$

$$\psi(\mathbf{r}, t) = [R_1(r) + u_1(\mathbf{r}, t) + iv_1(\mathbf{r}, t)] e^{-i\mu_1 t} \quad (\text{G.14})$$

$$\psi(\mathbf{r}, t) = [R_2(r) + u_2(\mathbf{r}, t) + iv_2(\mathbf{r}, t)] e^{-i\mu_2 t}, \quad (\text{G.15})$$

with  $u_1, v_1, u_2, v_2 \in \mathbb{R}$ . The linear system can now be written as

$$\frac{\partial}{\partial t} \begin{pmatrix} u_1 \\ v_1 \\ u_2 \\ v_2 \end{pmatrix} = \begin{pmatrix} 0 & \hat{L}_0^{(1)} & 0 & 0 \\ -\hat{L}_1^{(1)} & 0 & -\hat{L}_{12} & 0 \\ 0 & 0 & 0 & \hat{L}_0^{(2)} \\ -\hat{L}_{12} & 0 & -\hat{L}_1^{(2)} & 0 \end{pmatrix} \begin{pmatrix} u_1 \\ v_1 \\ u_2 \\ v_2 \end{pmatrix}, \quad (\text{G.16})$$

with the following differential operators

$$\hat{L}_0^{(1)} = -\mu_1 - \frac{1}{2} \nabla^2 + \tilde{g}_{11} R_1^2 + \tilde{g}_{12} R_2^2 \quad (\text{G.17})$$

$$\hat{L}_1^{(1)} = -\mu_1 - \frac{1}{2} \nabla^2 + 3\tilde{g}_{11} R_1^2 + \tilde{g}_{12} R_2^2, \quad (\text{G.18})$$

$(\hat{L}_0^{(2)}, \hat{L}_1^{(2)})$  being deduced from  $(\hat{L}_0^{(1)}, \hat{L}_1^{(1)})$  by exchanging the indices 1 and 2 in these last equations. We also introduced an operator  $\hat{L}_{12}$  coupling the two components

$$\hat{L}_{12} = 2\tilde{g}_{12} R_1 R_2. \quad (\text{G.19})$$



# Appendix H

## Publications

During this thesis, the projects I was involved in led to the following publications

- *Dynamical symmetry and breathers in a two-dimensional Bose gas*, R. Saint-Jalm, P. C. M. Castilho, É. Le Cerf, B. Bakali-Hassani, J.-L. Ville, S. Nascimbene, J. Beugnon, J. Dalibard, [Physical Review X](#) **9**, 021035 (May 2019).
- *Magnetic dipolar interaction between hyperfine clock states in a planar alkali Bose gas*, Y. -Q. Zou, B. Bakali-Hassani, C. Maury, É. Le Cerf, S. Nascimbene, J. Dalibard and J. Beugnon, [Physical Review Letters](#) **125**, 233604 (December 2020).
- *Tan's two-body contact across the superfluid transition of a planar Bose gas*, Y. -Q. Zou, B. Bakali-Hassani, C. Maury, É. Le Cerf, S. Nascimbene, J. Dalibard and J. Beugnon, [Nature Communications](#) **12**, 760 (February 2021).
- *Optical control of the density and spin spatial profiles of a planar Bose gas*, Y. -Q. Zou, É. Le Cerf, B. Bakali-Hassani, C. Maury, G. Chauveau, P. C. M. Castilho, R. Saint-Jalm, S. Nascimbene, J. Dalibard and J. Beugnon, [Journal of Physics B: Atomic, Molecular and Optical Physics](#) **54**, 08LT01 (April 2021).
- *Realization of a Townes soliton in a two-component planar Bose gas*, B. Bakali-Hassani, C. Maury, Y. -Q. Zou, É. Le Cerf, R. Saint-Jalm, P. C. M. Castilho, S. Nascimbene, J. Dalibard and J. Beugnon, [Physical Review Letters](#) **127**, 023603 (July 2021).

All these articles are reproduced in the following pages, except for the last one which is extensively discussed in the main text.

# Dynamical Symmetry and Breathers in a Two-Dimensional Bose Gas

R. Saint-Jalm, P. C. M. Castilho, É. Le Cerf, B. Bakkali-Hassani, J.-L. Ville, S. Nascimbene, J. Beugnon, and J. Dalibard\*

*Laboratoire Kastler Brossel, Collège de France, CNRS, ENS-PSL University, Sorbonne Université,  
11 Place Marcelin Berthelot, 75005 Paris, France*



(Received 19 March 2019; published 21 May 2019)

A fluid is said to be *scale invariant* when its interaction and kinetic energies have the same scaling in a dilation operation. In association with the more general conformal invariance, scale invariance provides a dynamical symmetry which has profound consequences both on the equilibrium properties of the fluid and its time evolution. Here we investigate experimentally the far-from-equilibrium dynamics of a cold two-dimensional rubidium Bose gas. We operate in the regime where the gas is accurately described by a classical field obeying the Gross-Pitaevskii equation, and thus possesses a dynamical symmetry described by the Lorentz group  $SO(2,1)$ . With the further simplification provided by superfluid hydrodynamics, we show how to relate the evolutions observed for different initial sizes, atom numbers, trap frequencies, and interaction parameters by a scaling transform. Finally, we show that some specific initial shapes—uniformly filled triangles or disks—may lead to a periodic evolution corresponding to a novel type of breather for the two-dimensional Gross-Pitaevskii equation.

DOI: [10.1103/PhysRevX.9.021035](https://doi.org/10.1103/PhysRevX.9.021035)

Subject Areas: Atomic and Molecular Physics,  
Nonlinear Dynamics, Superfluidity

## I. INTRODUCTION

Symmetries play a central role in the investigation of a physical system. Most often, they are at the origin of conserved quantities, which considerably simplify the study of the equilibrium states and the evolution of the system. For example, spatial symmetries associated with translation and rotation lead to the conservation of linear and angular momentum. More generally, it is interesting to determine the dynamical (or hidden) symmetries of the system under study, which can lead to more subtle conserved quantities. These symmetries are described by the group of all transformations of space and time that leave the action, therefore, the equations of motion, invariant. A celebrated example is the  $1/r$  potential in three dimensions, where there exists a dynamical symmetry described by the group  $O(4)$  for the bounded orbits [1]. When treated by classical mechanics, it leads to the conservation of the Laplace-Runge-Lenz vector from which one deduces that the bounded orbits are actually closed trajectories.

Among the systems that display rich dynamical symmetries are the ones whose action is left invariant by a dilation transformation of space and time. Such

scale-invariant systems were initially introduced in particle physics to explain scaling laws in high-energy collisions [2]. We consider here the nonrelativistic version of scale invariance, which applies to the dynamics of a fluid of particles. We consider the simultaneous change of length and time coordinates of each particle according to the scaling

$$\mathbf{r} \rightarrow \mathbf{r}/\lambda, \quad t \rightarrow t/\lambda^2. \quad (1)$$

In this dilation, the velocity of a particle is changed as  $\mathbf{v} \rightarrow \lambda\mathbf{v}$ . Therefore, the kinetic energy of the fluid scales as  $E_{\text{kin}} \rightarrow \lambda^2 E_{\text{kin}}$ , which ensures that the corresponding part of the action ( $\propto \int E_{\text{kin}} dt$ ) remains invariant in the transformation (1). If the interaction energy has the same scaling  $E_{\text{int}} \rightarrow \lambda^2 E_{\text{int}}$ , the total action of the fluid is invariant in the dilation. The simplest example of such a fluid is a collection of nonrelativistic particles, either noninteracting ( $E_{\text{int}} = 0$ ) or with pairwise interactions described by a  $1/r^2$  potential. A scale-invariant fluid possesses remarkably simple thermodynamic properties: For example, its equation of state depends only on the ratio of chemical potential to temperature instead of being an independent function of these two variables.

Most physical systems exhibiting scale invariance also possess a more general conformal invariance, where time and space are modified by conformal transformations instead of the simple dilations given in Eq. (1) [3]. In the nonrelativistic domain, this conformal invariance exists for the Schrödinger equation describing the motion of the two systems mentioned

\*jean.dalibard@lkb.ens.fr

Published by the American Physical Society under the terms of the [Creative Commons Attribution 4.0 International license](https://creativecommons.org/licenses/by/4.0/). Further distribution of this work must maintain attribution to the author(s) and the published article's title, journal citation, and DOI.

above, free particles [4,5] and particles interacting with a  $1/r^2$  potential [6]. In both cases, the dynamical symmetry group associated with this scale and conformal invariance is the Lorentz group  $SO(2,1)$ . This is also the case for the three-dimensional pseudo-spin-1/2 Fermi gas in the unitary regime (for a review, see, e.g., Ref. [7]). There, the scattering length between the two components diverges, ensuring the required disappearance of a length scale related to interactions. In addition to the existence of a universal equation of state, this dynamical symmetry leads to a vanishing bulk viscosity [8,9] and also to general relations between the moments of the total energy and those of the trapping energy in a harmonic potential [10].

In this article, we consider another example of a scale- and conformal-invariant fluid with the  $SO(2,1)$  dynamical symmetry, the “weakly interacting” two-dimensional (2D) Bose gas. The concept of “weak interaction” means in this context that the state of the gas is well described by a classical field  $\psi(\mathbf{r}, t)$ . This field is normalized to unity ( $\int |\psi|^2 d^2r = 1$ ) so that the density of the gas reads  $n(\mathbf{r}, t) = N|\psi(\mathbf{r}, t)|^2$  where  $N$  is the number of particles. In the scaling of positions, the 2D matter-wave field changes as  $\psi(\mathbf{r}) \rightarrow \lambda\psi(\lambda\mathbf{r})$ , which guarantees that the norm is preserved and that the dynamical part of the action  $\propto i\hbar \int dt \int d^2r \psi^* \partial_t \psi$  is invariant. The interaction energy of the gas then reads for contact interaction

$$E_{\text{int}} = \frac{N^2 \hbar^2}{2m} \tilde{g} \int |\psi(\mathbf{r})|^4 d^2r, \quad (2)$$

where  $m$  is the mass of a particle, and  $\tilde{g}$  the dimensionless parameter characterizing the strength of the interaction. One can immediately check that  $E_{\text{int}}$  obeys the  $\lambda^2$  scaling required for scale invariance, which can be viewed as a consequence of the dimensionless character of  $\tilde{g}$ . The classical field description used here is valid if one restricts to the case of a small coupling strength  $\tilde{g} \ll 1$  [11]. This restriction is necessary because of the singularity of the contact interaction  $(\hbar^2/m)\tilde{g}\delta(\mathbf{r})$  in 2D when it is treated at the level of quantum field theory. Note that the condition  $\tilde{g} \ll 1$  does not constrain the relative values of the interaction and kinetic energies. Actually, in the following we often consider situations where  $E_{\text{int}} \gg E_{\text{kin}}$  (Thomas-Fermi regime).

So far, the scale and conformal invariance of the weakly interacting 2D Bose gas has been mainly exploited to measure its equation of state [12,13]. Also, one of its dynamical consequences in an isotropic 2D harmonic potential of frequency  $\omega$  has been explored: The frequency of the breathing mode was predicted to be exactly equal to  $2\omega$  for any  $\tilde{g}$  [14–16], as tested in Refs. [17,18]. Note that in the presence of a harmonic potential, the whole system is not scale invariant anymore, but it still possesses a dynamical symmetry described by the group  $SO(2,1)$ , as

shown in Ref. [15]. Recently, deviations from this prediction for  $\tilde{g} \gtrsim 1$ , an example of a *quantum anomaly* [19], have been observed [20,21].

The purpose of our work is to go beyond static properties of the weakly interacting 2D Bose gas and its single-mode oscillation in a harmonic potential and to reveal more general features associated with its dynamical symmetry. To do so, we study the evolution of the gas in a 2D harmonic potential of frequency  $\omega$ , starting from a uniformly filled simple area (disk, triangle, or square). Here, we use  $\tilde{g} \leq 0.16$  so that the classical field description is legitimate. We first check (Sec. II) the prediction from Ref. [15] that  $E_{\text{kin}} + E_{\text{int}}$  should have a periodic evolution in the trap with the frequency  $2\omega$ . We then investigate the transformations linking different solutions of the equations of motion. These transformations are at the heart of the dynamical symmetry group  $SO(2,1)$ . In practice, we first link the evolution of clouds with the same atom number and homothetic initial wave functions in harmonic potentials with different frequencies (Sec. III). Then, restricting to the case where superfluid hydrodynamics is valid, we derive and test a larger family of transformations that allows one to connect the evolutions of two initial clouds of similar shapes with different sizes, atoms numbers, trap frequencies, and interaction strengths (Sec. IV). Finally, in Sec. V we explore a property that goes beyond the symmetry group of the system and that is specific to triangular and disk-shaped distributions in the hydrodynamic limit: We find numerically that these distributions evolve in a periodic manner in the harmonic trap, and we confirm this prediction over the accessible range for our experiment (typically, two full periods of the trap  $4\pi/\omega$ ). These particular shapes can therefore be viewed as two-dimensional breathers for the Gross-Pitaevskii (nonlinear Schrödinger) equation in the hydrodynamic limit [22]. They also constitute a novel example of universal dynamics in a quantum system prepared far from equilibrium [23–25].

## II. EVOLUTION OF POTENTIAL ENERGY

Our experiment starts with a 3D Bose-Einstein condensate of  $^{87}\text{Rb}$  that we load around a single node of a vertical ( $z$ ) standing wave created with a laser of wavelength 532 nm. The confining potential along  $z$  is approximately harmonic with a frequency  $\omega_z/(2\pi)$  up to 4.9 kHz. The interaction parameter is  $\tilde{g} = \sqrt{8\pi}a_s/\ell_z$ , where  $a_s$  is the 3D  $s$ -wave scattering length and  $\ell_z = (\hbar/m\omega_z)^{1/2}$ . The interaction energy per particle and the residual temperature are both smaller than  $\hbar\omega_z$  so that the vertical degree of freedom is effectively frozen [26]. The initial confinement in the horizontal  $xy$  plane is ensured by “hard walls” made with a light beam also at 532 nm. This beam is shaped using a digital micromirror device (DMD), and a high-resolution optical system images the DMD pattern onto the atomic



plane [27], creating a box potential on the atoms. The cloud fills uniformly this box potential, and it is evaporatively cooled by adjusting the height of the walls of the box. For all data presented here, we keep the temperature low enough to operate deep in the superfluid regime with  $T/T_c < 0.3$ , where  $T_c$  is the critical temperature for the Berezinskii-Kosterlitz-Thouless transition. At this stage, the atoms are prepared in the  $F = 1$ ,  $m_F = 0$  hyperfine (ground) state, which is insensitive to magnetic field.

Once the gas reaches equilibrium in the 2D box, we suddenly switch off the confinement in the  $xy$  plane and simultaneously transfer the atoms to the field-sensitive state  $F = 1$ ,  $m_F = -1$  using two consecutive microwave transitions. Most of the experiments are performed in the presence of a magnetic field that provides the internal state  $F = 1$ ,  $m_F = -1$  with an isotropic harmonic confinement in the  $xy$  plane, with  $\omega/2\pi$  around 19.5 Hz. We estimate the anisotropy of the potential to be  $\lesssim 2\%$ . We let the cloud evolve in the harmonic potential for an adjustable time before making an *in situ* measurement of the spatial density  $n(\mathbf{r}) = N|\psi(\mathbf{r})|^2$  by absorption imaging.

The measurement of  $n(\mathbf{r})$  gives access to both the interaction energy (2) and the potential energy in the harmonic trap

$$E_{\text{pot}} = \frac{N}{2} m \omega^2 \int r^2 |\psi(\mathbf{r})|^2 d^2 r. \quad (3)$$

Since the gas is an isolated system, we expect the total energy  $E_{\text{tot}} = E_{\text{kin}} + E_{\text{int}} + E_{\text{pot}}$  to be conserved during the evolution, where the kinetic energy  $E_{\text{kin}}$  reads

$$E_{\text{kin}} = \frac{N \hbar^2}{2m} \int |\nabla \psi|^2 d^2 r. \quad (4)$$

The SO(2,1) symmetry for a 2D harmonically trapped gas brings a remarkable result:  $E_{\text{kin}} + E_{\text{int}}$  and  $E_{\text{pot}}$  should oscillate sinusoidally at frequency  $2\omega$  [15]. More precisely, using the 2D Gross-Pitaevskii equation, one obtains the relations

$$\frac{dE_{\text{pot}}}{dt} = -\frac{d(E_{\text{kin}} + E_{\text{int}})}{dt} = \omega W, \quad (5)$$

$$\frac{dW}{dt} = 2\omega(E_{\text{kin}} + E_{\text{int}} - E_{\text{pot}}), \quad (6)$$

where we define  $W = \omega m \int \mathbf{r} \cdot \mathbf{v} n d^2 r$  and the velocity field  $\mathbf{v}(\mathbf{r}) = (\hbar/m) \text{Im}[\psi^*(\mathbf{r}) \nabla \psi(\mathbf{r})] / |\psi(\mathbf{r})|^2$ . Initially, the gas is prepared in a steady state in the box potential so that  $\mathbf{v} = 0$ ; hence,  $W(0)$  is also null. Therefore, the potential energy evolves as

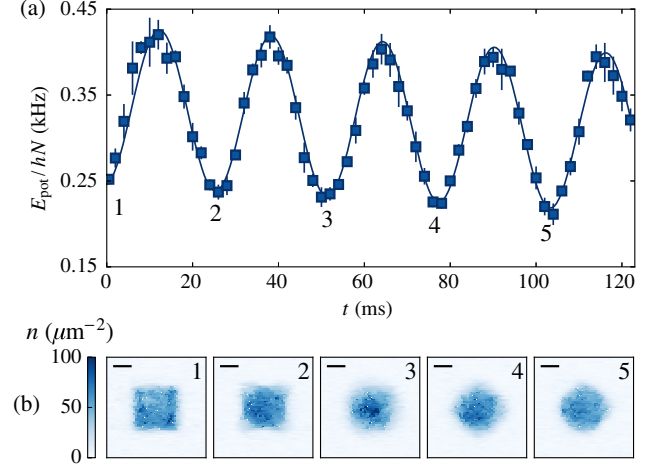


FIG. 1. Time evolution of the potential energy per particle of a 2D gas of  $^{87}\text{Rb}$  atoms in an isotropic harmonic potential of frequency  $\omega$  for a square of side length  $27.6(5) \mu\text{m}$  with  $4.1(2) \times 10^4$  atoms. (a) Evolution of the potential energy per particle. Each point is an average of seven to ten realizations, and the error bars indicate the standard deviation of these different realizations. The frequency of the trap is measured with the oscillation of the center of mass:  $\omega/2\pi = 19.3(1)$  Hz. The oscillations of  $E_{\text{pot}}$  are fitted with a cosine function and an additional linear slope (continuous line). This slope is  $-0.25(4)$  Hz/ms and accounts for the loss of particles from the trap. The fitted frequency is  $38.5(1)$  Hz, which is compatible with  $\omega/\pi$ , as predicted by the SO(2,1) symmetry of the gas. (b) Density distribution of an initially uniform gas after the evolution in a harmonic potential at times  $\omega t = 0, \pi, 2\pi, 3\pi, 4\pi$ , corresponding to the first periods of the potential energy indicated by the labels from 1 to 5. The horizontal black lines represent  $10 \mu\text{m}$ .

$$E_{\text{pot}}(t) = \frac{1}{2} E_{\text{tot}} + \Delta E \cos(2\omega t), \quad (7)$$

where  $\Delta E = \frac{1}{2} [E_{\text{pot}}(0) - E_{\text{kin}}(0) - E_{\text{int}}(0)]$  can be positive or negative. A similar result holds for the sum  $E_{\text{kin}} + E_{\text{int}}$  (with  $\Delta E$  replaced by  $-\Delta E$ ) but not for the individual energies  $E_{\text{kin}}$  or  $E_{\text{int}}$ .

We show in Fig. 1(a) the evolution of the potential energy per particle for an initially uniformly filled square. Although the density distribution is not periodic [see Fig. 1(b)], the potential energy  $E_{\text{pot}}$  evolves periodically and is well fitted by a cosine function with a period that matches the  $2\omega$  prediction and the expected zero initial phase. For a better adjustment of the data, we add a (small) negative linear function to the fitting cosine. Its role is likely to account for the residual evaporation rate of atoms from the trap (approximately  $0.1 \text{ s}^{-1}$ ).

This simple dynamics can be viewed as a generalization of the existence of the undamped breathing mode at frequency  $2\omega$  that we mention in the Introduction [14,15]. We emphasize that this result is a consequence of the SO(2,1) symmetry and does not hold for the Gross-Pitaevskii equation in 1D or 3D.

### III. GENERAL SCALING LAWS

An important consequence of the dynamical symmetry of the 2D Gross-Pitaevskii equation is the ability to link two solutions  $\psi_{1,2}$  of this equation corresponding to homothetic initial conditions: One can relate  $\psi_1(\mathbf{r}, t)$  and  $\psi_2(\mathbf{r}', t')$ , provided they evolve with the same parameter  $\tilde{g}N$  and the same trap frequency  $\omega_1 = \omega_2$ . By using a simple scaling on space and time, this link can be further extended to the case  $\omega_1 \neq \omega_2$ .

The general procedure is presented in the Appendix, and we start this section by summarizing the main results. Consider a solution of the Gross-Pitaevskii equation  $\psi_1(\mathbf{r}, t)$  for the harmonic potential of frequency  $\omega_1$ :

$$i\hbar \frac{\partial \psi_1}{\partial t} = -\frac{\hbar^2}{2m} \nabla^2 \psi_1 + \frac{\hbar^2 \tilde{g}N}{m} |\psi_1|^2 \psi_1 + \frac{1}{2} m \omega_1^2 \mathbf{r}^2 \psi_1. \quad (8)$$

Using scale and conformal invariance, we can construct a solution  $\psi_2(\mathbf{r}', t')$  of the Gross-Pitaevskii equation with the frequency  $\omega_2 = \zeta \omega_1$  using

$$\psi_2(\mathbf{r}', t') = f(\mathbf{r}, t) \psi_1(\mathbf{r}, t), \quad (9)$$

where space is rescaled by  $\mathbf{r}' = \mathbf{r}/\lambda(t)$  with

$$\lambda(t) = \left[ \frac{1}{\alpha^2} \cos^2(\omega_1 t) + \alpha^2 \zeta^2 \sin^2(\omega_1 t) \right]^{1/2}, \quad (10)$$

and the dimensionless parameter  $\alpha$  is the homothetic ratio between the initial states. The relation between the times  $t$  and  $t'$  in frames 1 and 2 is

$$\tan(\omega_2 t') = \zeta \alpha^2 \tan(\omega_1 t), \quad (11)$$

and the multiplicative function  $f$  is

$$f(\mathbf{r}, t) = \lambda(t) \exp \left( -i \frac{m \dot{\lambda} \mathbf{r}^2}{2\hbar \lambda} \right), \quad (12)$$

where  $\dot{\lambda} \equiv [(d\lambda)/(dt)]$ . The two solutions  $\psi_{1,2}(t)$  correspond to the evolution of two clouds with the same parameter  $\tilde{g}_1 N_1 = \tilde{g}_2 N_2$ . At  $t = 0$ , these two wave functions correspond to the ground states of the Gross-Pitaevskii equation in the box potentials with characteristic lengths  $L_{1,2}$ , with  $L_2 = \alpha L_1$ . Both initial wave functions  $\psi_{1,2}(0)$  can be chosen real, and the scale invariance of the (time-independent) 2D Gross-Pitaevskii equation ensures that they are homothetic:  $\alpha \psi_2(\alpha \mathbf{r}, 0) = \psi_1(\mathbf{r}, 0)$ . For example, in the limit  $E_{\text{int}} \gg E_{\text{kin}}$ ,  $\psi(0)$  corresponds to a uniform density in the bulk and goes to zero at the edges on a scale given by the healing length  $\xi \equiv [N\hbar^2/(2mE_{\text{int}})]^{1/2}$ . For two box potentials of homothetic shapes filled with the same number of particles, the ratio  $\xi_2/\xi_1$  is equal to the ratio  $L_2/L_1$ .

We explore experimentally this mapping between two evolutions in the particular case  $L_1 = L_2$  and  $\omega_1 \rightarrow 0$ , i.e.,  $\alpha = 1$  and  $\zeta \rightarrow +\infty$ . We thus compare the evolution of clouds with the same shape and the same size either in a harmonic potential or in free (2D) space. The choice of the initial shape is arbitrary; here we start from a uniform triangle of side length  $40.2(3) \mu\text{m}$  with  $3.9(3) \times 10^4$  atoms and let it evolve either in a harmonic potential of frequency  $\omega_2/(2\pi) = 19.7(2) \text{ Hz}$  or without any potential ( $\omega_1 = 0$ ). In both cases, we record images of the evolution, examples of which are given in Figs. 2(a) and 2(b). These two evolutions should be linked via Eq. (9). The relation (11) between  $t$  and  $t'$  reads

$$\tan(\omega_2 t') = \omega_2 t, \quad (13)$$

and the relation (10) becomes

$$\lambda(t) = (1 + \omega_2^2 t^2)^{1/2}. \quad (14)$$

The relation (13) indicates that the scaling transformation maps the first quarter of the oscillation period in the harmonic trap  $\omega_2 t' \leq \pi/2$  onto the ballistic expansion from  $t = 0$  to  $t = \infty$ . In the absence of interactions, this result has a simple physical interpretation: After the ballistic expansion between  $t = 0$  to  $t = \infty$ , the asymptotic position distribution reveals the initial velocity distribution of the gas, whereas the evolution in the harmonic trap during a quarter of oscillation period exchanges initial positions and initial velocities. We emphasize that the mapping (13) also holds for an interacting system as a consequence of the SO(2,1) symmetry underlying the 2D Gross-Pitaevskii equation [28].

In order to reconstruct the scaling laws (13) and (14) from the measured evolutions, we compare each image  $n_1(\mathbf{r}, t)$  for the free evolution with the set of images  $n_2(\mathbf{r}', t')$  obtained for the in-trap evolution. More precisely, we start by defining the overlap  $\mathcal{O}[n_1, n_2]$  between two images in the following way:

- (i) We introduce the scalar product  $(n_1|n_2)$  between two images

$$(n_1|n_2) = \int n_1(\mathbf{r}) n_2(\mathbf{r}) d^2 r \quad (15)$$

and the norm of an image  $\|n_1\| = \sqrt{(n_1|n_1)}$ .

- (ii) In order to relate two images that differ by a spatial scaling factor  $\lambda$ , we introduce the quantity

$$p[n_1, n_2, \lambda] = \frac{(n_1^{(\lambda)}|n_2)}{\|n_1^{(\lambda)}\| \|n_2\|}, \quad (16)$$

where  $n_1^{(\lambda)}(\mathbf{r}) = \lambda^2 n_1(\lambda \mathbf{r})$  is the image rescaled from  $n_1(\mathbf{r})$  by the factor  $\lambda$ , with the same atom number:

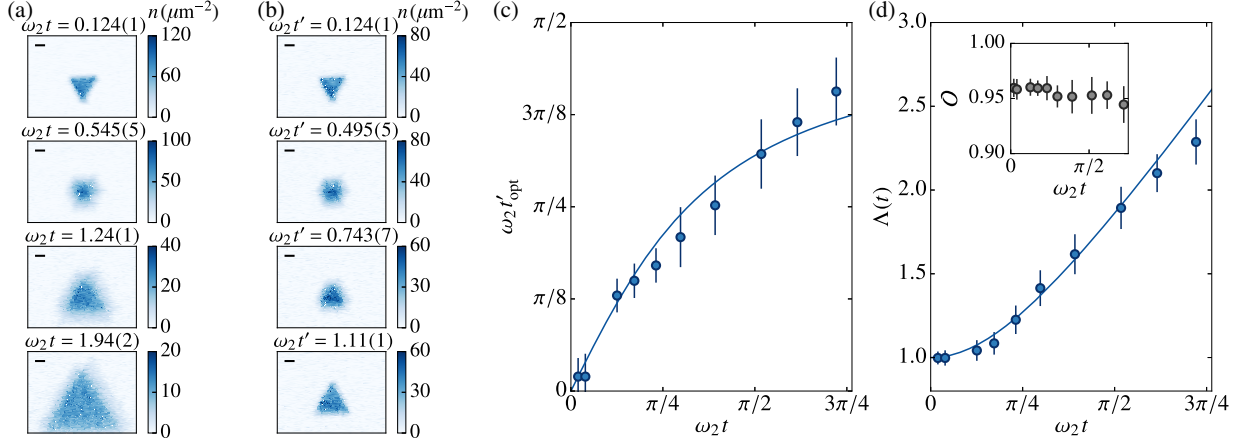


FIG. 2. Evolution of a gas with triangular shape [side length  $40.2(3) \mu\text{m}$ ,  $3.9(3) \times 10^4$  atoms] for two different values of the harmonic trapping frequency. (a),(b) Averaged images of the density distribution after a variable evolution time in the harmonic potential of frequency  $\omega_1 = 0$  and  $\omega_2/2\pi = 19.7(2)$  Hz, respectively. The images are an average over five to ten realizations, and the horizontal black lines represent  $10 \mu\text{m}$ . Pairs of images with approximately corresponding evolution times are shown. (c) Optimal time  $t'_{\text{opt}}(t)$  for which the overlap between images of the first and the second evolutions is maximum. (d) Optimal rescaling factor between the corresponding images  $n_1(t)$  and  $n_2(t'_{\text{opt}})$ . In the two graphs (c) and (d), the solid lines are the theoretical predictions given by Eqs. (13) and (14). The inset of (d) presents the overlap between the corresponding images of the two series. In (c) and (d), the error bars indicate the confidence intervals within 2 standard deviations of the fits used to reconstruct the scaling laws.

$N_1 = \int n_1(\mathbf{r}) d^2r = \int n_1^{(\lambda)}(\mathbf{r}) d^2r$ . Note that the definition of the norm given above entails  $\|n_1^{(\lambda)}\| = \lambda \|n_1\|$ . By construction, the quantity  $p[n_1, n_2, \lambda]$  is always smaller or equal to 1, and it is equal to 1 only when the image  $n_1^{(\lambda)}$  is identical to  $n_2$  up to a multiplicative factor.

- (iii) Finally, for a couple of images  $(n_1, n_2)$ , we vary  $\lambda$  and define their overlap as

$$\mathcal{O}[n_1, n_2] = \max_{\lambda} p[n_1, n_2, \lambda]. \quad (17)$$

In practice, for each image  $n_1(t)$  acquired at a given time  $t$ , we determine the time  $t'_{\text{opt}}$  where the overlap between  $n_1(t)$  and  $n_2(t')$  is optimal. We denote  $\Lambda(t)$  as the value of the scaling parameter  $\lambda$  for which the value  $\mathcal{O}[n_1(t), n_2(t'_{\text{opt}})]$  is reached (see the Supplemental Material [30] for more details). Since the center of the images may drift during the evolution, we also allow for a translation of  $n_2$  with respect to  $n_1$  when looking for the optimum in Eqs. (16) and (17).

The result of this mapping between the two evolutions is shown in Figs. 2(c) and 2(d). In Fig. 2(c), we plot  $t'_{\text{opt}}$  as a function of  $t$ . The prediction (13) is shown as a continuous line and is in good agreement with the data. In Fig. 2(d), we show the variation of the corresponding optimal scaling parameter  $\Lambda(t)$ . Here again, the prediction (14) drawn as a continuous line is in good agreement with the data. The overlap between the density distributions at the corresponding times is shown in the inset of Fig. 2(d) and is always around 0.95, confirming that these density distributions

have very similar shapes. Indeed, the overlap between two images averaged over a few experimental realizations taken in the same conditions ranges from 0.98 to 0.99 due to experimental imperfections.

Finally, we note that here we connect solutions of the Gross-Pitaevskii equation (8) with the same atom number  $N_1 = N_2$ . Actually, the results derived above also apply to pairs of solutions with  $\tilde{g}_1 N_1 = \tilde{g}_2 N_2$ , since only the product  $\tilde{g}N$  enters in the Gross-Pitaevskii equation (8).

#### IV. SCALING LAWS IN THE HYDRODYNAMIC REGIME

In the previous section, we link the evolution of two clouds with the same atom number  $N$  (or the same  $\tilde{g}N$ ). We show now that it is also possible to link evolutions with different  $N$ 's and  $\tilde{g}$ 's, provided we restrict to the so-called hydrodynamic (or Thomas-Fermi) regime, where the healing length  $\xi$  is very small compared to the size of the gas.

##### A. General formulation

The Gross-Pitaevskii equation (8) can be equivalently written in terms of the density and the velocity fields as

$$\partial_t n + \nabla \cdot (n\mathbf{v}) = 0, \quad (18)$$

$$m\partial_t \mathbf{v} + \nabla \left( \frac{1}{2} m v^2 + \frac{\hbar^2}{m} \tilde{g} n + \frac{1}{2} m \omega^2 r^2 + P(n) \right) = 0, \quad (19)$$

where  $P(n) = -\hbar^2/2m(\nabla^2 \sqrt{n})/\sqrt{n}$  is the so-called quantum pressure. When the characteristic length scales over

which the density and velocity vary are much larger than the healing length  $\xi$ , one can neglect the contribution of the quantum pressure in Eq. (19):

$$m\partial_t \mathbf{v} + \nabla \left( \frac{1}{2} m v^2 + \frac{\hbar^2}{m} \tilde{g} n + \frac{1}{2} m \omega^2 r^2 \right) = 0. \quad (20)$$

This approximation corresponding to the Thomas-Fermi limit leads to the regime of quantum hydrodynamics for the evolution of the density  $n$  and the irrotational velocity field  $\mathbf{v}$  [31]. It enriches the dynamical symmetries of the problem, as we see in the following. For our experimental parameters, this approximation is legitimate since the healing length is a fraction of a micrometer only, much smaller than the characteristic size of our clouds (tens of micrometers).

We consider two homothetic shapes, e.g., two boxlike potentials with a square shape, with sizes  $L_{1,2}$  and filled with  $N_{1,2}$  atoms. We assume that we start in both cases with the ground state of the cloud in the corresponding shape so that the initial velocity fields are zero. Note that contrary to the case of Sec. III, the ratio between the healing lengths  $\xi_2/\xi_1$  is not anymore equal to  $L_2/L_1$  so that the initial wave functions are not exactly homothetic, but this mismatch occurs only close to the edges over the scale of  $\xi_{1,2} \ll L_{1,2}$ . As before, at time  $t = 0$  we switch off the potential creating the shape under study and switch on a harmonic potential with frequency  $\omega_{1,2}$ . Our goal is to relate the two evolutions with parameters  $(\tilde{g}_1 N_1, L_1, \omega_1)$  and  $(\tilde{g}_2 N_2, L_2, \omega_2)$ .

The general transformation involves three dimensionless constant parameters  $\mu, \alpha, \zeta$ :

$$\tilde{g}_2 N_2 = \mu^2 \tilde{g}_1 N_1, \quad L_2 = \alpha L_1, \quad \omega_2 = \zeta \omega_1, \quad (21)$$

and reads

$$\tilde{g}_2 n_2(\mathbf{r}', t') = \lambda^2 \mu^2 \tilde{g}_1 n_1(\mathbf{r}, t), \quad (22)$$

$$\mathbf{v}_2(\mathbf{r}', t') = \lambda \mu \mathbf{v}_1(\mathbf{r}, t) - \mu \dot{\lambda} \mathbf{r} \quad (23)$$

with  $\dot{\lambda} = [(d\lambda)/(dt)]$ . The spatial variables are rescaled as  $\mathbf{r}' = \mathbf{r}/\lambda(t)$  with the function  $\lambda$  now given by

$$\lambda(t) = \left[ \frac{1}{\alpha^2} \cos^2(\omega_1 t) + \left( \frac{\zeta \alpha}{\mu} \right)^2 \sin^2(\omega_1 t) \right]^{1/2}, \quad (24)$$

and the relation between the times  $t$  and  $t'$  in frames 1 and 2 is

$$\tan(\omega_2 t') = \frac{\zeta \alpha^2}{\mu} \tan(\omega_1 t). \quad (25)$$

With a calculation similar to that detailed in the Appendix, one can readily show that if  $(n_1, \mathbf{v}_1)$  is a solution of the hydrodynamic equations (18) and (20) for the frequency

$\omega_1$ , then  $(n_2, \mathbf{v}_2)$  is a solution for the frequency  $\omega_2$ . If  $\mu = 1$ , these equations also apply beyond the Thomas-Fermi limit, as we show in Sec. III. More strikingly, they show that in the quantum hydrodynamic regime, the evolution of any cloud is captured by a universal dynamics that depends only on its initial geometry.

## B. Connecting evolutions with a fixed trap frequency, a fixed size, and different $\tilde{g}N$

We present here the experimental investigation of the scaling described above, focusing on the case  $L_1 = L_2$  and  $\omega_1 = \omega_2$ , i.e.,  $\alpha = \zeta = 1$ . In other words, we compare the evolution of two clouds with the same initial shape and density distribution, different atom numbers, and different interaction strengths in a given harmonic trap. For simplicity, we consider the result of the evolution at times  $t$  and  $t'$  such that  $\omega_1 t = \omega_2 t' = \pi/2$ , which satisfies the constraint (25). In this case,  $\lambda(t) = 1/\mu$  so that the general scaling (22) reads

$$\tilde{g}_2 n_2(\mu \mathbf{r}, t'_{\pi/2}) = \tilde{g}_1 n_1(\mathbf{r}, t_{\pi/2}). \quad (26)$$

We start with a cloud in a uniform box potential with the shape of an equilateral triangle of side length  $L = 38.2(3) \mu\text{m}$ . At  $t = 0$ , we transfer the atoms in the harmonic trap of frequency  $\omega/2\pi = 19.6 \text{ Hz}$  and remove the box potential. At  $t = \pi/(2\omega)$ , we image the cloud. We perform this experiment for different values of  $\tilde{g}$  (and slightly different atom numbers) corresponding to the product  $\tilde{g}N$  between 200 and 4000. This leads to a ratio  $\xi/L$  always smaller than 0.03, ensuring that we stay in the quantum hydrodynamic regime. The variation of  $\tilde{g}$  is achieved by changing the intensity  $I$  of the laser beams creating the vertical confinement with  $\tilde{g} \propto I^{1/4}$ . The values of  $\tilde{g}$  are obtained from the measurement of the vertical frequency  $\omega_z$  (see Supplemental Material [30]).

We analyze the series of images using the same general method as in Sec. III. We select arbitrarily one image as a reference point (here, the one corresponding to  $\tilde{g}N \approx 2000$  shown as a red square on Fig. 3). Then, we calculate the best overlap between this reference point and all other images obtained for different  $\tilde{g}N$ 's, and extract an optimal scaling parameter  $\Lambda$ . The results of this analysis are displayed on Fig. 3. The inset shows that the overlap is close to 1 for all values of  $\tilde{g}N$ , indicating that the clouds all have the same shape, as expected from Eq. (26). On the main graph of Fig. 3, we show the variations of  $\Lambda^{-2}$  with  $\tilde{g}N$ . The scaling law (24) predicts that  $\Lambda^{-2} = \mu^2 \propto \tilde{g}N$ , which is indicated by the solid line passing by the origin and the reference point. Here again, this prediction is in excellent agreement with the data, apart from the point for the largest  $\tilde{g}N$ . We attribute this discrepancy to the fact that the local defects of the vertical confinement play a more significant role at larger powers of the vertical confining laser beam.



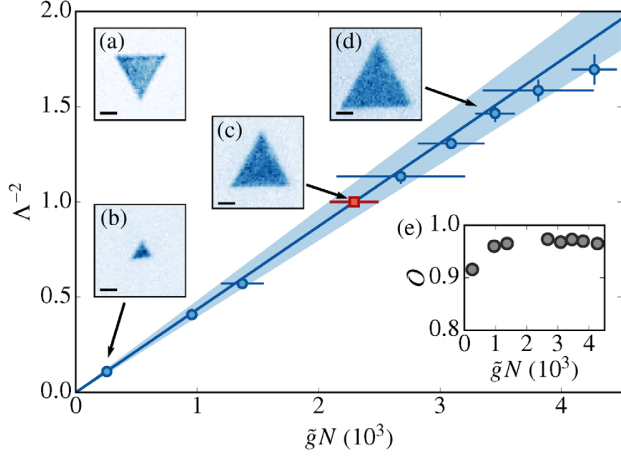


FIG. 3. Scaling factor at  $\omega t = \pi/2$  for different values of  $\tilde{g}N$ . (a) Initial density distribution of the cloud. (b)–(d) Density distributions of the cloud after an evolution during  $t = \pi/(2\omega)$  in the harmonic trap for different values of  $\tilde{g}N$ . For (a)–(d), the horizontal black lines represent  $10\ \mu\text{m}$ . Main graph: Best scaling factor  $\Lambda^{-2}$  as a function of  $\tilde{g}N$ . The red square corresponds to the reference image and its ordinate is fixed to 1. The solid line represents the prediction (26). The shaded area represents its uncertainty due to the one in the atom number of the reference point. The vertical error bars represent the precision at 2 standard deviations of the fit that determines  $\Lambda^{-2}$ . (e) Value of the overlap between the density distributions and the reference point. The error bars due to the fit are smaller than the black points.

Interestingly, the shape for  $t' = \pi/(2\omega)$ , i.e.,  $t = \infty$  for an evolution without any trap, is close to a uniformly filled triangle but inverted compared to the initial one (see insets of Fig. 3). The emergence of such a simple form after time-of-flight is reminiscent of the simple diamondlike shape obtained for the 3D expansion of a uniform gas initially confined in a cylindrical box [32]. Note that we also observe such a diamondlike shape at  $t = \pi/(2\omega)$  starting from a square box, albeit with a nonuniform density (see Supplemental Material [30]).

### C. Connecting evolutions with a fixed trap frequency, different sizes, and different $\tilde{g}N$

Finally, we compare the evolution of two clouds with homothetic shapes and  $\alpha, \mu \neq 1, \zeta = 1$ , which means clouds with different initial sizes, different atom numbers, and evolving in the same harmonic trap. We perform an experiment where the initial shape is a square with a uniform density. The first cloud has a side length  $L_1 = 27.0(5)\ \mu\text{m}$ , contains  $N_1 = 3.7(3) \times 10^4$  atoms, and its initial density distribution is shown on Fig. 4(a). The second one has a side length  $L_2 = 36.8(5)\ \mu\text{m}$  and contains  $N_2 = 5.4(3) \times 10^4$  atoms [Fig. 4(b)]. The ratio  $\xi/L$  is around 0.01 for these two clouds. We let them evolve in the same harmonic potential described above and with the same interaction parameter  $\tilde{g}$  and take pictures after

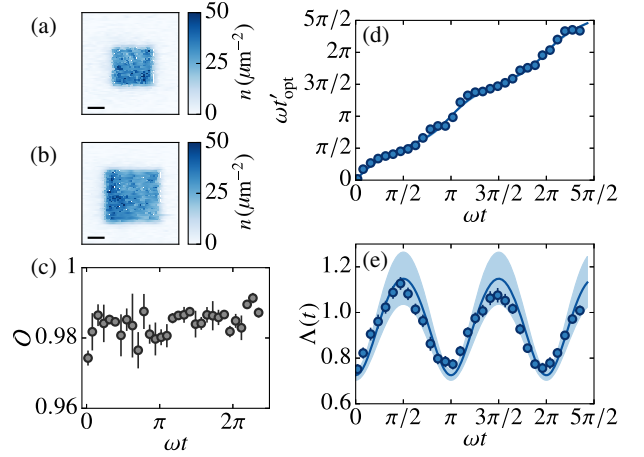


FIG. 4. Mapping between two clouds with the same shape, different sizes, and different atom numbers. (a), (b) Initial density distribution of the two clouds. The horizontal black lines represent  $10\ \mu\text{m}$ . (c) Best overlap between each image of the first series of images and the images of the second one. (d) Optimal time  $t'_{\text{opt}}$  of the second evolution as a function of the time  $t$  of the first evolution. (e) Optimal scaling factor  $\Lambda(t)$  between the first and second evolutions. In (d) and (e), the solid lines are the predictions (25) and (24) where the values of the parameters  $\alpha$  and  $\mu$  are measured independently. The uncertainty of these values is represented as a shaded area. In (d), this area is too narrow to be discernable. In (c)–(e), the error bars indicate the confidence intervals within 2 standard deviations of the fit that we use to reconstruct the scaling laws. They are too small to be seen on (d).

different evolution times. We expect that the two evolutions  $n_1(\mathbf{r}, t)$  of the first cloud and  $n_2(\mathbf{r}', t')$  of the second cloud are linked via Eqs. (22), (24), and (25), with parameters  $\alpha = L_2/L_1 = 1.36(4)$  and  $\mu = \sqrt{N_2/N_1} = 1.21(8)$ . We analyze the two series of images with the same procedure as in Sec. III and determine the scaling laws that link the two evolutions one to the other. The best overlaps between the images of the first and second series are shown in Fig. 4(c). They are all above 0.97, indicating that the two evolutions are indeed similar. The relation between the time  $t'$  of the second frame and the corresponding time  $t$  of the first frame is shown on Fig. 4(d), and the best scaling factor  $\Lambda(t)$  is shown on Fig. 4(e). The solid lines show the theoretical predictions (25) and (24), which are in very good agreement with the experimental data.

With the three experiments described in Secs. III and IV, the scaling laws (22)–(25) are tested independently for the three parameters  $\alpha, \mu$ , and  $\zeta$ , demonstrating that in the quantum hydrodynamic regime, the evolution of a cloud initially at rest depends only on its initial shape, up to scaling laws on space, time, and atom density.

## V. TWO-DIMENSIONAL BREATHERS

In Sec. II, we have shown that due to the  $\text{SO}(2,1)$  symmetry, the evolution of the potential energy  $E_{\text{pot}}$  is

periodic with period  $T/2 \equiv \pi/\omega$  for an arbitrary initial state  $\psi(\mathbf{r}, 0)$  [see Eq. (7)]. Of course, the existence of this periodicity does not put a strong constraint on the evolution of  $\psi(\mathbf{r}, t)$  itself. Because of the nonlinear character of the Gross-Pitaevskii equation, the evolution of  $\psi$  is not expected to be periodic, as illustrated in Fig. 1(b) for a square initial shape. When looking experimentally or numerically at various initial shapes like uniformly filled squares, pentagons, or hexagons, we indeed observe that even though  $E_{\text{pot}}(jT/2) = E_{\text{pot}}(0)$  for integer values of  $j$ , the shapes  $n(\mathbf{r}) = N|\psi(\mathbf{r})|^2$  at those times are notably different from the initial ones. We find two exceptions to this statement, which are the cases of an initial equilateral triangle and a disk. This section is devoted to the study of these very particular states that we call “breathers”.

In the present context of a fluid described by the Gross-Pitaevskii equation, we define a breather as a wave function  $\psi(\mathbf{r}, t)$  that undergoes a periodic evolution in an isotropic harmonic trap of frequency  $\omega$  (for a generalization to different settings, see, e.g., Refs. [22,33]). According to this definition, the simplest example of a breather is a steady-state  $\psi_S(\mathbf{r})$  of the Gross-Pitaevskii equation, e.g., the ground state. Other breathers are obtained by superposing  $\psi_S$  with one eigenmode of the Bogoliubov–de Gennes equations resulting from the linearization of the Gross-Pitaevskii equation around  $\psi_S$ . In principle (with the exception of the breathing mode [15]), the population of this mode should be vanishingly small to avoid damping via nonlinear mixing. Extending this scheme to the superposition of several modes in order to generate more complex types of breathers seems difficult. Indeed, the

eigenmode frequencies are, in general, noncommensurable with each other; therefore, the periodicity of the motion cannot occur as soon as several modes are simultaneously excited [34]. Note that for a negative interaction coefficient  $\tilde{g}$  in 1D, a bright soliton forms a stable steady state of the Gross-Pitaevskii equation (even for  $\omega \rightarrow 0$ ) and thus also matches our definition. In that particular 1D case, a richer configuration exhibiting explicitly the required time periodicity is the Kuznetsov-Ma breather, which is obtained by superposing a bright soliton and a constant background (see, e.g., Ref. [37] and references therein).

Here, we are interested in 2D breathers that go well beyond a single-mode excitation, and we start our study with the uniform triangular shape. In this case, for experiments performed with a gas in the Thomas-Fermi regime, we find that the evolution of the shape is periodic with period  $T/2$  within the precision of the measurement. As an illustration, we show in Fig. 5(a) four images taken between  $t = 0$  and  $T/2$ . The scalar product  $\langle n(0)|n(t) \rangle$  between the initial distribution and the one measured at times  $T/2$ ,  $T$ ,  $3T/2$ , and  $2T$  shown in Fig. 5(b) is indeed very close to 1. We can reproduce the same result for various initial atom numbers.

We did not find an analytical proof of this remarkable result, but we can confirm it numerically by simulating the evolution of a wave function  $\psi(\mathbf{r}, t)$  with the Gross-Pitaevskii equation [38]. We show in Fig. 6(a) a few snapshots of the calculated density distribution and in Fig. 6(b) the evolution of the modulus of the (usual) scalar product  $|\langle \psi(0)|\psi(t) \rangle|$  between the wave functions at times 0 and  $t$ . The calculation is performed on a square grid of

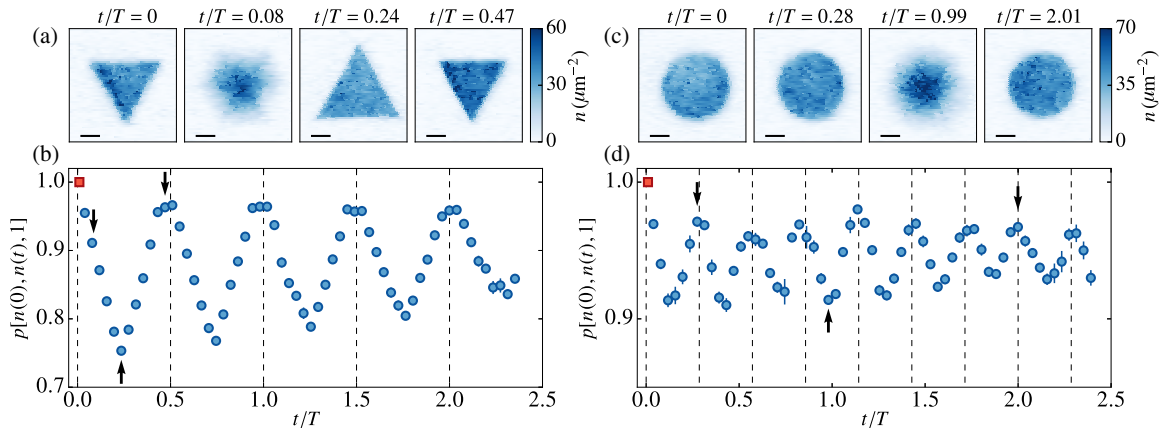


FIG. 5. (a) Density distributions of an initially triangular-shaped cloud at  $t/T = 0$ ,  $t/T = 0.08$ ,  $t/T \approx 1/4$ , and  $t/T \approx 1/2$ . The first and last distributions are close to each other. (b) Scalar product between the initial density distribution of a triangular-shaped cloud (red square) and the density distributions during its evolution in the harmonic trap. The first point is fixed at 1. The dashed lines indicate where  $t/T$  is a multiple of  $1/2$ . The shape seems to be periodic of period  $T/2$ . (c) Density distributions of an initially disk-shaped cloud at  $t/T = 0$ ,  $t/T \approx 2/7$ ,  $t/T \approx 1$ , and  $t/T \approx 2$ . The first two and the last distributions are close to each other. (d) Scalar product between the initial density distribution of a disk-shaped cloud (red square) and the density distributions during its evolution in the harmonic trap. The first point is fixed at 1. The dashed lines indicate where  $t/T$  is a multiple of  $2/7$ . The shape seems to be periodic of period  $2/7$ . In (a) and (c), the horizontal black lines represent  $10 \mu\text{m}$ . In (b) and (d), the black arrows indicate the point corresponding to density distributions shown in (a) and (c), respectively. The error bars represent the statistical error of the measurement.

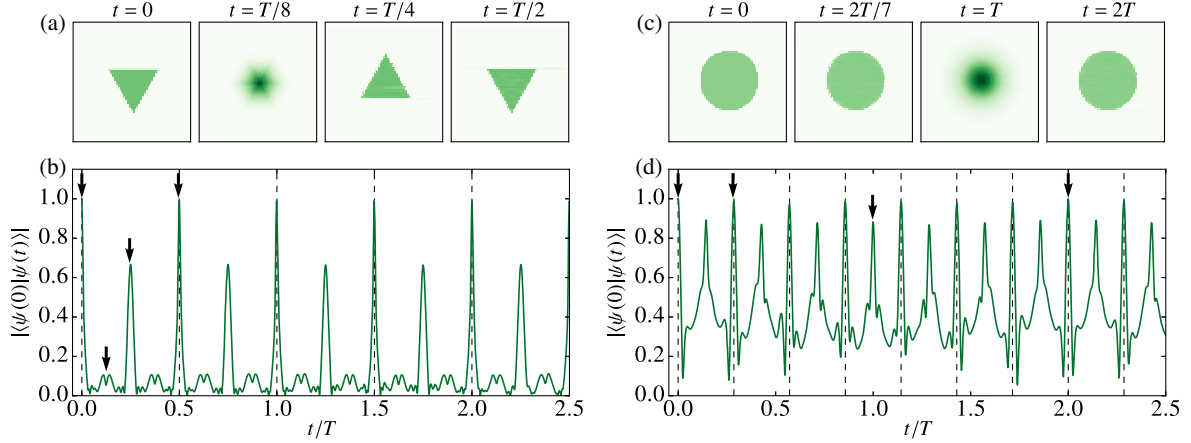


FIG. 6. (a) Calculated density distributions at times  $t/T = 0, 1/8, 1/4, 1/2$  and (b) calculated time evolution of  $|\langle\psi(0)|\psi(t)\rangle|$  starting from the ground state in a triangular box. The numerical integration of the Gross-Pitaevskii equation is performed on a  $512 \times 512$  grid. The triangle is centered on the grid, with a side length equal to half the grid size. We choose  $\tilde{g}N = 25\,600$  corresponding to an initial healing length  $\xi \approx \ell$ , where  $\ell$  is the grid step. (c) Calculated density distributions at times  $t/T = 0, 2/7, 1, 2$  and (d) calculated time evolution of  $|\langle\psi(0)|\psi(t)\rangle|$  starting from the ground state in a disk-shaped box. The numerical integration of the Gross-Pitaevskii equation is performed on a  $512 \times 512$  grid. The disk is centered on the grid, with a diameter equal to half the size of the grid. We choose  $\tilde{g}N = 12\,800$  leading to an initial healing length  $\xi \approx 2\ell$ , where  $\ell$  is the grid step. In (b) and (d), the black arrows indicate the times corresponding to the snapshots presented in (a) and (c).

size  $N_s \times N_s$  with  $N_s = 512$ . The initial wave function is the ground state of a triangular box with the side length  $N_s/2$  centered on the grid, obtained by imaginary time evolution for  $\tilde{g}N = 25\,600$ . Note that by contrast to the “scalar product between images” introduced above, the quantity  $|\langle\psi(0)|\psi(t)\rangle|$  is also sensitive to phase gradients of the wave functions. Its evolution shows clear revivals approaching unity for  $t$  close to multiples of  $T/2$ .

We show in Fig. 7(a) the finite-size scaling analysis of the value of the first maximum of this scalar product occurring at  $t_{\max} \approx T/2$  for increasing grid sizes  $N_s = 64, \dots, 1024$ . The product  $\tilde{g}N$  is adjusted such that the healing length  $\xi = [N\hbar^2/(2mE_{\text{int}})]^{1/2} = a\ell$ , where  $\ell$  is the grid spacing and  $a^2 = 0.5, 1, 2, 4, 8$ . The condition  $a \ll N_s$  ensures that  $\xi$  is much smaller than the size of the triangle (Thomas-Fermi regime), while having  $a \gtrsim 1$  provides an accurate sampling of the edges of the cloud. The overlap between  $|\psi(0)\rangle$  and  $|\psi(t_{\max})\rangle$  increases with the grid size and reaches 0.995 for the largest grid.

In the simulation, the trapping frequency  $\omega$  is adjusted such that  $|\Delta E| \ll E_{\text{tot}}$  in Eq. (7); the cloud then keeps an approximately constant area over time, which is favorable for the numerics. Note that this choice does not restrict the generality of the result, since the scaling laws seen in Sec. III allow one to connect the evolution of a given  $\psi(\mathbf{r}, t = 0)$  in traps with different frequencies. In particular, if the evolution starting from  $\psi(\mathbf{r}, 0)$  in a trap of frequency  $\omega_1$  is periodic with period  $\pi/\omega_1$ , the evolution in another trap with frequency  $\omega_2$  will be periodic with period  $\pi/\omega_2$  [see Eq. (11)].

Two simulations with the same ratio  $a/N_s \propto \xi/L$ , where  $L = \ell N_s/2$  is the size of the initial cloud, describe the same

physical system with a better accuracy as  $a$  and  $N_s$  are increased. For the results in Fig. 7(a), increasing the number of pixels  $N_s$  for a fixed  $a/N_s$  makes the scalar product closer to 1. If this result could be extended as such to arbitrary large values of  $N_s$ , this would demonstrate that the ground state of a triangular box evolves periodically in a harmonic potential. However, a closer look at the results of this finite-size scaling analysis seems to indicate that  $a$  should either be kept constant or increased at a slower rate than  $N_s$  to have the scalar product approaching 1 in an optimal way. Of course this conjecture deduced from our numerical analysis needs to be further explored with analytical tools, which is out of the scope of the present paper.

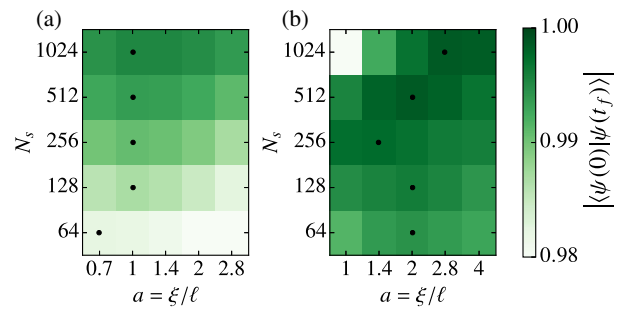


FIG. 7. Finite-size scaling for the numerical simulations. (a) Scalar product  $|\langle\psi(0)|\psi(T/2)\rangle|$  for an initial triangular shape. The size of the grid  $N_s$  and the sampling of the healing length  $a \equiv \xi/\ell$  are varied. The highest value is 0.9953 obtained for  $N_s = 1024$ ,  $a = 1$ . (b) Scalar product  $|\langle\psi(0)|\psi(2T)\rangle|$  for an initial disk shape. The highest value is 0.9986 obtained for  $N_s = 1024$ ,  $a = 2.8$ . On both figures, the black dots indicate the highest value of the scalar product for each line.

The requirement for the Thomas-Fermi regime ( $\xi/L \ll 1$ ) is necessary for obtaining a periodic evolution of the shape with period  $T/2$ . Indeed, in the ideal gas case ( $\tilde{g} = 0$ ), the evolution over  $T/2$  corresponds to an inversion of the initial shape with respect to the origin, i.e., a triangle pointing upwards for the case of interest here [Fig. 5(a)]. One may then wonder about the existence of a periodicity  $T$  for the triangular shape, irrespective of the product  $\tilde{g}N$ . Indeed this periodicity holds in both limiting cases  $\tilde{g} = 0$  (ideal gas) and  $\tilde{g}N$  large (Thomas-Fermi regime). However, numerical simulations show unambiguously that the evolution is not periodic in the intermediate case.

We also run the same simulations for other simple regular polygons (square, pentagons, hexagon). We do not observe a similar revival of the initial wave function over the time period  $(0, 5T)$  (see Supplemental Material [30] for details).

Finally, we turn to the case of a disk-shaped initial cloud [Fig. 5(c)]. The experiment is performed with a cloud prepared such that  $|\Delta E| \ll E_{\text{tot}}$  in Eq. (7), so that the potential energy is approximately constant over time. In this particular case, the experimental result shown in Fig. 5(d) seems to indicate a periodicity of approximately  $2T/7$  for the evolution of the overlap between  $n(\mathbf{r}, 0)$  and  $n(\mathbf{r}, t)$ . To illustrate this, Fig. 5(c) displays four density distributions at times between 0 and  $2T$ . Let us assume that this periodicity  $2T/7$  is exact when  $\Delta E = 0$ . For a disk-shaped initial distribution with any value of  $\Delta E$ , the evolution cannot be  $2T/7$  periodic. Indeed, the potential energy of the cloud is only  $T/2$  periodic, which is not a submultiple of  $2T/7$ . However, all the disk-shaped clouds should have a  $2T$  periodicity, which is the least common multiple of  $T/2$  and  $2T/7$ . As we show now, this  $2T$  periodicity is well supported by a numerical analysis.

We show in Fig. 6(c) snapshots of the calculated density distribution and in Fig. 6(d) the time evolution of the overlap  $|\langle \psi(0) | \psi(t) \rangle|$  starting from the ground state in a disk-shaped box potential centered on a  $512 \times 512$  grid. The disk diameter is chosen equal to half the grid size, and the simulation is run for  $\tilde{g}N = 12\,800$ . This simulation shows that the overlap between  $\psi(\mathbf{r}, 0)$  and  $\psi(\mathbf{r}, t)$  indeed recovers values close to 1 at times close to multiples of  $2T/7$ , as observed experimentally.

A closer inspection of Fig. 6(d) indicates that the time evolution of the overlap is in good approximation periodic with period  $2T$ , with a symmetry around  $t = T$  as well as around  $t = 2T$ . If the evolution is effectively periodic with period  $2T$ , the symmetry around these points is expected. Indeed, the wave function is chosen real for  $t = 0$ , and will thus be real also at  $2T$  (up to a global phase). Therefore, the evolution must be symmetric around those points thanks to time-reversal symmetry. On the other hand, this symmetry does not show up around the other local maxima  $j2T/7$  ( $j = 1, \dots, 6$ ), indicating that one does not expect a full overlap with the initial state for those points.

In order to investigate further the revival around  $2T$ , we run a finite-size scaling analysis for the same grid sizes as for the triangles and for  $a^2 = 1, 2, 4, 8, 16$  [Fig. 7(b)]. We find that the numerical results are compatible with a full recovery of the initial wave function at time  $2T$ , with a scalar product between the wave functions at times 0 and  $2T$  attaining a maximum of 0.9986 for the largest grid size  $N_s = 1024$  and  $a^2 = 8$ . In this case, the optimal value of  $a$  for a given  $N_s$  (marked with a dot in Fig. 7) increases with  $N_s$ ; note that the optimal ratio  $a/N_s \propto \xi/L$  decreases when  $N_s$  increases, which guarantees that the cloud remains in the Thomas-Fermi regime.

To conclude this section, we emphasize that the phenomenon described here is notably different from the existence of a breathing mode at frequency  $2\omega$  [14,15] that we mention in the Introduction and explore in Sec. II. Here, we observe a periodic motion of the whole cloud not just of the second moment  $\langle r^2 \rangle$  of the position. We also note that the observed phenomenon is a genuine nonlinear effect, which cannot be captured by a linearization of the motion of the cloud around an equilibrium position. Indeed, the state of the gas at an intermediate time may dramatically differ from the state at initial time or after a full period both in terms of size and shape. A proper analysis of these breathers may require a multimode approach, with the observed phenomenon resulting from a mode synchronization effect via nonlinear couplings.

## VI. SUMMARY AND OUTLOOK

In this paper, we investigate experimentally some important consequences of the dynamical symmetries of the two-dimensional Gross-Pitaevskii equation describing the evolution of a weakly interacting Bose gas in a harmonic potential. First, we show that the  $\text{SO}(2,1)$  symmetry leads to a periodic evolution of the potential energy and to scaling laws between the evolution of clouds with the same atom number and the same interaction parameter. Second, we show that in the quantum hydrodynamic regime, more symmetries allow one to describe the evolution of the gas by a single universal function irrespective of its size, atom number, trap frequency, and interaction parameter  $\tilde{g}$ . This universal evolution depends only on the initial shape and velocity field of the cloud. Third, we identify two geometrical boxlike potentials, equilateral triangle and disk, which lead to a periodic motion of the wave function when one starts with a gas uniformly filling these shapes and releases it in a harmonic potential of frequency  $\omega$ . The periods of these breathers are  $\pi/\omega$  and  $4\pi/\omega$  for the triangles and the disks, respectively. This result is confirmed by a numerical simulation for a cloud initially in the Thomas-Fermi regime of the boxlike potential, giving an overlap between the initial state and the state after one period larger than 0.995 and 0.998 for the triangle and the disk, respectively.



The existence of these breathers raises several interesting questions. First, it is not immediate that their existence is a direct consequence of the dynamical symmetries of the system. If this is the case, such breathers could appear also for other systems exhibiting the  $SO(2,1)$  symmetry, like a three-dimensional unitary Fermi gas or a cloud of particles with a  $1/r^2$  interaction potential. Remarkably, the latter case can be approached using classical (Newton) equations of motion; a preliminary numerical analysis with up to  $10^5$  particles indicates that an initial triangular (resp. disk) shape with uniform filling also leads to an approximate periodic evolution in a harmonic potential with same period  $T/2$  (resp.  $2T$ ) as the solution of the Gross-Pitaevskii equation. We also note that in the 1D case, the spectrum of the Hamiltonian of a gas of particles interacting with a repulsive  $1/r^2$  potential is composed of evenly spaced energy levels, ensuring a periodic evolution of the system for any initial state [39,40].

The allowed shapes for such breathers is also an intriguing question. In our exploration (both experimental and numerical), we find this behavior only for triangles and disks, but one cannot exclude that complex geometrical figures can show a similar phenomenon. Another issue is related with thermal effects. For all studies reported here, we operate with a gas deeply in the degenerate regime, which is well approximated by the zero-temperature Gross-Pitaevskii formalism. A natural extension of our work is therefore to study to which extent the present findings will subsist in the presence of a significant nonsuperfluid component. For our experimental setup, this will require a significant increase in the vertical trapping frequency so that the vertical degree of freedom remains frozen for the thermal component of the gas.

Finally, we recall that the  $SO(2,1)$  symmetry is only an approximation for the description of a two-dimensional Bose gas. It is valid when the gas can be modeled by a classical field analysis, hence, for a small interaction parameter  $\tilde{g} \ll 1$ . For stronger interactions, one has to turn to a quantum treatment of the fluid. This breaks the scale invariance and the  $SO(2,1)$  symmetry that exist at the classical field level, providing an example of a “quantum anomaly” [19,41,42]. For example, the frequency of the breathing mode of a gas in a harmonic potential then differs from its classical value  $2\omega$ . It remains to be understood if a similar quantum anomaly shows up for the breathers described in this work.

## ACKNOWLEDGMENTS

This work is supported by Domaine d'intérêt majeur (DIM) NanoK, ERC (Synergy UQUAM), QuantERA ERA-NET (NAQUAS project), and Grant No. ANR-18-CE30-0010. We thank Yvan Castin, Cheng Chin, Ignacio Cirac, Lei Feng, Jörg Schmiedmayer, and Steven Simon for stimulating discussions.

## APPENDIX: SYMMETRY GROUPS OF THE SCHRÖDINGER AND 2D GROSS-PITAEVSKII EQUATIONS

For completeness, we summarize in this Appendix the main properties of the transformations that leave invariant the Schrödinger equation (i) for a free particle and (ii) for a particle confined in a harmonic potential. The ensemble of these transformations forms a group called the maximal kinematical invariance group, which is parametrized in the 2D case by eight real numbers. In what follows, we are interested only in the subgroup that is relevant for scale and conformal invariance. For example, in the case of a free particle, five parameters are related to space translations, changes of Galilean frame, and rotations, which do not play a role in our study. We are then left with three parameters corresponding to time translations, dilations, and special conformal transformations. These transformations also leave the 2D Gross-Pitaevskii equation invariant. In the following, we identify their generators and show that they obey the  $SO(2,1)$  commutation algebra. We follow closely the approach of Refs. [5,43], which was developed for the Schrödinger equation describing the motion of a single particle but also applies with little modifications to the case of the nonlinear Gross-Pitaevskii equation. In this Appendix, we set  $\hbar = 1$  to simplify the notations.

### 1. Free particles

Although we are interested ultimately in the case where the particles evolve in a harmonic potential, we start by a brief summary of the free-particle case, for which the algebra is slightly simpler, while involving transformations of a similar type. In Ref. [5], it was shown that in addition to space translations, rotations, and Galilean transformations, the three following transformations leave invariant the free-particle Schrödinger equation:

- (i) The translations in time

$$\mathbf{r} \rightarrow \mathbf{r}, \quad t \rightarrow t + \beta, \quad (\text{A1})$$

since the Hamiltonian has no explicit time dependence.

- (ii) The dilations

$$\mathbf{r} \rightarrow \mathbf{r}/\lambda, \quad t \rightarrow t/\lambda^2 \quad (\text{A2})$$

already introduced in Eq. (1) of the main text.

- (iii) The so-called “expansions”

$$\mathbf{r} \rightarrow \frac{\mathbf{r}}{\gamma t + 1}, \quad t \rightarrow \frac{t}{\gamma t + 1}, \quad (\text{A3})$$

which correspond to a special conformal transformation for the time.

The combination of these transformations forms a three-parameter group with the most general transformation written as

$$\mathbf{r} \rightarrow g(\mathbf{r}, t) \equiv \frac{\mathbf{r}}{\gamma t + \delta}, \quad (\text{A4})$$

$$t \rightarrow h(t) \equiv \frac{\alpha t + \beta}{\gamma t + \delta}, \quad (\text{A5})$$

with the constraint  $\alpha\delta - \beta\gamma = 1$ . The dilation (A2) is obtained by setting  $\beta = \gamma = 0$ ,  $\delta = \lambda$ , and  $\alpha\delta = 1$ .

Let us consider a function  $\psi_1(\mathbf{r}, t)$  which is a solution of the Gross-Pitaevskii equation in free space:

$$\mathcal{P}_0[\psi_1; \mathbf{r}, t] = 0 \quad (\text{A6})$$

with

$$\mathcal{P}_0[\psi; \mathbf{r}, t] \equiv i \frac{\partial \psi}{\partial t} + \frac{1}{2m} \nabla_{\mathbf{r}}^2 \psi - \frac{\tilde{g}N}{m} |\psi|^2 \psi. \quad (\text{A7})$$

Starting from  $\psi_1(\mathbf{r}, t)$ , we define the function  $\psi_2(\mathbf{r}', t')$  as

$$\psi_2(\mathbf{r}', t') = f(\mathbf{r}, t) \psi_1(\mathbf{r}, t) \quad (\text{A8})$$

with  $\mathbf{r}'$ ,  $t'$  set as

$$\mathbf{r}' = g(\mathbf{r}, t), \quad t' = h(t) \quad (\text{A9})$$

and

$$f(\mathbf{r}, t) = (\gamma t + \delta) \exp\left(-i \frac{m\gamma r^2/2}{\gamma t + \delta}\right). \quad (\text{A10})$$

With a tedious but straightforward calculation, one can check that  $\psi_2(\mathbf{r}', t')$  is also a solution of the Gross-Pitaevskii equation

$$\mathcal{P}_0[\psi_2; \mathbf{r}', t'] = 0 \quad (\text{A11})$$

for any value of the parameters  $\alpha, \beta, \gamma, \delta$  with the constraint  $\alpha\delta - \beta\gamma = 1$ . The group of transformations (A4) and (A5) thus allows one to generate an infinite number of solutions of the Gross-Pitaevskii equation. We could pursue this analysis by determining the generators associated with the action of these transformations on the wave functions  $\psi(\mathbf{r}, t)$ , but we postpone it to the case of a harmonically confined system which is more relevant for our physical system. The two studies are anyway very similar, and the symmetry groups of the two systems have the same Lie algebra [5,43].

## 2. Particles in a harmonic trap

In the presence of an isotropic harmonic potential of frequency  $\omega$ , the general transformations on position and time leaving invariant the Schrödinger equation are also defined by a set of four numbers  $(\alpha, \beta, \gamma, \delta)$  with the constraint  $\alpha\delta - \beta\gamma = 1$  [43]. Setting

$$\eta = \tan(\omega t), \quad \eta' = \tan(\omega t'), \quad (\text{A12})$$

the change in position is

$$\mathbf{r} \rightarrow \mathbf{r}' = g(\mathbf{r}, t) \equiv \frac{\mathbf{r}}{\lambda(t)} \quad (\text{A13})$$

with

$$\lambda(t) = [[\alpha \sin(\omega t) + \beta \cos(\omega t)]^2 + [\gamma \sin(\omega t) + \delta \cos(\omega t)]^2]^{1/2}, \quad (\text{A14})$$

while the transformation on time  $t \rightarrow t' = h(t)$  reads

$$\eta' = \frac{\alpha\eta + \beta}{\gamma\eta + \delta}. \quad (\text{A15})$$

Note that the time translations belong to this set of transformations, as expected for a time-independent problem. They are obtained by taking  $\alpha = \delta = \cos(\omega t_0)$  and  $\beta = -\gamma = \sin(\omega t_0)$ .

We start with a solution  $\psi_1$  of the Gross-Pitaevskii equation in the trap

$$\mathcal{P}_\omega[\psi_1; \mathbf{r}, t] = 0 \quad (\text{A16})$$

with

$$\mathcal{P}_\omega[\psi; \mathbf{r}, t] = \mathcal{P}_0[\psi; \mathbf{r}, t] - \frac{1}{2} m \omega^2 r^2 \psi. \quad (\text{A17})$$

Using this group of transformations, we can generate another function  $\psi_2(\mathbf{r}', t')$  satisfying

$$\mathcal{P}_\omega[\psi_2; \mathbf{r}', t'] = 0 \quad (\text{A18})$$

following the definitions (A8) and (A9) with now

$$f(\mathbf{r}, t) = \lambda(t) \exp\left(-i \frac{m\lambda r^2}{2\lambda}\right). \quad (\text{A19})$$

The fact that  $\psi_2$  is a solution of the Gross-Pitaevskii equation was proven for the noninteracting case in Ref. [43], and one can check that the contribution of the interaction term proportional to  $|\psi|^2 \psi$  cancels in the 2D case thanks to the scaling  $f \propto \lambda$ .

In the main text, we use a specific version of the transformation  $(\mathbf{r}, t) \rightarrow (\mathbf{r}', t')$  that (i) maps the time  $t = 0$  onto the time  $t' = 0$ , and (ii) is such that  $\dot{\lambda}(0) = 0$  since we want to relate a real solution  $\psi_1$  onto another real solution  $\psi_2$  ( $\psi_1$  and  $\psi_2$  are both ground-state wave functions in a boxlike potential). These two conditions, in association with  $\alpha\delta - \beta\gamma = 1$ , impose  $\beta = \gamma = 0$  and  $\delta = 1/\alpha$ , hence,

$$\lambda(t) = \left[ \alpha^2 \sin^2(\omega t) + \frac{1}{\alpha^2} \cos^2(\omega t) \right]^{1/2} \quad (\text{A20})$$

and

$$\tan(\omega t') = \alpha^2 \tan(\omega t). \quad (\text{A21})$$

Finally, we note that the simple dilation transformation  $\mathbf{r}' = \mathbf{r}/\sqrt{\zeta}$ ,  $t' = t/\zeta$  allows one to relate a solution of the Gross-Pitaevskii equation  $\psi_1(\mathbf{r}, t)$  in a trap with frequency  $\omega_1$  to a solution

$$\psi_2(\mathbf{r}', t') = \sqrt{\zeta} \psi_1(\mathbf{r}, t) \quad (\text{A22})$$

in a trap with frequency  $\omega_2 = \zeta \omega_1$ :

$$\mathcal{P}_{\omega_1}[\psi_1; \mathbf{r}, t] = 0 \Rightarrow \mathcal{P}_{\omega_2}[\psi_2; \mathbf{r}', t'] = 0. \quad (\text{A23})$$

We can thus combine this dilation with the transformation (A20) and (A21) in order to obtain the transformation that links two (initially real) solutions  $\psi_1(\mathbf{r}, t)$  and  $\psi_2(\mathbf{r}', t')$  of the Gross-Pitaevskii equation for a given  $\tilde{g}N$  obtained in harmonic traps with frequencies  $\omega_{1,2}$  and starting with homothetic initial conditions with characteristic lengths  $L_{1,2}$ . This transformation reads

$$\mathbf{r}' = \frac{\mathbf{r}}{\lambda(t)}, \quad \tan(\omega_2 t') = \zeta \alpha^2 \tan(\omega_1 t) \quad (\text{A24})$$

with

$$\lambda(t) = \left[ \alpha^2 \zeta^2 \sin^2(\omega_1 t) + \frac{1}{\alpha^2} \cos^2(\omega_1 t) \right]^{1/2} \quad (\text{A25})$$

and  $\alpha = L_2/L_1$ ,  $\zeta = \omega_2/\omega_1$ . This transformation corresponds to the scaling (10) used in the main text.

### 3. Generators and SO(2,1) symmetry

We now look for the infinitesimal generators of the transformation  $\psi_1 \rightarrow \psi_2$  in the presence of a harmonic potential (Appendix Sec. II) and show that they fulfill the commutation algebra characteristic of the SO(2,1) group. We focus here on the transformation (A13)–(A15) which relates solutions of the Gross-Pitaevskii equation for the same nonlinear coefficient  $\tilde{g}N$  and the same trap frequency  $\omega$ .

We first note that the set of four numbers  $(\alpha, \beta, \gamma, \delta)$  with the constraint  $\alpha\delta - \beta\gamma = 1$  actually forms a set of three independent parameters for the free-particle case (Appendix Sec. I). To this set of numbers, we can associate a matrix

$$M = \begin{pmatrix} \alpha & \beta \\ \gamma & \delta \end{pmatrix} \quad (\text{A26})$$

of the group  $\text{SL}(2, R)$ . In order to simplify our discussion, we consider the following three subgroups of  $\text{SL}(2, R)$ , each parametrized by a single parameter  $s_j$ ,  $j = 1, 2, 3$ :

$$\begin{pmatrix} e^{s_1/2} & 0 \\ 0 & e^{-s_1/2} \end{pmatrix}, \quad \begin{pmatrix} \cosh(s_2/2) & \sinh(s_2/2) \\ \sinh(s_2/2) & \cosh(s_2/2) \end{pmatrix}, \quad (\text{A27})$$

and

$$\begin{pmatrix} \cos(s_3/2) & -\sin(s_3/2) \\ \sin(s_3/2) & \cos(s_3/2) \end{pmatrix}. \quad (\text{A28})$$

We obtain three independent generators by considering a small displacement from the unit matrix for each subgroup ( $|s_j| \ll 1$ ). In all three cases, we write the passage from  $\psi_1$  to  $\psi_2$  as

$$\psi_2(\mathbf{r}, t) \approx [\hat{1} - i s_j \hat{L}_j(t)] \psi_1(\mathbf{r}, t), \quad (\text{A29})$$

where we introduce the time-dependent generator  $\hat{L}_j(t)$ . The goal is to determine explicitly these operators and their commutation relation in order to check that they satisfy the SO(2,1) algebra.

(a) Generator associated with  $s_1$ . We have in this case

$$M \approx \hat{1} + \frac{s_1}{2} \hat{\sigma}_z, \quad (\text{A30})$$

where the  $\hat{\sigma}_j$ ,  $j = x, y, z$  are the Pauli matrices. We first get  $\lambda(t) = 1 - (s_1/2) \cos(2\omega t)$  so that

$$f(\mathbf{r}, t) = 1 - \frac{s_1}{2} \cos(2\omega t) - i s_1 \frac{m\omega r^2}{2} \sin(2\omega t), \quad (\text{A31})$$

and the infinitesimal changes in  $\mathbf{r}$ ,  $t$  are

$$g(\mathbf{r}, t) \approx \mathbf{r} \left( 1 + \frac{s_1}{2} \cos(2\omega t) \right), \quad h(t) = t + \frac{s_1}{2\omega} \sin(2\omega t). \quad (\text{A32})$$

These expressions allow one to determine the passage from  $\psi_1$  to  $\psi_2$  as in Eq. (A29) with

$$\begin{aligned} \hat{L}_1(t) = & -\frac{i}{2} \cos(2\omega t) (1 + \mathbf{r} \cdot \nabla) \\ & + \frac{1}{2\omega} \sin(2\omega t) (m\omega^2 r^2 - i\partial_t). \end{aligned} \quad (\text{A33})$$

(b) Generator associated with  $s_2$ . We find

$$M \approx \hat{1} + \frac{s_2}{2} \hat{\sigma}_x. \quad (\text{A34})$$

In this case,  $\lambda(t) = 1 + (s_2/2) \sin(2\omega t)$ , and

$$f(\mathbf{r}, t) = 1 + \frac{s_2}{2} \sin(2\omega t) - is_2 \frac{m\omega r^2}{2} \cos(2\omega t). \quad (\text{A35})$$

It also provides the transformation of space and time coordinates:

$$\begin{aligned} g(\mathbf{r}, t) &\approx \mathbf{r} \left( 1 - \frac{s_2}{2} \sin(2\omega t) \right), \\ h(t) &= t + \frac{s_2}{2\omega} \cos(2\omega t). \end{aligned} \quad (\text{A36})$$

This corresponds to a transformation similar to the one considered above in Eq. (A32) with the time translation  $t \rightarrow t + \pi/(4\omega)$ . The associated operator for the passage from  $\psi_1$  to  $\psi_2$  is thus

$$\begin{aligned} \hat{L}_2(t) &= \frac{1}{2\omega} \cos(2\omega t) (m\omega^2 r^2 - i\partial_t) \\ &\quad + \frac{i}{2} \sin(2\omega t) (1 + \mathbf{r} \cdot \nabla). \end{aligned} \quad (\text{A37})$$

(c) Generator associated with  $s_3$ . Finally, we have for the third case,

$$M \approx \hat{1} - \frac{s_3}{2} i\hat{\sigma}_y. \quad (\text{A38})$$

We simply have  $\lambda(t) = 1$ ,  $f(\mathbf{r}, t) = 1$ , and this case corresponds to the time translations mentioned above, for which we have

$$g(\mathbf{r}, t) = \mathbf{r}, \quad h(t) = t - s_3/2\omega. \quad (\text{A39})$$

The operator  $\hat{L}_3(t)$  is thus

$$\hat{L}_3(t) = \frac{i}{2\omega} \partial_t. \quad (\text{A40})$$

From the expressions of the three generators  $\hat{L}_j$ , we easily find the commutations relations valid at any time

$$[\hat{L}_1, \hat{L}_2] = -i\hat{L}_3, \quad [\hat{L}_2, \hat{L}_3] = i\hat{L}_1, \quad [\hat{L}_3, \hat{L}_1] = i\hat{L}_2, \quad (\text{A41})$$

which are characteristic of the Lorentz group  $\text{SO}(2,1)$ . As explained in Ref. [15], this set of commutation relations allows one to construct, in particular, families of solutions with an undamped breathing motion.

- 
- [1] M. Bander and C. Itzykson, *Group Theory and the Hydrogen Atom (I)*, *Rev. Mod. Phys.* **38**, 330 (1966).  
 [2] R. Jackiw, *Introducing Scale Symmetry*, *Phys. Today* **25**, No. 1, 23 (1972).

- [3] Y. Nakayama, *Scale Invariance vs Conformal Invariance*, *Phys. Rep.* **569**, 1 (2015).  
 [4] C. R. Hagen, *Scale and Conformal Transformations in Galilean-Covariant Field Theory*, *Phys. Rev. D* **5**, 377 (1972).  
 [5] U. Niederer, *The Maximal Kinematical Invariance Group of the Free Schrödinger Equation*, *Helv. Phys. Acta* **45**, 802 (1972).  
 [6] V. de Alfaro, S. Fubini, and G. Furlan, *Conformal Invariance in Quantum Mechanics*, *Nuovo Cimento Soc. Ital. Fis.* **34A**, 569 (1976).  
 [7] *The BCS-BEC Crossover and the Unitary Fermi Gas*, edited by W. Zwerger (Springer Science & Business Media, New York, 2011), Vol. 836.  
 [8] D. T. Son, *Vanishing Bulk Viscosities and Conformal Invariance of the Unitary Fermi Gas*, *Phys. Rev. Lett.* **98**, 020604 (2007).  
 [9] E. Elliott, J. A. Joseph, and J. E. Thomas, *Observation of Conformal Symmetry Breaking and Scale Invariance in Expanding Fermi Gases*, *Phys. Rev. Lett.* **112**, 040405 (2014).  
 [10] F. Werner and Y. Castin, *Unitary Gas in an Isotropic Harmonic Trap: Symmetry Properties and Applications*, *Phys. Rev. A* **74**, 053604 (2006).  
 [11] B. V. Svistunov, E. S. Babaev, and N. V. Prokof'ev, *Superfluid States of Matter* (CRC Press, Boca Raton, London, New York, 2015).  
 [12] C.-L. Hung, X. Zhang, N. Gemelke, and C. Chin, *Observation of Scale Invariance and Universality in Two-Dimensional Bose Gases*, *Nature (London)* **470**, 236 (2011).  
 [13] T. Yefsah, R. Desbuquois, L. Chomaz, K. J. Günter, and J. Dalibard, *Exploring the Thermodynamics of a Two-Dimensional Bose Gas*, *Phys. Rev. Lett.* **107**, 130401 (2011).  
 [14] Y. Kagan, E. L. Surkov, and G. V. Shlyapnikov, *Evolution of a Bose Gas under Variations of the Confining Potential*, *Phys. Rev. A* **54**, R1753 (1996).  
 [15] L. P. Pitaevskii and A. Rosch, *Breathing Mode and Hidden Symmetry of Trapped Atoms in Two Dimensions*, *Phys. Rev. A* **55**, R853 (1997).  
 [16] V. Gritsev, P. Barmettler, and E. Demler, *Scaling Approach to Quantum Non-Equilibrium Dynamics of Many-Body Systems*, *New J. Phys.* **12**, 113005 (2010).  
 [17] F. Chevy, V. Bretin, P. Rosenbusch, K. W. Madison, and J. Dalibard, *Transverse Breathing Mode of an Elongated Bose-Einstein Condensate*, *Phys. Rev. Lett.* **88**, 250402 (2002).  
 [18] E. Vogt, M. Feld, B. Fröhlich, D. Pertot, M. Koschorreck, and M. Köhl, *Scale Invariance and Viscosity of a Two-Dimensional Fermi Gas*, *Phys. Rev. Lett.* **108**, 070404 (2012).  
 [19] M. Olshanii, H. Perrin, and V. Lorent, *Example of a Quantum Anomaly in the Physics of Ultracold Gases*, *Phys. Rev. Lett.* **105**, 095302 (2010).  
 [20] T. Peppler, P. Dyke, M. Zamorano, I. Herrera, S. Hoinka, and C. J. Vale, *Quantum Anomaly and 2D-3D Crossover in Strongly Interacting Fermi Gases*, *Phys. Rev. Lett.* **121**, 120402 (2018).  
 [21] M. Holten, L. Bayha, A. C. Klein, P. A. Murthy, P. M. Preiss, and S. Jochim, *Anomalous Breaking of Scale*






- Invariance in a Two-Dimensional Fermi Gas*, *Phys. Rev. Lett.* **121**, 120401 (2018).
- [22] T. Dauxois and M. Peyrard, *Physics of Solitons* (Cambridge University Press, Cambridge, England, 2006).
- [23] C. Eigen, J. A. P. Glidden, R. Lopes, E. A. Cornell, R. P. Smith, and Z. Hadzibabic, *Universal Prethermal Dynamics of Bose Gases Quenched to Unitarity*, *Nature (London)* **563**, 221 (2018).
- [24] S. Erne, R. Bücke, T. Gasenzer, J. Berges, and J. Schmiedmayer, *Universal Dynamics in an Isolated One-Dimensional Bose Gas Far from Equilibrium*, *Nature (London)* **563**, 225 (2018).
- [25] M. Prüfer, P. Kunkel, H. Strobel, S. Lannig, D. Linnemann, C.-M. Schmied, J. Berges, T. Gasenzer, and M. K. Oberthaler, *Observation of Universal Dynamics in a Spinor Bose Gas Far from Equilibrium*, *Nature (London)* **563**, 217 (2018).
- [26] J. L. Ville, T. Bienaimé, R. Saint-Jalm, L. Corman, M. Aidelsburger, L. Chomaz, K. Kleinlein, D. Perconte, S. Nascimbène, J. Dalibard, and J. Beugnon, *Loading and Compression of a Single Two-Dimensional Bose Gas in an Optical Accordion*, *Phys. Rev. A* **95**, 013632 (2017).
- [27] M. Aidelsburger, J. L. Ville, R. Saint-Jalm, S. Nascimbène, J. Dalibard, and J. Beugnon, *Relaxation Dynamics in the Merging of  $N$  Independent Condensates*, *Phys. Rev. Lett.* **119**, 190403 (2017).
- [28] One may question the validity of the Gross-Pitaevskii equation (GPE), hence, of scale invariance, after a long expansion time when the gas occupies a large area  $R^2$ . If we were interested in the ground state of a box of size  $R \rightarrow \infty$  and a given  $\tilde{g}N$ , we would indeed expect deviations with respect to GPE because the relevant momenta  $k \sim R^{-1}$  would tend to 0, and logarithmic corrections in  $k$  to the coupling constant would become significant [29]. Here, this issue is absent because the initial interaction energy is converted into kinetic energy at the beginning of the expansion. The relevant atomic momenta thus remain approximately  $(2mE_{\text{int}}/N\hbar^2)^{1/2}$  at all times, which validates the use of the GPE.
- [29] D. S. Petrov, M. Holzmann, and G. V. Shlyapnikov, *Bose-Einstein Condensation in Quasi-2D Trapped Gases*, *Phys. Rev. Lett.* **84**, 2551 (2000).
- [30] See Supplemental Material at <http://link.aps.org/supplemental/10.1103/PhysRevX.9.021035> for details on the measurement of the vertical frequency and the experimental reconstruction of the scaling laws, for the measured density distributions starting from a cloud with a square shape, and for more results of numerical simulations starting from various geometrical shapes.
- [31] L. Pitaevskii and S. Stringari, *Bose-Einstein Condensation and Superfluidity*, 2nd ed. (Oxford University Press, Oxford, 2016).
- [32] I. Gotlibovych, T. F. Schmidutz, A. L. Gaunt, N. Navon, R. P. Smith, and Z. Hadzibabic, *Observing Properties of an Interacting Homogeneous Bose-Einstein Condensate: Heisenberg-Limited Momentum Spread, Interaction Energy, and Free-Expansion Dynamics*, *Phys. Rev. A* **89**, 061604(R) (2014).
- [33] A. R. Bishop, J. A. Krumhansl, and S. E. Trullinger, *Solitons in Condensed Matter: A Paradigm*, *Physica (Amsterdam)* **1D**, 1 (1980).
- [34] For the ground state of a harmonically confined 2D gas in the Thomas-Fermi limit, the mode frequencies are  $\omega(2n^2 + 2nm + 2n + m)^{1/2}$  with  $n, m$  positive or null integers [35,36].
- [35] S. Stringari, *Dynamics of Bose-Einstein Condensed Gases in Highly Deformed Traps*, *Phys. Rev. A* **58**, 2385 (1998).
- [36] T.-L. Ho and M. Ma, *Quasi 1 and 2d Dilute Bose Gas in Magnetic Traps: Existence of Off-Diagonal Order and Anomalous Quantum Fluctuations*, *J. Low Temp. Phys.* **115**, 61 (1999).
- [37] L.-C. Zhao, L. Ling, and Z.-Y. Yang, *Mechanism of Kuznetsov-Ma Breathers*, *Phys. Rev. E* **97**, 022218 (2018).
- [38] Despite the fact that our parameters are well within the Thomas-Fermi regime, we perform the numerical analysis using the Gross-Pitaevskii equation (8) and not the quantum hydrodynamic equations (18) and (20). The reason is that the discontinuity of the density that appears in the latter case on the edge of the sample may lead to numerical singularities in the subsequent dynamics.
- [39] F. Calogero, *Solution of the One-Dimensional  $N$ -Body Problems with Quadratic and/or Inversely Quadratic Pair Potentials*, *J. Math. Phys.* **12**, 419 (1971).
- [40] B. Sutherland, *Exact Results for a Quantum Many-Body Problem in One Dimension. II*, *Phys. Rev. A* **5**, 1372 (1972).
- [41] B. R. Holstein, *Anomalies for Pedestrians*, *Am. J. Phys.* **61**, 142 (1993).
- [42] A. Cabo, J. L. Lucio, and H. Mercado, *On Scale Invariance and Anomalies in Quantum Mechanics*, *Am. J. Phys.* **66**, 240 (1998).
- [43] U. Niederer, *The Maximal Kinematical Invariance Group of the Harmonic Oscillator*, *Helv. Phys. Acta* **46**, 191 (1973).

## ARTICLE

<https://doi.org/10.1038/s41467-020-20647-6>

OPEN

# Tan's two-body contact across the superfluid transition of a planar Bose gas

Y.-Q. Zou<sup>1</sup>, B. Bakkali-Hassani<sup>1</sup>, C. Maury<sup>1</sup>, É. Le Cerf<sup>1</sup>, S. Nascimbene<sup>1</sup> , J. Dalibard<sup>1</sup>  & J. Beugnon<sup>1</sup>  <sup>✉</sup>

Tan's contact is a quantity that unifies many different properties of a low-temperature gas with short-range interactions, from its momentum distribution to its spatial two-body correlation function. Here, we use a Ramsey interferometric method to realize experimentally the thermodynamic definition of the two-body contact, i.e., the change of the internal energy in a small modification of the scattering length. Our measurements are performed on a uniform two-dimensional Bose gas of  $^{87}\text{Rb}$  atoms across the Berezinskii-Kosterlitz-Thouless superfluid transition. They connect well to the theoretical predictions in the limiting cases of a strongly degenerate fluid and of a normal gas. They also provide the variation of this key quantity in the critical region, where further theoretical efforts are needed to account for our findings.

<sup>1</sup>Laboratoire Kastler Brossel, Collège de France, CNRS, ENS-PSL Research University, Sorbonne Université, 11 Place Marcelin Berthelot, 75005 Paris, France.  
✉email: [beugnon@lkb.ens.fr](mailto:beugnon@lkb.ens.fr)

The thermodynamic equilibrium of any homogeneous fluid is characterized by its equation of state. This equation gives the variations of a thermodynamic potential, e.g., the internal energy  $E$ , with respect to a set of thermodynamics variables such as the number of particles, temperature, size, and interaction potential. All items in this list are mere real numbers, except for the interaction potential whose characterization may require a large number of independent variables, making the determination of a generic equation of state challenging.

A considerable simplification occurs for ultra-cold atomic fluids when the average distance between particles  $d$  is much larger than the range of the potential between two atoms. Binary interactions can then be described by a single number, the s-wave scattering length  $a$ . Considering  $a$  as a thermodynamic variable, one can define its thermodynamic conjugate, the so-called Tan's contact<sup>1–9</sup>

$$C \equiv \frac{8\pi m a^2}{\hbar^2} \frac{\partial E}{\partial a}, \quad (1)$$

where the derivative is taken at constant atom number, volume, and entropy, and  $m$  is the mass of an atom. For a pseudo-spin 1/2 Fermi gas with zero-range interactions, one can show that the conjugate pair  $(a, C)$  is sufficient to account for all possible regimes for the gas, including the strongly interacting case  $a \gtrsim d$ <sup>10,11</sup>. For a Bose gas, the situation is more complicated: formally, one needs to introduce also a parameter related to three-body interactions, and in practice, this three-body contact can play a significant role in the strongly interacting regime<sup>12–15</sup>.

Since the pioneering experimental works of refs. 16,17, the two-body contact has been used to relate numerous measurable quantities regarding interacting Fermi gases: the tail of the momentum distribution, short-distance behavior of the two-body correlation function, radio-frequency spectrum in a magnetic resonance experiment, etc. (see refs. 18,19 and references therein). Its generalization to low-dimensional gases has also been widely discussed<sup>13,20–28</sup>. For the Bose gas case of interest here, experimental determinations of two- and three-body contacts are much more scarce, and concentrated so far on either the quasi-pure BEC regime<sup>29,30</sup> or the thermal one<sup>29,31</sup>. Here, we use a two-pulse Ramsey interferometric scheme to map out the variations of the two-body contact from the strongly degenerate, superfluid case to the non-degenerate, normal one.

We operate with a uniform, weakly interacting two-dimensional (2D) Bose gas where the superfluid transition is of Berezinskii–Kosterlitz–Thouless (BKT) type<sup>32,33</sup>. For our relatively low spatial density, effects related to the three-body contact are negligible and we focus on the two-body contact. It is well known that for the BKT transition, all thermodynamic functions are continuous at the critical point, except for the superfluid density<sup>34</sup>. Our measurements confirm that the two-body contact is indeed continuous at this point. We also show that the (approximate) scale invariance in 2D allows us to express it as a function of a single parameter, the phase-space density  $\mathcal{D} = n\lambda^2$ , where  $n$  is the 2D density,  $\lambda = (2\pi\hbar^2/mk_B T)^{1/2}$  the thermal wavelength, and  $T$  the temperature. Our measurements around the critical point of the BKT transition provides an experimental milestone, which shows the limits of the existing theoretical predictions in the critical region.

## Results

Our ultra-cold Bose gas is well described by the Hamiltonian  $\hat{H}$ , sum of the kinetic energy operator, the confining potential, and the interaction potential  $\hat{H}_{\text{int}} = a\hat{K}$  with

$$\hat{K} = \frac{2\pi\hbar^2}{m} \int \int \hat{\psi}^\dagger(\mathbf{r}) \hat{\psi}^\dagger(\mathbf{r}') \hat{\delta}(\mathbf{r} - \mathbf{r}') \hat{\psi}(\mathbf{r}') \hat{\psi}(\mathbf{r}) d^3r d^3r'. \quad (2)$$

Here  $\hat{\delta}(\mathbf{r})$  is the regularized Dirac function entering in the definition of the pseudo-potential<sup>35</sup> and the field operator  $\hat{\psi}(\mathbf{r})$  annihilates a particle in  $\mathbf{r}$ . Using Hellmann–Feynman theorem, one can rewrite the contact defined in Eq. (1) as  $C = 8\pi m a^2 \langle \hat{K} \rangle / \hbar^2$ .

In our experiment, the gas is uniform in the horizontal  $xy$  plane, and it is confined with a harmonic potential of frequency  $\omega_z$  along the vertical direction. We choose  $\hbar\omega_z$  larger than both the interaction energy and the temperature, so that the gas is thermodynamically two-dimensional (2D). On the other hand, the extension of the gas  $a_z = (\hbar/m\omega_z)^{1/2}$  along the direction  $z$  is still large compared to the 3D scattering length  $a$ , so that the collisions keep their 3D character<sup>36</sup>. Therefore, the definition (1) of the contact and the expression (2) of the interaction potential remain relevant, and the interaction strength is characterized by the dimensionless parameter  $\tilde{g} = \sqrt{8\pi}a/a_z \approx 0.16$ .

If the zero-range potential  $\delta(\mathbf{r} - \mathbf{r}')$  appearing in (2) did not need any regularization, the contact  $C$  would be equal simply to  $g_2(0)C_0$  where

$$C_0 \equiv 4(2\pi)^{3/2} \frac{a^2 \bar{n} N}{a_z} \quad (3)$$

sets the scale of Tan's contact, with  $\bar{n}$  the average 2D density and  $N$  the atom number. The in-plane two-body correlation function is defined by  $g_2(\mathbf{r}) = \langle : \hat{n}(\mathbf{r}) \hat{n}(0) : \rangle / \bar{n}^2$ , where  $\hat{n}(\mathbf{r})$  is the operator associated with the 2D density and the average value is calculated after setting the particle creation and annihilation operators in normal order. We recall that for an ideal Bose gas, the value of  $g_2(0)$  varies from 2 to 1 when one goes from the non-condensed regime to the fully condensed one<sup>37</sup>.

It is well known that  $g_2(0)$  is generally an ill-defined quantity for an interacting fluid. For example, in a Bose gas with zero-range interactions, one expects  $g_2(r)$  to diverge as  $1/r^2$  in 3D and  $(\log r)^2$  in 2D when  $r \rightarrow 0$ <sup>12,13</sup>. On the other hand, when one properly regularizes the zero-range potential  $\hat{\delta}$  in Eq. (2), Tan's contact is well-behaved. In the zero-temperature limit, the mean-field energy of the 2D gas is  $E = (\hbar^2/2m)\tilde{g}\bar{n}N$ <sup>38</sup>, leading to  $C = C_0$ . In the large temperature, non-degenerate limit (but still assuming the s-wave scattering regime), one can use the virial expansion (see Supplementary Note 4 and ref. 35) to calculate the deviation of the free energy  $F(N, A, T, a)$  of a uniform quasi-2D gas with  $N$  atoms in an area  $A$  with respect to the ideal classical (Boltzmann) gas value. It reads  $F - F_{\text{Boltzmann}} = (\hbar^2/m)\tilde{g}\bar{n}N$ , from which the value of the contact  $C = 2C_0$  is obtained using  $C = (8\pi m a^2 / \hbar^2) (\partial F / \partial a)_{N,A,T}$ .

In this work, we determine the contact experimentally by measuring the change in energy per atom  $\hbar\Delta\nu = \Delta E/N$  when the scattering length is changed by the small amount  $\Delta a$ . Replacing  $\partial E / \partial a$  by  $\Delta E / \Delta a$  in the definition (1), we obtain

$$\frac{C}{C_0} \approx \sqrt{2\pi} \frac{m a_z}{\hbar \bar{n}} \frac{\Delta\nu}{\Delta a}. \quad (4)$$

To measure the energy change  $\hbar\Delta\nu$  resulting from a small modification of the scattering length, we take advantage of a particular feature of the <sup>87</sup>Rb atom: All scattering lengths  $a_{ij}$ , with  $(i, j)$  any pair of states belonging to the ground-level manifold, take very similar values<sup>39</sup>. For example, ref. 40 predicts  $a_{11} = 100.9 a_0$ ,  $a_{22} = 94.9 a_0$  and  $a_{12} = 98.9 a_0$ , where the indices 1 and 2 refer to the two states  $|1\rangle \equiv |F=1, m_z=0\rangle$  and  $|2\rangle \equiv |F=2, m_z=0\rangle$  used in this work and  $a_0$  is the Bohr radius. For an isolated atom, this pair of states forms the so-called clock transition at frequency  $\nu_0 \simeq 6.8$  GHz, which is insensitive (at first order) to the ambient magnetic field. Starting from a gas at equilibrium in  $|1\rangle$ , we use a Ramsey interferometric scheme to measure the microwave frequency required to transfer all atoms

to the state  $|2\rangle$ . The displacement of this frequency with respect to  $\nu_0$  provides the shift  $\Delta\nu$  due to the small modification of scattering length  $\Delta a = a_{22} - a_{11}$ .

The Ramsey scheme consists of two identical microwave pulses, separated by a duration  $\tau_1 = 10$  ms. Their duration  $\tau_2 \sim 100$   $\mu$ s is adjusted to have  $\pi/2$  pulses, i.e., each pulse brings an atom initially in  $|1\rangle$  or  $|2\rangle$  into a coherent superposition of these two states with equal weights. Just after the second Ramsey pulse, we measure the 2D spatial density  $\bar{n}$  in state  $|2\rangle$  in a disk-shaped region of radius 9  $\mu$ m, using the absorption of a probe beam nearly resonant with the optical transition connecting  $|2\rangle$  to the excited state  $5P_{3/2}$ ,  $F' = 3$ . We infer from this measurement the fraction of atoms transferred into  $|2\rangle$  by the Ramsey sequence, and we look for the microwave frequency  $\nu_m$  that maximizes this fraction.

An example of a spectroscopic signal is shown in Fig. 1. In order to determine the bare transition frequency  $\nu_0$ , we also perform a similar measurement on a cloud in ballistic expansion, for which the 3D spatial density has been divided by more than 100 and interactions play a negligible role. The uncertainty on the measured interaction-induced shift  $\Delta\nu = \nu_m - \nu_0$  is on the order of 1 Hz. In principle, the precision of our measurements could be increased further by using a larger  $\tau_1$ . In practice, however, we have to restrict  $\tau_1$  to a value such that the spatial dynamics of the cloud, originating from the non-miscibility of the 1–2 mixture ( $a_{12}^2 > a_{11}a_{22}$ ), plays a negligible role (Supplementary Note 2). We also checked that no detectable spin-changing collisions appear on this time scale: more than 99 % of the atoms stay in the clock state basis. Another limitation to  $\tau_1$  comes from atom losses, mostly due to 2-body inelastic processes involving atoms in  $|2\rangle$ .

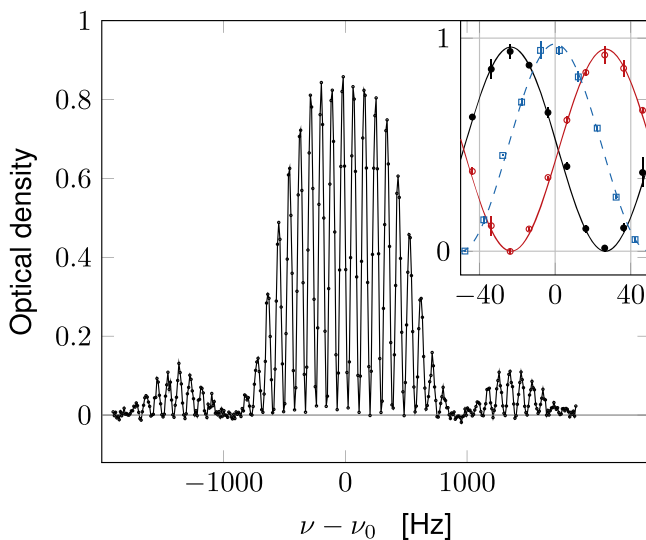


**Fig. 1 Ramsey signal.** Example of an interferometric Ramsey signal showing the optical density of the fraction of the gas in state  $|2\rangle$  after the second Ramsey pulse, as a function of the microwave frequency  $\nu$ . These data were recorded for  $\bar{n} \approx 40$  atoms/ $\mu\text{m}^2$  and  $T \sim 22$  nK,  $\tau_1 = 10$  ms. Here,  $\tau_2$  has been increased to 1 ms to limit the number of fringes for better visibility. Inset. Filled black disks (resp. open red circles): central fringe for atoms in  $|2\rangle$  (resp.  $|1\rangle$ ) in our standard configuration  $\tau_2 = 0.1$  ms. The density in  $|1\rangle$  is obtained by applying a microwave  $\pi$ -pulse just before the absorption imaging phase. When atoms are maximally transferred in state  $|2\rangle$ , we observe no significant population in state  $|1\rangle$ , compatible with a full transfer induced by the Ramsey pulses. Blue squares: single-atom response measured during the ballistic expansion of the cloud by imaging atoms in  $|2\rangle$ . The lines in the inset are sinusoidal fits to the data. The vertical error bars of the inset correspond to the standard deviation of the three repetitions made for this measurement.

For  $\tau_1 = 10$  ms, these losses affect  $<5\%$  of the total population and can be safely neglected.

We see in the inset of Fig. 1 that there indeed exists a frequency  $\nu_m$  for which nearly all atoms are transferred from  $|1\rangle$  to  $|2\rangle$ , so that  $E(N, a_{22}) - E(N, a_{11}) = N h(\nu_m - \nu_0)$  (see the Supplementary Note 1 for details). We note that for an interacting system, the existence of such a frequency is by no means to be taken for granted. Here, it is made possible by the fact that the inter-species scattering length  $a_{12}$  is close to  $a_{11}$  and  $a_{22}$ . We are thus close to the SU(2) symmetry point where all three scattering lengths coincide. The modeling of the Ramsey process detailed in Supplementary Note 1 shows that this quasi-coincidence allows one to perform a Taylor expansion of the energy  $E(N_1, N_2)$  (with  $N_1 + N_2 = N$ ) of the mixed system between the two Ramsey pulses, and to expect a quasi-complete rephasing of the contributions of all possible couples  $(N_1, N_2)$  for the second Ramsey pulse. The present situation is thus quite different from the one exploited in ref. 31, for example, where  $a_{11}$  and  $a_{12}$  were vanishingly small. It also differs from the generic situation prevailing in the spectroscopic measurements of Tan's contact in two-component Fermi gases, where a microwave pulse transfers the atoms to a third, non-interacting<sup>16</sup> or weakly-interacting state<sup>19</sup>.

We show in Fig. 2 our measurements of the shift  $\Delta\nu$  for densities ranging from 10 to 40 atoms/ $\mu\text{m}^2$ , and temperatures from 10 to 170 nK. Since  $\hbar\omega_z/k_B = 210$  nK, all data shown here are in the thermodynamic 2D regime  $k_B T < \hbar\omega_z$ . More precisely, the population of the ground state of the motion along  $z$ , estimated from the ideal Bose gas model<sup>41</sup>, is always  $\gtrsim 90\%$ . All shifts are negative as a consequence of  $a_{22} < a_{11}$ : the interaction energy of the gas in state  $|2\rangle$  is slightly lower than in state  $|1\rangle$ . For a given density, the measured shift increases in absolute value with temperature. This is in line with the naive prediction of  $C \propto g_2(0)$  since density fluctuations are expected to be an

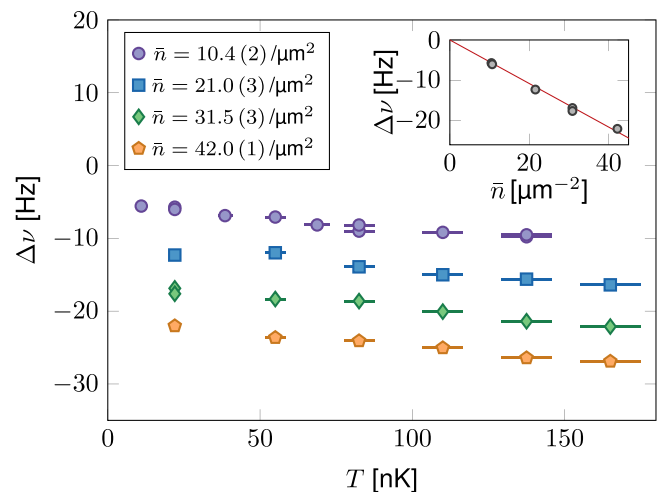


**Fig. 2 Frequency shift of the resonance.** Variations of the shift  $\Delta\nu$  with temperature for various 2D spatial densities. The horizontal error bars represent the statistical uncertainty on the temperature calibration, except for the points at very low temperature (10–22 nK). These ultra-cold points are deeply in the Thomas-Fermi regime, where thermometry based on the known equation of state of the gas is not sensitive enough. The temperature is thus inferred from an extrapolation with an evaporation barrier height of the higher temperature points. The error on the frequency measurement is below 1 Hz and is not shown in this graph. Inset: Variations of the shift  $\Delta\nu$  with density at low temperature  $T \sim 22$  nK, i.e., a strongly degenerate gas. The straight line is the mean-field prediction corresponding to  $\Delta a = -5.7 a_0$ .



increasing function of  $T$ . Conversely for a given temperature, the shift is (in absolute value) an increasing function of density.

For the lowest temperatures investigated here, we reach the fully condensed regime in spite of the 2D character of the sample, as a result of finite size effects. In this case, the mean-field prediction for the shift reads  $\Delta\nu = \bar{n} \hbar \Delta a / (\sqrt{2\pi} m a_z)$  [i.e.,  $C = C_0$  in Eq. (4)]. Our measurements confirm the linear variation of  $\Delta\nu$  with  $\bar{n}$ , as shown in the inset of Fig. 2 summarizing the data for  $T = 22$  nK. A linear fit to these data gives  $\Delta a/a_0 = -5.7$  (1.0) where the error mostly originates from the uncertainty on the density calibration. In the following, we use this value of  $\Delta a$  for inferring the value of  $C/C_0$  from the measured shift at any temperature, using Eq. (4). We note that this estimate for  $\Delta a$  is in good agreement with the prediction  $\Delta a/a_0 = -6$  quoted in ref. 40. The first corrections to the linear mean-field prediction were derived (in the 3D case) by Lee, Huang, and Yang in ref. 42. For our densities, they have a relative contribution on the order of 5 % of the main signal ( $\Delta\nu \lesssim 1$  Hz) (Supplementary Note 3), and their detection is borderline for our current precision.

We summarize all our data in Fig. 3, where we show the normalized contact  $C/C_0$  defined in Eq. (4) as a function of the phase-space density  $\mathcal{D}$ . All data points collapse on a single curve within the experimental error, which is a manifestation of the approximate scale invariance of the Bose gas, valid for a relatively weak interaction strength  $\tilde{g} \lesssim 1$ <sup>43,44</sup>.

## Discussion

We now compare our results in Fig. 3 to three theoretical predictions. The first one is derived from the Bogoliubov approximation applied to a 2D quasi-condensate<sup>45</sup>. This prediction is expected to be valid only for  $\mathcal{D}$  notably larger than the phase-space density at the critical point  $\mathcal{D}_c$  (see “Methods” section) and it accounts well for our data in the superfluid region. Within this approximation, one can also calculate the two-body correlation function and write it as  $g_2(r) = g_2^{T=0}(r) + g_2^{\text{thermal}}(r)$ . One can then show the result (Supplementary Note 3)

$$\frac{C}{C_0} = 1 + g_2^{\text{thermal}}(0), \quad (5)$$

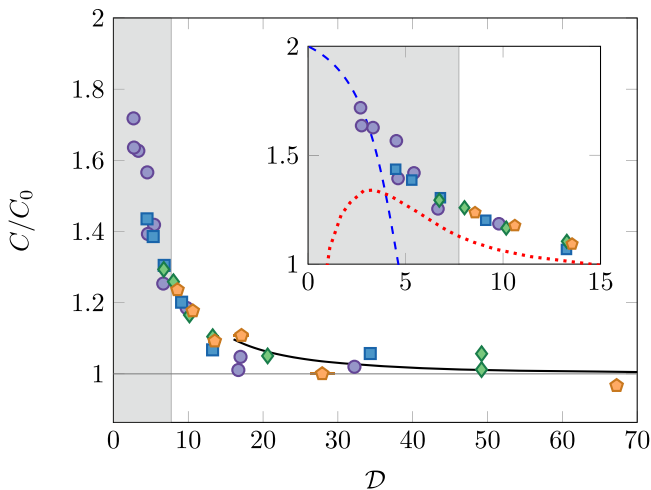


**Fig. 3 Contact measurement.** Variations of the normalized Tan’s contact  $C/C_0$  with the phase-space density  $\mathcal{D}$ . The encoding of the experimental points is the same as in Fig. 2. The colored zone indicates the non-superfluid region, corresponding to  $\mathcal{D} < \mathcal{D}_c \approx 7.7$ . The continuous black line shows the prediction derived within the Bogoliubov approximation. Inset: Zoom on the critical region. The dashed blue line is the prediction from ref. 46, resulting from a virial expansion for the 2D Bose gas. The dotted red line shows the results of the classical field simulation of ref. 47.

which provides a quantitative relation between the contact and the pair correlation function, in spite of the already mentioned singularity of  $g_2^{T=0}(r)$  in  $r = 0$ .

For low phase-space densities, one can perform a systematic expansion of various thermodynamic functions in powers of the (properly renormalized) interaction strength<sup>46</sup>, and obtain a prediction for  $C$  (dashed blue line in the inset of Fig. 3). By comparing the 0th, 1st, and 2nd orders of this virial-type expansion, one can estimate that it is valid for  $\mathcal{D} \lesssim 3$  for our parameters. When  $\mathcal{D} \rightarrow 0$ , the result of ref. 46 gives  $C/C_0 \rightarrow 2$ , which is the expected result for an ideal, non-degenerate Bose gas. The prediction of ref. 46 for  $\mathcal{D} \sim 3$  compares favorably with our results in the weakly degenerate case.

Finally, we also show in Fig. 3 the results of the classical field simulation of ref. 47 (red dotted line), which are in principle valid both below and above the critical point. Contrary to the quantum case, this classical analysis does not lead to any singularity for  $\langle n^2(0) \rangle$ , so that we can directly plot this quantity as it is provided in ref. 47 in terms of the quasi-condensate density. For our interaction strength, we obtain a non-monotonic variation of  $C$ . This unexpected behavior, which does not match the experimental observations, probably signals that the present interaction strength  $\tilde{g} = 0.16$  (see “Methods” section and the Supplementary Note 5) is too large for using these classical field predictions, as already suggested in ref. 47.

Using the Ramsey interferometric scheme on a many-body system, we have measured the two-body contact of a 2D Bose gas over a wide range of phase-space densities. We could implement this scheme on our fluid thanks to the similarities of the three scattering lengths in play,  $a_{11}, a_{22}, a_{12}$ , corresponding to an approximate SU(2) symmetry for interactions. Our method can be generalized to the strongly interacting case  $a_{ij} \gtrsim a_z$ , as long as a Fano-Feshbach resonance allows one to stay close to the SU(2) point. One could then address the LHY-type corrections at zero temperature<sup>48,49</sup>, the contributions of the weakly-bound dimer state and of three-body contact<sup>13,14</sup>, or the breaking of scale invariance expected at non-zero temperature.

Finally, we note that even for our moderate interaction strength, classical field simulations seem to fail to reproduce our results, although they could properly account for the measurement of the equation of state itself<sup>43,44</sup>. The semi-classical treatment of ref. 50 and the quantum Monte Carlo approach of ref. 51 (see also ref. 52) should provide a reliable path to the modeling of this system. This would be particularly interesting in the vicinity of the BKT transition point where the usual approach based on the XY model<sup>53</sup>, which neglects any density fluctuation, does not provide relevant information on Tan’s contact. It would allow one to address the fundamental question raised for example in ref. 26, regarding the behavior of the contact  $C(\mathcal{D})$  or its derivatives in the vicinity of the phase transition, and the possibility to signal the position of the critical point either by a singularity or at least a fast variation of Tan’s contact around this point.

## Methods

The preparation and the characterization of our sample have been detailed in<sup>54,55</sup> and we briefly outline the main properties of the clouds explored in this work. In the  $xy$  plane, the atoms are confined in a disk of radius  $12 \mu\text{m}$  by a box-like potential, created by a laser beam properly shaped with a digital micromirror device. We use the intensity of this beam, which determines the height of the potential barrier around the disk, as a control parameter for the temperature. The confinement along the  $z$  direction is provided by a large-period optical lattice, with a single node occupied and  $\omega_z(2\pi) = 4.41$  (1) kHz. We set a magnetic field  $B = 0.701$  (1) G along the vertical direction  $z$ , which defines the quantization axis. We use the expression  $\mathcal{D}_c = \ln(380/\tilde{g})$  for the phase-space density at the critical point of the superfluid transition<sup>56</sup>. Here,  $\tilde{g} = \sqrt{8\pi} a_{11}/a_z = 0.16$  is the dimensionless interaction strength in 2D, leading to  $\mathcal{D}_c = 7.7$ . We study Bose gases from the normal regime ( $\mathcal{D} = 0.3\mathcal{D}_c$ ) to the strongly degenerate, superfluid regime ( $\mathcal{D} > 3\mathcal{D}_c$ ).

**Data availability**

The data sets generated and analyzed during the current study are available from the corresponding author on request.

Received: 28 July 2020; Accepted: 11 December 2020;

Published online: 03 February 2021

**References**

1. Tan, S. Large momentum part of a strongly correlated Fermi gas. *Ann. Phys.* **323**, 2971–2986 (2008).
2. Baym, G., Pethick, C. J., Yu, Z. & Zwierlein, M. W. Coherence and clock shifts in ultracold Fermi gases with resonant interactions. *Phys. Rev. Lett.* **99**, 190407 (2007).
3. Punk, M. & Zwerger, W. Theory of rf-spectroscopy of strongly interacting fermions. *Phys. Rev. Lett.* **99**, 170404 (2007).
4. Braaten, E. & Platter, L. Exact relations for a strongly interacting Fermi gas from the operator product expansion. *Phys. Rev. Lett.* **100**, 205301 (2008).
5. Werner, F., Tarruell, L. & Castin, Y. Number of closed-channel molecules in the BEC-BCS crossover. *Eur. Phys. J. B* **68**, 401–415 (2009).
6. Zhang, S. & Leggett, A. J. Universal properties of the ultracold Fermi gas. *Phys. Rev. A* **79**, 023601 (2009).
7. Combescot, R., Alzetto, F. & Leyronas, X. Particle distribution tail and related energy formula. *Phys. Rev. A* **79**, 053640 (2009).
8. Haussmann, R., Punk, M. & Zwerger, W. Spectral functions and rf response of ultracold fermionic atoms. *Phys. Rev. A* **80**, 063612 (2009).
9. Braaten, E. In *BCS-BEC Crossover and the Unitary Fermi Gas* (ed. Zwerger, W.) (Springer, 2011).
10. Petrov, D. S. Three-body problem in Fermi gases with short-range interparticle interaction. *Phys. Rev. A* **67**, 010703 (2003).
11. Endo, S. & Castin, Y. Absence of a four-body Efimov effect in the  $2 + 2$  fermionic problem. *Phys. Rev. A* **92**, 053624 (2015).
12. Braaten, E., Kang, D. & Platter, L. Universal relations for identical bosons from three-body physics. *Phys. Rev. Lett.* **106**, 153005 (2011).
13. Werner, F. & Castin, Y. General relations for quantum gases in two and three dimensions. II. Bosons and mixtures. *Phys. Rev. A* **86**, 053633 (2012).
14. Smith, D. H., Braaten, E., Kang, D. & Platter, L. Two-body and three-body contacts for identical bosons near unitarity. *Phys. Rev. Lett.* **112**, 110402 (2014).
15. Barth, M. & Hofmann, J. Efimov correlations in strongly interacting Bose gases. *Phys. Rev. A* **92**, 062716 (2015).
16. Stewart, J. T., Gaebler, J. P., Drake, T. E. & Jin, D. S. Verification of universal relations in a strongly interacting Fermi gas. *Phys. Rev. Lett.* **104**, 235301 (2010).
17. Kuhnle, E. D. et al. Universal behavior of pair correlations in a strongly interacting Fermi gas. *Phys. Rev. Lett.* **105**, 070402 (2010).
18. Carcy, C. et al. Contact and sum rules in a near-uniform Fermi gas at unitarity. *Phys. Rev. Lett.* **122**, 203401 (2019).
19. Mukherjee, B. et al. Spectral response and contact of the unitary Fermi gas. *Phys. Rev. Lett.* **122**, 203402 (2019).
20. Barth, M. & Zwerger, W. Tan relations in one dimension. *Ann. Phys.* **326**, 2544–2565 (2011).
21. Valiente, M., Zinner, N. T. & Mølmer, K. Universal properties of Fermi gases in arbitrary dimensions. *Phys. Rev. A* **86**, 043616 (2012).
22. Hofmann, J. et al. Quantum anomaly, universal relations, and breathing mode of a two-dimensional Fermi gas. *Phys. Rev. Lett.* **108**, 185303 (2012).
23. Langmack, C., Barth, M., Zwerger, W. & Braaten, E. Clock shift in a strongly interacting two-dimensional Fermi gas. *Phys. Rev. Lett.* **108**, 060402 (2012).
24. Vignolo, P. & Minguzzi, A. Universal contact for a Tonks-Girardeau gas at finite temperature. *Phys. Rev. Lett.* **110**, 020403 (2013).
25. Barth, M. & Hofmann, J. Pairing effects in the nondegenerate limit of the two-dimensional Fermi gas. *Phys. Rev. A* **89**, 013614 (2014).
26. Chen, Y.-Y., Jiang, Y.-Z., Guan, X.-W. & Zhou, Q. Critical behaviours of contact near phase transitions. *Nat. Commun.* **5**, 1–8 (2014).
27. Decamp, J., Albert, M. & Vignolo, P. Tan's contact in a cigar-shaped dilute Bose gas. *Phys. Rev. A* **97**, 033611 (2018).
28. He, M. & Zhou, Q.  $s$ -wave contacts of quantum gases in quasi-one-dimensional and quasi-two-dimensional traps. *Phys. Rev. A* **100**, 012701 (2019).
29. Wild, R. J., Makotyn, P., Pino, J. M., Cornell, E. A. & Jin, D. S. Measurements of Tan's contact in an atomic Bose-Einstein condensate. *Phys. Rev. Lett.* **108**, 145305 (2012).
30. Lopes, R. et al. Quasiparticle energy in a strongly interacting homogeneous Bose-Einstein condensate. *Phys. Rev. Lett.* **118**, 210401 (2017).
31. Fletcher, R. J. et al. Two- and three-body contacts in the unitary Bose gas. *Science* **355**, 377–380 (2017).
32. Berezinskii, V. L. Destruction of long-range order in one-dimensional and two-dimensional system possessing a continuous symmetry group - ii. quantum systems. *Sov. Phys. JETP* **34**, 610 (1971).
33. Kosterlitz, J. M. & Thouless, D. J. Ordering, metastability and phase transitions in two dimensional systems. *J. Phys. C* **6**, 1181 (1973).
34. Kosterlitz, J. M. Nobel lecture: Topological defects and phase transitions. *Rev. Mod. Phys.* **89**, 040501 (2017).
35. Huang, K. *Statistical Mechanics* (Wiley, New York, 1987).
36. Petrov, D. S. & Shlyapnikov, G. V. Interatomic collisions in a tightly confined Bose gas. *Phys. Rev. A* **64**, 012706 (2001).
37. Naraschewski, M. & Glauber, R. J. Spatial coherence and density correlations of trapped Bose gases. *Phys. Rev. A* **59**, 4595–4607 (1999).
38. Hadzibabic, Z. & Dalibard, J. Two-dimensional Bose fluids: an atomic physics perspective. *Riv. del Nuovo Cim.* **34**, 389–434 (2011).
39. van Kempen, E. G. M., M. F. Kokkelmans, S. J. J., Heinzen, D. J. & Verhaar, B. J. Isotope determination of ultracold rubidium interactions from three high-precision experiments. *Phys. Rev. Lett.* **88**, 093201 (2002).
40. Altin, P. A. et al. Optically trapped atom interferometry using the clock transition of large  $^{87}\text{Rb}$  Bose-Einstein condensates. *N. J. Phys.* **13**, 065020 (2011).
41. Chomaz, L. et al. Emergence of coherence via transverse condensation in a uniform quasi-two-dimensional Bose gas. *Nat. Commun.* **6**, 6162 (2015).
42. Lee, T. D., Huang, K. & Yang, C. N. Eigenvalues and eigenfunctions of a Bose system of hard spheres and its low-temperature properties. *Phys. Rev.* **106**, 1135 (1957).
43. Hung, C.-L., Xibo, Z., Nathan, G. & Cheng, C. Observation of scale invariance and universality in two-dimensional Bose gases. *Nature* **470**, 236 (2011).
44. Yefsah, T., Desbuquois, R., Chomaz, L., Günter, K. J. & Dalibard, J. Exploring the thermodynamics of a two-dimensional Bose gas. *Phys. Rev. Lett.* **107**, 130401 (2011).
45. Mora, C. & Castin, Y. Extension of Bogoliubov theory to quasicondensates. *Phys. Rev. A* **67**, 053615 (2003).
46. Ren, H.-C. The virial expansion of a dilute Bose gas in two dimensions. *J. Stat. Phys.* **114**, 481–501 (2004).
47. Prokof'ev, N. V. & Svistunov, B. V. Two-dimensional weakly interacting Bose gas in the fluctuation region. *Phys. Rev. A* **66**, 043608 (2002).
48. Mora, C. & Castin, Y. Ground state energy of the two-dimensional weakly interacting Bose gas: first correction beyond Bogoliubov theory. *Phys. Rev. Lett.* **102**, 180404 (2009).
49. Fournais, S., Napiorkowski, M., Reuvers, R. & Solovej, J. P. Ground state energy of a dilute two-dimensional Bose gas from the Bogoliubov free energy functional. *J. Math. Phys.* **60**, 071903 (2019).
50. Giorgetti, L., Carusotto, I. & Castin, Y. Semiclassical field method for the equilibrium Bose gas and application to thermal vortices in two dimensions. *Phys. Rev. A* **76**, 013613 (2007).
51. Holzmann, M. & Krauth, W. Kosterlitz-Thouless transition of the quasi-two-dimensional trapped Bose gas. *Phys. Rev. Lett.* **100**, 190402 (2008).
52. Raçon, A. & Dupuis, N. Universal thermodynamics of a two-dimensional Bose gas. *Phys. Rev. A* **85**, 063607 (2012).
53. Nelson, D. R. & Kosterlitz, J. M. Universal jump in the superfluid density of two-dimensional superfluids. *Phys. Rev. Lett.* **39**, 1201 (1977).
54. Ville, J. L. et al. Loading and compression of a single two-dimensional Bose gas in an optical accordion. *Phys. Rev. A* **95**, 013632 (2017).
55. Ville, J. L. et al. Sound propagation in a uniform superfluid two-dimensional Bose gas. *Phys. Rev. Lett.* **121**, 145301 (2018).
56. Prokof'ev, N. V., Ruebenacker, O. & Svistunov, B. V. Critical point of a weakly interacting two-dimensional Bose gas. *Phys. Rev. Lett.* **87**, 270402 (2001).

**Acknowledgements**

We thank Paul Julienne, Raphael Lopes, Félix Werner, Tarik Yefsah, Martin Zwierlein, Wilhem Zwerger, Johannes Hofmann, Markus Holzmann, and Qi Zhou for useful discussions. We acknowledge the contribution of Raphaël Saint-Jalm at the early stage of the project. This work was supported by ERC (Synergy Grant UQUAM), Quanter ERA-NET (NAQUAS project), and the ANR-18-CE30-0010 grant. Our team is a member of the SIRTEQ network of Région Ile-de-France.

**Author contributions**

Y.-Q.Z., B.B.-H., and C.M. performed the experiment and carried out the preliminary data analysis. Y.-Q.Z. performed detailed data analysis. E.L.C. participated in the preparation of the experimental setup. S.N., J.D., and J.B. contributed to the development of the theoretical model. J.D. and J.B. wrote the manuscript with contributions from all authors.

**Competing interests**

The authors declare no competing interests.

**Additional information**

**Supplementary information** is available for this paper at <https://doi.org/10.1038/s41467-020-20647-6>.

**Correspondence** and requests for materials should be addressed to J.B.

**Peer review information** *Nature Communications* thanks the anonymous reviewers for their contribution to the peer review of this work. Peer reviewer reports are available.

**Reprints and permission information** is available at <http://www.nature.com/reprints>

**Publisher's note** Springer Nature remains neutral with regard to jurisdictional claims in published maps and institutional affiliations.



**Open Access** This article is licensed under a Creative Commons Attribution 4.0 International License, which permits use, sharing, adaptation, distribution and reproduction in any medium or format, as long as you give appropriate credit to the original author(s) and the source, provide a link to the Creative Commons license, and indicate if changes were made. The images or other third party material in this article are included in the article's Creative Commons license, unless indicated otherwise in a credit line to the material. If material is not included in the article's Creative Commons license and your intended use is not permitted by statutory regulation or exceeds the permitted use, you will need to obtain permission directly from the copyright holder. To view a copy of this license, visit <http://creativecommons.org/licenses/by/4.0/>.

© The Author(s) 2021

**Magnetic Dipolar Interaction between Hyperfine Clock States in a Planar Alkali Bose Gas**Y.-Q. Zou, B. Bakali-Hassani, C. Maury, É. Le Cerf, S. Nascimbene<sup>✉</sup>, J. Dalibard, and J. Beugnon<sup>\*</sup>*Laboratoire Kastler Brossel, Collège de France, CNRS, ENS-PSL University,  
Sorbonne Université, 11 Place Marcelin Berthelot, 75005 Paris, France*

(Received 28 July 2020; accepted 4 November 2020; published 2 December 2020)

In atomic systems, clock states feature a zero projection of the total angular momentum and thus a low sensitivity to magnetic fields. This makes them widely used for metrological applications like atomic fountains or gravimeters. Here, we show that a mixture of two such nonmagnetic states still displays magnetic dipole-dipole interactions comparable to the one expected for the other Zeeman states of the same atomic species. Using high-resolution spectroscopy of a planar gas of  $^{87}\text{Rb}$  atoms with a controlled in plane shape, we explore the effective isotropic and extensive character of these interactions and demonstrate their tunability. Our measurements set strong constraints on the relative values of the  $s$ -wave scattering lengths  $a_{ij}$  involving the two clock states.

DOI: [10.1103/PhysRevLett.125.233604](https://doi.org/10.1103/PhysRevLett.125.233604)

Quantum atomic gases constitute unique systems to investigate many-body physics thanks to the precision with which one can control their interactions [1,2]. Usually, in the ultralow temperature regime achieved with these gases, contact interactions described by the  $s$ -wave scattering length dominate. In recent years, nonlocal interaction potentials have been added to the quantum gas toolbox. Long-range interactions can be mediated thanks to optical cavities inside which atoms are trapped [3]. Electric dipole-dipole interactions are routinely achieved via excitation of atoms in Rydberg electronic states [4]. Atomic species with large magnetic moments in the ground state, like Cr, Er, or Dy, offer the possibility to explore the role of magnetic dipole-dipole interactions (MDDIs) [5]. The latter case has led, for instance, to the observation of quantum droplets [6], roton modes [7], or spin dynamics in lattices with off site interactions [8–10].

For alkali-metal atoms, which are the workhorse of many cold-atom experiments, the magnetic moment is limited to  $\lesssim 1$  Bohr magneton ( $\mu_B$ ) and in most cases, MDDIs have no sizeable effect on the gas properties [11]. However, some paths have been investigated to evidence their role also for these atomic species. A first route consists of specifically nulling the  $s$ -wave scattering length using a Feshbach resonance [12,13], so that MDDIs become dominant. A second possibility is to operate with a multicomponent (or spinor) gas [14], using several states from the ground-level manifold of the atoms. One can then take advantage of a possible coincidence of the various scattering lengths in play. When it occurs, the spin-dependent contact interaction is much weaker than the spin-independent one, and MDDIs can have a significant effect [15], e.g., on the generation of spin textures [16,17] and on magnon spectra [18]. In all instances studied so far with these multicomponent gases, each component possesses a nonzero

magnetic moment and creates a magnetic field that influences its own dynamics, as well as the dynamics of the other component(s).

In this Letter, we present another, yet unexplored, context in which MDDIs can influence significantly the physics of a two-component gas of alkali-metal atoms. We operate with a superposition of the two hyperfine states of  $^{87}\text{Rb}$  involved in the so-called hyperfine clock transition,  $|1\rangle \equiv |F=1, m_Z=0\rangle$  and  $|2\rangle \equiv |F=2, m_Z=0\rangle$ , where the quantization axis  $Z$  is aligned with the uniform external magnetic field [Fig. 1(a)]. For a single-component gas prepared in one of these two states, the average magnetization is zero by symmetry and MDDIs have no effect. However, when atoms are simultaneously present in these two states, we show that magnetic interactions between them are nonzero, and that the corresponding MDDIs can modify significantly the position of the clock transition frequency.

Our Letter constitutes a magnetic analog of the observation of electric dipole-dipole interactions (EDDIs) between molecules in a Ramsey interferometric scheme [19]. There, in spite of the null value of the electric dipole moment of a molecule prepared in an energy eigenstate, it was shown that EDDIs can be induced in a molecular gas by preparing a coherent superposition of two rotational states. Both in our Letter and in [19], the coupling between two partners results in a pure exchange interaction, with one partner switching from  $|1\rangle$  to  $|2\rangle$  and the other one from  $|2\rangle$  to  $|1\rangle$ . This exchange Hamiltonian also appears for resonant EDDIs between atoms prepared in different Rydberg states [20].

In spite of their different origin, the physical manifestations of MDDIs in our setup are similar to the standard ones. Here, we study it for a 2D gas using high-resolution Ramsey spectroscopy [Fig. 1(b)] and we explicitly test two important features of dipole-dipole interactions in this



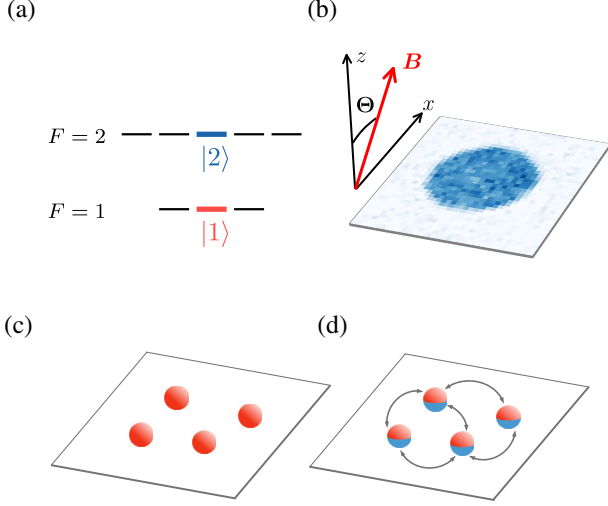


FIG. 1. (a) Level diagram of the hyperfine ground-level manifold showing the two states relevant to this Letter:  $|1\rangle \equiv |F=1, m_Z=0\rangle$  and  $|2\rangle \equiv |F=2, m_Z=0\rangle$ . (b) Image of the atomic cloud obtained through absorption imaging along the direction perpendicular to the atomic plane. Atoms are confined in the  $xy$  plane in a disk of radius  $12\ \mu\text{m}$ . The orientation of the magnetic field  $\mathbf{B}$  is tuned in the  $xz$  plane. (c) Schematics of atoms prepared in the state  $|1\rangle$ , with no MDDIs in this case. MDDIs are also absent when all atoms are in  $|2\rangle$ . (d) Significant MDDIs occur for atoms in a linear superposition of  $|1\rangle$  and  $|2\rangle$ .

planar geometry: their effect does not depend on the in plane shape of the cloud (isotropy), nor on its size (extensivity). More precisely, we recast the role of MDDIs as a modification of the  $s$ -wave interspecies scattering length  $a_{12}$  and show the continuous tuning of  $a_{12}$  by changing the orientation of the external magnetic field with respect to the atom plane. We obtain in this way accurate information on the relative values of intra- and interspecies bare scattering lengths of the studied states.

We start with the restriction of the MDDIs Hamiltonian to the clock state manifold [21], using the magnetic interaction between two electronic spins  $\hat{\mathbf{s}}_A$  and  $\hat{\mathbf{s}}_B$  with magnetic moments  $\mathbf{m}_{A,B} = 2\mu_B \mathbf{s}_{A,B}$ ,

$$\hat{V}_{dd}(\mathbf{r}, \mathbf{u}) = \frac{\mu_0 \mu_B^2}{\pi r^3} [\hat{\mathbf{s}}_A \cdot \hat{\mathbf{s}}_B - 3(\hat{\mathbf{s}}_A \cdot \mathbf{u})(\hat{\mathbf{s}}_B \cdot \mathbf{u})], \quad (1)$$

where  $r$  is the distance between the two dipoles and  $\mathbf{u}$  is the unit vector connecting them. The calculation detailed in the Supplemental Material [22] shows that MDDIs do not modify the interactions between atoms in the same state  $|1\rangle$  or  $|2\rangle$ , but induce a nonlocal, angle-dependent exchange interaction [Figs. 1(c) and 1(d)]. The second-quantized Hamiltonian of the MDDIs for the clock states is thus

$$\hat{H}_{dd}^{(1,2)} = \frac{\mu_0 \mu_B^2}{4\pi} \iint d^3 r_A d^3 r_B \frac{1 - 3 \cos^2 \theta}{r^3} \times \hat{\Psi}_2^\dagger(\mathbf{r}_A) \hat{\Psi}_1^\dagger(\mathbf{r}_B) \hat{\Psi}_2(\mathbf{r}_B) \hat{\Psi}_1(\mathbf{r}_A), \quad (2)$$

where the  $\hat{\Psi}_i(\mathbf{r}_a)$  are the field operators annihilating a particle in state  $|i\rangle$  at position  $\mathbf{r}_a$ ,  $r = |\mathbf{r}_A - \mathbf{r}_B|$ , and  $\theta$  is the angle between  $\mathbf{r}_A - \mathbf{r}_B$  and the quantization axis.

We now investigate the spatial average value of  $\hat{H}_{dd}^{(1,2)}$ . We note first that, for a 3D isotropic gas, the angular integration gives  $\langle \hat{H}_{dd}^{(1,2)} \rangle_{3D} = 0$ , as usual for MDDIs [5]. We then consider a homogeneous quasi-2D Bose gas confined isotropically in the  $xy$  plane with area  $L^2$ . We assume that the gas has a Gaussian density profile along the third direction  $z$ ,  $n_{1,2}(z) = N_{1,2} e^{-z^2/\ell_z^2} / \sqrt{\pi} \ell_z L^2$ , where  $\ell_z = \sqrt{\hbar/m\omega_z}$  is the extension of the ground state of the harmonic confinement of frequency  $\omega_z$  for particles of mass  $m$ , and  $N_{1,2}$  is the atom number in states  $|1\rangle$ ,  $|2\rangle$ . One then finds [23–25]

$$\langle \hat{H}_{dd}^{(1,2)} \rangle_{2D} = \frac{\mu_0 \mu_B^2 N_1 N_2}{3\sqrt{2\pi} \ell_z L^2} (3 \cos^2 \Theta - 1), \quad (3)$$

where  $\Theta$  is the angle between the external magnetic field  $\mathbf{B}$  and the direction perpendicular to the atomic plane. This energy is maximal and positive for  $\mathbf{B}$  perpendicular to the atomic plane ( $\Theta = 0$ ) and minimal and negative for  $\mathbf{B}$  in the atomic plane ( $\Theta = \pi/2$ ). Equation (3) shows that the energy per atom in state  $|1\rangle$  depends only on the spatial density  $N_2/L^2$  of atoms in state  $|2\rangle$ , which proves the extensivity.

In 2D, the Fourier transform of the dipole-dipole Hamiltonian possesses a well-defined value at the origin  $\mathbf{k} = 0$  [23]. Consequently, for a large enough sample (typically,  $L \gg \ell_z$ ), the average energy  $\langle \hat{H}_{dd}^{(1,2)} \rangle_{2D}$ , evaluated by switching the integral (2) to Fourier space, is independent of the system shape. This contrasts with the 3D case, for which the MDDIs energy changes sign when switching from an oblate to a prolate cloud [5,26]. Considering the effective isotropy of the MDDIs in this 2D configuration, it is convenient to describe their role as a change  $\delta a_{12}$  of the interspecies scattering length with respect to its bare value defined as  $a_{12}^{(0)}$ . In 2D, interspecies contact interactions lead to  $\langle \hat{H}_{\text{contact}}^{(1,2)} \rangle_{2D} = \sqrt{8\pi} a_{12} \hbar^2 N_1 N_2 / (m \ell_z L^2)$  and we deduce

$$\delta a_{12}(\Theta) = a_{dd} (3 \cos^2 \Theta - 1), \quad (4)$$

where  $a_{dd} = \mu_0 \mu_B^2 m / (12\pi \hbar^2)$  is the so-called dipole length that quantifies the strength of MDDIs [27].

We now tackle the experimental observation of this modification of the interspecies scattering length in a quasi-2D Bose gas. The experimental setup was described in [30,31]. Basically, a cloud of  $^{87}\text{Rb}$  atoms in state  $|1\rangle$  is confined in a 2D box potential: A “hard-wall” potential provides a uniform in plane confinement inside a  $12\ \mu\text{m}$  radius disk, unless otherwise stated. The vertical confinement can be approximated by a harmonic potential

with frequency  $\omega_z/2\pi = 4.4(1)$  kHz, corresponding to  $\ell_z = 160$  nm. We operate in the weakly interacting regime characterized by the dimensionless coupling constant  $\tilde{g} = \sqrt{8\pi}a_{11}/\ell_z = 0.16(1)$ , where  $a_{11}$  is the  $s$ -wave scattering length for atoms in  $|1\rangle$ . The in plane density of the cloud is  $\bar{n} \approx 95/\mu\text{m}^2$  and we operate at the lowest achievable temperature in our setup  $T < 30$  nK. A  $\approx 0.7$  G bias magnetic field  $\mathbf{B}$  with tunable orientation is fixed during the experiment.

Spectroscopy is performed thanks to a Ramsey sequence similar to [32]. Atoms initially in  $|1\rangle$  are coupled to state  $|2\rangle$  with a microwave field tuned around the hyperfine splitting of 6.8 GHz. A first Ramsey pulse with a typical duration of a few tens of microseconds, creates a superposition of the two clock states with a tunable weight. After an “interrogation time”  $T_R = 10$  ms, a second identical Ramsey pulse is applied [33]. After this second pulse, we perform absorption imaging to determine the population in  $|2\rangle$ . We measure the variation of this population as a function of the frequency of the microwave field, see Figs. 2(a) and 2(b). We fit a sinusoidal function to the data, so as to determine the resonance frequency of the atomic cloud. All frequency measurements  $\Delta\nu$  are reported with respect to reference measurements of the single-atom response that we perform on a dilute cloud. The typical dispersion of the measurement of this single-atom response is about 1 Hz and provides an estimate of our uncertainty on the frequency measurements. We checked that the measured resonance frequencies are independent of  $T_R$  in the range 5–20 ms. Shorter delays lead to a lower accuracy on the frequency measurement. For longer delays, we observe demixing dynamics [34] between the two components and a modification of the resonance frequency.

In the following, we restrict to the case of strongly degenerate clouds [35] described in the mean-field approximation. Consider first the case of a uniform 3D gas. The resonant frequency  $\Delta\nu$  can be computed by evaluating the difference of mean-field shifts for the two components [32],

$$\Delta\nu = \frac{\hbar}{m} n[a_{22} - a_{11} + (2a_{12} - a_{11} - a_{22})f]. \quad (5)$$

Here the  $a_{ij}$  are the inter- and intraspecies scattering lengths,  $n = n_1 + n_2$  is the total 3D density of the cloud where each component  $i$  has a density  $n_i$  after the first Ramsey pulse and  $f = (n_1 - n_2)/(n_1 + n_2)$  describes the population imbalance between the two states.

It is interesting to discuss briefly two limiting cases of Eq. (5). In the low transfer limit  $f \approx 1$ , the first Ramsey pulse produces only a few atoms in state  $|2\rangle$ , imbedded in a bath of state  $|1\rangle$  atoms. Interactions within pairs of state  $|2\rangle$  atoms then play a negligible role, so that the shift  $\Delta\nu$  does not depend on  $a_{22}$ . It is proportional to  $(a_{12} - a_{11})$ , hence sensitive to MDDIs. In the balanced case  $f = 0$ , the Ramsey sequence transforms a gas initially composed only of atoms in state  $|1\rangle$  into a gas composed only of atoms in

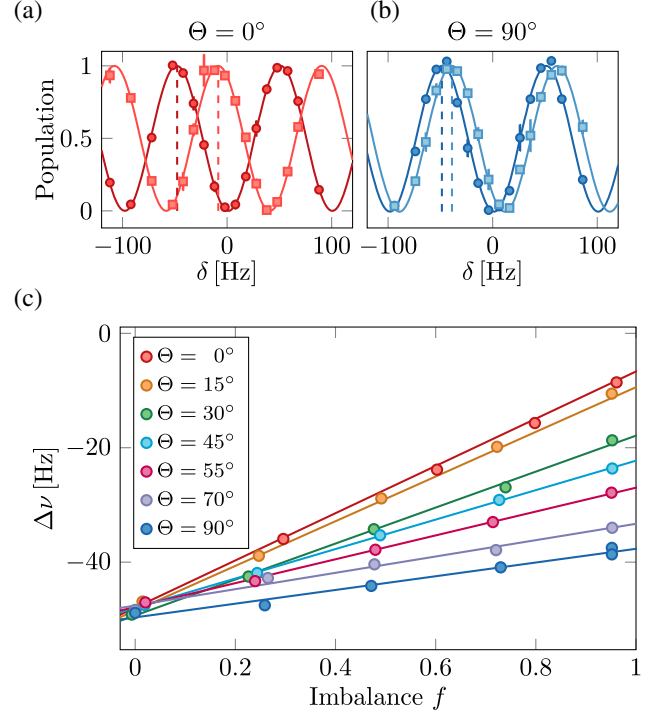


FIG. 2. (a),(b) Normalized Ramsey oscillations measured for  $\mathbf{B}$  perpendicular ( $\Theta = 0^\circ$ ) or parallel ( $\Theta = 90^\circ$ ) to the atomic plane. For both cases, we show the transferred population as a function of detuning  $\delta$  to the single-atom resonance. In each case the resonance is marked by a vertical dashed line. The circles (respectively, squares) correspond to a balanced (respectively, unbalanced) mixture  $f = 0$  (respectively,  $f \approx 0.95$ ). Vertical error bars represent the standard deviation from the two measurements realized for each points. (c) Variation of the frequency shift  $\Delta\nu$  with the imbalance  $f$ . We restrict to positive imbalances, for which the population in  $|2\rangle$  remains small enough to limit the role of two-body relaxation and spin-changing collisions. For each angle, the solid line is a linear fit to the data.

state  $|2\rangle$ . The energy balance between initial and final states then gives a contribution  $\Delta\nu \propto (a_{22} - a_{11})$ , which is insensitive to MDDIs.

It is important to note that the validity of Eq. (5) for a many-body system is not straightforward and requires some care [36,37]. We discuss in Ref. [38] the applicability of this approach to our experimental system and show that it relies on the almost equality of the three relevant scattering lengths  $a_{ij}$  of the problem. Note also that in our geometry, even if the gas is uniform in plane, the density distribution along  $z$  is inhomogeneous and the spectroscopy measurement is thus sensitive to the integrated density  $\bar{n}(x, y) = \int dz n(x, y, z)$ .

We now discuss the measurement of the frequency shift  $\Delta\nu$  as a function of the imbalance  $f$  for different orientations of the magnetic field with respect to the atomic plane, see Fig. 2(c). For each orientation, we confirm the linear behavior expected from Eq. (5). The variation of the slope

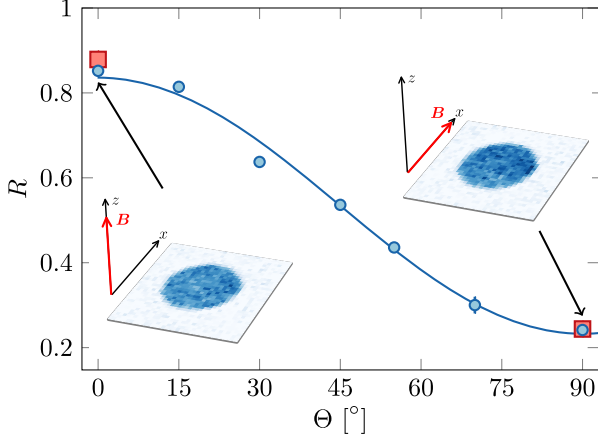


FIG. 3. Variation of the ratio  $R(\Theta)$  determined from the data of Fig. 2(c) with the magnetic field orientation  $\Theta$ . Blue circles (respectively, red squares) correspond to the measurement at maximum density (respectively, half density). The variation of this ratio is well fitted by a cosine variation compatible with the prediction for MDDIs. The amplitude and offset of this variation allow one to determine accurately relative values of the scattering lengths. Vertical error bars represent the uncertainty obtained from the fitting procedure of the data in Fig. 2. The uncertainty on the determination of the angles is limited by the geometrical arrangement of the coils generating the field  $\mathbf{B}$ , estimated here at the level of  $1^\circ$ .

$d\Delta\nu/df$  for different orientations reflects the expected modification of  $a_{12}$  with  $\Theta$  of Eq. (4). More quantitatively, we fit a linear function to the data for each  $\Theta$ . The ratio of the slope to the intercept of this line is  $R(\Theta) = [a_{22} + a_{11} - 2a_{12}(\Theta)]/(a_{22} - a_{11})$ . Interestingly, this ratio is independent of the density calibration and is thus a robust observable.

The evolution of the measured ratio for different angles is shown in Fig. 3. For  $\Theta = 0^\circ$  and  $90^\circ$ , we also show the ratio measured for a density approximately twice as small as the one of Fig. 2. These two points overlap well with the main curve, which confirms the insensitivity of  $R$  with respect to  $\bar{n}$ . We fit a sinusoidal variation  $\Theta \mapsto \alpha + \beta \cos(2\Theta)$  to  $R(\Theta)$  from which we extract  $\alpha = 0.53(1)$  and  $\beta = 0.30(1)$ . We then determine  $a_{22} - a_{11} = -3a_{dd}/\beta$  and  $a_{12}^{(0)} - a_{11} = a_{dd}(3\alpha - 3 - \beta)/(2\beta)$ . Using  $a_{dd} = 0.70a_0$ , with  $a_0$  the Bohr radius, we find  $a_{22} - a_{11} = -7.0(2)a_0$  and  $a_{12}^{(0)} - a_{11} = -2.0(1)a_0$ . These results are in good agreement with the values predicted in [39],  $a_{11} = 100.9a_0$ ,  $a_{22} - a_{11} = -6.0a_0$ , and  $a_{12}^{(0)} - a_{11} = -2.0a_0$ .

All experiments described so far have been realized with a fixed disk geometry. As stated above, the description of the contribution of MDDIs as a modification of the interspecies scattering length relies on the effective isotropy of the interaction in our 2D system. We investigate this issue by measuring the frequency shift of the clock transition for an in plane magnetic field orientation

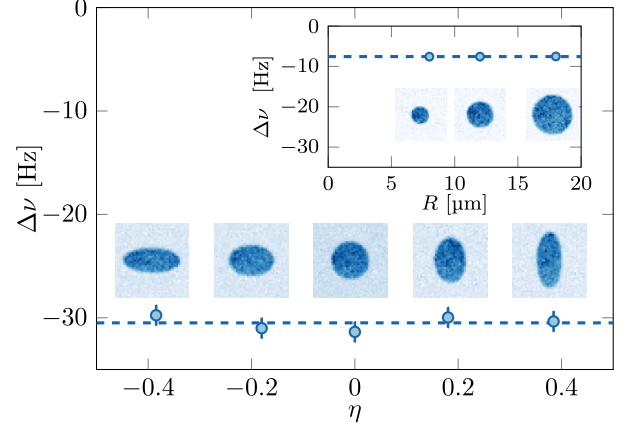


FIG. 4. Interaction shift  $\Delta\nu$  as a function of the anisotropy parameter  $\eta$ . For a fixed density and an in plane magnetic field, we vary the anisotropy of the elliptically shaped 2D cloud. No dependence on the shape of the cloud is observed, in agreement with the expected isotropic character of MDDIs in 2D when  $R_{x,y} \gg \ell_z$ . Vertical error bars represent the estimated 1 Hz accuracy on the determination of the single-atom resonance frequency. Inset: interaction shift as a function of the size of the cloud, for  $\mathbf{B}$  normal to the atom plane.

( $\Theta = 90^\circ$ ), which breaks the rotational symmetry of the system. We operate with a fixed density ( $\bar{n} \approx 80/\mu\text{m}^2$ ) and a varying elliptical shape. We choose a large imbalance  $f \approx 0.95$  to have the highest sensitivity to possible modifications of  $a_{12}$ . We define an anisotropy parameter  $\eta = (R_y - R_x)/(R_x + R_y)$  for the ratio of the lengths  $R_x$  and  $R_y$  of the two axes of the ellipse. We report in Fig. 4 the measured shifts as a function of  $\eta$  and confirm, within our experimental accuracy, the independence of the MDDIs energy with respect to the cloud shape. We have also investigated the influence of the size of the cloud on  $\Delta\nu$  (inset of Fig. 4). Here we choose a disk-shaped cloud and a magnetic field perpendicular to the atomic plane. We observe no detectable change of  $\Delta\nu$  when changing the disk radius from 8 to  $18 \mu\text{m}$ , which confirms the absence of significant finite-size effects.

In conclusion, thanks to high-resolution spectroscopy we revealed the non-negligible role of magnetic dipolar interactions between states with a zero average magnetic moment. We observed and explained the modification of the interspecies scattering length in a two-component cloud. Because of the smallness of MDDIs for alkali-metal atoms, we did not observe any modification of the global shape of the cloud. This contrasts with the case of single-component highly magnetic dipolar gases where the shape of a trapped gas has been modified with a static [40–42] or time-averaged-field [11,43]. Nevertheless, the effect observed here provides a novel control on the dynamics of two-component gases. For example, the effective interaction parameter between two atoms in state  $|2\rangle$  mediated by a bath of atoms in state  $|1\rangle$  can be written as



$\tilde{g}_{22}^{\text{eff}} = \tilde{g}_{22} - \tilde{g}_{12}^2/\tilde{g}_{11}$ , where  $\tilde{g}_{ij} = \sqrt{8\pi}a_{ij}/\ell_z$  [44]. With our parameters, we achieve a variation by a factor 7 of  $\tilde{g}_{22}^{\text{eff}}$ , which will lead to important modifications of polaron dynamics. Similarly, it can be exploited to tune the miscibility of mixtures or the dynamics of spin textures. The distance to the critical point for miscibility, whose position is given by  $\tilde{g}_{22}\tilde{g}_{11} = \tilde{g}_{12}^2$ , is also strongly sensitive to a variation of  $\tilde{g}_{12}$ . For instance, the length scale of spin textures appearing in phase separation dynamics of a balanced mixture will be modified, for our parameters, by a factor of almost 3 when  $\Theta$  is switched from  $0^\circ$  to  $90^\circ$  [34]. In addition, one can exploit the nonlocal character of MDDIs by confining the atoms in a deep lattice at unit filling, where the exchange coupling evidenced here will implement the so-called quantum XX model [45] without requiring any tunneling between lattice sites. The extreme sensitivity of the clock transition and its protection from magnetic perturbations will then provide a novel, precise tool to detect the various phases of matter predicted within this model.

This work is supported by ERC (Synergy UQUAM), European Union's Horizon 2020 Programme (QuantERA-NAQUAS project), and the ANR-18-CE30-0010 grant. We thank F. Pereira dos Santos, M. Zwierlein, and P. Julienne for stimulating discussions. We acknowledge the contribution of R. Saint-Jalm at the early stage of the project.

\*beugnon@lkb.ens.fr

- [1] C. Chin, R. Grimm, P. Julienne, and E. Tiesinga, Feshbach resonances in ultracold gases, *Rev. Mod. Phys.* **82**, 1225 (2010).
- [2] I. Bloch, J. Dalibard, and W. Zwerger, Many-body physics with ultracold gases, *Rev. Mod. Phys.* **80**, 885 (2008).
- [3] K. Baumann, C. Guerlin, F. Brennecke, and T. Esslinger, Dicke quantum phase transition with a superfluid gas in an optical cavity, *Nature (London)* **464**, 1301 (2010).
- [4] R. Löw, H. Weimer, J. Nipper, J. B. Balewski, B. Butscher, H. P. Büchler, and T. Pfau, An experimental and theoretical guide to strongly interacting Rydberg gases, *J. Phys. B* **45**, 113001 (2012).
- [5] T. Lahaye, C. Menotti, L. Santos, M. Lewenstein, and T. Pfau, The physics of dipolar bosonic quantum gases, *Rep. Prog. Phys.* **72**, 126401 (2009).
- [6] I. Ferrier-Barbut, H. Kadau, M. Schmitt, M. Wenzel, and T. Pfau, Observation of Quantum Droplets in a Strongly Dipolar Bose Gas, *Phys. Rev. Lett.* **116**, 215301 (2016).
- [7] L. Chomaz, R. M. W. van Bijnen, D. Petter, G. Faraoni, S. Baier, J. H. Becher, M. J. Mark, F. Waechtler, L. Santos, and F. Ferlaino, Observation of Roton mode population in a dipolar quantum gas, *Nat. Phys.* **14**, 442 (2018).
- [8] A. de Paz, A. Sharma, A. Chotia, E. Maréchal, J. H. Huckans, P. Pedri, L. Santos, O. Gorceix, L. Vernac, and B. Laburthe-Tolra, Nonequilibrium Quantum Magnetism in a Dipolar Lattice Gas, *Phys. Rev. Lett.* **111**, 185305 (2013).
- [9] S. Baier, M. J. Mark, D. Petter, K. Aikawa, L. Chomaz, Z. Cai, M. Baranov, P. Zoller, and F. Ferlaino, Extended Bose-Hubbard models with ultracold magnetic atoms, *Science* **352**, 201 (2016).
- [10] S. Lepoutre, J. Schachenmayer, L. Gabardos, B. Zhu, B. Naylor, E. Maréchal, O. Gorceix, A. M. Rey, L. Vernac, and B. Laburthe-Tolra, Out-of-equilibrium quantum magnetism and thermalization in a spin-3 many-body dipolar lattice system, *Nat. Commun.* **10**, 1714 (2019).
- [11] S. Giovanazzi, A. Görlitz, and T. Pfau, Tuning the Dipolar Interaction in Quantum Gases, *Phys. Rev. Lett.* **89**, 130401 (2002).
- [12] M. Fattori, G. Roati, B. Deissler, C. D'Errico, M. Zaccanti, M. Jona-Lasinio, L. Santos, M. Inguscio, and G. Modugno, Magnetic Dipolar Interaction in a Bose-Einstein Condensate Atomic Interferometer, *Phys. Rev. Lett.* **101**, 190405 (2008).
- [13] S. E. Pollack, D. Dries, M. Junker, Y. P. Chen, T. A. Corcovilos, and R. G. Hulet, Extreme Tunability of Interactions in a  $^7\text{Li}$  Bose-Einstein Condensate, *Phys. Rev. Lett.* **102**, 090402 (2009).
- [14] D. M. Stamper-Kurn and M. Ueda, Spinor Bose gases: Symmetries, magnetism, and quantum dynamics, *Rev. Mod. Phys.* **85**, 1191 (2013).
- [15] S. Yi, L. You, and H. Pu, Quantum Phases of Dipolar Spinor Condensates, *Phys. Rev. Lett.* **93**, 040403 (2004).
- [16] M. Vengalattore, S. R. Leslie, J. Guzman, and D. M. Stamper-Kurn, Spontaneously Modulated Spin Textures in a Dipolar Spinor Bose-Einstein Condensate, *Phys. Rev. Lett.* **100**, 170403 (2008).
- [17] Y. Eto, H. Saito, and T. Hirano, Observation of Dipole-Induced Spin Texture in an  $^{87}\text{Rb}$  Bose-Einstein Condensate, *Phys. Rev. Lett.* **112**, 185301 (2014).
- [18] G. E. Marti, A. MacRae, R. Olf, S. Lourette, F. Fang, and D. M. Stamper-Kurn, Coherent Magnon Optics in a Ferromagnetic Spinor Bose-Einstein Condensate, *Phys. Rev. Lett.* **113**, 155302 (2014).
- [19] B. Yan, S. A. Moses, B. Gadway, J. P. Covey, K. R. A. Hazzard, A. M. Rey, D. S. Jin, and J. Ye, Observation of dipolar spin-exchange interactions with lattice-confined polar molecules, *Nature (London)* **501**, 521 (2013).
- [20] S. de Léséleuc, D. Barredo, V. Lienhard, A. Browaeys, and T. Lahaye, Optical Control of the Resonant Dipole-Dipole Interaction between Rydberg Atoms, *Phys. Rev. Lett.* **119**, 053202 (2017).
- [21] For all experiments reported here, the fraction of atoms in any other spin state remains below our detection sensitivity of 1%.
- [22] See Supplemental Material at <http://link.aps.org/supplemental/10.1103/PhysRevLett.125.233604> for details on the calculation of the effective interspecies scattering length  $a_{12}$ .
- [23] U. R. Fischer, Stability of quasi-two-dimensional Bose-Einstein condensates with dominant dipole-dipole interactions, *Phys. Rev. A* **73**, 031602(R) (2006).
- [24] A. K. Fedorov, I. L. Kurbakov, Y. E. Schchadilova, and Yu. E. Lozovik, Two-dimensional Bose gas of tilted dipoles: Roton instability and condensate depletion, *Phys. Rev. A* **90**, 043616 (2014).
- [25] C. Mishra and R. Nath, Dipolar condensates with tilted dipoles in a pancake-shaped confinement, *Phys. Rev. A* **94**, 033633 (2016).

- [26] S. Yi and L. You, Trapped atomic condensates with anisotropic interactions, *Phys. Rev. A* **61**, 041604(R) (2000).
- [27] We use the definition of Ref. [5]. Other definitions with a different numerical factor are found in the literature, see for instance, [28,29].
- [28] D. C. E. Bortolotti, S. Ronen, J. L. Bohn, and D. Blume, Scattering Length Instability in Dipolar Bose-Einstein Condensates, *Phys. Rev. Lett.* **97**, 160402 (2006).
- [29] M. A. Baranov, M. Dalmonte, G. Pupillo, and P. Zoller, Condensed matter theory of dipolar quantum gases, *Chem. Rev.* **112**, 5012 (2012).
- [30] J. L. Ville, T. Bienaimé, R. Saint-Jalm, L. Corman, M. Aidelsburger, L. Chomaz, K. Kleinlein, D. Perconte, S. Nascimbène, J. Dalibard, and J. Beugnon, Loading and compression of a single two-dimensional Bose gas in an optical accordion, *Phys. Rev. A* **95**, 013632 (2017).
- [31] R. Saint-Jalm, P. C. M. Castilho, É. Le Cerf, B. Bakali-Hassani, J.-L. Ville, S. Nascimbene, J. Beugnon, and J. Dalibard, Dynamical Symmetry and Breathers in a Two-Dimensional Bose Gas, *Phys. Rev. X* **9**, 021035 (2019).
- [32] D. M. Harber, H. J. Lewandowski, J. M. McGuirk, and E. A. Cornell, Effect of cold collisions on spin coherence and resonance shifts in a magnetically trapped ultracold gas, *Phys. Rev. A* **66**, 053616 (2002).
- [33] The imbalance  $f$  is tuned mostly by changing the pulse duration but for small pulses area it is more convenient to also decrease the Rabi frequency to avoid using very short microwave pulses.
- [34] E. Timmermans, Phase Separation of Bose-Einstein Condensates, *Phys. Rev. Lett.* **81**, 5718 (1998).
- [35] At nonzero temperature, quantum statistics of thermal bosons lead to multiply this shift by a factor which varies from 1 in the very degenerate regime to 2 for a thermal cloud.
- [36] M. J. Martin, M. Bishof, M. D. Swallows, X. Zhang, C. Benko, J. von Stecher, A. V. Gorshkov, A. M. Rey, and J. Ye, A quantum many-body spin system in an optical lattice clock, *Science* **341**, 632 (2013).
- [37] R. J. Fletcher, R. Lopes, J. Man, N. Navon, R. P. Smith, M. W. Zwierlein, and Z. Hadzibabic, Two- and three-body contacts in the unitary Bose gas, *Science* **355**, 377 (2017).
- [38] Y.-Q. Zou, B. Bakali-Hassani, C. Maury, É. Le Cerf, S. Nascimbene, J. Dalibard, and J. Beugnon, Tan's two-body contact across the superfluid transition of a planar Bose gas, [arXiv:2007.12385](https://arxiv.org/abs/2007.12385).
- [39] P. A. Altin, G. McDonald, D. Döring, J. E. Debs, T. H. Barter, J. D. Close, N. P. Robins, S. A. Haine, T. M. Hanna, and R. P. Anderson, Optically trapped atom interferometry using the clock transition of large  $^{87}\text{Rb}$  Bose-Einstein condensates, *New J. Phys.* **13**, 065020 (2011).
- [40] D. H. J. O'Dell, S. Giovanazzi, and C. Eberlein, Exact Hydrodynamics of a Trapped Dipolar Bose-Einstein Condensate, *Phys. Rev. Lett.* **92**, 250401 (2004).
- [41] J. Stuhler, A. Griesmaier, T. Koch, M. Fattori, T. Pfau, S. Giovanazzi, P. Pedri, and L. Santos, Observation of Dipole-Dipole Interaction in a Degenerate Quantum Gas, *Phys. Rev. Lett.* **95**, 150406 (2005).
- [42] T. Lahaye, T. Koch, B. Fröhlich, M. Fattori, J. Metz, A. Griesmaier, S. Giovanazzi, and T. Pfau, Strong dipolar effects in a quantum ferrofluid, *Nature (London)* **448**, 672 (2007).
- [43] Y. Tang, W. Kao, K. Y. Li, and B. L. Lev, Tuning the Dipole-Dipole Interaction in a Quantum Gas with a Rotating Magnetic Field, *Phys. Rev. Lett.* **120**, 230401 (2018).
- [44] C. J. Pethick and H. Smith, *Bose-Einstein Condensation in Dilute Gases* (Cambridge University Press, Cambridge, England, 2008).
- [45] S. Sachdev, *Quantum Phase Transitions* (Cambridge University Press, Cambridge, England, 2006).

## Letter

# Optical control of the density and spin spatial profiles of a planar Bose gas

Y-Q Zou<sup>1,4</sup>, É Le Cerf<sup>1,4</sup>, B Bakkali-Hassani<sup>1</sup>, C Maury<sup>1</sup>, G Chauveau<sup>1</sup>,  
P C M Castilho<sup>2</sup>, R Saint-Jalm<sup>3</sup>, S Nascimbene<sup>1</sup> , J Dalibard<sup>1</sup> and  
J Beugnon<sup>1,\*</sup> 

<sup>1</sup> Laboratoire Kastler Brossel, Collège de France, CNRS, ENS-PSL University, Sorbonne Université, 11 Place Marcelin Berthelot, 75005 Paris, France

<sup>2</sup> Instituto de Física de São Carlos, Universidade de São Paulo, CP 369, 13560-970 São Carlos, Brazil

<sup>3</sup> Department of Physics, Ludwig-Maximilians-Universität München, Schellingstr. 4, D-80799 München, Germany

E-mail: [beugnon@lkb.ens.fr](mailto:beugnon@lkb.ens.fr)

Received 13 February 2021, revised 19 March 2021

Accepted for publication 25 March 2021

Published 30 April 2021



## Abstract

We demonstrate the arbitrary control of the density profile of a two-dimensional Bose gas by shaping the optical potential applied to the atoms. We use a digital micromirror device (DMD) directly imaged onto the atomic cloud through a high resolution imaging system. Our approach relies on averaging the response of many pixels of the DMD over the diffraction spot of the imaging system, which allows us to create an optical potential with an arbitrary intensity profile and with micron-scale resolution. The obtained density distribution is optimized with a feedback loop based on the measured absorption images of the cloud. Using the same device, we also engineer arbitrary spin distributions thanks to a two-photon Raman transfer between internal ground states.

Keywords: quantum gases, spatial light modulator, spin textures

(Some figures may appear in colour only in the online journal)

## 1. Introduction

Ultracold quantum gases are ideal platforms to study physical phenomena, thanks to their high flexibility and their isolation from the environment. They are widely used for quantum simulations [1] and metrological applications [2]. Various trap geometries have been realized to confine atomic clouds. Historically, harmonic confinements have been the norm in cold atom experiments due to their ease of implementation [3, 4].

The recent realization of uniform systems opened new perspectives to explore the thermodynamic properties and dynamical behavior of quantum gases [5–8]. Other trap potentials have been applied to explore physics in specific geometries, such as supercurrents in ring potentials [9–12], analog sonic black holes in more complex potentials [13], and low-entropy phases in lattice systems [14].

In the past years, several approaches have been developed to generate complex optical potential profiles [15–22]. Most of them rely on the development of spatial light modulators, which can modulate the phase or the intensity of a light beam. Digital micromirror devices (DMDs) are one of the most widely used in cold atom experiments thanks to their low cost, simple use and high refresh rates. They consist of millions of individual micromirrors which can be set in two different ori-

<sup>4</sup> These authors contributed equally to this work.

\* Author to whom any correspondence should be addressed.

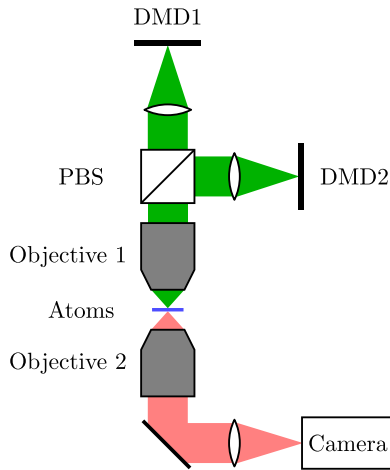


**Figure 1.** Sketch of the experimental setup for arbitrary density control. Two DMDs are used to project an optical potential onto the atoms with a high NA microscope objective (objective 1). Both of them are illuminated by a blue-detuned 532 nm laser. DMD1 provides the hard-wall potential, while DMD2 adds an additional potential for density control. The light fields from the two DMDs are mixed on a polarizing beam splitter with orthogonal polarizations so that they do not interfere with each other. The atoms are imaged onto the camera with a second identical objective (objective 2). We use absorption imaging to measure the 2D density profiles on a CCD camera.

entations, hence corresponding to a ‘black’ or ‘white’ signal in a chosen image plane of the DMD chip. They have been used to correct optical aberrations when working as a programmable amplitude hologram in a Fourier plane [23], and to produce different potential profiles by direct imaging [21, 24–26].

In this article, we demonstrate arbitrary control of the density profile of two-dimensional (2D) Bose gases by tailoring the in-plane trapping potential using DMDs. We program a pattern on the DMD chip and simply image it onto the atomic cloud. The limitation due to the binary status of the DMD pixels (black or white) is overcome by realizing a spatial average of the response of  $\sim 25$  pixels over the point spread function of the imaging system. This gives us access to several levels of grey for the optical potential at a given position in the atomic plane. The DMD pattern is computed thanks to an error diffusion algorithm combined with a feedback loop to directly optimize the measured atomic density distribution. The method is proved to be efficient and robust to optical imperfections. In addition, we demonstrate the realization of arbitrary spin distributions with the same protocol by using spatially resolved two-photon Raman transitions.

## 2. Apparatus and main results

We work with a degenerate 2D Bose gas of  $^{87}\text{Rb}$  atoms. The main experimental setup has been described previously in [27, 28]. Briefly, about  $10^5$  Rb atoms in the  $F = 1, m = 0$  hyperfine ground state are loaded into a 2D box potential. The vertical confinement is provided by a vertical lattice. All atoms are trapped around a single node of the lattice in an approximately harmonic potential with a measured trap fre-

quency  $\omega_z/2\pi = 4.1(1)$  kHz. The in-plane trap is provided by a hard-wall potential created by a first DMD (DMD1 in the following)<sup>5</sup>. All laser beams used for creating the 2D box potential have a wavelength of 532 nm and thus repel Rb atoms from high intensity regions. The cloud temperature is controlled by lowering the in-plane potential height, thus enabling evaporative cooling. We reach temperatures below 30 nK and an average 2D atom density of  $\sim 80 \mu\text{m}^{-2}$ , corresponding to a regime where the cloud is well described by the Thomas–Fermi approximation. Both the interaction energy and thermal energy are smaller than the vertical trapping frequency and the atom cloud is thus in the so-called quasi-2D regime.

We show in figure 1 a sketch of the experimental setup for arbitrary density control. We modify the density distribution by using another DMD (DMD2) to impose an additional repulsive optical potential to the hard-wall potential made by DMD1. The pattern on DMD2 is imaged onto the atomic plane thanks to an imaging system of magnification  $\approx 1/70$ . The pixel size of DMD2 is  $13.7 \mu\text{m}$ , leading to an effective size of  $0.2 \mu\text{m}$  in the atomic plane. The numerical aperture ( $\text{NA} \sim 0.4$ ) is limited by a microscope objective above the vacuum glass cell containing the atoms and leads to a spatial resolution around  $1 \mu\text{m}$ . Consequently, the area defined by the diffraction spot of the imaging system typically corresponds to a region where  $5 \times 5$  pixels of DMD2 are imaged, which makes possible the realization of grey levels of light intensity. DMD2 is illuminated by a blue-detuned 532 nm laser with a waist of  $w \sim 55 \mu\text{m}$  in the atomic plane. The intensity of the beam is set to provide a maximum repulsive potential around  $2\mu$  where  $\mu$  is the chemical potential of the gas for a density of  $80 \mu\text{m}^{-2}$ . The potential is added before the final evaporation stage in the box potential.

The 2D atomic density profile is obtained by absorption imaging with a second identical microscope objective placed below the glass cell. This imaging system has a similar optical resolution and the effective pixel size of the camera in the atomic plane is  $1.15 \mu\text{m}$ . We probe the atoms in the trap using a  $10 \mu\text{s}$  pulse of light on the  $\text{D}_2$  line resonant between the  $F = 2$  ground state and the  $F' = 3$  excited state. Before detection, a microwave pulse is applied to transfer a controlled fraction of atoms into the ground level from  $F = 1, m = 0$  to  $F = 2, m = 0$ , which thus absorbs light from the imaging beam. The transferred fraction is controlled so that the measured optical depth (OD) is always smaller than 1.5 to reduce nonlinear imaging effects.

Figure 2 presents a selection of 2D density profiles realized in our experiment. For each example, we show in figures 2(a)–(d) averaged absorption images and in figures 2(e)–(h) the corresponding mean OD integrated along one or two spatial directions. Figure 2(a) shows a uniform profile in which we have corrected the inhomogeneities caused by residual defects of the overall box potential created by the combination of DMD1 and vertical lattice beams. Figures 2(b)–(d)

<sup>5</sup> All DMDs used in this work are DLP7000 from Texas Instruments and interfaced by Vialux GmbH.



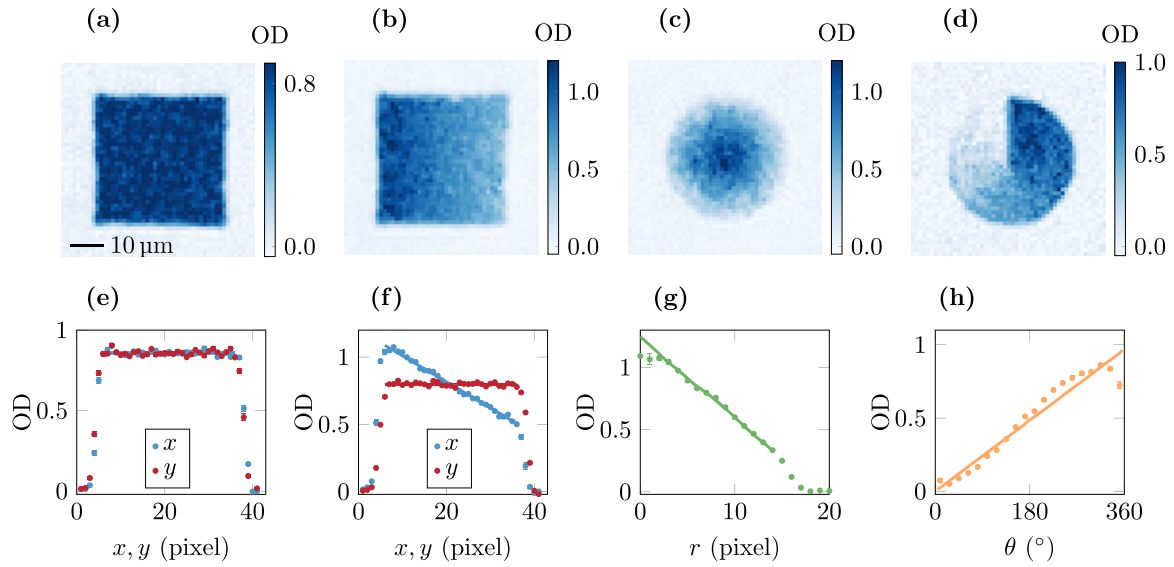


**Figure 2.** Various density profiles realized in our experiment. From left to right, we show a uniform profile and linearly varying density profiles along  $x$ , along the radial direction and along the azimuthal direction. (a)–(d) Averaged absorption images (50, 99, 50, 20 shots respectively). (e)–(h) Corresponding OD profiles integrated over one direction ( $x$  and  $y$  in (e) and (f), azimuthal in (g) and radial in (h)). The solid lines represent the OD profiles of the target density distributions. Error bars show the statistical error corresponding to one standard error of the mean.

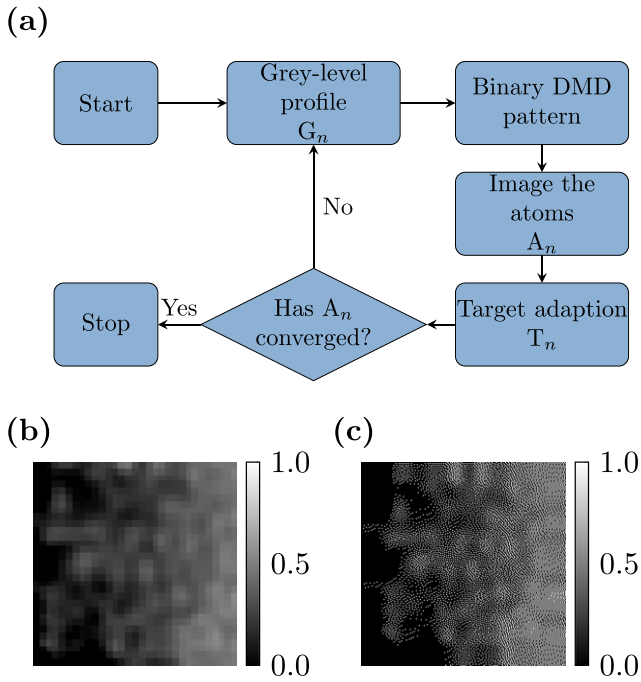


**Figure 3.** (a) Diagram of the iterative algorithm. (b) Example of grey-level profile  $G_n$  obtained during the optimization loop used to create the linearly varying profile shown in figure 2(b). (c) Corresponding dithered image computed with the error diffusion algorithm and programmed on the DMD. The grey level ranges from 0 to 1, with an effective pixel size of  $1.15 \mu\text{m}$  equal to the one of the absorption image. The DMD pattern is binary with an effective pixel size of  $0.2 \mu\text{m}$ .

### 3. Detailed implementation

One could naively think that for a given target density profile, the suitable pattern on DMD2 could be directly computed and imaged onto the atoms. However, several features prevent such a simple protocol. First, the DMD is a binary modulator. Then, for a finite number of pixels, it is not possible to create an arbitrary grey-level pattern with perfect accuracy. Here, we use the well-known error diffusion technique to generate the binary pattern for a given grey-level profile [29, 30] (see the [appendix](#) for a short description). Second, the imaging system from DMD2 to the atoms has an optical response that leads to a modification of the ideal image, mainly because of the finite aperture of the optical elements. Third, any imperfection on the optical setup (inhomogeneity of the laser beam, optical aberrations...) also degrades the imaging of the DMD pattern onto the atomic cloud. Finally, the atomic density distribution is obtained through absorption imaging, which adds noise mostly coming from the photonic shot noise induced by the imaging beam. Hence, an iterative method is needed to obtain the optimal DMD pattern that gives a density distribution as close as possible to the target. The working principle of the optimization loop is simply to add (remove) light at the positions where there are more (fewer) atoms than the target until the density profile converges to the target one.

Figure 3(a) shows the steps of the iterative loop. The basic idea of each step  $n$  consists in computing the difference between the measured density distribution  $A_n$  and the target image  $T_n$ , and adding it with a suitable gain  $K$  to the previous grey-level intensity profile  $G_n$ . This gives the grey-level profile of iteration  $n + 1$  (see figure 3(b)),

$$G_{n+1} = G_n + K(A_n - T_n), \quad (1)$$

correspond to linearly varying density distributions respectively along the  $x$  direction, along the radial direction and along the azimuthal direction.

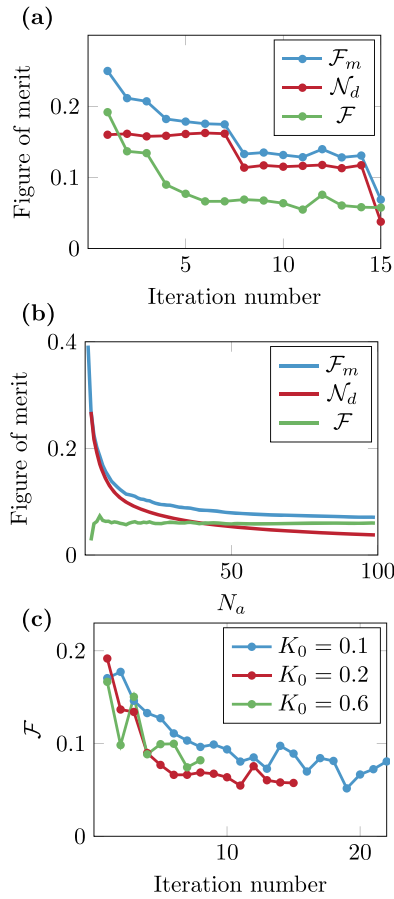


**Figure 4.** Convergence of the iterative algorithm. (a) Plot of  $\mathcal{F}_m$ ,  $\mathcal{N}_d$  and  $\mathcal{F}$  with iteration number. Target profile is a linear density distribution along  $x$  in a square box (of figure 2(b)).  $\mathcal{F}$  converges very fast and stays around 0.06 after iteration 6.  $\mathcal{N}_d$  decreases suddenly at iteration 8 and 15 because  $N_a$  (number of absorption images for averaging) changes from 5 to 10 at iteration 8 and to 99 at iteration 15. For  $\mathcal{F}_m$ , we show the estimated statistical error bars to give an illustrative indication of our typical uncertainties. These error bars are obtained from a bootstrap approach on the different repetitions of the experiment in the same conditions. (b) For the last iteration (iteration 15), we plot  $\mathcal{F}_m$ ,  $\mathcal{N}_d$  and  $\mathcal{F}$  versus the number of images  $N_a$  used for averaging. Both  $\mathcal{F}_m$  and  $\mathcal{N}_d$  decrease with  $N_a$  while  $\mathcal{F}$  does not depend on  $N_a$ . (c) Evolution of  $\mathcal{F}$  for different  $K_0$ 's.

which is then discretized thanks to the error diffusion algorithm (see figure 3(c)) and imaged onto the atoms. Besides this general idea, we detail below some specific features of our loop:

- We initialize the optimization with a grey-level profile  $G_0$  which can either be uniformly 0 or 1.
- To avoid border effects, we select on the absorption images a region slightly inside the box potential (two pixels smaller in each direction) for density control and we extrapolate the grey-level profile  $G_n$  outside the box. The extrapolation is done by simply duplicating the value of the outermost pixels of  $G_n$  by three more pixels along each side for a square box or along the radial direction for a disk.
- The image  $A_n$  of the density distribution is obtained from the average of several repetitions of the experiment with

the same parameters to limit the contribution of detection noise.

- The measured image of the atomic distribution is convoluted with a Gaussian function of rms width 1 pixel of the camera of the imaging system. This convolution acts as a low pass filter which reduces high spatial frequency noise, especially detection noise.
- Considering the Gaussian shape of the beam illuminated on DMD, we choose  $K$  to be position dependent  $K(x, y) = K_0 \times e^{\frac{2((x-x_0)^2 + (y-y_0)^2)}{w^2}}$ , where  $w$  is the waist of the beam in the atomic plane and  $x_0$  and  $y_0$  are the coordinates of the center of the beam. It makes the effective gain approximately the same for all the pixels.
- At each iteration, we rescale the amplitude of the target profile to obtain the same mean OD as the one of  $A_n$ . This avoids taking into account errors coming from the shot-to-shot variation of the atom number which would lead to a global error that we are not interested in. Note that this variation is smaller than 10% during the optimization loop.

#### 4. Characterization of the loop

We stop the optimization loop when the measured density distribution has converged to the target one, up to a predefined precision. To estimate the deviation from the target, we define a figure of merit  $\mathcal{F}_m$  corresponding to the measured root-mean-square deviation:

$$\mathcal{F}_m = \sqrt{\frac{N_{\text{pix}} \sum_{(i,j) \in A} (\text{OD}(i, j) - \text{OD}_T(i, j))^2}{(\sum_{(i,j) \in A} \text{OD}(i, j))^2}}, \quad (2)$$

where  $A$  is the region of interest containing  $N_{\text{pix}}$  pixels and  $\text{OD}(i, j)$  (resp.  $\text{OD}_T(i, j)$ ) is the measured average OD (resp. target OD). The value of the figure of merit  $\mathcal{F}_m$  results from two kinds of contributions. Obviously, there is the actual deviation of the density distribution from the target. In addition, several features of the measurement method give an undesired contribution to  $\mathcal{F}_m$ . Indeed, thermal fluctuations of the atomic cloud, projection noise due the partial transfer imaging discussed above and photonic shot noise in absorption imaging lead to unavoidable residual noise. For our parameters, we computed in a separate work that the two dominant mechanisms are photonic and projection noise with a similar weight, whose exact values depend on the studied density distribution. In the low temperature regime explored here thermal fluctuations are almost negligible.

The contributions coming from photonic shot noise and projection noise can be reduced by averaging more images. However, for the typical repetition rate of our experiment ( $\sim 30$  s), the number of averaged images has to be limited to a few tens for realistic applications. To characterize the optimization loop, we compute this noise contribution  $\mathcal{N}_d$  so as to remove it from the measured  $\mathcal{F}_m$ . We directly estimate  $\mathcal{N}_d$  from the set of images taken with the same parameters by computing the dispersion of the measured absorption images from the averaged image,

$$\mathcal{N}_d = \sqrt{\frac{N_{\text{pix}} \sum_k \sum_{(i,j) \in A} (\text{OD}^k(i,j) - \text{OD}(i,j))^2}{N_a^2 (\sum_{(i,j) \in A} \text{OD}(i,j))^2}}, \quad (3)$$

where the index  $k$  refers to the  $k$ th absorption image among the  $N_a$  pictures taken for the average. We thus define the corrected figure of merit:

$$\mathcal{F} = \sqrt{\mathcal{F}_m^2 - \mathcal{N}_d^2}, \quad (4)$$

which quantifies the distance of the density profile from the target while removing measurement noise.

In figure 4(a), we show the evolution of  $\mathcal{F}_m$ ,  $\mathcal{N}_d$  and  $\mathcal{F}$  as a function of the number of iterations in the example case of a linear profile in a square box (as shown in figure 2(b)). We initialize the loop with a grey-level profile equal to zero and we choose  $K_0 = 0.2$ . The number of pictures which are averaged is 5 for the first 7 iterations, 10 up to iteration 14 and 99 for the last iteration. This leads to clear jumps of  $\mathcal{N}_d$  with the iteration number. Interestingly, we see that  $\mathcal{F}$  converges almost monotonously to about 0.06 after the first 6 iterations and then stays approximately constant whatever the value of  $N_a$  is. This indicates that the contribution of measurement noise is well subtracted. This is confirmed in figure 4(b), where we plot  $\mathcal{F}_m$ ,  $\mathcal{N}_d$  and  $\mathcal{F}$  as a function of  $N_a$  using the data of the final iteration of figure 4(a). As expected, both  $\mathcal{F}_m$  and  $\mathcal{N}_d$  decrease with  $N_a$  while  $\mathcal{F}$  does not change.

We also studied the behavior of the iterative loop with different  $K'_0$ s varying from 0.1 to 0.6. The convergence of  $\mathcal{F}$  is plotted in figure 4(c). The iterative algorithm works well for a large range of values of  $K_0$ . We observe that increasing  $K_0$  speeds up the convergence, but too large values of  $K_0$  lead to strong local variations in the measured images. In practice, for most target distributions, we use  $K_0 = 0.2$  as a good compromise between these two trends.

In the [appendix](#), we study through simple numerical simulations the remaining limitations that contribute to the experimentally obtained  $\mathcal{F}$ . The main limitation comes from the number of iterations used in the experiment ( $\sim 15$ ). We show that the figure of merit  $\mathcal{F}$  decreases slowly down to  $\sim 0.02$  for larger iteration numbers but reaching such a limit would require prohibitively long experimental times.

## 5. Arbitrary spin distribution

Using a similar protocol, we also demonstrate arbitrary spin distributions by shaping a pair of copropagating Raman beams which couple the  $|F=1, m=0\rangle$  ( $|1\rangle$ ) and  $|F=2, m=0\rangle$  ( $|2\rangle$ ) states by a two-photon Raman transition. The two Raman beams originate from the same laser and have a wavelength of  $\sim 790$  nm, in between the  $D_1$  and  $D_2$  line of  $^{87}\text{Rb}$  atoms. One beam is frequency shifted with respect to the other by  $\sim 6.8$  GHz to fulfill the two-photon resonance between the two states. The two beams are coupled into the same single-mode optical fiber with orthogonal linear polarizations. After reflection on a third DMD (DMD3, not shown in figure 1) they are overlapped with the two beams coming from DMD1 and DMD2 and are imaged onto the atomic plane with a magnification of  $\approx 1/40$  and a waist of  $40 \mu\text{m}$ .

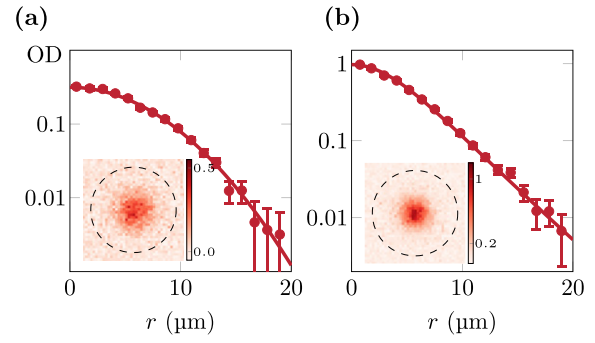


**Figure 5.** Imprinting a spatial spin texture. We show the density distribution of atoms in  $|2\rangle$  immersed in a bath of atoms in  $|1\rangle$ . The total density of the gas is uniform in a  $20 \mu\text{m}$  radius disk ( $\sim 80 \mu\text{m}^{-2}$ , corresponding to  $\text{OD} \sim 8$ ). The main figures show the radial profiles of component  $|2\rangle$  in semilog scale for (a) a Gaussian profile and (b) a solitary Townes profile. The solid lines are the target radial profiles. Error bars show the statistical error corresponding to one standard error of the mean. Insets show the corresponding averaged absorption images (20 shots). The dashed lines represent the edges of the bath of atoms in  $|1\rangle$ .

Starting from a cloud of atoms in state  $|1\rangle$  of uniform density, we pulse the Raman beams with a duration of a few tens of  $\mu\text{s}$  to coherently transfer a controlled fraction of atoms to state  $|2\rangle$ . In this protocol, the total density of the cloud remains uniform. We then image the density distribution of atoms in state  $|2\rangle$  prior to any spin dynamics and apply an optimization protocol identical to the one developed for creating arbitrary density distributions. We show in figure 5 two examples of spin profiles realized in our system at the end of the optimization loop: a Gaussian profile (figure 5(a)) and the so-called Townes profile (figure 5(b)), which is a solitonic solution of the 2D attractive non-linear Schrödinger equation that decreases almost exponentially with  $r$  at large  $r$  [31]. The measured profiles are very close to the target over typically two orders of magnitude in density.

## 6. Discussion and outlook

In conclusion, we have demonstrated the arbitrary control of the density profile of an ultracold 2D quantum gas by tailoring a repulsive optical potential. We have also demonstrated the arbitrary creation of spin textures using spatially resolved Raman transitions. An iterative method was applied, making the method robust to technical imperfections. The approach described here can be straightforwardly applied to other atomic species. It opens new possibilities for studying the dynamics of single or multi-component low-dimensional gases where, for instance, the presence of scale-invariance or integrability leads to a rich variety of non-trivial time evolutions [32–35].

## Acknowledgments

This work is supported by ERC (Synergy UQUAM and TORYD), European Union's Horizon 2020 Program (QUANTERA NAQUAS project) and the ANR-18-CE30-0010 grant.



## Appendix A

### A.1. Error diffusion algorithm

We briefly recall in this paragraph the main features of the error diffusion algorithm, which we use to compute the pattern programmed on the DMD. Error diffusion is used to convert a grey-level image where each pixel takes arbitrary values into an image with only zeros and ones. Starting for instance from the top left pixel of the image, one chooses the status of the corresponding DMD pixel by rounding to 0 or 1 the targeted grey level. This binary choice results in an error which is ‘diffused’ to the remaining neighboring pixels with a given weight. In this work, we use the method developed in reference [29]. We process the pixels from left to right and from top to bottom. The error made when choosing the state of a pixel (denoted by a  $\star$  in equation (5)) is diffused to its first right neighbor and the three nearest neighbors of the following line with weights given by

$$\begin{pmatrix} & - & \star & \frac{7}{16} & \cdots \\ \cdots & \frac{3}{16} & \frac{5}{16} & \frac{1}{16} & \cdots \end{pmatrix}. \quad (5)$$

### A.2. Simulations

In this section, we simulate the experiment to understand the various contributions to the obtained value of the figure of merit  $\mathcal{F}$  for the density correction. In the simulation, we start with a ‘test’ density profile  $A_0$ , which is obtained from an experiment with DMD2 being off. It is an averaged image of 100 experimental shots so that the detection noise is mostly averaged out. We follow the same procedure which was described in figure 3(a) but in a ‘numerical experiment’. We simulate the action of the potential shaped by the DMD by using the local density approximation in the Thomas–Fermi regime. Thus, for each iteration  $n$  of the loop we compute the density profile as

$$A_n = A_0 - \alpha C_n, \quad (6)$$

where  $C_n$  is the light intensity profile given by the DMD pattern after a convolution step that simulates the finite numerical aperture of the optical system. We use here a Gaussian profile with an rms width  $\sigma = 0.5 \mu\text{m}$ . The parameter  $\alpha$  is introduced to represent the effect of the light potential on the atomic density. We use as an input to the simulation experimental images of the OD distribution ( $\text{OD} \sim 1$ ) and we choose  $\alpha = 2$  to be as close as possible to the calibrated experimental parameters. We add an offset to  $A_n$  to keep the mean OD constant. We also have the possibility to add some noise to  $A_n$  to simulate the experimental fluctuations.

We show in figure 6 the simulated evolution of  $\mathcal{F}$  as a function of the iteration number. The target is a linear profile along the  $x$  direction, same as the one studied in figures 2(b) and 4. The blue and red curves show the simulated results with the parameters used in the experiment:  $K_0 = 0.2$  and the absorption image is convolved with a Gaussian function of an rms width 1 pixel. For the blue curve, we add independently on each pixel of  $A_n$  a Gaussian noise corresponding to  $\mathcal{N}_d = 0.09$ ,

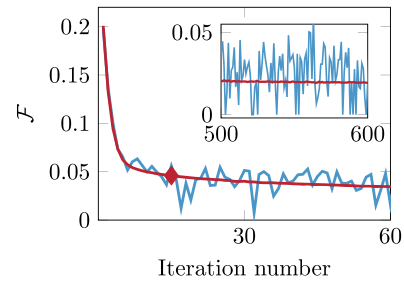


**Figure 6.** Numerical simulation of the experiment. Evolution of  $\mathcal{F}$  as a function of iteration number with (blue) or without (red) noise. The target distribution is a linear density profile along  $x$ . The diamond corresponds to the number of iterations used in figure 4(a). The inset shows the same curves at large iteration number.

which is the typical noise obtained in the experiment for the average of 10 repetitions of the sequence. For the red curve, no detection noise is added, i.e.  $\mathcal{N}_d = 0$ . The marker on the red curve corresponds to the point when the iterative loop is terminated for the experimental data shown in figure 4(a). Here,  $\mathcal{F} = 0.046$ , in qualitative good agreement with the obtained experimental value of 0.06.

We finally discuss the limitations to the obtained figure of merit. We show in the inset of figure 6 the evolution of the figure of merit at large iteration number. Better values ( $\sim 0.02$ ) are obtained for larger number of iterations ( $\sim 600$ ) but with a slow convergence largely hidden by the typical experimental noise. This regime is not reachable in practice with our typical experimental cycle time. The residual value could be explained by the filtering made when convolving the absorption image and also by the residual defects coming from the error diffusion protocol.

### ORCID iDs

S Nascimbene  <https://orcid.org/0000-0002-3931-9436>

J Beugnon  <https://orcid.org/0000-0003-1701-8533>

### References

- [1] Bloch I, Dalibard J and Nascimbène S 2012 Quantum simulations with ultracold quantum gases *Nat. Phys.* **8** 267–76
- [2] Cronin A D, Schmiedmayer J and Pritchard D E 2009 Optics and interferometry with atoms and molecules *Rev. Mod. Phys.* **81** 1051–129
- [3] Pritchard D E 1983 Cooling neutral atoms in a magnetic trap for precision spectroscopy *Phys. Rev. Lett.* **51** 1336–9
- [4] Grimm R, Weidemüller M and Ovchinnikov Y B 2000 Optical dipole traps for neutral atoms *Adv. At. Mol. Opt. Phys.* **42** 95–170
- [5] Gaunt A L, Schmidutz T F, Gotlibovych I, Smith R P and Hadzibabic Z 2013 Bose–Einstein condensation of atoms in a uniform potential *Phys. Rev. Lett.* **110** 200406
- [6] Chomaz L, Corman L, Bienaimé T, Desbuquois R, Weitenberg C, Nascimbène S, Beugnon J and Dalibard J 2015 Emergence of coherence via transverse condensation in a uniform quasi-two-dimensional Bose gas *Nat. Commun.* **6** 6162

- [7] Mukherjee B, Yan Z, Patel P B, Hadzibabic Z, Yefsah T, Struck J and Zwierlein M W 2017 Homogeneous atomic Fermi gases *Phys. Rev. Lett.* **118** 123401
- [8] Hueck K, Luick N, Sobirey L, Siegl J, Lompe T and Moritz H 2018 Two-dimensional homogeneous Fermi gases *Phys. Rev. Lett.* **120** 060402
- [9] Ryu C, Andersen M F, Cladé P, Natarajan V, Helmerson K and Phillips W D 2007 Observation of persistent flow of a Bose–Einstein condensate in a toroidal trap *Phys. Rev. Lett.* **99** 260401
- [10] Moulder S, Beattie S, Smith R P, Tammuz N and Hadzibabic Z 2012 Quantized supercurrent decay in an annular Bose–Einstein condensate *Phys. Rev. A* **86** 013629
- [11] Corman L, Chomaz L, Bienaimé T, Desbuquois R, Weitenberg C, Nascimbène S, Dalibard J and Beugnon J 2014 Quench-induced supercurrents in an annular Bose gas *Phys. Rev. Lett.* **113** 135302
- [12] Guo Y, Dubessy R, de Goër de Herve M, Kumar A, Badr T, Perrin A, Longchambon L and Perrin H 2020 Supersonic rotation of a superfluid: a long-lived dynamical ring *Phys. Rev. Lett.* **124** 025301
- [13] Lahav O, Itah A, Blumkin A, Gordon C, Rinott S, Zayats A and Steinhauer J 2010 Realization of a sonic black hole analog in a Bose–Einstein condensate *Phys. Rev. Lett.* **105** 240401
- [14] Chiu C S, Ji G, Mazurenko A, Greif D and Greiner M 2018 Quantum state engineering of a Hubbard system with ultracold fermions *Phys. Rev. Lett.* **120** 243201
- [15] Mogensen P C and Glückstad J 2000 Dynamic array generation and pattern formation for optical tweezers *Opt. Commun.* **175** 75–81
- [16] Bergamini S, Darquié B, Jones M, Jacubowicz L, Browaeys A and Grangier P 2004 Holographic generation of micro-trap arrays for single atoms by use of a programmable phase modulator *J. Opt. Soc. Am. B* **21** 1889–94
- [17] Pasienski M and DeMarco B 2008 A high-accuracy algorithm for designing arbitrary holographic atom traps *Opt. Express* **16** 2176
- [18] Henderson K, Ryu C, MacCormick C and Boshier M G 2009 Experimental demonstration of painting arbitrary and dynamic potentials for Bose-Einstein condensates *New J. Phys.* **11** 043030
- [19] Gaunt A L and Hadzibabic Z 2012 Robust digital holography for ultracold atom trapping *Sci. Rep.* **2** 721
- [20] Nogrette F, Labuhn H, Ravets S, Barredo D, Béguin L, Vernier A, Lahaye T and Browaeys A 2014 Single-atom trapping in holographic 2D arrays of microtraps with arbitrary geometries *Phys. Rev. X* **4** 021034
- [21] Gauthier G, Lenton I, McKay Parry N, Baker M, Davis M J, Rubinsztein-Dunlop H and Neely T W 2016 Direct imaging of a digital-micromirror device for configurable microscopic optical potentials *Optica* **3** 1136
- [22] Ohl de Mello D, Schäffner D, Werkmann J, Preuschoff T, Kohfahl L, Schlosser M and Birkel G 2019 Defect-free assembly of 2D clusters of more than 100 single-atom quantum systems *Phys. Rev. Lett.* **122** 203601
- [23] Zupancic P, Preiss P M, Ma R, Lukin A, Eric Tai M, Rispoli M, Islam R and Greiner M 2016 Ultra-precise holographic beam shaping for microscopic quantum control *Opt. Express* **24** 13881
- [24] Jinyang L, Kohn R N, Becker M F and Heinzen D J 2009 1.5% root-mean-square flat-intensity laser beam formed using a binary-amplitude spatial light modulator *Appl. Opt.* **48** 1955–62
- [25] Ha L C, Clark L W, Parker C V, Anderson B M and Chin C 2015 Roton-maxon excitation spectrum of Bose condensates in a shaken optical lattice *Phys. Rev. Lett.* **114** 055301
- [26] Tajik M, Rauer B, Schweigler T, Cataldini F, Sabino J, Møller F S, Ji S-C, Mazets I E and Schmiedmayer J 2019 Designing arbitrary one-dimensional potentials on an atom chip *Opt. Express* **27** 33474
- [27] Ville J L *et al* 2017 Loading and compression of a single two-dimensional Bose gas in an optical accordion *Phys. Rev. A* **95** 013632
- [28] Ville J L, Saint-Jalm R, Le Cerf, Aidelburger M, Nascimbène S, Dalibard J and Beugnon J 2018 Sound propagation in a uniform superfluid two-dimensional Bose gas *Phys. Rev. Lett.* **121** 145301
- [29] Floyd R W 1976 An adaptive algorithm for spatial grey-scale *Proc. of the Society of Information Display* vol 17
- [30] Dorrer C and Zuegel J D 2007 Design and analysis of binary beam shapers using error diffusion *J. Opt. Soc. Am. B* **24** 1268–75
- [31] Chiao R Y, Garmire E and Townes C H 1964 Self-trapping of optical beams *Phys. Rev. Lett.* **13** 479
- [32] Cazalilla M A, Citro R, Giamarchi T, Orignac E and Rigol M 2011 One dimensional bosons: from condensed matter systems to ultracold gases *Rev. Mod. Phys.* **83** 1405–66
- [33] Saint-Jalm R, Castilho P C M, Le Cerf É, Bakkaï-Hassani B, Ville J-L, Nascimbène S, Beugnon J and Dalibard J 2019 Dynamical symmetry and breathers in a two-dimensional Bose gas *Phys. Rev. X* **9** 021035
- [34] Lv C, Zhang R and Zhou Q 2020 SU(1,1) echoes for breathers in quantum gases *Phys. Rev. Lett.* **125** 253002
- [35] Shi Z-Y, Gao C and Zhai H 2020 Idealized hydrodynamics (arXiv:2011.01415)



# Bibliography

- [1] M. ARNDT, O. NAIRZ, J. VOS-ANDREAE, C. KELLER, G. VAN DER ZOUW & A. ZEILINGER; “Wave–particle duality of C60 molecules”; [Nature](#) **401**, pp. 680–682 (1999). [Cited on page 11]
- [2] Y. Y. FEIN, P. GEYER, P. ZWICK, F. KIALKA, S. PEDALINO, M. MAYOR, S. GERLICH & M. ARNDT; “Quantum superposition of molecules beyond 25 kDa”; [Nature Physics](#) **15**, pp. 1242–1245 (2019). [Cited on page 11]
- [3] A. SHAYEGHI, P. RIESER, G. RICHTER, U. SEZER, J. H. RODEWALD, P. GEYER, T. J. MARTINEZ & M. ARNDT; “Matter-wave interference of a native polypeptide”; [Nature Communications](#) **11**, p. 1447 (2020). [Cited on page 11]
- [4] A. EINSTEIN; “Quantentheorie des einatomigen idealen Gases”; Sitzungsberichte der Preussischen Akademie der Wissenschaften pp. 261–267 (1924). [Cited on pages 11, 17, and 37]
- [5] R. P. FEYNMAN; “Chapter II - Application of Quantum Mechanics to Liquid Helium”; ; pp. 17–53 (Elsevier) (1955). [Cited on page 11]
- [6] P. G. DE GENNES; *Superconductivity of Metals and Alloys*; Advanced book classics (Perseus, Cambridge, MA). (1999). [Cited on pages 11 and 102]
- [7] K. B. DAVIS, M. O. MEWES, M. R. ANDREWS, N. J. VAN DRUTEN, D. S. DURFEE, D. M. KURN & W. KETTERLE; “Bose-Einstein Condensation in a Gas of Sodium Atoms”; [Physical Review Letters](#) **75**, pp. 3969–3973 (1995). [Cited on page 12]
- [8] M. H. ANDERSON, J. R. ENSHER, M. R. MATTHEWS, C. E. WIEMAN & E. A. CORNELL; “Observation of Bose-Einstein Condensation in a Dilute Atomic Vapor”; [Science](#) **269**, pp. 198–201 (1995). [Cited on page 12]
- [9] M. R. ANDREWS, C. G. TOWNSEND, H.-J. MIESNER, D. S. DURFEE, D. M. KURN & W. KETTERLE; “Observation of Interference Between Two Bose Condensates”; [Science](#) **275**, pp. 637–641 (1997). [Cited on page 12]
- [10] F. CHARRU; *Instabilités hydrodynamiques* ([EDP Sciences](#)) (2021). [Cited on page 12]
- [11] J. S. RUSSELL; “Report on Waves”; British Association for the Advancement of Science (1845). [Cited on pages 12 and 54]
- [12] N. J. ZABUSKY & M. D. KRUSKAL; “Interaction of ”Solitons” in a Collisionless Plasma and the Recurrence of Initial States”; [Physical Review Letters](#) **15**, pp. 240–243 (1965). [Cited on pages 12, 54, 56, and 109]

- [13] M. PEYRARD & T. DAUXOIS; *Physique des Solitons*. (2004). [Cited on pages 12, 53, and 55]
- [14] Y. V. KARTASHOV, G. E. ASTRAKHARCHIK, B. A. MALOMED & L. TORNER; “Frontiers in multidimensional self-trapping of nonlinear fields and matter”; *Nature Reviews Physics* **1**, pp. 185–197 (2019). [Cited on pages 12 and 61]
- [15] J. H. V. NGUYEN, P. DYKE, D. LUO, B. A. MALOMED & R. G. HULET; “Collisions of matter-wave solitons”; *Nature Physics* **10**, p. 918–922 (2014). [Cited on pages 12, 58, and 109]
- [16] G. A. ASKARYAN; “Effect of the Gradient of a Strong Electromagnetic Ray on Electrons and Atoms”; *Zhur. Eksptl’. i Teoret. Fiz.* **42** (1962). [Cited on pages 13, 57, and 60]
- [17] R. Y. CHIAO, E. GARMIRE & C. H. TOWNES; “Self-Trapping of Optical Beams”; *Physical Review Letters* **13**, pp. 479–482 (1964). [Cited on pages 13, 60, and 64]
- [18] V. I. TALANOV; “Self-Focusing of Electromagnetic Waves in Non-Linear Media ”; *Izv. Vysshikh Uchebn. Zavedenii, Radiofiz.* **7** (1964). [Cited on pages 13 and 60]
- [19] J. E. BJORKHOLM & A. A. ASHKIN; “cw Self-Focusing and Self-Trapping of Light in Sodium Vapor”; *Physical Review Letters* **32**, pp. 129–132 (1974). [Cited on pages 13 and 60]
- [20] L. F. MOLLENAUER, R. H. STOLEN & J. P. GORDON; “Experimental Observation of Picosecond Pulse Narrowing and Solitons in Optical Fibers”; *Physical Review Letters* **45**, pp. 1095–1098 (1980). [Cited on pages 13 and 57]
- [21] A. BARTHELEMY, S. MANEUF & C. FROEHLI; “Propagation soliton et auto-confinement de faisceaux laser par non linearité optique de kerr”; *Optics Communications* **55**, pp. 201–206 (1985). [Cited on pages 13 and 57]
- [22] S. BURGER, K. BONGS, S. DETTMER, W. ERTMER, K. SENGSTOCK, A. SANPERA, G. V. SHLYAPNIKOV & M. LEWENSTEIN; “Dark Solitons in Bose-Einstein Condensates”; *Physical Review Letters* **83**, pp. 5198–5201 (1999). [Cited on pages 13 and 58]
- [23] L. KHAYKOVICH, F. SCHRECK, G. FERRARI, T. BOURDEL, J. CUBIZOLLES, L. D. CARR, Y. CASTIN & C. SALOMON; “Formation of a Matter-Wave Bright Soliton”; *Science* **296**, pp. 1290–1293 (2002). [Cited on pages 13 and 58]
- [24] K. E. STRECKER, G. B. PARTRIDGE, A. G. TRUSCOTT & R. G. HULET; “Formation and propagation of matter-wave soliton trains”; *Nature* **417**, p. 150–153 (2002). [Cited on pages 13, 58, and 73]
- [25] N. NAVON, R. P. SMITH & Z. HADZIBABIC; “Quantum Gases in Optical Boxes”; (2021); [2106.09716](#). [Cited on page 13]
- [26] D. M. STAMPER-KURN & M. UEDA; “Spinor Bose gases: Symmetries, magnetism, and quantum dynamics”; *Review of Modern Physics* **85**, pp. 1191–1244 (2013). [Cited on pages 13 and 29]

- [27] A. FAROLFI, D. TRYPOGEORGOS, C. MORDINI, G. LAMPORESI & G. FERRARI; “Observation of Magnetic Solitons in Two-Component Bose-Einstein Condensates”; *Physical Review Letters* **125**, p. 030401 (2020). [Cited on pages 13 and 58]
- [28] X. CHAI, D. LAO, K. FUJIMOTO, R. HAMAZAKI, M. UEDA & C. RAMAN; “Magnetic Solitons in a Spin-1 Bose-Einstein Condensate”; *Physical Review Letters* **125**, p. 030402 (2020). [Cited on pages 13 and 58]
- [29] C. CHIN, R. GRIMM, P. JULIENNE & E. TIESINGA; “Feshbach resonances in ultracold gases”; *Review of Modern Physics* **82**, pp. 1225–1286 (2010). [Cited on pages 13 and 33]
- [30] D. S. PETROV; “Quantum Mechanical Stabilization of a Collapsing Bose-Bose Mixture”; *Physical Review Letters* **115**, p. 155302 (2015). [Cited on pages 13, 60, 61, 106, and 115]
- [31] C. R. CABRERA, L. TANZI, J. SANZ, B. NAYLOR, P. THOMAS, P. CHEINEY & L. TARRUELL; “Quantum liquid droplets in a mixture of Bose-Einstein condensates”; *Science* **359**, pp. 301–304 (2018). [Cited on pages 13 and 61]
- [32] G. SEMEGHINI, G. FERIOLO, L. MASI, C. MAZZINGHI, L. WOLSWIJK, F. MINARDI, M. MODUGNO, G. MODUGNO, M. INGUSCIO & M. FATTORI; “Self-Bound Quantum Droplets of Atomic Mixtures in Free Space”; *Physical Review Letters* **120**, p. 235301 (2018). [Cited on pages 13 and 61]
- [33] I. FERRIER-BARBUT, H. KADAU, M. SCHMITT, M. WENZEL & T. PFAU; “Observation of Quantum Droplets in a Strongly Dipolar Bose Gas”; *Physical Review Letters* **116**, p. 215301 (2016). [Cited on pages 14 and 61]
- [34] L. CHOMAZ, S. BAIER, D. PETTER, M. J. MARK, F. WÄCHTLER, L. SANTOS & F. FERLAINO; “Quantum-Fluctuation-Driven Crossover from a Dilute Bose-Einstein Condensate to a Macrodroplet in a Dipolar Quantum Fluid”; *Physical Review X* **6**, p. 041039 (2016). [Cited on pages 14 and 61]
- [35] M. CASAS & S. STRINGARI; “Elementary excitations of  $^4\text{He}$  clusters”; *Journal of Low Temperature Physics* **79**, pp. 135–149 (1990). [Cited on pages 14 and 109]
- [36] G. E. VOLOVIK; *The Universe in a Helium Droplet*; International Series of Monographs on Physics (Oxford University Press, Oxford) (2009). [Cited on pages 14 and 109]
- [37] M. BARRANCO, R. GUARDIOLA, S. HERNÁNDEZ, R. MAYOL, J. NAVARRO & M. PI; “Helium Nanodroplets: An Overview”; *Journal of Low Temperature Physics* **142**, p. 1 (2006). [Cited on pages 14 and 109]
- [38] A. J. LEGGETT; “Can a Solid Be ”Superfluid”?” *Physical Review Letters* **25**, pp. 1543–1546 (1970). [Cited on page 14]
- [39] Y. POMEAU & S. RICA; “Dynamics of a model of supersolid”; *Physical Review Letters* **72**, pp. 2426–2429 (1994). [Cited on page 14]
- [40] L. CHOMAZ, D. PETTER, P. ILZHÖFER, G. NATALE, A. TRAUTMANN, C. POLITI, G. DURASTANTE, R. M. W. VAN BIJNEN, A. PATSCHEIDER, M. SOHMEN, M. J. MARK & F. FERLAINO; “Long-Lived and Transient Supersolid Behaviors in Dipolar Quantum Gases”; *Physical Review X* **9**, p. 021012 (2019). [Cited on page 14]



- [41] F. BÖTTCHER, J.-N. SCHMIDT, M. WENZEL, J. HERTKORN, M. GUO, T. LANGEN & T. PFAU; “Transient Supersolid Properties in an Array of Dipolar Quantum Droplets”; [Physical Review X](#) **9**, p. 011051 (2019). [Cited on page 14]
- [42] L. TANZI, S. M. ROCCUZZO, E. LUCIONI, F. FAMÀ, A. FIORETTI, C. GABBANINI, G. MODUGNO, A. RECATI & S. STRINGARI; “Supersolid symmetry breaking from compressional oscillations in a dipolar quantum gas”; [Nature](#) **574**, pp. 382–385 (2019). [Cited on page 14]
- [43] J. LÉONARD, A. MORALES, P. ZUPANCIC, T. ESSLINGER & T. DONNER; “Supersolid formation in a quantum gas breaking a continuous translational symmetry”; [Nature](#) **543**, pp. 87–90 (2017). [Cited on page 14]
- [44] J.-R. LI, J. LEE, W. HUANG, S. BURCHESKY, B. SHTEYNAS, F. . TOP, A. O. JAMISON & W. KETTERLE; “A stripe phase with supersolid properties in spin–orbit-coupled Bose–Einstein condensates”; [Nature](#) **543**, pp. 91–94 (2017). [Cited on page 14]
- [45] B. BAKKALI-HASSANI, C. MAURY, Y.-Q. ZOU, É. LE CERF, R. SAINT-JALM, P. C. M. CASTILHO, S. NASCIMBENE, J. DALIBARD & J. BEUGNON; “Realization of a Townes Soliton in a Two-Component Planar Bose Gas”; [Physical Review Letters](#) **127**, p. 023603 (2021). [Cited on pages 14, 75, and 121]
- [46] C.-A. CHEN & C.-L. HUNG; “Observation of Universal Quench Dynamics and Townes Soliton Formation from Modulational Instability in Two-Dimensional Bose Gases”; [Physical Review Letters](#) **125**, p. 250401 (2020). [Cited on pages 14, 53, 60, 71, 73, and 74]
- [47] C.-A. CHEN & C.-L. HUNG; “Observation of Scale Invariance in Two-Dimensional Matter-Wave Townes Solitons”; [Physical Review Letters](#) **127**, p. 023604 (2021). [Cited on pages 14, 53, 60, 71, 72, 73, and 74]
- [48] Y.-Q. ZOU, É. LE CERF, B. BAKKALI-HASSANI, C. MAURY, G. CHAUVEAU, P. C. M. CASTILHO, R. SAINT-JALM, S. NASCIMBENE, J. DALIBARD & J. BEUGNON; “Optical control of the density and spin spatial profiles of a planar Bose gas”; [Journal of Physics B: Atomic, Molecular and Optical Physics](#) **54**, p. 08LT01 (2021). [Cited on pages 14, 23, and 25]
- [49] R. SAINT-JALM, P. C. M. CASTILHO, É. LE CERF, B. BAKKALI-HASSANI, J.-L. VILLE, S. NASCIMBENE, J. BEUGNON & J. DALIBARD; “Dynamical Symmetry and Breathers in a Two-Dimensional Bose Gas”; [Physical Review X](#) **9**, p. 021035 (2019). [Cited on pages 15, 22, 44, 45, 123, and 124]
- [50] R. SAINT-JALM; *Exploring two-dimensional physics with Bose gases in box potentials: phase ordering and dynamical symmetry*; PhD Thesis; Université Paris Sciences et Lettres (2019). [Cited on pages 15, 17, 20, 22, 29, 30, 43, 52, 105, 123, and 124]
- [51] Y.-Q. ZOU, B. BAKKALI-HASSANI, C. MAURY, É. LE CERF, S. NASCIMBENE, J. DALIBARD & J. BEUGNON; “Tan’s two-body contact across the superfluid transition of a planar Bose gas”; [Nature Communications](#) **12**, p. 760 (2021). [Cited on pages 15, 28, 49, and 79]



- [52] Y.-Q. ZOU, B. BAKKALI-HASSANI, C. MAURY, É. LE CERF, S. NASCIMBENE, J. DALIBARD & J. BEUGNON; “Magnetic Dipolar Interaction between Hyperfine Clock States in a Planar Alkali Bose Gas”; *Physical Review Letters* **125** (2020). [Cited on pages 15, 33, 35, 87, and 88]
- [53] É. LE CERF; *Demixing phenomena in 2D Bose gases*; PhD Thesis; Sorbonne Université (2020). [Cited on pages 15, 17, 23, 29, 30, 76, 77, 91, and 94]
- [54] I. BLOCH, J. DALIBARD & W. ZWERGER; “Many-body physics with ultracold gases”; *Review of Modern Physics* **80**, pp. 885–964 (2008). [Cited on page 17]
- [55] D. A. STECK; “Rubidium 87 D Line Data”; (2019). <http://steck.us/alkalidata>. [Cited on page 17]
- [56] K. KLEINLEIN; *Setting up a new experiment for investigating artificial magnetism of two-dimensional Bose gases*; Master’s Thesis; Ludwig-Maximilians-Universität – München (2014). [Cited on page 17]
- [57] L. CORMAN; *The two-dimensional Bose Gas in box potentials*; PhD Thesis; Université Paris sciences et lettres (2016). [Cited on page 17]
- [58] J.-L. VILLE; *Quantum gases in box potentials : sound and light in bosonic Flatland*; PhD Thesis; Université Paris sciences et lettres (2018). [Cited on page 17]
- [59] T. C. LI, H. KELKAR, D. MEDELLIN & M. G. RAIZEN; “Real-time control of the periodicity of a standing wave: an optical accordion”; *Optics Express* **16**, pp. 5465–5470 (2008). [Cited on page 20]
- [60] J. L. VILLE, T. BIENAIMÉ, R. SAINT-JALM, L. CORMAN, M. AIDELSBURGER, L. CHOMAZ, K. KLEINLEIN, D. PERCONTE, S. NASCIMBÈNE, J. DALIBARD & J. BEUGNON; “Loading and compression of a single two-dimensional Bose gas in an optical accordion”; *Physical Review A* **95**, p. 013632 (2017). [Cited on page 20]
- [61] L. D. LANDAU & E. M. LIFSHITZ; *Course of Theoretical Physics. Volume 1. Mechanics (Course of Theoretical Physics)*. (1960). [Cited on page 21]
- [62] M. E. GEHM, K. M. O’HARA, T. A. SAVARD & J. E. THOMAS; “Dynamics of noise-induced heating in atom traps”; *Physical Review A* **58**, pp. 3914–3921 (1998). [Cited on page 21]
- [63] J. L., J. RUDOLPH N. K., M. F. B. & D. J. H.; “1.5% root-mean-square flat-intensity laser beam formed using a binary-amplitude spatial light modulator”; *Applied Optics* **48**, pp. 1955–1962 (2009). [Cited on page 23]
- [64] P. ZUPANCIC, P. M. PREISS, R. MA, A. LUKIN, M. E. TAI, M. RISPOLI, R. ISLAM & M. GREINER; “Ultra-precise holographic beam shaping for microscopic quantum control”; *Optics Express* **24**, pp. 13881–13893 (2016). [Cited on page 23]
- [65] C. DORRER & J. D. ZUEGEL; “Design and analysis of binary beam shapers using error diffusion”; *Journal of the Optical Society of America B* **24**, pp. 1268–1275 (2007). [Cited on page 23]
- [66] M. TAJIK, B. RAUER, T. SCHWEIGLER, F. CATALDINI, J. SABINO, F. S. MØLLER, JI, S.-C. IGOR E. MAZETS & J. SCHMIEDMAYER; “Designing arbitrary one-dimensional potentials on an atom chip”; *Optics Express* **27**, pp. 33474–33487 (2019). [Cited on page 23]

- [67] N. PROKOF'EV & B. SVISTUNOV; "Two-dimensional weakly interacting Bose gas in the fluctuation region"; *Physical Review A* **66**, p. 043608 (2002). [Cited on page 27]
- [68] C.-L. HUNG, X. ZHANG, N. GEMELKE & C. CHIN; "Observation of scale invariance and universality in two-dimensional Bose gases"; *Nature* **470**, pp. 236–239 (2011). [Cited on pages 27 and 49]
- [69] T. YEFSAH, R. DESBUQUOIS, L. CHOMAZ, K. J. GÜNTER & J. DALIBARD; "Exploring the Thermodynamics of a Two-Dimensional Bose Gas"; *Physical Review Letters* **107**, p. 130401 (2011). [Cited on page 27]
- [70] K. HUECK, N. LUICK, L. SOBIREY, J. SIEGL, T. LOMPE & H. MORITZ; "Two-Dimensional Homogeneous Fermi Gases"; *Physical Review Letters* **120**, p. 060402 (2018). [Cited on page 27]
- [71] L. CHOMAZ, L. CORMAN, T. YEFSAH, R. DESBUQUOIS & J. DALIBARD; "Absorption imaging of a quasi-two-dimensional gas: a multiple scattering analysis"; *New Journal of Physics* **14**, p. 055001 (2012). [Cited on page 27]
- [72] L. CORMAN, J. L. VILLE, R. SAINT-JALM, M. AIDELSBURGER, T. BIENAIMÉ, S. NASCIMBÈNE, J. DALIBARD & J. BEUGNON; "Transmission of near-resonant light through a dense slab of cold atoms"; *Physical Review A* **96**, p. 053629 (2017). [Cited on page 27]
- [73] D. M. HARBER, H. J. LEWANDOWSKI, J. M. MCGUIRK & E. A. CORNELL; "Effect of cold collisions on spin coherence and resonance shifts in a magnetically trapped ultracold gas"; *Physical Review A* **66**, p. 053616 (2002). [Cited on page 28]
- [74] P. A. ALTIN, G. McDONALD, D. DÖRING, J. E. DEBS, T. H. BARTER, J. D. CLOSE, N. P. ROBINS, S. A. HAINE, T. M. HANNA & R. P. ANDERSON; "Optically trapped atom interferometry using the clock transition of large87Rb Bose–Einstein condensates"; *New Journal of Physics* **13**, p. 065020 (2011). [Cited on pages 29 and 33]
- [75] H. SCHMALJOHANN, M. ERHARD, J. KRONJÄGER, M. KOTTKE, S. VAN STAA, L. CACCIAPUOTI, J. J. ARLT, K. BONGS & K. SENGSTOCK; "Dynamics of  $F = 2$  Spinor Bose-Einstein Condensates"; *Physical Review Letters* **92** (2004). [Cited on pages 32 and 33]
- [76] C. J. PETHICK & H. SMITH; *Bose–Einstein Condensation in Dilute Gases*; 2nd edition (Cambridge University Press) (2008). [Cited on pages 32, 77, and 105]
- [77] S. E. POLLACK, D. DRIES, M. JUNKER, Y. P. CHEN, T. A. CORCOVILOS & R. G. HULET; "Extreme Tunability of Interactions in a  $^7\text{Li}$  Bose-Einstein Condensate"; *Physical Review Letters* **102**, p. 090402 (2009). [Cited on page 33]
- [78] M. FATTORI, G. ROATI, B. DEISSLER, C. D'ERRICO, M. ZACCANTI, M. JONALASINIO, L. SANTOS, M. INGUSCIO & G. MODUGNO; "Magnetic Dipolar Interaction in a Bose-Einstein Condensate Atomic Interferometer"; *Physical Review Letters* **101**, p. 190405 (2008). [Cited on page 33]
- [79] M. VENGALATTORE, S. R. LESLIE, J. GUZMAN & D. M. STAMPER-KURN; "Spontaneously Modulated Spin Textures in a Dipolar Spinor Bose-Einstein Condensate"; *Physical Review Letters* **100**, p. 170403 (2008). [Cited on page 33]

- [80] Y. ETO, H. SAITO & T. HIRANO; “Observation of Dipole-Induced Spin Texture in an  $^{87}\text{Rb}$  Bose-Einstein Condensate”; [Physical Review Letters](#) **112**, p. 185301 (2014). [Cited on page 33]
- [81] U. R. FISCHER; “Stability of quasi-two-dimensional Bose-Einstein condensates with dominant dipole-dipole interactions”; [Physical Review A](#) **73**, p. 031602 (2006). [Cited on pages 34 and 131]
- [82] J. DALIBARD; “Collisional dynamics of ultra-cold atomic gases”; Proceedings of the International School of Physics Enrico Fermi (1998). [Cited on page 34]
- [83] T. LAHAYE, C. MENOTTI, L. SANTOS, M. LEWENSTEIN & T. PFAU; “The physics of dipolar bosonic quantum gases”; [Reports on Progress in Physics](#) **72**, p. 126401 (2009). [Cited on pages 34 and 134]
- [84] L. D. LANDAU & L. M. LIFSHITZ; *Quantum Mechanics Non-Relativistic Theory, Third Edition: Volume 3 (Course of Theoretical Physics)*; 3rd edition (Butterworth-Heinemann). (1981). [Cited on page 34]
- [85] J. DALIBARD; “Les interactions entre atomes dans les gaz quantiques. De l’universalité de van der Waals aux résonances de Fano–Feshbach”; Cours du Collège de France (2021). [Cited on pages 34 and 38]
- [86] Z. HADZIBABIC & J. DALIBARD; “Two-dimensional Bose fluids: An atomic physics perspective”; [La Rivista del Nuovo Cimento](#) **34**, pp. 389–434 (2011). [Cited on pages 37, 39, 49, and 50]
- [87] J. DALIBARD; “Fluides quantiques de basse dimension et transition de Kosterlitz–Thouless”; Cours du Collège de France (2017). [Cited on pages 37, 46, and 49]
- [88] D. S. PETROV, D. M. GANGARDT & G. V. SHLYAPNIKOV; “Low-dimensional trapped gases”; [Journal de Physique IV](#) **116**, pp. 5–44 (2004). [Cited on page 39]
- [89] L. PITAEVSKII & S. STRINGARI; *Bose-Einstein Condensation and Superfluidity*; International Series of Monographs on Physics ([Oxford University Press, Oxford](#)) (2016). [Cited on pages 40, 109, and 143]
- [90] L. D. CARR & C. W. CLARK; “Vortices and ring solitons in Bose-Einstein condensates”; [Physical Review A](#) **74**, p. 043613 (2006). [Cited on page 41]
- [91] N. N. BOGOLIUBOV; “On the theory of superfluidity”; *Izvestiya vuz. Fizika* **11**, pp. 23–32 (1947). [Cited on pages 42 and 48]
- [92] L. LANDAU; “Theory of the Superfluidity of Helium II”; [Physical Review](#) **60**, pp. 356–358 (1941). [Cited on page 42]
- [93] J. L. VILLE, R. SAINT-JALM, E. LE CERF, M. AIDELSBURGER, S. NASCIMBÈNE, J. DALIBARD & J. BEUGNON; “Sound Propagation in a Uniform Superfluid Two-Dimensional Bose Gas”; [Physical Review Letters](#) **121**, p. 145301 (2018). [Cited on page 42]
- [94] M. BOHLEN, L. SOBIREY, N. LUICK, H. BISS, T. ENSS, T. LOMPE & H. MORITZ; “Sound Propagation and Quantum-Limited Damping in a Two-Dimensional Fermi Gas”; [Physical Review Letters](#) **124**, p. 240403 (2020). [Cited on page 42]

- [95] P. CHRISTODOULOU, M. GAŁKA, N. DOGRA, R. LOPES, J. SCHMITT & Z. HADZIBABIC; “Observation of first and second sound in a BKT superfluid”; *Nature* **594**, pp. 191–194 (2021). [Cited on pages 42 and 52]
- [96] C. MORA & Y. CASTIN; “Extension of Bogoliubov theory to quasicondensates”; *Physical Review A* **67**, p. 053615 (2003). [Cited on page 42]
- [97] E. NOETHER; “Invariante Variationsprobleme”; Nachrichten von der Gesellschaft der Wissenschaften zu Göttingen, Mathematisch-Physikalische Klasse **1918**, pp. 235–257 (1918). [Cited on page 43]
- [98] U. NIEDERER; “The maximal kinematical invariance group of the free Schrodinger equation.” *Helvetica Physica Acta* **45**, pp. 802–810 (1972). [Cited on pages 43, 123, and 124]
- [99] B. SUTHERLAND; “Quantum Many-Body Problem in One Dimension: Ground State”; *Journal of Mathematical Physics* **12**, pp. 246–250 (1971). [Cited on page 43]
- [100] B. SUTHERLAND; *Beautiful Models* (World Scientific) (2004). [Cited on page 43]
- [101] W. ZWERGER; “The BCS-BEC crossover and the unitary Fermi gas”; (2012). <https://doi.org/10.1007/978-3-642-21978-8>. [Cited on page 43]
- [102] F. WERNER & Y. CASTIN; “The Unitary gas in an isotropic harmonic trap: Symmetry properties and applications”; *Physical Review A* **74**, p. 053604 (2006). [Cited on page 43]
- [103] V. EFIMOV; “Energy levels arising from resonant two-body forces in a three-body system”; *Physics Letters B* **33**, pp. 563–564 (1970). [Cited on pages 43 and 102]
- [104] F. WERNER & Y. CASTIN; “Unitary Quantum Three-Body Problem in a Harmonic Trap”; *Phys. Rev. Lett.* **97**, p. 150401 (2006). [Cited on page 43]
- [105] U. NIEDERER; “The maximal kinematical invariance group of the harmonic oscillator”; *Helvetica Physica Acta* **46**, pp. 191–200 (1973). [Cited on pages 44 and 124]
- [106] L. P. PITAEVSKII & A. ROSCH; “Breathing modes and hidden symmetry of trapped atoms in two dimensions”; *Physical Review A* **55**, pp. R853–R856 (1997). [Cited on page 44]
- [107] W. KOHN; “Cyclotron Resonance and de Haas-van Alphen Oscillations of an Interacting Electron Gas”; *Physical Review* **123**, pp. 1242–1244 (1961). [Cited on page 44]
- [108] F. CHEVY, V. BRETIN, P. ROSENBUSCH, K. W. MADISON & J. DALIBARD; “Transverse Breathing Mode of an Elongated Bose-Einstein Condensate”; *Physical Review Letters* **88**, p. 250402 (2002). [Cited on page 45]
- [109] E. VOGT, M. FELD, B. FRÖHLICH, D. PERTOT, M. KOSCHORRECK & M. KÖHL; “Scale Invariance and Viscosity of a Two-Dimensional Fermi Gas”; *Physical Review Letters* **108**, p. 070404 (2012). [Cited on page 45]
- [110] J. TORRENTS, V. DUNJKO, M. GONCHENKO, G. E. ASTRAKHARCHIK & M. OLSHANII; “The origin of the period- $2T/7$  quasi-breathing in disk-shaped Gross-Pitaevskii breathers”; (2021); [2108.09915](https://arxiv.org/abs/2108.09915). [Cited on page 45]

- [111] Z.-Y. SHI, C. GAO & H. ZHAI; “Idealized Hydrodynamics”; (2020); [2011.01415](#). [Cited on page 45]
- [112] M. OLSHANII, D. DESHOMMES, J. TORRENTS, M. GONCHENKO, V. DUNJKO & G. E. ASTRAKHARCHIK; “Triangular Gross-Pitaevskii breathers and Damski-Chandrasekhar shock waves”; [SciPost Physics](#) **10** (2021). [Cited on page 45]
- [113] B. DAMSKI; “Formation of shock waves in a Bose-Einstein condensate”; [Physical Review A](#) **69** (2004). [Cited on page 45]
- [114] S. K. ADHIKARI; “Quantum scattering in two dimensions”; [American Journal of Physics](#) **54**, pp. 362–367 (1986). [Cited on page 46]
- [115] D. S. PETROV & G. V. SHLYAPNIKOV; “Interatomic collisions in a tightly confined Bose gas”; [Physical Review A](#) **64**, p. 012706 (2001). [Cited on page 46]
- [116] B. R. HOLSTEIN; “Anomalies for pedestrians”; [American Journal of Physics](#) **61**, pp. 142–147 (1993). [Cited on pages 46 and 106]
- [117] M. OLSHANII, H. PERRIN & V. LORENT; “Example of a Quantum Anomaly in the Physics of Ultracold Gases”; [Physical Review Letters](#) **105**, p. 095302 (2010). [Cited on page 46]
- [118] M. HOLTEN, L. BAYHA, A. C. KLEIN, P. A. MURTHY, P. M. PREISS & S. JOCHIM; “Anomalous Breaking of Scale Invariance in a Two-Dimensional Fermi Gas”; [Physical Review Letters](#) **121**, p. 120401 (2018). [Cited on page 46]
- [119] T. PEPPLER, P. DYKE, M. ZAMORANO, I. HERRERA, S. HOINKA & C. J. VALE; “Quantum Anomaly and 2D-3D Crossover in Strongly Interacting Fermi Gases”; [Physical Review Letters](#) **121**, p. 120402 (2018). [Cited on page 46]
- [120] M. BREWCZYK, M. GAJDA & K. RZAŻEWSKI; “Classical fields approximation for bosons at nonzero temperatures”; [Journal of Physics B: Atomic, Molecular and Optical Physics](#) **40**, pp. R1–R37 (2007). [Cited on page 47]
- [121] P. B. BLAKIE, A. S. BRADLEY, M. J. DAVIS, R. J. BALLAGH & C. GARDINER; “Dynamics and statistical mechanics of ultra-cold Bose gases using c-field techniques”; [Advances in Physics](#) **57**, pp. 363–455 (2008). [Cited on page 47]
- [122] N. P. PROUKAKIS & B. JACKSON; “Finite-temperature models of Bose–Einstein condensation”; [41](#), p. 203002 (2008). [Cited on page 47]
- [123] Y. CASTIN; “Bose-Einstein condensates in atomic gases: simple theoretical results”; *Les Houches Summer School* **72**, p. 1 (2000). [Cited on page 48]
- [124] M. NARASCHEWSKI & R. J. GLAUBER; “Spatial coherence and density correlations of trapped Bose gases”; [Physical Review A](#) **59**, pp. 4595–4607 (1999). [Cited on page 48]
- [125] C. COHEN-TANNOUDJI, B. DIU & F. LALOË; *Mécanique quantique. Tome III. Fermions, bosons, photons, corrélations et intrication*. (2017). [Cited on page 48]
- [126] O. PENROSE & L. ONSAGER; “Bose-Einstein Condensation and Liquid Helium”; [Physical Review](#) **104**, pp. 576–584 (1956). [Cited on page 48]



- [127] Y. KAGAN, B. V. SVISTUNOV & G. V. SHLYAPNIKOV; “Influence on inelastic processes of the phase transition in a weakly collisional two-dimensional Bose gas”; *Journal of Experimental and Theoretical Physics* **66**, p. 552 (1987). [Cited on page 48]
- [128] D. S. PETROV, M. HOLZMANN & G. V. SHLYAPNIKOV; “Bose-Einstein Condensation in Quasi-2D Trapped Gases”; *Physical Review Letters* **84**, pp. 2551–2555 (2000). [Cited on page 48]
- [129] Y. KAGAN, V. A. KASHURNIKOV, A. V. KRASAVIN, N. V. PROKOF’EV & B. SVISTUNOV; “Quasicondensation in a two-dimensional interacting Bose gas”; *Physical Review A* **61**, p. 043608 (2000). [Cited on page 48]
- [130] P. CLADÉ, C. RYU, A. RAMANATHAN, K. HELMERSON & W. D. PHILLIPS; “Observation of a 2D Bose Gas: From Thermal to Quasicondensate to Superfluid”; *Physical Review Letters* **102**, p. 170401 (2009). [Cited on page 49]
- [131] S. TUNG, G. LAMPORESI, D. LOBSEY, L. XIA & E. A. CORNELL; “Observation of the Presuperfluid Regime in a Two-Dimensional Bose Gas”; *Physical Review Letters* **105**, p. 230408 (2010). [Cited on page 49]
- [132] F. WERNER & Y. CASTIN; “General relations for quantum gases in two and three dimensions. II. Bosons and mixtures”; *Physical Review A* **86** (2012). [Cited on page 49]
- [133] S. TAN; “Energetics of a strongly correlated Fermi gas”; *Annals of Physics* **323**, p. 2952–2970 (2008). [Cited on page 49]
- [134] S. TAN; “Generalized virial theorem and pressure relation for a strongly correlated Fermi gas”; *Annals of Physics* **323**, p. 2987–2990 (2008). [Cited on page 49]
- [135] S. TAN; “Large momentum part of a strongly correlated Fermi gas”; *Annals of Physics* **323**, p. 2971–2986 (2008). [Cited on page 49]
- [136] R. PEIERLS; “Quelques propriétés typiques des corps solides”; *Annales de l’institut Henri Poincaré* **5**, pp. 177–222 (1935). [Cited on page 49]
- [137] N. N. BOGOLIUBOV; “Quasimittelwerte in Problemen der Statistischen Mechanik I, II”; *Physikalische Abhandlungen Soviet Union* **6**, pp. 1, 113, 229 (1962). [Cited on page 49]
- [138] P. C. HOHENBERG; “Existence of Long-Range Order in One and Two Dimensions”; *Physical Review* **158**, pp. 383–386 (1967). [Cited on page 49]
- [139] N. D. MERMIN & H. WAGNER; “Absence of Ferromagnetism or Antiferromagnetism in One- or Two-Dimensional Isotropic Heisenberg Models”; *Physical Review Letters* **17**, pp. 1133–1136 (1966). [Cited on page 49]
- [140] D. R. NELSON & B. I. HALPERIN; “Dislocation-mediated melting in two dimensions”; *Physical Review B* **19**, pp. 2457–2484 (1979). [Cited on page 50]
- [141] P. MINNHAGEN; “The two-dimensional Coulomb gas, vortex unbinding, and superfluid-superconducting films”; *Review Modern Physics* **59**, pp. 1001–1066 (1987). [Cited on page 50]

- [142] D. J. BISHOP & J. D. REPPY; “Study of the Superfluid Transition in Two-Dimensional  $^4\text{He}$  Films”; [Physical Review Letters](#) **40**, pp. 1727–1730 (1978). [Cited on pages 50 and 51]
- [143] J. KASPRZAK, M. RICHARD, S. KUNDERMANN, A. BAAS, P. JEAMBRUN, J. M. J. KEELING, F. M. MARCHETTI, M. H. SZYMAŃSKA, R. ANDRÉ, J. L. STAEHLI, V. SAVONA, P. B. LITTLEWOOD, B. DEVEAUD & L. S. DANG; “Bose–Einstein condensation of exciton polaritons”; [Nature](#) **443**, pp. 409–414 (2006). [Cited on page 50]
- [144] V. SCHWEIKHARD, S. TUNG & E. A. CORNELL; “Vortex Proliferation in the Berezinskii-Kosterlitz-Thouless Regime on a Two-Dimensional Lattice of Bose-Einstein Condensates”; [Physical Review Letters](#) **99**, p. 030401 (2007). [Cited on page 50]
- [145] B. SVISTUNOV, E. BABAEV & N. PROKOF’EV; *Superfluid States of Matter* (CRC Press) (2015). [Cited on pages 50 and 106]
- [146] J. M. KOSTERLITZ & D. J. THOULESS; “Ordering, metastability and phase transitions in two-dimensional systems”; [Journal of Physics C: Solid State Physics](#) **6**, pp. 1181–1203 (1973). [Cited on page 50]
- [147] V. L. BEREZINSKY; “Destruction of Long-range Order in One-dimensional and Two-dimensional Systems Possessing a Continuous Symmetry Group. II. Quantum Systems.” [Journal of Experimental and Theoretical Physics](#) **34**, p. 610 (1972). [Cited on page 50]
- [148] N. PROKOF’EV, O. RUEBENACKER & B. SVISTUNOV; “Critical Point of a Weakly Interacting Two-Dimensional Bose Gas”; [Physical Review Letters](#) **87**, p. 270402 (2001). [Cited on page 51]
- [149] Z. HADZIBABIC, P. KRÜGER, M. CHENEAU, B. BATTELIER & J. DALIBARD; “Berezinskii–Kosterlitz–Thouless crossover in a trapped atomic gas”; [Nature](#) **441**, pp. 1118–1121 (2006). [Cited on page 52]
- [150] N. R. COOPER & Z. HADZIBABIC; “Measuring the Superfluid Fraction of an Ultracold Atomic Gas”; [Physical Review Letters](#) **104**, p. 030401 (2010). [Cited on page 52]
- [151] S. T. JOHN, Z. HADZIBABIC & N. R. COOPER; “Spectroscopic method to measure the superfluid fraction of an ultracold atomic gas”; [Physical Review A](#) **83**, p. 023610 (2011). [Cited on page 52]
- [152] W. H. NITSCHKE, N. Y. KIM, G. ROUMPOS, C. SCHNEIDER, M. KAMP, S. HÖFLING, A. FORCHEL & Y. YAMAMOTO; “Algebraic order and the Berezinskii-Kosterlitz-Thouless transition in an exciton-polariton gas”; [Physical Review B](#) **90**, p. 205430 (2014). [Cited on page 52]
- [153] P. A. MURTHY, I. BOETTCHER, L. BAYHA, M. HOLZMANN, D. KEDAR, M. NEIDIG, M. G. RIES, A. N. WENZ, G. ZÜRN & S. JOCHIM; “Observation of the Berezinskii-Kosterlitz-Thouless Phase Transition in an Ultracold Fermi Gas”; [Physical Review Letters](#) **115**, p. 010401 (2015). [Cited on page 52]



- [154] S. SUNAMI, V. P. SINGH, D. GARRICK, A. BEREGLI, A. J. BARKER, K. LUKSCH, E. BENTINE, L. MATHEY & C. J. FOOT; “Observation of the BKT Transition in a 2D Bose Gas via Matter-Wave Interferometry”; (2021); [2108.08840](#). [Cited on page 52]
- [155] D. J. KORTEWEG & G. DE VRIES; “XLI. On the change of form of long waves advancing in a rectangular canal, and on a new type of long stationary waves”; [The London, Edinburgh, and Dublin Philosophical Magazine and Journal of Science](#) **39**, pp. 422–443 (1895). [Cited on page 54]
- [156] E. FERMI, P. PASTA, S. ULAM & M. TSINGOU; “Studies of Nonlinear Problems”; (1955). [Cited on pages 54 and 55]
- [157] C. S. GARDNER, J. M. GREENE, M. D. KRUSKAL & R. M. MIURA; “Method for Solving the Korteweg-deVries Equation”; [Phys. Rev. Lett.](#) **19**, pp. 1095–1097 (1967). [Cited on pages 55 and 56]
- [158] C. SULEM & P.-L. SULEM; *The Nonlinear Schrödinger Equation. Self-Focusing and Wave Collapse*; volume 139 ([Springer-Verlag New York](#)) (1999). [Cited on pages 55, 61, 62, and 68]
- [159] V. E. ZAKHAROV; “Collapse of Langmuir Waves”; [Soviet Journal of Experimental and Theoretical Physics](#) **62**, pp. 1745–1759 (1972). [Cited on page 55]
- [160] E. A. KUZNETSOV, A. M. RUBENCHIK & V. E. ZAKHAROV; “Soliton stability in plasmas and hydrodynamics”; [Physics Reports](#) **142**, pp. 103–165 (1986). [Cited on page 55]
- [161] V. E. ZAKHAROV & n. SHABAT, A.; “Exact Theory of Two-dimensional Self-focusing and One-dimensional Self-modulation of Waves in Nonlinear Media”; [Soviet Journal of Experimental and Theoretical Physics](#) **34**, p. 62 (1972). [Cited on page 56]
- [162] D. H. PEREGRINE; “Water waves, nonlinear Schrödinger equations and their solutions”; [The Journal of the Australian Mathematical Society. Series B. Applied Mathematics](#) **25**, p. 16–43 (1983). [Cited on page 56]
- [163] T. TSUZUKI; “Nonlinear waves in the Pitaevskii-Gross equation”; [Journal of Low Temperature Physics](#) **4**, pp. 441–457 (1971). [Cited on page 56]
- [164] A. HASEGAWA & F. TAPPERT; “Transmission of stationary nonlinear optical pulses in dispersive dielectric fibers. I. Anomalous dispersion”; [Applied Physics Letters](#) **23**, pp. 142–144 (1973). [Cited on page 57]
- [165] A. M. WEINER, J. P. HERITAGE, R. J. HAWKINS, R. N. THURSTON, E. M. KIRSCHNER, D. E. LEAIRD & W. J. TOMLINSON; “Experimental Observation of the Fundamental Dark Soliton in Optical Fibers”; [Physical Review Letters](#) **61**, pp. 2445–2448 (1988). [Cited on page 57]
- [166] V. E. ZAKHAROV & S. WABNITZ; *Optical Solitons: Theoretical Challenges and Industrial Perspectives*; volume 12 ([Springer-Verlag Berlin Heidelberg](#)) (1998). [Cited on page 57]
- [167] M. J. ABLOWITZ, G. BIONDINI & L. A. OSTROVSKY; “Optical solitons: Perspectives and applications”; [Chaos: An Interdisciplinary Journal of Nonlinear Science](#) **10**, pp. 471–474 (2000). [Cited on page 57]

- [168] A. L. MARCHANT, T. P. BILLAM, T. P. WILES, M. M. H. YU, S. A. GARDINER & S. L. CORNISH; “Controlled formation and reflection of a bright solitary matter-wave”; *Nature Communications* **4** (2013). [Cited on page 58]
- [169] A. DI CARLI, C. D. COLQUHOUN, G. HENDERSON, S. FLANNIGAN, G.-L. OPPO, A. J. DALEY, S. KUHR & E. HALLER; “Excitation Modes of Bright Matter-Wave Solitons”; *Physical Review Letters* **123**, p. 123602 (2019). [Cited on page 58]
- [170] G. D. McDONALD, C. C. N. KUHN, K. S. HARDMAN, S. BENNETTS, P. J. EVERITT, P. A. ALTIN, J. E. DEBS, J. D. CLOSE & N. P. ROBINS; “Bright Solitonic Matter-Wave Interferometer”; *Physical Review Letters* **113**, p. 013002 (2014). [Cited on page 58]
- [171] V. M. MALKIN & E. G. SHAPIRO; “Elementary excitations for solitons of the nonlinear Schrödinger equation”; *Physica D: Nonlinear Phenomena* **53**, pp. 25–32 (1991). [Cited on pages 58, 66, 111, 123, 125, 126, and 127]
- [172] J. DENSCHLAG, J. E. SIMSARIAN, D. L. FEDER, C. W. CLARK, L. A. COLLINS, J. CUBIZOLLES, L. DENG, E. W. HAGLEY, K. HELMERSON, W. P. REINHARDT, S. L. ROLSTON, B. I. SCHNEIDER & W. D. PHILLIPS; “Generating Solitons by Phase Engineering of a Bose-Einstein Condensate”; *Science* **287**, pp. 97–101 (2000). [Cited on page 58]
- [173] C. QU, L. P. PITAEVSKII & S. STRINGARI; “Magnetic Solitons in a Binary Bose-Einstein Condensate”; *Physical Review Letters* **116**, p. 160402 (2016). [Cited on page 58]
- [174] B. A. MALOMED; “Multidimensional solitons: Well-established results and novel findings”; *The European Physical Journal Special Topics* **225**, p. 2507–2532 (2016). [Cited on pages 58 and 62]
- [175] V. E. ZAKHAROV & A. M. RUBENCHIK; “Instability of waveguides and solitons in nonlinear media”; *Soviet Journal of Experimental and Theoretical Physics* **38**, p. 494 (1974). [Cited on page 59]
- [176] E. GARMIRE, R. Y. CHIAO & C. H. TOWNES; “Dynamics and Characteristics of the Self-Trapping of Intense Light Beams”; *Physical Review Letters* **16**, pp. 347–349 (1966). [Cited on page 60]
- [177] R. Y. CHIAO, E. GARMIRE, M. A. JOHNSON, S. KRINSKY, H. A. SMITH & C. H. TOWNES; “A New Class of Trapped Light Filaments”; *IEEE Journal of Quantum Electronics* **2**, pp. 467–469 (1966). [Cited on page 60]
- [178] Y. R. SHEN; “Self-focusing: Experimental”; *Progress in Quantum Electronics* **4**, pp. 1–34 (1975). [Cited on pages 60 and 73]
- [179] G. C. DUREE, J. L. SHULTZ, G. J. SALAMO, M. SEGEV, A. YARIV, B. CROSIGNANI, P. DI PORTO, E. J. SHARP & R. R. NEURGAONKAR; “Observation of self-trapping of an optical beam due to the photorefractive effect”; *Physical Review Letters* **71**, pp. 533–536 (1993). [Cited on page 60]
- [180] W. E. TORRUELLAS, Z. WANG, D. J. HAGAN, E. W. VANSTRYLAND, G. I. STEGEMAN, L. TORNER & C. R. MENYUK; “Observation of Two-Dimensional Spatial Solitary Waves in a Quadratic Medium”; *Physical Review Letters* **74**, pp. 5036–5039 (1995). [Cited on page 60]

- [181] A. S. REYNA, K. C. JORGE & C. B. DE ARAÚJO; “Two-dimensional solitons in a quintic-septimal medium”; *Physical Review A* **90**, p. 063835 (2014). [Cited on page 60]
- [182] J. W. FLEISCHER, M. SEGEV, N. K. EFREMIDIS & D. N. CHRISTODOULIDES; “Observation of two-dimensional discrete solitons in optically induced nonlinear photonic lattices”; *Nature* **422**, pp. 147–150 (2003). [Cited on page 60]
- [183] E. A. CERDA-MÉNDEZ, D. SARKAR, D. N. KRIZHANOVSKII, S. S. GAVRILOV, K. BIERMANN, M. S. SKOLNICK & P. V. SANTOS; “Exciton-Polariton Gap Solitons in Two-Dimensional Lattices”; *Physical Review Letters* **111**, p. 146401 (2013). [Cited on page 60]
- [184] S. MINARDI, F. EILENBERGER, Y. V. KARTASHOV, A. SZAMEIT, U. RÖPKE, J. KOBELKE, K. SCHUSTER, H. BARTELT, S. NOLTE, L. TORNER, F. LEDERER, A. TÜNNERMANN & T. PERTSCH; “Three-Dimensional Light Bullets in Arrays of Waveguides”; *Physical Review Letters* **105**, p. 263901 (2010). [Cited on page 60]
- [185] E. L. FALCÃO FILHO, C. B. DE ARAÚJO, G. BOUDEBS, H. LEBLOND & V. SKARKA; “Robust Two-Dimensional Spatial Solitons in Liquid Carbon Disulfide”; *Physical Review Letters* **110**, p. 013901 (2013). [Cited on page 60]
- [186] Y. SILBERBERG; “Collapse of optical pulses”; *Optics Letters* **15**, pp. 1282–1284 (1990). [Cited on page 60]
- [187] M. UEDA & A. J. LEGGETT; “Macroscopic Quantum Tunneling of a Bose-Einstein Condensate with Attractive Interaction”; *Physical Review Letters* **80**, pp. 1576–1579 (1998). [Cited on page 60]
- [188] S. L. CORNISH, S. T. THOMPSON & C. E. WIEMAN; “Formation of Bright Matter-Wave Solitons during the Collapse of Attractive Bose-Einstein Condensates”; *Physical Review Letters* **96**, p. 170401 (2006). [Cited on pages 60, 61, and 109]
- [189] N. G. PARKER, A. M. MARTIN, S. L. CORNISH & C. S. ADAMS; “Collisions of bright solitary matter waves”; *Journal of Physics B: Atomic, Molecular and Optical Physics* **41**, p. 045303 (2008). [Cited on page 60]
- [190] N. MEYER, H. PROUD, M. PEREA-ORTIZ, C. O’NEALE, M. BAUMERT, M. HOLYNSKI, J. KRONJÄGER, G. BARONTINI & K. BONGS; “Observation of Two-Dimensional Localized Jones-Roberts Solitons in Bose-Einstein Condensates”; *Physical Review Letters* **119**, p. 150403 (2017). [Cited on page 60]
- [191] T. D. LEE, K. HUANG & C. N. YANG; “Eigenvalues and Eigenfunctions of a Bose System of Hard Spheres and Its Low-Temperature Properties”; *Physical Review* **106**, pp. 1135–1145 (1957). [Cited on page 60]
- [192] D. S. PETROV & G. E. ASTRAKHARCHIK; “Ultradilute Low-Dimensional Liquids”; *Physical Review Letters* **117**, p. 100401 (2016). [Cited on page 60]
- [193] P. CHEINEY, C. R. CABRERA, J. SANZ, B. NAYLOR, L. TANZI & L. TARRUELL; “Bright Soliton to Quantum Droplet Transition in a Mixture of Bose-Einstein Condensates”; *Physical Review Letters* **120**, p. 135301 (2018). [Cited on page 61]
- [194] P. L. KELLEY; “Self-Focusing of Optical Beams”; *Physical Review Letters* **15**, pp. 1005–1008 (1965). [Cited on pages 61 and 70]

- [195] E. J. WOODBURY & W. K. NG; “Ruby laser operation in near IR”; Proceedings of the Institute of Radio Engineers (1962). [Cited on page 61]
- [196] M. HERCHER; “Laser-induced Damage in Transparent Media”; Journal of the Optical Society of America **54**, p. 563 (1964). [Cited on page 61]
- [197] S. BACKUS, C. G. DURFEE, M. M. MURNANE & H. C. KAPTEYN; “High power ultrafast lasers”; [Review of Scientific Instruments](#) **69**, pp. 1207–1223 (1998). [Cited on page 61]
- [198] G. FIBICH; *The Nonlinear Schrödinger Equation. Singular Solutions and Optical Collapse*; volume 192 ([Springer International Publishing](#)) (2015). [Cited on pages 61, 68, and 71]
- [199] E. A. DONLEY, N. R. CLAUSSEN, S. L. CORNISH, J. L. ROBERTS, E. A. CORNELL & C. E. WIEMAN; “Dynamics of collapsing and exploding Bose–Einstein condensates”; [Nature](#) **412**, pp. 295–299 (2001). [Cited on page 62]
- [200] C. EIGEN, A. L. GAUNT, A. SULEYMANZADE, N. NAVON, Z. HADZIBABIC & R. P. SMITH; “Observation of Weak Collapse in a Bose-Einstein Condensate”; [Physical Review X](#) **6**, p. 041058 (2016). [Cited on page 62]
- [201] H. A. HAUS; “Higher Order Trapped Light Beam Solutions”; [Applied Physics Letters](#) **8**, pp. 128–129 (1966). [Cited on pages 63, 65, and 66]
- [202] Z. K. YANKAUSKAS; “Radial field distributions in a self-focusing light beam”; [Soviet Radiophysics](#) **9**, pp. 261–263 (1966). [Cited on pages 63 and 65]
- [203] M. DESAIX, D. ANDERSON & M. LISAK; “Variational approach to collapse of optical pulses”; [Journal of the Optical Society of America B](#) **8**, pp. 2082–2086 (1991). [Cited on pages 65 and 129]
- [204] V. E. ZAKHAROV, V. V. SOBOLEV & V. C. SYNAKH; “Behavior of Light Beams in Nonlinear Media”; Soviet Journal of Experimental and Theoretical Physics (1971). [Cited on pages 66 and 67]
- [205] V. E. ZAKHAROV; “Instability of Self-Focusing of Light”; Soviet Journal of Experimental and Theoretical Physics (1968). [Cited on pages 66 and 125]
- [206] N. G. VAKHITOV & A. A. KOLOKOLOV; “Stationary solutions of the wave equation in a medium with nonlinearity saturation”; [Radiophysics and Quantum Electronics](#) **16**, pp. 783–789 (1973). [Cited on pages 66, 67, 68, and 125]
- [207] M. I. WEINSTEIN; “Modulational Stability of Ground States of Nonlinear Schrödinger Equations”; [SIAM Journal on Mathematical Analysis](#) **16**, pp. 472–491 (1985). [Cited on pages 66 and 125]
- [208] T. J. ALEXANDER & L. BERGE; “Ground states and vortices of matter-wave condensates and optical guided waves”; [Physical Review E](#) **65**, p. 026611 (2002). [Cited on page 67]
- [209] L. D. CARR & C. W. CLARK; “Vortices in Attractive Bose-Einstein Condensates in Two Dimensions”; [Physical Review Letters](#) **97**, p. 010403 (2006). [Cited on pages 67 and 127]

- [210] J. YANG & Z. H. MUSSLIMANI; “Fundamental and vortex solitons in a two-dimensional optical lattice”; *Optics Letters* **28**, pp. 2094–2096 (2003). [Cited on page 67]
- [211] Y. V. KARTASHOV, B. A. MALOMED & L. TORNER; “Solitons in nonlinear lattices”; *Reviews of Modern Physics* **83**, pp. 247–305 (2011). [Cited on page 67]
- [212] G. D. MONTESINOS, V. M. PEREZ-GARCIA & P. TORRES; “Stabilization of solitons of the multidimensional nonlinear Schrödinger equation: matter-wave breathers”; *Physica D: Nonlinear Phenomena* **191**, p. 193–210 (2004). [Cited on page 67]
- [213] V. M. MALKIN; “On the analytical theory for stationary self-focusing of radiation”; *Physica D: Nonlinear Phenomena* **64**, pp. 251–266 (1993). [Cited on pages 67, 70, and 71]
- [214] N. ROSANOV, A. VLADIMIROV, D. SKRYABIN & W. FIRTH; “Internal oscillations of solitons in two-dimensional NLS equation with nonlocal nonlinearity”; *Physics Letters A* **293**, pp. 45–49 (2002). [Cited on pages 67, 100, 103, 112, 113, 147, and 149]
- [215] E. L. DAWES & J. H. MARBURGER; “Computer Studies in Self-Focusing”; *Physical Reviews* **179**, pp. 862–868 (1969). [Cited on page 68]
- [216] V. E. ZAKHAROV; “The Nature of the Self-Focusing Singularity”; *Soviet Journal of Experimental and Theoretical Physics* **68**, pp. 940–947 (1975). [Cited on page 68]
- [217] G. FIBICH & G. PAPANICOLAOU; “Self-Focusing In The Perturbed And Unperturbed Nonlinear Schrödinger Equation In Critical Dimension”; *SIAM Journal on Applied Mathematics* (1999). [Cited on page 69]
- [218] M. I. WEINSTEIN; “Nonlinear Schrödinger equations and sharp interpolation estimates”; *Communications in Mathematical Physics* **87**, pp. 567–576 (1983). [Cited on pages 69 and 127]
- [219] G. FIBICH & A. L. GAETA; “Critical power for self-focusing in bulk media and in hollow waveguides”; *Optics Letters* **25**, pp. 335–337 (2000). [Cited on pages 70, 73, and 130]
- [220] S. A. AKHMANOV, A. P. SUKHORUKOV & R. V. KHOKHLOV; “Self-Focusing and Diffraction of Light in a Nonlinear Medium”; *Soviet Physics Uspekhi* **10**, pp. 609–636 (1968). [Cited on page 70]
- [221] K. D. MOLL, A. L. GAETA & G. FIBICH; “Self-Similar Optical Wave Collapse: Observation of the Townes Profile”; *Physical Review Letters* **90**, p. 203902 (2003). [Cited on pages 70 and 71]
- [222] M. I. WEINSTEIN; “The nonlinear Schrödinger equation: singularity formation, stability and dispersion”; *Contemporary Mathematic* **99**, pp. 213–232 (1989). [Cited on page 71]
- [223] G. M. FRAIMAN; “The asymptotic stability of the manifold of self-similar solutions in the presence of self-focusing”; *Zhurnal Eksperimentalnoi i Teoreticheskoi Fiziki* **88**, pp. 390–400 (1985). [Cited on page 71]



- [224] D. W. McLAUGHLIN, G. C. PAPANICOLAOU, C. SULEM & P. L. SULEM; “Focusing singularity of the cubic Schrödinger equation”; [Physical Review A](#) **34**, pp. 1200–1210 (1986). [Cited on page 71]
- [225] V. E. ZAKHAROV & L. OSTROVSKY; “Modulation instability: The beginning”; *Physica D: Nonlinear Phenomena* **238**, pp. 540–548 (2009). [Cited on page 73]
- [226] L. SALASNICH, A. PAROLA & L. REATTO; “Modulational Instability and Complex Dynamics of Confined Matter-Wave Solitons”; [Physical Review Letters](#) **91**, p. 080405 (2003). [Cited on page 73]
- [227] W. B. COLSON & A. L. FETTER; “Mixtures of Bose liquids at finite temperature”; [Journal of Low Temperature Physics](#) **33**, pp. 231–242 (1978). [Cited on page 76]
- [228] Z. DUTTON & C. W. CLARK; “Effective one-component description of two-component Bose-Einstein condensate dynamics”; *Physical Review A* . [Cited on page 77]
- [229] E. TIMMERMANS; “Phase Separation of Bose-Einstein Condensates”; [Physical Review Letters](#) **81**, pp. 5718–5721 (1998). [Cited on pages 92 and 93]
- [230] P. AO & S. T. CHUI; “Binary Bose-Einstein condensate mixtures in weakly and strongly segregated phases”; [Physical Review A](#) **58**, pp. 4836–4840 (1998). [Cited on pages 92 and 93]
- [231] R. A. BARANKOV; “Boundary of two mixed Bose-Einstein condensates”; [Physical Review A](#) **66**, p. 013612 (2002). [Cited on pages 92 and 114]
- [232] J. BARDEEN, G. BAYM & D. PINES; “Effective Interaction of  $\text{He}^3$  Atoms in Dilute Solutions of  $\text{He}^3$  in  $\text{He}^4$  at Low Temperatures”; [Physical Review](#) **156**, pp. 207–221 (1967). [Cited on pages 102 and 143]
- [233] M. D. SCHWARTZ; *Quantum Field Theory and the Standard Model* (Cambridge University Press). (2014). [Cited on page 102]
- [234] B. J. DESALVO, K. PATEL, G. CAI & C. CHIN; “Observation of fermion-mediated interactions between bosonic atoms”; [Nature](#) **568**, pp. 61–64 (2019). [Cited on page 102]
- [235] G. MODUGNO; “Fermi-Bose mixture with tunable interactions”; **164** (2007). [Cited on page 102]
- [236] P. NAIDON; “Two Impurities in a Bose–Einstein Condensate: From Yukawa to Efimov Attracted Polarons”; [Journal of the Physical Society of Japan](#) **87**, p. 043002 (2018). [Cited on page 102]
- [237] F. GRUSDT & E. DEMLER; “The effective mass of the polaron”; *Journal of Experimental and Theoretical Physics* **18**, pp. 419–423 (1948). [Cited on page 104]
- [238] H. FRÖHLICH; “Electrons in lattice fields”; [Advances in Physics](#) **3**, pp. 325–361 (1954). [Cited on pages 104 and 146]
- [239] F. GRUSDT & E. DEMLER; “New theoretical approaches to Bose polarons”; (2015); 1510.04934. [Cited on pages 104, 145, and 146]

- [240] A. LAMPO, S. H. LIM, M. . GARCÍA-MARCH & M. LEWENSTEIN; “Bose polaron as an instance of quantum Brownian motion”; [Quantum](#) **1**, p. 30 (2017). [Cited on pages 104 and 122]
- [241] Z. YU & C. J. PETHICK; “Induced interactions in dilute atomic gases and liquid helium mixtures”; [Physical Review A](#) **85**, p. 063616 (2012). [Cited on page 105]
- [242] V. N. POPOV; “On the theory of the superfluidity of two- and one-dimensional Bose systems”; [Theoretical and Mathematical Physics](#) **11**, pp. 565–573 (1972). [Cited on page 105]
- [243] A. ROY, M. OTA, A. RECATI & F. DALFOVO; “Finite-temperature spin dynamics of a two-dimensional Bose-Bose atomic mixture”; [Physical Review Research](#) **3**, p. 013161 (2021). [Cited on page 105]
- [244] T. YEFSAH; *Thermodynamique du gaz de Bose à deux dimensions*; PhD Thesis; Université Pierre et Marie Curie - Paris VI (2011). [Cited on page 105]
- [245] S. SINHA, A. Y. CHERNY, D. KOVRIZHIN & J. BRAND; “Friction and Diffusion of Matter-Wave Bright Solitons”; [Physical Review Letters](#) **96**, p. 030406 (2006). [Cited on page 105]
- [246] L. M. AYCOCK, H. M. HURST, D. K. EFIMKIN, D. GENKINA, H.-I. LU, V. M. GALITSKI & I. B. SPIELMAN; “Brownian motion of solitons in a Bose–Einstein condensate”; [Proceedings of the National Academy of Sciences](#) **114**, pp. 2503–2508 (2017). [Cited on page 105]
- [247] H.-W. HAMMER & D. T. SON; “Universal Properties of Two-Dimensional Boson Droplets”; [Physical Review Letters](#) **93**, p. 250408 (2004). [Cited on pages 106 and 107]
- [248] D. LEE; “Large- $N$  droplets in two dimensions”; [Physical Review A](#) **73**, p. 063204 (2006). [Cited on page 106]
- [249] B. BAZAK & D. S. PETROV; “Energy of  $N$  two-dimensional bosons with zero-range interactions”; [New Journal of Physics](#) **20**, p. 023045 (2018). [Cited on page 106]
- [250] P. NAIDON & D. S. PETROV; “Mixed Bubbles in Bose-Bose Mixtures”; [Physical Review Letters](#) **126**, p. 115301 (2021). [Cited on page 107]
- [251] J. CHRISTENSEN-DALSGAARD; “Helioseismology”; [Reviews of Modern Physics](#) **74**, p. 1073–1129 (2002). [Cited on page 109]
- [252] G. I. STEGEMAN & M. SEGEV; “Optical Spatial Solitons and Their Interactions: Universality and Diversity”; [Science](#) **286**, pp. 1518–1523 (1999). [Cited on page 109]
- [253] S. GATZ & J. HERRMANN; “Propagation of optical beams and the properties of two-dimensional spatial solitons in media with a local saturable nonlinear refractive index”; [Journal of the Optical Society of America B](#) **14**, pp. 1795–1806 (1997). [Cited on page 109]
- [254] G. D. MONTESINOS, V. M. PÉREZ-GARCÍA & H. MICHINEL; “Stabilized Two-Dimensional Vector Solitons”; . [Cited on pages 109 and 120]



- [255] S. LANNIG, C.-M. SCHMIED, M. PRÜFER, P. KUNKEL, R. STROHMAIER, H. STROBEL, T. GASENZER, P. G. KEVREKIDIS & M. K. OBERTHALER; “Collisions of Three-Component Vector Solitons in Bose-Einstein Condensates”; [Physical Review Letters](#) **125**, p. 170401 (2020). [Cited on page 109]
- [256] G. FERIOLO, G. SEMEGHINI, L. MASI, G. GIUSTI, G. MODUGNO, M. INGUSCIO, A. GALLEMÍ, A. RECATI & M. FATTORI; “Collisions of Self-Bound Quantum Droplets”; [Physical Review Letters](#) **122**, p. 090401 (2019). [Cited on page 109]
- [257] D. E. PELINOVSKY, Y. S. KIVSHAR & V. V. AFANASJEV; “Internal modes of envelope solitons”; [Physica D: Nonlinear Phenomena](#) **116**, pp. 121–142 (1998). [Cited on page 111]
- [258] C. TICKNOR; “Dispersion relation and excitation character of a two-component Bose-Einstein condensate”; [Physical Review A](#) **89**, p. 053601 (2014). [Cited on page 113]
- [259] I. E. MAZETS; “Waves on an interface between two phase-separated Bose-Einstein condensates”; [Physical Review A](#) **65**, p. 033618 (2002). [Cited on page 113]
- [260] L. D. LANDAU & E. M. LIFSHITZ; *Fluid Mechanics, Second Edition: Volume 6 (Course of Theoretical Physics)*. (1987). [Cited on page 113]
- [261] L. D. AKULENKO & S. V. NESTEROV; “Azimuthal wave motions on the surface of a rotating fluid cylinder”; [Fluid Dynamics](#) **33**, pp. 402–406 (1998). [Cited on page 114]
- [262] K. SASAKI, N. SUZUKI, D. AKAMATSU & H. SAITO; “Rayleigh-Taylor instability and mushroom-pattern formation in a two-component Bose-Einstein condensate”; [Physical Review A](#) **80**, p. 063611 (2009). [Cited on page 115]
- [263] H. TAKEUCHI, N. SUZUKI, K. KASAMATSU, H. SAITO & M. TSUBOTA; “Quantum Kelvin-Helmholtz instability in phase-separated two-component Bose-Einstein condensates”; [Physical Review B](#) **81**, p. 094517 (2010). [Cited on pages 115 and 119]
- [264] K. SASAKI, N. SUZUKI & H. SAITO; “Capillary instability in a two-component Bose-Einstein condensate”; [Physical Review A](#) **83**, p. 053606 (2011). [Cited on page 115]
- [265] M. TRIPPENBACH, Y. B. BAND & P. S. JULIENNE; “Theory of four-wave mixing of matter waves from a Bose-Einstein condensate”; [Physical Review A](#) **62**, p. 023608 (2000). [Cited on page 119]
- [266] K. SASAKI, N. SUZUKI & H. SAITO; “Dynamics of bubbles in a two-component Bose-Einstein condensate”; [Physical Review A](#) . [Cited on page 119]
- [267] B. ALLARD, T. PLISSON, M. HOLZMANN, G. SALOMON, A. ASPECT, P. BOUYER & T. BOURDEL; “Effect of disorder close to the superfluid transition in a two-dimensional Bose gas”; [Physical Review A](#) **85**, p. 033602 (2012). [Cited on page 122]
- [268] A. LUKIN, M. RISPOLI, R. SCHITTKO, M. E. TAI, A. M. KAUFMAN, S. CHOI, V. KHEMANI, J. LÉONARD & M. GREINER; “Probing entanglement in a many-body-localized system”; [Science](#) **364**, pp. 256–260 (2019). [Cited on page 122]
- [269] M. MOCHOL, M. PŁODZIEŃ & K. SACHA; “Dark soliton in a disorder potential”; [Physical Review A](#) **85**, p. 023627 (2012). [Cited on page 122]

- [270] D. J. PAPOULAR, G. V. SHLYAPNIKOV & J. DALIBARD; “Microwave-induced Fano-Feshbach resonances”; [Physical Review A](#) **81**, p. 041603 (2010). [Cited on page 122]
- [271] V. I. TALANOV; “Self-modeling wave beams in a nonlinear dielectric”; [Soviet Radio-physics](#) **9**, pp. 260–261 (1966). [Cited on page 128]
- [272] V. M. PÉREZ-GARCÍA, H. MICHINEL, J. I. CIRAC, M. LEWENSTEIN & P. ZOLLER; “Low Energy Excitations of a Bose-Einstein Condensate: A Time-Dependent Variational Analysis”; [Physical Review Letters](#) **77**, pp. 5320–5323 (1996). [Cited on page 129]
- [273] Y. TANG, W. KAO, K.-Y. LI & B. L. LEV; “Tuning the Dipole-Dipole Interaction in a Quantum Gas with a Rotating Magnetic Field”; [Physical Review Letters](#) **120**, p. 230401 (2018). [Cited on page 134]
- [274] S. GIOVANAZZI, A. GÖRLITZ & T. PFAU; “Tuning the Dipolar Interaction in Quantum Gases”; [Physical Review Letters](#) **89**, p. 130401 (2002). [Cited on page 134]
- [275] J. STUHLER, A. GRIESMAIER, T. KOCH, M. FATTORI, T. PFAU, S. GIOVANAZZI, P. PEDRI & L. SANTOS; “Observation of Dipole-Dipole Interaction in a Degenerate Quantum Gas”; [Physical Review Letters](#) **95**, p. 150406 (2005). [Cited on page 134]
- [276] W. BAO, D. JAKSCH & P. A. MARKOWICH; “Numerical solution of the Gross-Pitaevskii equation for Bose-Einstein condensation”; [Journal of Computational Physics](#) **187**, pp. 318–342 (2003). [Cited on page 137]
- [277] J. JAVANAINEN & J. RUOSTEKOSKI; “Symbolic calculation in development of algorithms: split-step methods for the Gross-Pitaevskii equation”; [Journal of Physics A: Mathematical and General](#) **39**, pp. L179–L184 (2006). [Cited on page 137]
- [278] BADDOUR, N.; “The Discrete Hankel Transform”; [IntechOpen](#) (2019). [Cited on pages 140 and 141]